

Paul Wilhelm Hoffrogge

**UNDERSTANDING DEGRADATION
PHENOMENA IN SOLID-OXIDE
FUEL-CELL ANODES BY PHASE-FIELD
MODELING AND ANALYTICS**

SCHRIFTENREIHE DES INSTITUTS
FÜR ANGEWANDTE MATERIALIEN

BAND 121



Scientific
Publishing

Paul Wilhelm Hoffrogge

**Understanding Degradation Phenomena in
Solid-Oxide Fuel-Cell Anodes by Phase-Field
Modeling and Analytics**

**Schriftenreihe
des Instituts für Angewandte Materialien
*Band 121***

Karlsruher Institut für Technologie (KIT)
Institut für Angewandte Materialien (IAM)

Eine Übersicht aller bisher in dieser Schriftenreihe erschienenen Bände
finden Sie am Ende des Buches.

Understanding Degradation Phenomena in Solid-Oxide Fuel-Cell Anodes by Phase-Field Modeling and Analytics

by
Paul Wilhelm Hoffrogge

Karlsruher Institut für Technologie
Institut für Angewandte Materialien

Understanding Degradation Phenomena in Solid-Oxide
Fuel-Cell Anodes by Phase-Field Modeling and Analytics

Zur Erlangung des akademischen Grades eines Doktors der Ingenieur-
wissenschaften von der KIT-Fakultät für Maschinenbau des Karlsruher
Instituts für Technologie (KIT) genehmigte Dissertation

von Paul Wilhelm Hoffrogge, M.Sc.

Tag der mündlichen Prüfung: 19. Dezember 2023

Referent: Prof. Dr. rer. nat. Britta Nestler

Korreferent: PD Dr.-Ing. André Weber

Impressum



Karlsruher Institut für Technologie (KIT)
KIT Scientific Publishing
Straße am Forum 2
D-76131 Karlsruhe

KIT Scientific Publishing is a registered trademark
of Karlsruhe Institute of Technology.
Reprint using the book cover is not allowed.

www.ksp.kit.edu



*This document – excluding parts marked otherwise, the cover, pictures and graphs –
is licensed under a Creative Commons Attribution 4.0 International License (CC BY 4.0):
<https://creativecommons.org/licenses/by/4.0/deed.en>*



*The cover page is licensed under a Creative Commons
Attribution-NonCommercial 4.0 International License (CC BY-ND 4.0):
<https://creativecommons.org/licenses/by-nd/4.0/deed.en>*

Print on Demand 2024 – Gedruckt auf FSC-zertifiziertem Papier

ISSN 2192-9963

ISBN 978-3-7315-1363-6

DOI 10.5445/KSP/1000170482

Kurzfassung

In der vorliegenden Arbeit werden numerische und analytische Verfahren angewendet, um die quantitative Mikrostrukturmodellierung in Materialsystemen zu erleichtern, die sowohl Volumendiffusion als auch Grenzflächendiffusion beinhalten. Dies wird erreicht, indem ein existierendes Multiphasenfeldmodell für Multikomponentensysteme um einen Term erweitert wird, der Diffusion entlang von Korn- und Phasengrenzen erlaubt. Eine detaillierte analytische Untersuchung der Kombination von Oberflächen- und Volumendiffusion liefert das Verhalten des Modells für eine verschwindende Grenzflächenbreite. Die dadurch erhaltene Gesetzmäßigkeit ist mit einer erweiterten Oberflächenbilanz konsistent und kann quantitativ mit der Oberflächendiffusionstheorie in Einklang gebracht werden. Zusätzlich werden analytische Vorhersagen hoher Ordnung vorgestellt, die den Einfluss von Interpolationsfunktionen in Phasenfeldmodellen des Hindernistyps beleuchten. Die Analyse deckt zum ersten Mal das nichtlineare Modellverhalten in Bezug auf eine Veränderung in der Grenzflächenbreite und -geschwindigkeit auf. Dieser Effekt kann in numerischen Simulationen reproduziert werden. Das erweiterte Multiphasenfeldmodell wird auf Nickelvergrößerung in konventionellen Nickel-YSZ Festoxidbrennstoffzellenanoden angewandt. Eine große Anzahl von dreidimensionalen Simulationsstudien werden durchgeführt, basierend sowohl auf künstlich generierten, als auch experimentell rekonstruierten Mikrostrukturen. Der Einfluss einer Variation in der initialen Mikrostruktur wird in Bezug auf zeitliche Veränderungen von mikrostrukturellen Kenngrößen diskutiert. Die Simulationen der künstlich generierten Strukturen zeigen, dass eine feine Verteilung des YSZ die Vergrößerung des Nickels einschränkt. Dieses mildert schlussendlich die Degradation des Anodenmaterials ab. Die Simulationen basierend auf einer realistischen, durch FIB-SEM Mikroskopie rekonstruierten Mikrostruktur, zeigen

zusätzlich, dass ein geringfügiger Nickelzusatz den Anteil an Nickelinseln reduziert. Es wird gezeigt, dass dies die Langlebigkeit der Anode erhöht. Die räumlich und zeitlich aufgelösten Mikrostrukturdaten, welche durch die Phasenfeldsimulationen bereitgestellt werden, können als Eingangsgrößen für ein Kettenleitermodell verwendet werden. Dies ermöglicht eine Abschätzung der elektrochemischen Eigenschaften der Anode während des Betriebs. Zukunftsperspektiven für die Forschung werden durch die Oberflächenerweiterung erreicht, da diese nicht ausschließlich für die Vergrößerung von Nickel formuliert ist. Dadurch kann eine große Bandbreite von Systemen genauer beschrieben werden, in denen der Transport entlang von Grenzflächen eine entscheidende Rolle spielt, was zuvor nicht möglich war. Die Kombination der Phasenfeldmethode mit Kettenleitermodellen scheint ein zukunftsträchtiger Werkzeugkasten zu sein, da er leicht erweiterbar ist indem man beispielsweise die Komplexität des Kettenleiteransatzes erhöht und auf eine erweiterte Palette von mikrostrukturellen Parametern zurückgreift.

Abstract

The current work combines numerical and analytical techniques to facilitate quantitative microstructure modeling in material systems which include not only bulk diffusion but also diffusion along interfaces. This is achieved by extending an existing multiphase-field model for multicomponent systems with a term allowing diffusion of species along grain and phase boundaries. A detailed analytical investigation delivers the sharp-interface limit of the phase-field model for a combination of surface and bulk diffusion. The obtained governing law is consistent with an extended interfacial balance and can be quantitatively related to surface-diffusion theory. Additionally, high-order analytical predictions are presented concerning the effect of a choice of interpolation function in phase-field models of obstacle type. The analysis unravels for the first time nonlinear model behavior in terms of variations in interface thickness and velocity. This effect is shown to be reproducible in numerical simulations. The extended multiphase-field model is applied to nickel coarsening in conventional nickel-YSZ solid-oxide fuel cell anodes. A large number of three-dimensional simulation studies are performed based on artificially generated as well as experimentally reconstructed microstructures. The influence of variations in the initial microstructure is discussed concerning the evolution of selected key microstructural properties. The simulations on artificially generated structures show that a fine YSZ network can partially suppress the coarsening of nickel which in turn mitigates degradation of the anode material. The simulations on a realistic FIB-SEM reconstructed anode show in addition that a slight increase in nickel content reduces the amount of nickel islands which improves its durability. The spatially and temporally resolved microstructural data provided by phase-field simulations can be used as input for

a transmission-line model providing an estimate of the electrochemical properties of the anode during operation. Future research perspectives are enabled by the surface diffusion extension since it is not exclusively formulated for nickel coarsening. Therefore, a large variety of systems can be accurately rendered where transport along interfaces plays an important role which was not possible before. Combining the phase-field method with transmission-line models seems to be a toolchain with good prospects since it can easily be advanced further e.g. by increasing the complexity of the TLM and incorporating a larger amount of microstructural properties.

Vorwort

Die vorliegende Arbeit entstand am Karlsruher Institut für Technologie (KIT) unter der Betreuung von Prof. Britta Nestler, welche stets von einer großen individuellen Freiheit geprägt war. Daher möchte ich zunächst Frau Prof. Britta Nestler herzlich für die Möglichkeiten der freien und eigenständigen Arbeit und das herübergebrachte Vertrauen danken.

Obwohl die Brennstoffzelle als Anwendung den Fokus der Arbeit bildet, war mein persönliches Ziel stets ein umfassendes theoretisches Verständnis der zugrundeliegenden Mechanismen und Vorgänge zu erlangen. Der Titel und Inhalt der Arbeit kann dies leider nur bedingt widerspiegeln, da die erlangten theoretischen Erkenntnisse für einen externen Betrachter weder neu noch originell erscheinen. An dieser Stelle möchte ich Daniel Schneider, Arnab Mukherjee und Sumanth Nani Enugala besonders danken, die mich in schwierigen Phasen ermutigt haben, dass es sich lohnt, die manchmal unlösbar erscheinenden Aufgaben mit Ruhe und Gelassenheit anzugehen. Andreas Prahs ermöglichte mir einen ganz neuen Einblick auf die Problematik, indem ich auf seinen umfassenden Literaturüberblick bezüglich Bilanzgleichungen auf singulären Oberflächen zurückgreifen konnte. Die vielfältigen Diskussionen und empfohlenen Quellen sind für einen signifikanten Teil des Theoriekapitels verantwortlich.

Für das Korrekturlesen des Dokuments und wertvolle Anmerkungen danke ich Sumanth Nani Enugala, Markus Hoffrogge, Andreas Prahs und Martin Dominik Reder.

Ganz besonders danke ich meinem Gruppenleiter Daniel Schneider, der nicht nur als überaus fachlich versierter Ansprechpartner zur Verfügung stand, sondern

auch auf meine privaten Herausforderungen stets mit Verständnis, Ermutigung und Bestärkung reagiert hat. Auf den kollektiven Wissensschatz von Ephraim Schoof, Felix Konrad Schwab, Johannes Hötzer, Lukas Schöller, Martin Dominik Reder wie auch Simon Daubner und Weiteren konnte ich stets aufbauen, was in einigen Fällen auch erfolgreiche Veröffentlichungen hervorgebracht hat. Unserem Admin Christof Ratz danke ich insbesondere für seine schnellen und unbürokratischen Hilfestellungen bei Computerthemen und seinem unglaublichen Linuxwissen, von dem ich mir einiges aneignen konnte. Des Weiteren danke ich meinen Kollegen Andreas Reiter, Akash Kumar, Henrik Hierl, Lars Cristoph Griem, Ling Fan, Marcel Weichel, Marco Seiz, Michael Späth, Muhammad Umar, Nishant Prajapati, Olena Abramova, Thea Kannenberg, Walter Werner, Willfried Kunz, Xiaoying Liu als auch Weiteren für viele nette berufliche wie auch private Gespräche und Diskussionen. Weiterer Dank geht an Anika Maruszyk, Patricia Haremski und Matthias Wieler von der Robert Bosch GmbH als auch an Florian Wankmüller und André Weber vom IAM-ET des KIT für vielfältige Diskussionen zur Modellierung der Brennstoffzellanoden.

Meinen Verwandten und Freunden danke ich für ihr offenes Ohr während der Zeit in Karlsruhe. Meiner Frau Hana danke ich außerordentlich für die unglaubliche Unterstützung bei der Erziehung unserer beiden Kinder und für vieles andere mehr.

Karlsruhe, im Oktober 2023

Paul Wilhelm Hoffrogge

Preface

This thesis was written at the Karlsruhe Institute of Technology (KIT) under the supervision of Prof. Britta Nestler, which was always characterized by a great deal of individual freedom. Therefore, I would like to thank Prof. Britta Nestler first of all for the possibilities of free and independent work and the trust she has placed in me.

Although the fuel cell as an application is the focus of the thesis, my personal goal was always to gain a comprehensive theoretical understanding of the underlying mechanisms and processes. Unfortunately, the title and content of the thesis can only partially reflect this, as the theoretical insights gained appear neither new nor original from an external point of view. At this point I would like to give special thanks to Daniel Schneider, Arnab Mukherjee and Sumanth Nani Enugala, who encouraged me in difficult phases that it is worthwhile to approach the sometimes seemingly unsolvable tasks with calmness and composure. Andreas Prahs provided me with whole new insights into the problem by allowing me to draw on his extensive literature regarding balance equations on singular surfaces. The diverse discussions and recommended sources are responsible for a significant part of the theory chapter.

For proofreading and valuable comments I would like to thank Sumanth Nani Enugala, Markus Hoffrogge, Andreas Prahs, and Martin Dominik Reder.

I would especially like to thank my group leader Daniel Schneider, who was not only available as an extremely knowledgeable peer, but also always responded to my private challenges with understanding, encouragement and reinforcement. I was always able to build on the collective wealth of knowledge of Ephraim

Schoof, Felix Konrad Schwab, Johannes Hötzer, Lukas Schöller, Martin Dominik Reder as well as Simon Daubner and others, which in some cases also resulted in successful publications. I especially thank our admin Christof Ratz for his fast and unbureaucratic help with computer topics and his incredible Linux knowledge, from which I was able to acquire a lot. Furthermore I would like to thank my colleagues Andreas Reiter, Akash Kumar, Henrik Hierl, Lars Cristoph Griem, Ling Fan, Marcel Weichel, Marco Seiz, Michael Späth, Muhammad Umar, Nishant Prajapati, Olena Abramova, Thea Kannenberg, Walter Werner, Willfried Kunz and Xiaoying Liu, as well as others for many pleasant professional as well as private conversations and discussions. Further thanks go to Anika Marusczyk, Patricia Haremski and Matthias Wieler from Robert Bosch GmbH as well as to Florian Wankmüller and André Weber from IAM-ET at KIT for various discussions on the modeling of fuel cell anodes.

I thank my relatives and friends for lending an ear during the time in Karlsruhe. I thank my wife Hana extraordinarily for her incredible support in raising our two children and for much more.

Karlsruhe, October 2023

Paul Wilhelm Hoffrogge

Nomenclature

Physical Constants

R	Ideal gas constant
ϵ_0	Permittivity of free space

Latin Symbols

A	Thermodynamic prefactor / Surface area
a	Gradient energy prefactor / Dummy variable
A'	Rate constant for bulk diffusion
B	Amount of extensive quantity / Rate constant for surface diffusion
b	Potential energy prefactor / Dummy variable
c_i^m	Concentration of i 'th component
c_i	Composition of i 'th component
D	Diffusivity
D_s	Surface diffusivity
d_{50}	Mean diameter
e	Euler's number
e_{rel}	Relative error
F	Free energy functional
f	Free energy density

g	Auxiliary function
H	Height of a domain
h	Interpolation function / Height
I	Electric current
i	Indicating chemical component
I_g	Dimensionless prefactor
j	Imaginary unit / Scalar flux density
K	Number of chemical components
k	Dummy variable
L	Length of a domain
l_c	Characteristic length
M	Mass / Chemical mobility
m	Interface mobility
m_0	Groove slope
N	Number (of phases)
n	Free integer or real / Indicating normal direction
N_{ref}	Number of refinements
p	Dimensionless parameter relating surface and volume diffusion / Spearman coefficient
P_M^N	Padé approximant of orders M and N
P_N	Partial sum of order N
Q	Electric charge
q	Electric charge density
R	Electric resistance
r	Radial coordinate / Signed distance
R_{pol}	Polarization resistance
s	Arc length / Indicating surface quantity

T	Temperature
t	Time
U	Voltage
u	Moving coordinate
u_E	Model-specific energy unit
u_l	Model-specific length unit
u_t	Model-specific time unit
v	Scalar velocity
V_m	Molar volume
v_n	Normal velocity of interface
W	Width of a domain
X	Macroscopic volume fraction
x	First Cartesian coordinate
$x_0(t)$	Moving interface location
y	Second Cartesian coordinate
z	Third Cartesian coordinate
Z_{TLM}	Impedance of transmission-line model

Greek Symbols

α	Indicating phase α
β	Indicating phase β
Γ	Gamma function
γ	Interfacial energy (parameter)
δ	Indicating phase δ / Interface thickness
$\Delta\Box$	Difference
ε	Interface thickness parameter
ζ	Reaction-related impedance

η	Dimensionless signed distance
θ	Wetting angle
κ	Total curvature (twice mean curvature)
λ	Lagrange multiplier / Penetration depth
μ	Chemical potential
π	Ratio of a circle's circumference to its diameter
ρ	Mass density
ρ_s	Number of atoms per unit area on the surface
σ	Interfacial energy
τ	Relaxation constant (inverse of interface mobility)
τ	Tortuosity
ϕ	Order parameter ranging from 0 to 1
φ	Order parameter ranging from -1 to 1
χ_1	Specific ionic resistance
Ψ	Grand potential functional
ψ	Grand potential density
Ω	Spatial domain
ω	Frequency

Bold Symbols

\mathbf{B}	Magnetic field vector
\mathbf{E}	Electric field vector
\mathbf{j}	Flux density
\mathbf{n}	Normal vector
$\mathbf{q}_{\alpha\beta}$	Generalized gradient vector
\mathbf{s}	Tangential coordinate vector
\mathbf{t}	Unit tangential vector

\boldsymbol{v}	Velocity vector
\boldsymbol{w}	General vector-valued function
\boldsymbol{x}	Position vector

Calligraphic Symbols

\mathcal{B}	General extensive quantity
\mathcal{G}	Gibbs function

Superscripts and Subscripts

$\dot{\square}$	Partial time derivative
$\ddot{\square}$	Normal time derivative
\square^b	Related to bulk
\square^m	Molar
$\square_\alpha / \square^\alpha$	Related to phase α
\square_{bulk}	Bulk contribution
\square_b	Related to density b / related to bulk
\square_i	Related to component i
\square_n	Normal component
\square_s	Related to a surface
\square_t	Tangential component
\square_+ / \square^+	Corresponding to right-hand (positive) side
\square_- / \square^-	Corresponding to left-hand (negative) side
$\square_{\alpha\beta} / \square^{\alpha\beta}$	Related to interface between phase α and β
\square_{el}	Electric
\square_{ion}	Ionic
\square_{ij}	Related to interaction of components i and j
$\tilde{\square}$	Dimensionless quantity

Operators

$\frac{d^n}{dx^n}$	Ordinary derivative of order n w.r.t. x
$\frac{\partial^n}{\partial x^i}$	Partial derivative of order n w.r.t. x
$\frac{\delta^n}{\delta x^i}$	Functional derivative of order n w.r.t. x
∇	Gradient
∇_s	Surface Gradient
$\nabla \cdot$	Divergence
$\nabla_s \cdot$	Surface Divergence
∇^2	Laplacian
∇_s^2	Surface Laplacian

Abbreviations

AFL	Anode functional layer
ATPB	Active triple-phase boundary
CT	Charge transfer
FIB-SEM	Focused ion beam - scanning electron microscopy
LHS	Left-hand side
LSR	Line specific resistance
MPF	Multiphase field
Ni	Nickel
ODE	Ordinary differential equation
PF	Phase field
PSD	Particle size distribution
RHS	Right-hand side
SOF	Solid-oxide fuel
SOFC	Solid-oxide fuel cell

TLM	Transmission-line model
TPB	Triple-phase boundary
TPBL	Triple-phase boundary length
YSZ	Yttria-stabilized zirconia

Contents

Kurzfassung	i
Abstract	iii
Vorwort	v
Preface	vii
Nomenclature	ix
1 Introduction	1
1.1 Fuel-Cell Technology	1
1.2 Phase-field Modeling	2
1.3 Research Objectives	4
1.4 Key Novelties	5
1.5 Structure of the Thesis	6
2 Theoretical Background	7
2.1 Continuum and Microscopic Models	7
2.2 Balance Laws	11
2.2.1 General Balance	11
2.2.2 Balance of Mass	13
2.2.3 Balance of Chemical Species	14
2.2.4 Balance of Electric Charge	18
2.3 Interface Phenomena	19
2.3.1 Surface Parameterization	19
2.3.2 Derivatives on a Surface	21

2.3.3	Interfacial Balance	26
2.3.4	Surface-Excess Properties	28
2.3.5	Surface Diffusion	32
2.3.6	Rate-Reaction Theory	34
2.3.7	Surface Diffusion and Attachment Kinetics	34
2.4	Phase-field Models	35
2.4.1	Two-Phase Models	36
2.4.2	Multiphase-Field Models	41
2.4.3	Models to Couple Diffusion and Phase Transformation	44
2.4.4	Phase-Field Models for Surface Diffusion	49
3	Multiphase-Field Model for Surface and Bulk Diffusion	55
3.1	Model Formulation	56
3.2	Sharp-Interface Limiting Behavior	60
3.2.1	Preliminaries	61
3.2.2	Derivation	74
3.3	Thermal Grooving Study	83
3.3.1	Sharp-Interface Solution	84
3.3.2	Phase-Field Simulation	87
3.4	Conclusion	100
4	Regarding the Choice of Interpolation Function	103
4.1	Introduction	103
4.1.1	Motivation	103
4.1.2	Considered Interpolation Functions	106
4.2	Problem Formulation	107
4.2.1	Statement of the PDE for a Two-Phase System	107
4.2.2	Transformation to an Ordinary Differential Equation	108
4.2.3	Non-Dimensionalization	110
4.3	Exact Solutions	113
4.3.1	General Properties	113
4.3.2	Solution for h_0	117
4.3.3	Solution for h_d	122

4.4	Approximate Asymptotic Solutions	123
4.4.1	Solution Framework	123
4.4.2	Solution at Low Orders	127
4.4.3	Solution at Higher Orders	133
4.4.4	Summation Strategy	141
4.5	Numerical Comparison	144
4.5.1	Setup and Parameterization	145
4.5.2	Results	146
4.6	Discussion	151
4.6.1	Origin of No-Solutions	151
4.6.2	Separation of Numerical and Analytical Errors	152
4.6.3	Remaining Challenges	153
4.7	Conclusion and Outlook	154
5	Nickel Coarsening in SOFC Anodes	157
5.1	Working Principle of SOFCs	158
5.2	Analysis Tools	160
5.2.1	Tortuosity Calculation	160
5.2.2	Triplephase-Boundary Detection	170
5.2.3	Particle Size Distributions	175
5.3	Simulation Studies	178
5.3.1	Model Setup	179
5.3.2	Voronoi Structures	182
5.3.3	Experimentally-Based Structures	198
5.4	Relation to Performance	208
5.5	Conclusion	212
6	Conclusion	215
6.1	Summary	215
6.2	Outlook	216
A	Appendix	219
A.1	Rate Constant for Volume Diffusion	219

A.2 Derivation of PSD for Cylinder with Neck 224

A.3 Transmission-Line Model 227

List of Figures 233

List of Tables 239

Bibliography 241

1 Introduction

Since carbon dioxide emissions from fossil fuels are considered as a principal cause for climate change, countries worldwide committed to implement legal actions for their reduction through the Paris Agreement from 2015. In this light, sustainable technologies are required that can meet the ongoing demand for energy with reduced emission of greenhouse gases such as carbon dioxide.

1.1 Fuel-Cell Technology

Fuel-cell technology is one possible candidate which enables to efficiently generate electricity from a variety of fuels such as hydrogen. There exist different types of fuel cells which can be classified based on the used electrolyte and fuels [1]. For instance, a proton exchange membrane fuel cell (PEMFC) utilizes a water-based electrolyte and its operation temperature is thus limited well below 100 °C. In contrast, solid oxide fuel cells (SOFCs) are based on ceramic electrolytes and operate at temperatures of up to 1000 °C. Each type of fuel cell has its own range of applicability [2]. Compared to other types of fuel cells, SOFCs are highly efficient but are less flexible in terms of variations in load. In contrast they feature a high fuel flexibility, which allows utilization of a large number of different fuels ranging from natural gas over methanol or ethanol to hydrogen. In turn they do not rely on a hydrogen infrastructure a priori, enabling a smooth shift towards environmentally friendly fuel sources as they become more and more available. To date, SOFCs are mostly used for stationary applications. In combination with cogeneration of power and heat, SOFCs can reach a total efficiency of more than 80 % [3].

Therefore, SOFCs constitute a promising alternative to conventional power generation and are gaining an increasing amount of attention recently.

Due to the typically extended operating times of SOFCs, a long lifetime of SOF cells is vital for a cost-effective operation. The elevated operating temperatures of SOFCs lead to high requirements regarding the durability of the materials of which an SOF cell is comprised. Currently, substantial degradation of the cells and their components is limiting the lifetime.

One of the major contributions to cell degradation is attributed to microstructural changes within the SOFC anode functional layer (AFL). Here, nickel coarsening is one of the dominant mechanisms leading to a continuous decay in performance with time [4]. In order to mitigate performance losses attributed to nickel coarsening, a better understanding of the underlying mechanisms is needed.

Experiments aimed at measuring degradation losses can become lengthy and costly because they have to be performed over exhaustive time spans of at least multiple weeks. In addition, detailed in-situ insights at the microscale are often difficult if not impossible to achieve.

In this regard, phase-field modeling constitutes a suitable tool to obtain in-situ information at a high level of detail and to accelerate the investigation of microstructural processes that occur slowly in real time.

1.2 Phase-field Modeling

The phase-field method is a versatile and established tool for modeling microstructural evolution in material science and engineering [5–7]. A distinctive feature of a phase-field model is that an interface is treated as a volumetric region with a small but nonzero thickness (see Fig. 1.1). The advantage of such a depiction is that an explicit parameterization of the interface is circumvented which in turn means that the costly and complex construction of a surface mesh can be avoided.

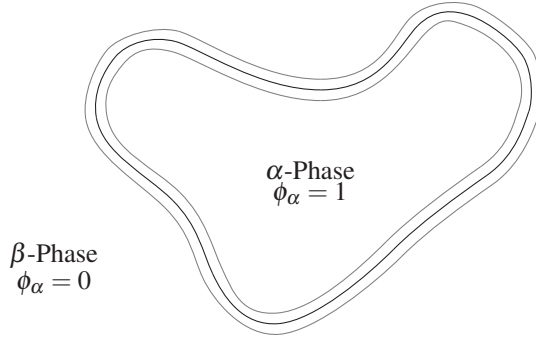


Figure 1.1: Sketch of a two-phase system described by a continuously varying phase field $\phi_\alpha(x, t)$. The finite volumetric region corresponding to the interface (black) between the α and β phase is enclosed by gray curves.

This is particularly helpful because the studied interfaces are not simple stationary entities but evolve in space in a complex manner. Additionally, a realistic microstructure comprises of a large number of interconnected particles that may occasionally break up, coalesce or even disappear. Treating such topological events requires special care such as by joining previously independent meshes in a sharp-interface setup. In contrast, such tasks are trivial in a phase-field model, because they are inherently included in the partial differential equations which define any such model.

The development of phase-field models is an own field of study and bases on first works of [8–10]. There are at least three major breakthroughs worth mentioning in the development of phase-field models.

A first landmark corresponds to the thin-interface corrections proposed in [11–13] which enabled the quantitative modeling of solidification by removing spurious interface-thickness related terms in the model. The improvement was achieved by employing a mathematical technique called *asymptotic analysis* which allows to gain a deep analytical understanding of the model behavior without the need to perform numerical calculations.

The second major advance corresponds to the formulation of multiphase-field models by [14–17]. These type of models are capable to handle not only two distinct phases but an arbitrary number of grains or phases. This tremendously widened the range of applicability of phase-field models.

Lastly, recent developments [18–20] generalized the multiphase-field method to multicomponent systems. This makes the quantitative modeling of phase transformations in alloys possible. Nowadays, complex materials such as steels can be handled by such models (see e.g. [21]) which can also be coupled to the evolution of mechanical stresses and strains [22, 23].

This marks the starting point of the current thesis.

1.3 Research Objectives

The following aims of the thesis are identified:

1. Gain a deeper understanding of both the microstructural processes occurring in a solid-oxide fuel cell anode during operation as well as the phase-field method.
2. Develop a quantitative phase-field model suitable for but not limited to nickel coarsening in SOFC anodes.
3. Apply the model to a realistic SOFC-anode microstructure at operating conditions for a significant amount of time (more than 1000h of operation).
4. Extract key microstructural properties from the time series simulation data and relate them to the performance of the anode.
5. Formulate suggestions to improve the long-term performance of the anode based on the gained insights.

1.4 Key Novelties

The current thesis provides advancements on the following aspects.

Firstly, the grand-potential model could successfully be extended for surface diffusion. Since it rests on the incorporation of any surface diffusion coefficient, it makes this model not only suitable for the treatment of nickel coarsening in SOFC anodes but can also easily be applied to alloys or other materials.

Asymptotic analysis has been performed to show that the model reduces to the appropriate sharp-interface problem for a vanishing interface thickness. Here, the conventional procedure was modified to suit the strictly finite interface width imprinted in the multiphase-field model at hand.

This enabled a further significant advancement: For a much simpler model the asymptotic analysis was employed not only until zeroth or first order but up to eleven orders and could in principle be applied up to arbitrary orders. This presents a major advancement of one of the landmarks in phase-field modeling and has great potential to enable deeper analytical insights into many available phasefield-models.

Thirdly, extensive three-dimensional simulation studies of multiple SOFC anode structures have been performed. The simulations provide new and interesting insights into the mechanisms responsible for anode degradation. Here, microstructure-property relations have been established by means of an existing transmission-line model. This enables an estimation of the evolution of the anode performance with time.

1.5 Structure of the Thesis

The thesis comprises of four main chapters.

Chapter 2 recalls important notions and theories and presents a literature overview covering state-of-the-art phase-field models for surface diffusion. The theories and mathematical techniques presented in this chapter are used in the following chapters in various ways, e.g. as a reference for the results obtained in the asymptotic calculations as well as for several derivations.

Chapter 3 presents the developed multiphase-field model applicable for a combination of surface and volume diffusion in multicomponent systems. In this chapter, asymptotic analysis is performed analyzing the sharp-interface limit of the model which is a generalization of the derivation presented in [24] where pure surface diffusion was treated. An additional section shows a comparative study of thermal (or grain-boundary) grooving, comparing the result from the multiphase-field model with an analytical solution [25].

Chapter 4 provides analytical travelling-wave solutions of planar interfaces for phase-field models of obstacle type. This chapter unravels the differences between different interpolation functions which are a key ingredient in any phase-field model. It contains both exact results as well as approximate solutions, the latter being accurate to very high order.

In chapter 5, the developed multiphase-field model is applied to nickel coarsening in solid-oxide fuel cell anodes under operating conditions. This chapter contains results from a large number of large-scale three-dimensional simulations of both artificially generated as well as experimentally-based structures. Several microstructural quantities and their temporal evolution are discussed in detail using advanced analysis tools. The relation of the microstructural quantities to performance is discussed.

2 Theoretical Background

The strangest thing about a hole is its edge. It's still part of the Something, but it constantly overlooks the Nothing—a border guard of matter. Nothingness has no such guard; while the molecules at the edge of a hole get dizzy because they are staring into a hole, the molecules of the hole get... firmy? There's no word for it. For our language was created by the Something people; the Hole people speak a language of their own.

Kurt Tucholsky "The Social Psychology of Holes"

2.1 Continuum and Microscopic Models

Motivation In designing a mathematical model for a problem at hand, it is often desirable to work with field quantities, i.e. continuous functions that describe the local state of the system at each point in space. Such a model is considered as a continuum model. Possible field quantities are densities of an extensive quantity, such as the mass density, or concentration of a certain species. As one zooms into matter with a microscope of sufficient resolution, it is found that the continuum description is in fact inaccurate, as e.g. a composition or mass density cannot be

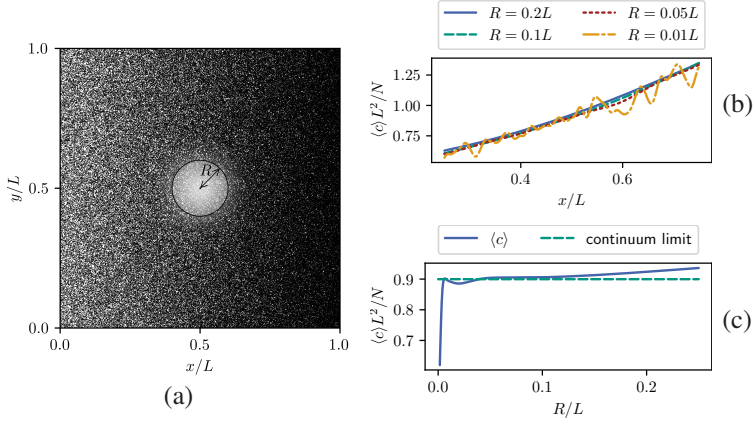


Figure 2.1: $N = 4 \times 10^5$ particles are randomly placed in a 2D-domain of size $L \times L$. The locations are picked from a distribution that increases exponentially with x , resulting in a concentration which ramps up nonlinearly by a factor 5 from $x = 0$ to $x = L$. The coarse-graining procedure with a Gaussian kernel is applied to derive concentration profiles along $y = L/2$ for different widths of the Gaussian R (b). The limiting behavior is shown for the center point ($x = L/2$, $y = L/2$) in (c).

assigned to a single atom. Therefore, a continuum model can only be accurate on length scales that are much larger than interatomic distances, or it is accurate only in a statistical (average) sense. In contrast, one might consider a microscopic model by assigning specific locations to each of the particles (atoms or molecules). Then, the interaction of the individual particles governs the material behavior.

Coarse Graining A connection between the microscopic and the continuum viewpoint might be established through coarse graining, such a procedure is schematically shown in Fig. 2.1. In the microscopic model, the position of a particle p is denoted as \mathbf{x}_p and the amount B of an extensive quantity \mathcal{B} in Ω is given by a discrete sum over all the individual amounts B_p associated with a particle

$$B = \sum_{\mathbf{x}_p \in \Omega} B_p. \quad (2.1)$$

For instance, let B be the mass M , then M_p denotes the mass of an individual atom or molecule. Let V be the volume of the domain,

$$V = \int_{\Omega} dV, \quad (2.2)$$

then one may define a mean density of the extensive quantity by dividing the amount in the domain by its volume

$$\langle b \rangle = \frac{B}{V} = \frac{\sum_{\mathbf{x}_p \in \Omega} B_p}{\int_{\Omega} dV}. \quad (2.3)$$

If one wants to define a density in the continuum sense, a prescription is needed to assign values of $\langle b \rangle$ to each point in space. A possible choice among others (cf. [26, Eq. 1.5]), is choosing a Gaussian convolution kernel centered around the point \mathbf{x} with thickness R :

$$\langle b \rangle(\mathbf{x}) = \frac{\sum_{\mathbf{x}_p \in \Omega} B_p \exp\left(-\frac{|\mathbf{x}-\mathbf{x}_p|^2}{R^2}\right)}{\int_{\mathbf{y} \in \Omega} \exp\left(-\frac{|\mathbf{x}-\mathbf{y}|^2}{R^2}\right) dV}. \quad (2.4)$$

The field $\langle b \rangle(\mathbf{x})$ in general depends on the choice of R , but already is a continuous function of space, that is tractable in a continuum model.

Continuum Limit A remaining problem is the missing knowledge of the size of the coarse-graining cell R , when the solution provided by a continuum model is considered. A possible attempt would be to define the density b of an extensive quantity as a limiting process

$$b(\mathbf{x}) \equiv \lim_{R \rightarrow R_0} \langle b \rangle(\mathbf{x}). \quad (2.5)$$

Unfortunately there is no point of choosing $R_0 = 0$, since then b will be either zero or undefined, depending whether the point \mathbf{x} corresponds to one of the particle locations \mathbf{x}_p or not (Fig. 2.1 (b) showcases the typical oscillatory behavior for a

small $R = 0.01L$). The hypothesis is as follows: If R_0 is chosen in a range much larger than the interatomic distance but small enough to capture the inherent nonlinearities in the corresponding densities, b will only be weakly dependent on R_0 , thus the exact choice of R_0 needs not be necessarily defined. Then Eq. (2.5) may be regarded as the continuum limit of $\langle b \rangle$. In applying a continuum model, one usually assumes, that such a continuum limit exists.

In this book, it is assumed that the continuum limits exist and coarse-grained functions can be obtained that do not depend significantly on the choice of $[R_0]$. Balluffi et al. [26, p. 10]

In the continuum model the amount of \mathcal{B} in Ω is then defined as a volume integral of the density

$$B = \int_{\Omega} b \, dV, \quad (2.6)$$

which is the continuum equivalent to Eq. (2.1).

In the current work, the viewpoint of a continuum model is mostly adopted, whereas references to microscopic or atomistic pictures are pointed out whenever considered necessary.

Interfaces Gradual changes in the microscopic arrangements of atoms or molecules can be readily handled with the coarse-graining procedure established. However, at interfaces, atomic arrangements change at very short ranges on the order of the interatomic distances. These changes might be accompanied by changes in orientation or concentrations (grain and phase boundaries), crystallinity (solid-liquid interfaces), or density (solid-vapor or liquid-vapor interfaces), or a combination thereof. A change in concentration at an interface is schematically shown in Fig. 2.2. It is found, that the coarse-grained concentration profile across the interface (Fig. 2.2 (b)) is crucially determined by the choice of convolution function. This poses a clear restriction on the applicability of a continuum description, and shows that continuum limits do not always exist. To overcome the restrictions

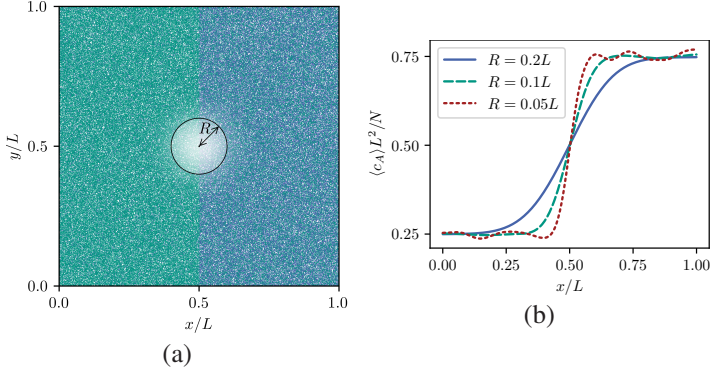


Figure 2.2: $N = 4 \times 10^5$ particles of two different kinds A and B are randomly placed in a 2D-domain of size $L \times L$. The locations are picked from piecewise uniform distributions to create two regions divided at $x = 0.5L$ of differing concentrations. The same coarse-graining procedure as in Fig. 2.1 is applied to derive concentration profiles for species A along $y = L/2$ for different widths of the Gaussian R , which reveals the lack of a continuum limit at $x = 0.5L$ (b).

in a continuum model, an interface in the continuum description might be associated with a discontinuity in the density b (Eq. (2.5)). To deal with interfacial phenomena in continuum models is an own field of study [27, 28], and usually requires special care, as e.g. per the introduction of surface excess properties (cf. subsection 2.3.4). Points at which discontinuities exist are commonly called *singular points* and interfaces in the continuum model are mathematically treated by so-called *singular surfaces* (cf. Moeckel [29]).

2.2 Balance Laws

2.2.1 General Balance

A common observation of nature is that various quantities remain conserved, such as mass, energy or momentum. These quantities are extensive quantities, but may be tensors of varying order (mass and energy are scalars, whereas momentum is a vector quantity). It is customary to start with a general form of a balance law,

as all the above quantities share the same structure of the equation. This notion is put forward by Müller [30, Ch. 3] and Deen [31, Ch. 2.2]. Balance laws are independent of the material behavior which is described by additional constitutive laws Moeckel [29, Ch. 8].

2.2.1.1 Integral Form

Let us consider a possibly time-varying domain Ω with volume V (Eq. (2.2)). Let $d\Omega$ be the surface bounding Ω , then a change in the amount of \mathcal{B} in Ω (Eq. (2.6)) may be either through the normal component of a flux density \mathbf{j}_b (a flux per unit area) on the surface, a source term¹ s_b (amount per unit time and volume) inside the domain, or by a movement of the boundary with velocity \mathbf{v}_s [31, Eq. 2.2-2]:

$$\frac{d}{dt} \left(\int_{\Omega} b dV \right) = - \int_{d\Omega} \mathbf{j}_b \cdot \mathbf{n} dA + \int_{\Omega} s_b dV + \int_{d\Omega} b \mathbf{v}_s \cdot \mathbf{n} dA. \quad (2.7)$$

For scalar quantities, the flux density $\mathbf{j}_b = b\mathbf{v}_b$ may be expressed in terms of a velocity \mathbf{v}_b by which the quantity is transported. Here \mathbf{n} is the unit normal vector of $d\Omega$ pointing outwards of Ω . A quantity where $s_b = 0$ holds is considered as conserved. A domain is called a fixed control volume, when $\mathbf{v}_s \cdot \mathbf{n} = 0$ holds at all points on the surface.

2.2.1.2 Differential Form

Assuming b is differentiable in time, and applying the Leibniz rule to the left-hand side of Eq. (2.7), one finds first that

$$\int_{\Omega} \frac{\partial b}{\partial t} dV = - \int_{d\Omega} \mathbf{j}_b \cdot \mathbf{n} dA + \int_{\Omega} s_b dV \quad (2.8)$$

¹ The source term is often decomposed into a supply and production term, where supply is considered as an externally controllable quantity.

holds. Assuming b is differentiable in space, one can convert the remaining surface integral into a volume integral by using the divergence theorem:

$$\int_{\Omega} \frac{\partial b}{\partial t} + \nabla \cdot \mathbf{j}_b - s_b dV = 0. \quad (2.9)$$

Considering that the choice of Ω is arbitrary, for instance by subdividing the original domain into smaller and smaller subvolumes, one finds by the mean value theorem that

$$\frac{\partial b}{\partial t} + \nabla \cdot \mathbf{j}_b - s_b = 0 \quad (2.10)$$

has to hold for any point in space where b is differentiable. This is known as the differential form of balance law.

2.2.2 Balance of Mass

An important application of the general balance law regards to mass. The mass M of a body in kg

$$M = \int_{\Omega} \rho dV \quad (2.11)$$

is written in terms of the mass density ρ (units of kg/m³).

Integral Form The corresponding integral balance law

$$\frac{d}{dt} \left(\int_{\Omega} \rho dV \right) = - \int_{d\Omega} \mathbf{j}_m \cdot \mathbf{n} dA + \int_{\Omega} s_m dV + \int_{d\Omega} \rho \mathbf{v}_s \cdot \mathbf{n} dA \quad (2.12)$$

includes the momentum density (units of kg/(m²s)) $\mathbf{j}_m = \rho \mathbf{v}$ that can be expressed in terms of the mass-averaged velocity \mathbf{v} (units of m/s), and the mass source s_m . Mass may be converted into energy by radioactive decay which can

be neglected in most practical applications. Under this assumption, one obtains conservation of mass ($s_m = 0$).

Differential Form The differential form of mass balance reads

$$\frac{\partial \rho}{\partial t} + \nabla \cdot (\rho \mathbf{v}) = 0, \quad (2.13)$$

assuming conservation of mass.

2.2.3 Balance of Chemical Species

Matter is comprised of atoms and molecules of different species, the corresponding extensive quantity is the number of atoms or molecules N_i in a body in mol

$$N_i = \int_{\Omega} c_i^m dV \quad (2.14)$$

for a species i (e.g. Aluminum) with concentration c_i^m as the number of atoms or molecules per unit volume (units of mol/m³)².

Integral Form The integral form of the balance of species then writes as follows

$$\frac{d}{dt} \left(\int_{\Omega} c_i^m dV \right) = - \int_{d\Omega} \mathbf{j}_i^m \cdot \mathbf{n} dA + \int_{\Omega} s_i^m dV + \int_{d\Omega} c_i^m \mathbf{v}_s \cdot \mathbf{n} dA, \quad (2.15)$$

where \mathbf{j}_i^m is the flux density of component i in units of mol/(m² s), and s_i^m is the rate of creation of a certain atom or molecule in mol/(m³ s).

² The superscript m is used to indicate that the concentration is a molar quantity, contrasting the dimensionless composition c_i .

Differential Form The differential form of species balance reads

$$\frac{\partial c_i^m}{\partial t} + \nabla \cdot \mathbf{j}_i^m - s_i^m = 0. \quad (2.16)$$

Decomposition of Mass Balance Considering that any molecule or atom carries a so-called molecular mass $M_i = \text{const}$ in units of kg/mol, the balance of mass can be obtained from the balance of chemical species:

$$\begin{aligned} \sum_i \frac{d}{dt} \left(\int_{\Omega} M_i c_i^m dV \right) &= - \sum_i \int_{d\Omega} M_i \mathbf{j}_i^m \cdot \mathbf{n} dA + \sum_i \int_{\Omega} M_i s_i^m dV \\ &+ \sum_i \int_{d\Omega} M_i c_i^m \mathbf{v}_s \cdot \mathbf{n} dA. \end{aligned} \quad (2.17)$$

Here, summation is over all possible species. By introducing the species mass density $\rho_i \equiv M_i c_i^m$ and species mass flux density $\mathbf{j}_{m,i} \equiv M_i \mathbf{j}_i^m$ and the species mass reaction rate $s_{m,i} \equiv M_i s_i^m$, one may write

$$\begin{aligned} \frac{d}{dt} \left(\int_{\Omega} \sum_i \rho_i dV \right) &= - \int_{d\Omega} \sum_i \mathbf{j}_{m,i} \cdot \mathbf{n} dA + \int_{\Omega} \sum_i s_{m,i} dV \\ &+ \int_{d\Omega} \sum_i \rho_i \mathbf{v}_s \cdot \mathbf{n} dA. \end{aligned} \quad (2.18)$$

Since the total mass density is given by the sum over the mass density of all constituents $\rho = \sum_i \rho_i$, it can be seen that the mass balance holds and that the quantities are related by $\rho \mathbf{v} = \sum_i M_i \mathbf{j}_i^m$ and $s_m = \sum_i s_{m,i}$. Thus, in case of mass conservation, a restriction on s_i^m is found as $\sum_i M_i s_i^m = 0$. Therefore, the species balance may be seen as a decomposition of the balance of mass.³ A similar exposition can be found in Müller [30, Sec. 3.2.2].

³ Numerous authors use the term *mass balance* loosely also for the balance of chemical species (cf. e.g. [17, 32, 33]). A separate treatment that aligns well with the current thesis can be found in Deen [31, Ch. 2.6] and Müller [30, Sec. 3.2.2].

Example: Chemical Reactions An important example for cases where s_i^m is nonzero pertains to chemical reactions. For instance consider the reaction $\text{H}_2 + \frac{1}{2} \text{O}_2 \longleftrightarrow \text{H}_2\text{O}$. One may introduce concentrations $c_{\text{H}_2}^m$, $c_{\text{O}_2}^m$ and $c_{\text{H}_2\text{O}}^m$ for each of the molecules involved. The chemical reaction demands that for each creation of a mole of H_2O , a mole of H_2 and half a mole of O_2 is needed. Hence $s_{\text{H}_2}^m = -s_{\text{H}_2\text{O}}^m$ and $s_{\text{O}_2}^m = -1/2 s_{\text{H}_2\text{O}}^m$ holds, where $s_{\text{H}_2\text{O}}^m$ is the reaction rate. Therefore, species are not conserved in case of chemical reactions. To see whether the derived relations fulfill the conservation of mass, one calculates the sum $s_m = M_{\text{H}_2} s_{\text{H}_2}^m + M_{\text{O}_2} s_{\text{O}_2}^m + M_{\text{H}_2\text{O}} s_{\text{H}_2\text{O}}^m = s_{\text{H}_2}^m 2\text{u} + s_{\text{O}_2}^m 32\text{u} + s_{\text{H}_2\text{O}}^m 18\text{u}$, which in fact becomes zero according to the relations between s_i^m stated above.

Molar Volume The molar volume may be defined in a mean sense as the volume of the system divided by the number of particles [34, p. 10]

$$\bar{V}_m \equiv \frac{V}{\sum_i N_i} = \frac{\int_{\Omega} dV}{\int_{\Omega} \sum_i c_i^m dV}. \quad (2.19)$$

Taking the limit as $V \rightarrow 0$ by shrinking the control volume down to a point, in analogy with [35, Eq. (2.3)], the limiting value may be interpreted as the local molar volume

$$V_m \equiv \lim_{V \rightarrow 0} \bar{V}_m = \frac{1}{\sum_i c_i^m}. \quad (2.20)$$

Composition (Mole Fractions) The mole fraction corresponding to species i may be defined again in an integral sense:

$$\bar{c}_i \equiv \frac{N_i}{\sum_i N_i} = \frac{\int_{\Omega} c_i^m dV}{\int_{\Omega} \sum_i c_i^m dV}. \quad (2.21)$$

Taking the limit $V \rightarrow 0$ one finds a local definition for the mole fraction as

$$c_i \equiv \lim_{V \rightarrow 0} \bar{c}_i = V_m c_i^m, \quad (2.22)$$

which is a dimensionless quantity in the range $0 \leq c_i \leq 1$. In the current work, the terms *composition* and *mole fraction* are used analogously.

The local sum of all compositions is always unity

$$\sum_i c_i = 1 \quad (2.23)$$

owing to the definition of the molar volume (Eq. (2.20)).

Special Case 1: Nonreacting Systems For a system, where no chemical reactions take place, $s_i^m = 0 \forall i$ holds. Under this assumption, Eq. (2.16) simplifies to:

$$\frac{\partial c_i^m}{\partial t} = -\nabla \cdot \mathbf{j}_i^m. \quad (2.24)$$

Special Case 2: Constant Molar Volume In case of a time-invariant V_m , one finds a constraint on the evolution of c_i^m as:

$$\sum_i \frac{\partial c_i^m}{\partial t} = \sum_i (\nabla \cdot \mathbf{j}_i^m - s_i^m) = 0. \quad (2.25)$$

Assuming that V_m is also space-invariant, Eq. (2.15) can be multiplied with V_m , to obtain a balance for the composition

$$\frac{d}{dt} \left(\int_{\Omega} c_i dV \right) = - \int_{d\Omega} \mathbf{j}_i \cdot \mathbf{n} dA + \int_{\Omega} s_i dV + \int_{d\Omega} c_i \mathbf{v}_s \cdot \mathbf{n} dA, \quad (2.26)$$

where $\mathbf{j}_i \equiv V_m \mathbf{j}_i^m$ is a flux density in m/s and $s_i \equiv V_m s_i^m$ is a source term in $1/(\text{m}^3 \text{s})$. The corresponding differential form writes

$$\frac{\partial c_i}{\partial t} + \nabla \cdot \mathbf{j}_i - s_i = 0. \quad (2.27)$$

Application: Fick's Laws of Diffusion Fick's laws of diffusion are often used to describe the random atomic motion occurring in a bulk material [36].

Fick's first law is a constitutive relation, relating a flux density of a single species to the gradient in concentration:

$$\mathbf{j}_i^m = -D_i \nabla c_i^m. \quad (2.28)$$

where D_i is the diffusion coefficient in m^2/s . Fick's second law

$$\frac{\partial c_i^m(\mathbf{x}, t)}{\partial t} = \nabla \cdot (D_i \nabla c_i^m) \quad (2.29)$$

follows from the differential species balance (Eq. (2.16)) assuming a nonreacting system.

Applying additionally the assumption of spatially and temporally constant molar volume, multiplying with V_m , Eq. (2.27) yields

$$\frac{\partial c_i(\mathbf{x}, t)}{\partial t} = \nabla \cdot (D_i \nabla c_i) \quad (2.30)$$

the corresponding evolution equation of the composition. Fick's law of diffusion can be generalized to multiple components by introducing interdiffusivities D_{ij} .

2.2.4 Balance of Electric Charge

The electric charge Q of a body in C

$$Q = \int_{\Omega} q \, dV \quad (2.31)$$

is determined from the charge density q in C/m^3 .

Integral Form Since electric charge is conserved, the corresponding integral form of balance is given as

$$\frac{d}{dt} \left(\int_{\Omega} q dV \right) = - \int_{d\Omega} \mathbf{j}_{\text{el}} \cdot \mathbf{n} dA + \int_{d\Omega} q v_s \cdot \mathbf{n} dA, \quad (2.32)$$

where \mathbf{j}_{el} is the electric current density in A/m².

Differential Form The differential form of electric charge balance reads

$$\frac{\partial q}{\partial t} = -\nabla \cdot \mathbf{j}_{\text{el}} \quad (2.33)$$

cf. [37, Eq. (13.8)].

2.3 Interface Phenomena

Motivation In studying microstructures, one is often concerned with the geometry and spatial arrangement of the underlying grains and phases. Grains and phases are separated by interfaces. A change in the spatial distribution of the particles in a microstructure requires a movement of these interfaces. By studying phase transformations in terms of mathematical models, it is necessary to introduce a treatment which allows expressing the partial differential equations from the viewpoint of a moving interface.

2.3.1 Surface Parameterization

A two-dimensional surface is illustrated in Fig. 2.3. Here, the points of which the surface is comprised may be written in terms of a function

$$\mathbf{x} = \mathbf{x}_0(a_1, a_2, t) \quad (2.34)$$

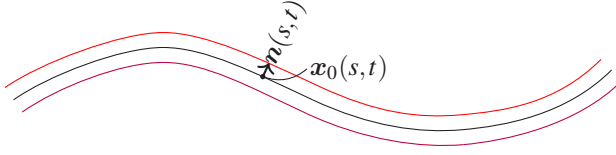


Figure 2.3: Schematic of a moving curvilinear coordinate system comprising of points $\mathbf{x}_0(s, t)$ that are functions of arclength s and time t . Two lines of constant signed distance away from the curve are additionally depicted.

which depends on the surface parameters a_1 and a_2 and time t . The two former dependencies allows one to move tangential to the surface at a fixed time, the latter dependency provides the movement of a surface point holding surface parameters constant. The vector

$$\mathbf{s}_i = \frac{\partial \mathbf{x}_0(a_1, a_2, t)}{\partial a_i} \quad (2.35)$$

is a vector tangential to the interface. If a_i are arclengths, $|\mathbf{s}_i| = 1$. The normal to the surface \mathbf{n} is a unit vector which depends on the location of the curve and is perpendicular to \mathbf{s}_i , hence $\mathbf{n} \cdot \mathbf{s}_i = 0$ holds. Based on the normal vector, one may write points interior and exterior to the surface in terms of a signed distance r

$$\mathbf{x}(a_1, a_2, r, t) = \mathbf{x}_0(a_1, a_2, t) + r\mathbf{n}(a_1, a_2, t). \quad (2.36)$$

The interior might be identified by the condition $r < 0$ and the exterior by $r > 0$. Therefore,

$$\mathbf{n}(a_1, a_2, t) = \frac{\partial \mathbf{x}(a_1, a_2, r, t)}{\partial r} \quad (2.37)$$

is a function solely of the location on the basesurface $\mathbf{x}_0(a_1, a_2, t)$ at a given time. The set of points with $r = \text{const}$ itself can be identified as a surface with a constant distance from the basecurve $\mathbf{x}_0(a_1, a_2, t)$. Two of such curves are illustrated in Fig. 2.3. Assuming that the parameterization through Eq. (2.36) is invertible, one may introduce functions $a_i(\mathbf{x}, t)$ and $r(\mathbf{x}, t)$ that provide for a given point in space

\mathbf{x} the location of the nearest point on the surface and the corresponding distance, respectively.

2.3.2 Derivatives on a Surface

Field quantities are written as functions of the form

$$\phi = \phi(\mathbf{x}, t) \quad (2.38)$$

dependent on the location \mathbf{x} and time t . The function

$$\phi(r, a_1, a_2, t) = \phi(\mathbf{x}(a_1, a_2, r, t), t) \quad (2.39)$$

returns the value of the field quantity evaluated in terms of the surface parameterization (Eq. (2.36)).

However, surface properties such as the curvature, are only meaningfully defined on points making up the surface. Therefore, a surface function is identified as a function of the surface parameters a_i

$$\phi = \phi_s(a_1, a_2, t). \quad (2.40)$$

Based on this description, a normal extension of the function may be defined as follows

$$\phi_{s,n}(\mathbf{x}, t) = \phi_s(a_1(\mathbf{x}, t), a_2(\mathbf{x}, t), t) \quad (2.41)$$

which is constant in the normal direction.

Surface Gradient The surface gradient for a scalar surface field is defined as

$$\nabla_s \phi_s(a_1, a_2, t) \equiv \frac{\partial \phi_s}{\partial a_1} \frac{1}{|\mathbf{s}_1|^2} \mathbf{s}_1 + \frac{\partial \phi_s}{\partial a_2} \frac{1}{|\mathbf{s}_2|^2} \mathbf{s}_2 \quad (2.42)$$

for an orthogonal parameterization, i.e. $\mathbf{s}_1 \cdot \mathbf{s}_2 = 0$. The more general equation for arbitrary parameterizations is given in [28, Eq. A.2.2-4]. The gradient for a scalar field ϕ can be written in a Cartesian coordinate system ($\mathbf{s}_1 \cdot \mathbf{s}_2 = 0$, and $|\mathbf{s}_i| = 1$) for points on the surface ($r = 0$) as

$$\nabla\phi(\mathbf{x}, t) = \frac{\partial\phi}{\partial a_1}\mathbf{s}_1 + \frac{\partial\phi}{\partial a_2}\mathbf{s}_2 + \frac{\partial\phi}{\partial r}\mathbf{n}. \quad (2.43)$$

Accordingly,

$$\nabla\phi(\mathbf{x}, t) = \nabla_s\phi + \frac{\partial\phi}{\partial r}\mathbf{n} \quad (2.44)$$

holds there. Therefore, the surface gradient of a scalar field evaluated at points on the surface is given by projecting the gradient onto the surface.

Surface Divergence The surface divergence for a vector surface field \mathbf{w}_s is defined as

$$\nabla_s \cdot \mathbf{w}_s(a_1, a_2, t) \equiv \frac{\partial \mathbf{w}_s}{\partial a_1} \cdot \frac{\mathbf{s}_1}{|\mathbf{s}_1|^2} + \frac{\partial \mathbf{w}_s}{\partial a_2} \cdot \frac{\mathbf{s}_2}{|\mathbf{s}_2|^2} \quad (2.45)$$

for an orthogonal parameterization. A general equation can be found in [28, Eq. A.5.1-6].

Surface Laplacian The surface Laplacian of a scalar surface field is defined as

$$\nabla_s^2 \phi_s \equiv \nabla_s \cdot \nabla_s \phi_s \quad (2.46)$$

[38, Eq. (75.5)] also known as the Laplace-Beltrami operator. It is a scalar which is invariant with respect to the parameterization of the surface.

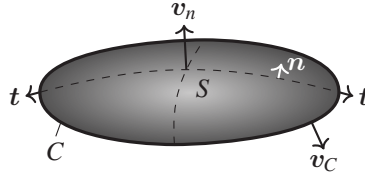


Figure 2.4: Schematic of a moving surface S bounded by a moving curve C . The unit vector \mathbf{t} is tangential to S and normal to C . $\mathbf{v}_C = v_C \mathbf{t}$ is component of the velocity of the curve C which is normal to C and tangential to S .

Surface Divergence Theorem The surface divergence theorem [28, p. 670] can be written as follows:

$$\int_S \nabla_s \cdot \mathbf{w}_s \, dA = \int_C \mathbf{w}_s \cdot \mathbf{t} \, ds + \int_S \kappa \mathbf{w}_s \cdot \mathbf{n} \, dA \quad (2.47)$$

Here \mathbf{w}_s is a vector-valued function on the surface S (assumed to be differentiable along the surface). S is bounded by a simple closed curve C , \mathbf{t} is a unit vector tangential to S and normal to C , pointing outwards of S (cf. Fig. 2.4). s is the arclength measured along C . $\kappa = \nabla_s \cdot \mathbf{n}$ is twice the mean curvature of the surface.

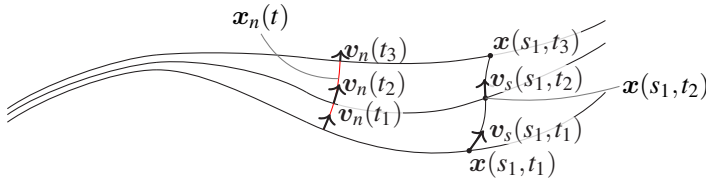


Figure 2.5: Schematic of an evolving surface comprising of points $\mathbf{x}(s,t)$. The parameterization-dependent velocity \mathbf{v}_s is shown indicating how points traverse holding arc length $s = s_1$ constant. Additionally, the vector normal velocity \mathbf{v}_n is shown with the corresponding normal trajectory $\mathbf{x}_n(t)$ for a specific location on the curve.

Normal Time Derivative The partial time derivative

$$\dot{\phi} \equiv \frac{\partial \phi(\mathbf{x}, t)}{\partial t} \quad (2.48)$$

gives the temporal change of the variable ϕ holding the position in space fixed. Consider the case of a moving surface, how does the temporal evolution of the same variable observed by moving attached to the surface relate to the partial time derivative? For that, one might introduce the quantity

$$\frac{\partial \phi(r, a_1, a_2, t)}{\partial t} \quad (2.49)$$

which gives the change of the variable, holding the location and distance to the surface in terms of parameters a_i and r fixed. Employing the chain rule to Eq. (2.39), one obtains

$$\frac{\partial \phi(r, a_1, a_2, t)}{\partial t} = \dot{\phi} + \mathbf{v}_s \cdot \nabla \phi \quad (2.50)$$

$$\mathbf{v}_s = \frac{\partial \mathbf{x}(a_1, a_2, r, t)}{\partial t} = \frac{\partial \mathbf{x}_0(a_1, a_2, t)}{\partial t} + r \frac{\partial \mathbf{n}(a_1, a_2, t)}{\partial t} \quad (2.51)$$

with the surface velocity \mathbf{v}_s which gives the movement of points holding surface parameters a_i and the distance to the basesurface constant. It is convenient to split up the surface velocity into tangential and normal components:

$$\mathbf{v}_s = \mathbf{v}_n + \mathbf{v}_t \quad (2.52)$$

$$\mathbf{v}_n \equiv v_n \mathbf{n} \quad (2.53)$$

$$\mathbf{v}_t \cdot \mathbf{n} = 0 \quad (2.54)$$

where

$$v_n(a_1, a_2, t) \equiv \mathbf{v}_s \cdot \mathbf{n} = \frac{\partial \mathbf{x}_0(a_1, a_2, t)}{\partial t} \cdot \mathbf{n} \quad (2.55)$$

is the scalar normal velocity and $\mathbf{n} \cdot \frac{\partial \mathbf{n}(a_1, a_2, t)}{\partial t} = 0$ can be neglected due to the constant length of the normal vector. Accordingly

$$\frac{\partial \phi(r, a_1, a_2, t)}{\partial t} = \dot{\phi} + v_n \frac{\partial \phi(r, a_1, a_2, t)}{\partial r} + \mathbf{v}_t \cdot \nabla_s \phi \quad (2.56)$$

holds. An important fact which was highlighted by [39] is that the value of v_t depends on the (somewhat arbitrary) choice of parameterization through a_i .

Therefore it is convenient to introduce a normal trajectory $\mathbf{x}_n(r, a_1^0, a_2^0, t)$ corresponding to a reference location parameterized by a_1^0, a_2^0 and time t_0 ,

$$\mathbf{x}_n(r, a_1^0, a_2^0, t_0) = \mathbf{x}(r, a_1^0, a_2^0, t_0) \quad (2.57)$$

$$\frac{\partial \mathbf{x}_n(r, a_1^0, a_2^0, t)}{\partial t} = \mathbf{v}_n \quad (2.58)$$

which means one follows the normal movement of the surface at a given point by accordingly adjusting the surface coordinates a_1 and a_2 . Then the normal time derivative is defined as

$$\overset{\square}{\phi} \equiv \frac{d\phi(\mathbf{x}_n(r, a_1^0, a_2^0, t), t)}{dt} \quad (2.59)$$

at $r = \text{const}$ which gives the observed temporal change of ϕ following the normal movement of the surface. It follows by chainrule that

$$\overset{\square}{\phi} = \dot{\phi} + v_n \frac{\partial \phi(r, a_1, a_2, t)}{\partial r} \quad (2.60)$$

and according to Eq. 2.56 it is obtained that the normal time derivative can be expressed as

$$\overset{\square}{\phi} = \frac{\partial \phi(r, a_1, a_2, t)}{\partial t} - \mathbf{v}_t \cdot \nabla_s \phi \quad (2.61)$$

in terms of the standard partial time derivative on the surface and the surface gradient and velocity.

Surface Transport Theorem The normal time derivative is useful for the surface transport theorem ([40, Eq. (21)] and [39, Eq. 3.14]) which reads

$$\frac{d}{dt} \int_S \varphi_s dA = \int_S \overset{\square}{\varphi}_s + \kappa v_n \varphi_s dA + \int_C \varphi_s v_C ds. \quad (2.62)$$

Here C is the simple closed curve bounding S (see Fig. 2.4), and v_C is the component of the velocity of the curve C which is tangential to S and normal to C and positive when the movement is outwards of S . As discussed earlier, the normal time derivative incorporates changes of the field itself following the normal trajectory. The additional term proportional to the curvature corresponds to changes in the amount by a local reduction in surface area and the last term incorporates changes through the temporally changing bounds of integration induced by a motion of the bounding curve C . It is worth noting that if C moves along the normal trajectory, $v_C = 0$.

2.3.3 Interfacial Balance

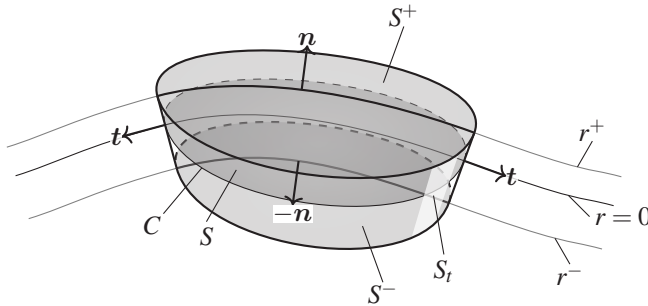


Figure 2.6: Schematic of a control volume which moves with the surface S ($r = 0$). S is bounded by a moving simple closed curve C (it moves with scalar velocity v_C (cf. Fig. 2.4)). Based on C , the control volume is bound by signed distances $r^- < r < r^+$ along normal lines.

So far balances are presented either in integral form or in its differential (or local) form (Sec. 2.2), assuming a spatial differentiability of the density. Often, certain densities such as the mass density change rapidly at interfaces, as shown in section 2.1. Therefore, a generalization of the balance for singular surfaces is needed.

Fig. 2.6 illustrates a control volume Ω which moves with the surface S , bounded by a moving simple closed curve C (for its velocity v_C and the definition of t see also Fig. 2.4). C is extended along normal lines to signed distances r in the range

$r^- < r < r^+$ to form a side surface S_l . The normal velocity of S_l is given by $v_l \mathbf{t}$ with $v_l(r=0) = v_C$. S^\pm are the top and bottom plane corresponding to $r = r^\pm$ with normals $\pm \mathbf{n}$.

For this control volume, the integral balance for a conserved quantity reads

$$\begin{aligned} \frac{d}{dt} \left(\int_{\Omega} b \, dV \right) = & \\ & - \int_{S^+} \mathbf{j}_b^+ \cdot \mathbf{n} \, dA + \int_{S^-} \mathbf{j}_b^- \cdot \mathbf{n} \, dA + \int_{S^+} b^+ v_n \, dA - \int_{S^-} b^- v_n \, dA \\ & - \int_{S_l} \mathbf{j}_b \cdot \mathbf{t} \, dA + \int_{S_l} b v_l \, dA \end{aligned} \quad (2.63)$$

where the density is given as

$$b(\mathbf{x}) = \begin{cases} b^+(\mathbf{x}) & r > 0 \\ b^-(\mathbf{x}) & r < 0 \end{cases} \quad (2.64)$$

and be possibly discontinuous at S ($r = 0$).

In the same manner, the flux density is given by

$$\mathbf{j}_b(\mathbf{x}) = \begin{cases} \mathbf{j}_b^+(\mathbf{x}) & r > 0 \\ \mathbf{j}_b^-(\mathbf{x}) & r < 0 \end{cases}. \quad (2.65)$$

Shrinking down the control volume towards S by letting $r^\pm \rightarrow 0$, one gets $S^\pm \rightarrow S$, $S_l \rightarrow C$ and $\Omega \rightarrow 0$ (which is also known as the pillbox argument [41, p. 15]). In this limit, one obtains

$$0 = \int_S (\mathbf{j}_b^- - \mathbf{j}_b^+) \cdot \mathbf{n} + (b^+ - b^-) v_n \, dA. \quad (2.66)$$

Since the choice of curve C is arbitrary, one localizes the integral and thus

$$v_n (b^+ - b^-) = (\mathbf{j}_b^+ - \mathbf{j}_b^-) \cdot \mathbf{n} \quad \forall \mathbf{x} = \mathbf{x}_0(a_1, a_2, t) \quad (2.67)$$

holds pointwise on the interface. Here b^\pm and \mathbf{j}_b^\pm are the limits evaluated as S is approached from the bulk from either side. This is the interfacial form of balance also known as the jump balance.

2.3.4 Surface-Excess Properties

In deriving the interfacial form of the general balance, a vanishing thickness of the interface was assumed. While this is the most prominent model of interfaces in the context of continuum theories, its limitations are not directly apparent. Since a real interface is comprised of atoms, its thickness is never exactly zero and thus for instance the mass carried by an interface is nonzero. Additionally, the constitutive relations that hold in the bulk are likely not applicable to the interfacial region. While it is difficult to measure for instance the mass density inside an interface, due to its small thickness, the effect of a deviation from the bulk behavior can be quantified by means of excess properties. With excess properties, one associates a surface excess density b_s (amount per unit area) and a surface excess flux density (flux per unit length) with the surface.

For the control volume shown in Fig. 2.6, the extended integral balance for a conserved quantity including a surface excess density b_s and a surface excess flux density $\mathbf{j}_{b,s}$ reads

$$\begin{aligned} \frac{d}{dt} \left(\int_{\Omega} b dV + \int_S b_s dA \right) = & \\ - \int_{S^+} \mathbf{j}_b^+ \cdot \mathbf{n} dA + \int_{S^-} \mathbf{j}_b^- \cdot \mathbf{n} dA + \int_{S^+} b^+ v_n dA - \int_{S^-} b^- v_n dA & \quad (2.68) \\ - \int_{S_t} \mathbf{j}_b \cdot \mathbf{t} dA + \int_{S_t} b v_t dA - \int_C \mathbf{j}_{b,s} \cdot \mathbf{t} ds + \int_C b_s v_C ds. & \end{aligned}$$

On the left-hand side, the balance includes an additional surface integral accounting for b_s and the last two line integrals incorporate contributions from the influx through $\mathbf{j}_{b,s}$ and the enlargement of S in tangential direction through v_C .

Shrinking down the control volume by $r^\pm \rightarrow 0$ as before, one obtains

$$\begin{aligned} \frac{d}{dt} \left(\int_S b_s dA \right) &= \int_S \mathbf{j}_b^- \cdot \mathbf{n} - \mathbf{j}_b^+ \cdot \mathbf{n} + (b^+ - b^-) v_n dA \\ &+ \int_C b_s v_C ds - \int_C \mathbf{j}_{b,s} \cdot \mathbf{t} ds. \end{aligned} \quad (2.69)$$

The surface transport theorem (Eq. (2.62)) can be used to rewrite the left-hand side of the equation to get

$$\int_S \overset{\square}{b}_s + \kappa v_n b_s + (\mathbf{j}_b^+ - \mathbf{j}_b^-) \cdot \mathbf{n} + (b^- - b^+) v_n dA + \int_C \mathbf{j}_{b,s} \cdot \mathbf{t} ds = 0 \quad (2.70)$$

The remaining line integral is rewritten using the surface divergence theorem (Eq. (2.47)) to obtain

$$\int_S \overset{\square}{b}_s + \kappa v_n b_s + (\mathbf{j}_b^+ - \mathbf{j}_b^-) \cdot \mathbf{n} + (b^- - b^+) v_n + \nabla_s \cdot \mathbf{j}_{b,s} - \kappa \mathbf{j}_{b,s} \cdot \mathbf{n} dA = 0. \quad (2.71)$$

Keeping in mind that the choice of curve C was completely arbitrary, one concludes that the integrand has to vanish and hence

$$\overset{\square}{b}_s + \kappa v_n b_s + (\mathbf{j}_b^+ - \mathbf{j}_b^-) \cdot \mathbf{n} + (b^- - b^+) v_n + \nabla_s \cdot \mathbf{j}_{b,s} - \kappa \mathbf{j}_{b,s} \cdot \mathbf{n} = 0 \quad (2.72)$$

is the extended interfacial balance including a surface excess density b_s and a surface excess flux $\mathbf{j}_{b,s}$ holding point-wise on the surface ($\forall \mathbf{x} = \mathbf{x}_0(a_1, a_2, t)$). For a tangential surface excess flux ($\mathbf{j}_{b,s} \cdot \mathbf{n} = 0$) and in the absence of a fluid velocity it is equivalent to [39, Eq. 7.5].

Dividing Surface How are the excess quantities interpreted with respect to the physical picture of an interface of finite thickness? Following [28, p. 56] instead of a density $b(\mathbf{x})$ which is given by the bulk behavior everywhere except with a jump at S , it is assumed that the density in an interfacial region bounded by r^- and r^+ is smooth but markedly different from the bulk density, given by $b_I(\mathbf{x})$.

$b_I(\mathbf{x}(r > r^+)) = b^+(\mathbf{x})$ and $b_I(\mathbf{x}(r < r^-)) = b^-(\mathbf{x})$. Similarly, the flux density is given by $\mathbf{j}_{b,I}(\mathbf{x})$ for $r^- < r < r^+$ and similarly approaches the bulk such that $\mathbf{j}_{b,I}(\mathbf{x}(r > r^+)) = \mathbf{j}_b^+(\mathbf{x})$ and $\mathbf{j}_{b,I}(\mathbf{x}(r < r^-)) = \mathbf{j}_b^-(\mathbf{x})$.

With this definitions at hand, the integral form of balance (Eq. (2.7)) for the control volume shown in Fig. 2.6 is written as

$$\begin{aligned}
 \frac{d}{dt} \left(\int_{\Omega} b_I dV \right) = & \\
 - \int_{S^+} \mathbf{j}_b^+ \cdot \mathbf{n} dA + \int_{S^-} \mathbf{j}_b^- \cdot \mathbf{n} dA + \int_{S^+} b^+ v_n dA - \int_{S^-} b^- v_n dA & \quad (2.73) \\
 - \int_{S_t} \mathbf{j}_{b,I} \cdot \mathbf{t} dA + \int_{S_t} b_I v_t dA &
 \end{aligned}$$

The following form is obtained by highlighting the difference with respect to a pure bulk behavior

$$\begin{aligned}
 \frac{d}{dt} \left(\int_{\Omega} b dV + \int_{\Omega} b_I - b dV \right) = & \\
 - \int_{S^+} \mathbf{j}_b^+ \cdot \mathbf{n} dA + \int_{S^-} \mathbf{j}_b^- \cdot \mathbf{n} dA + \int_{S^+} b^+ v_n dA - \int_{S^-} b^- v_n dA & \quad (2.74) \\
 - \int_{S_t} \mathbf{j}_b \cdot \mathbf{t} dA + \int_{S_t} b v_t dA - \int_{S_t} (\mathbf{j}_{b,I} - \mathbf{j}_b) \cdot \mathbf{t} dA + \int_{S_t} (b_I - b) v_t dA. &
 \end{aligned}$$

When the thickness of the interface is small compared to the radii of curvature ($|r^{\pm} \kappa_1| \ll 1$ and $|r^{\pm} \kappa_2| \ll 1$, where κ_n are principal curvatures) which should be the case for any real interface, one can make the following approximations

$$v_t \approx v_C \quad (2.75)$$

$$\int_{S_t} f dA \approx \int_C \int_{r^-}^{r^+} f dr ds \quad (2.76)$$

$$\int_{\Omega} f dV \approx \int_S \int_{r^-}^{r^+} f dr dA \quad (2.77)$$

to get

$$\begin{aligned}
 \frac{d}{dt} \left(\int_{\Omega} b \, dV + \int_S \int_{r^-}^{r^+} b_I - b \, dr \, dA \right) \approx \\
 - \int_{S^+} \mathbf{j}_b^+ \cdot \mathbf{n} \, dA + \int_{S^-} \mathbf{j}_b^- \cdot \mathbf{n} \, dA + \int_{S^+} b^+ v_n \, dA - \int_{S^-} b^- v_n \, dA \\
 - \int_{S_t} \mathbf{j}_b \cdot \mathbf{t} \, dA + \int_{S_t} b v_t \, dA \\
 - \int_C \int_{r^-}^{r^+} (\mathbf{j}_{b,I} - \mathbf{j}_b) \cdot \mathbf{t} \, dr \, ds + \int_C \int_{r^-}^{r^+} b_I - b \, dr \, v_C \, ds.
 \end{aligned} \tag{2.78}$$

By comparing this equation with the extended balance incorporating surface excess properties (Eq. (2.68)), one can identify the surface excess properties as

$$b_s = \int_{r^-}^{r^+} b_I - b \, dr \tag{2.79}$$

$$\mathbf{j}_{b,s} = \int_{r^-}^{r^+} \mathbf{j}_{b,I} - \mathbf{j}_b \, dr. \tag{2.80}$$

This means that the surface excess properties can be associated with the deviation of the densities in the interfacial region for a real interface of finite thickness. It is worth noting that from the physical point of view, the choice of $r = 0$ as the dividing surface was completely arbitrary. Any other choice of contour which lies within the bounds $r^- < r_0 < r^+$ might be equally valid. In the sharp-interface description one associates two distinct phases with either side of the interface, i.e.

$$b(\mathbf{x}) = \begin{cases} b^+(\mathbf{x}) & r > r_0 \\ b^-(\mathbf{x}) & r < r_0 \end{cases} \tag{2.81}$$

It turns out that the value of b_s then depends on the choice of dividing surface through r_0 . Only if $b^+(\mathbf{x}) = b^-(\mathbf{x}) \forall r^- < r < r^+$, the excess quantity is uniquely determined. For a more thorough discussion, the reader is referred to Mavrounitis and Brenner [27].

2.3.5 Surface Diffusion

In crystals, diffusion occurs in the bulk via the exchange of atoms with vacancies. It is thus clear that at any crystal defect, where atoms are displaced from their lattice positions, the random movement of atoms - what is known as diffusion - is enhanced. As interfaces are two-dimensional lattice defects, the corresponding effect is known as surface (or interface) diffusion. While on the one hand, the diffusivity in the interface may be orders of magnitudes higher compared to the bulk, it is confined to the very thin interfacial layer usually comprising only of a few atomic spacings.

A sharp-interface theory for surface diffusion in pure materials was formulated by [42]. It starts with the Gibbs-Thomson effect, namely the shift of the chemical potential μ with curvature κ :

$$\mu = \mu_{\text{eq}} + V_m \gamma \kappa \quad (2.82)$$

where μ_{eq} is the chemical potential in equilibrium with a flat interface. V_m is the molar volume and γ the interfacial energy.

It is assumed that an excess flux density \mathbf{j}_s acts tangentially to the interface which is driven against the surface gradient of chemical potential

$$\mathbf{j}_s = -\frac{D_s \rho_s}{RT} \nabla_s \mu. \quad (2.83)$$

Here D_s is introduced as the surface diffusivity (in m^2/s and the number of atoms per unit area ρ_s (in mol/m^2) on the surface is the proportionality factor to convert the volumetric quantity to a surface-excess property. The denominator RT is the Einstein relation consisting of the ideal gas constant R and temperature T .

The scalar normal velocity of the interface is given by

$$v_n = -V_m \nabla_s \cdot \mathbf{j}_s = \frac{V_m^2 D_s \rho_s \gamma}{RT} \nabla_s^2 \kappa \quad (2.84)$$

assuming the quantities to be constant along the surface.

This shows that the interface moves proportionally to the surface laplacian of curvature. The proportionality rate constant is given by

$$B \equiv \frac{V_m^2 D_s \rho_s \gamma}{RT} \quad (2.85)$$

and is of unit m^4/s .

It is worth noting the assumptions that lead to Eq. (2.84). This equation can be obtained from the extended interfacial balance (Eq. (2.72)) by the following assignments:

$$\mathbf{j}_b^+ = \mathbf{j}_b^- \rightarrow \mathbf{0} \quad (2.86)$$

$$b_s \rightarrow 0 \quad (2.87)$$

$$\mathbf{j}_{b,s} \rightarrow \mathbf{j}_s \quad (2.88)$$

$$b^- \rightarrow \frac{1}{V_m} \quad (2.89)$$

$$b^+ \rightarrow 0 \quad (2.90)$$

The last two identities show that it is a balance of a single chemical species under constant molar volume by comparing it with the definition of the molar volume (Eq. (2.20)) which leads to the replacement $b \rightarrow c^m$. The concentration in the vapor $c^{m,+}$ is assumed to be negligible and the composition in the solid is assumed to be $c^- = 1$ (see Eq. (2.22)). Additionally vanishing bulk flux densities are assumed both in the solid and in the vapor. A negligible surface excess concentration c_s^m is assumed and \mathbf{j}_s is a non-vanishing surface excess flux of solid atoms along the surface.

2.3.6 Rate-Reaction Theory

While surface diffusion dealt with the atomic transport tangential to the interface, the thermally activated jumps of atoms normal to an interface can cause a net flux away or towards the interface, leading to a reduction or increase of surface area, respectively. This may occur when one of the sides of the interface is energetically favored according to the rate-reaction theory by [43]. This well known theory is recalled in two famous textbooks for grain-boundary migration ([44, p.154] and [45, p.137]). In this theory, the interface normal velocity is directly proportional to a driving force Δf

$$v_n = m\Delta f \quad (2.91)$$

with the proportionality factor m which is a mobility of unit $\text{m}^4/(\text{Js})$. The driving force is of unit J/m^3 and can be seen either as an energy density or a pressure that acts normal to the interface. Note that Eq. (2.91) is not a balance equation but a constitutive relation relating the normal velocity of the interface to a driving force. For an overview of possible driving forces, including capillary forces intrinsic to the interface as well as bulk effects, the interested reader is referred to Gottstein and Shvindlerman [45, p. 141].

2.3.7 Surface Diffusion and Attachment Kinetics

A theory which combines the atomic movement normal to the interface according to rate-reaction theory with surface diffusion in tangential direction is presented in Cahn and Taylor [46]. Here, the normal velocity is defined by the following equation

$$v_n = -\nabla_s^2 \left(\frac{1}{m} \nabla_s^2 - \frac{\gamma}{B} \right)^{-1} \kappa \gamma. \quad (2.92)$$

Two separate processes are retrieved as limiting cases of the above equation, i.e. motion limited by the rate-reaction theory (also known as attachment kinetics) and motion solely according to surface diffusion. The length scale

$$l_c \equiv \sqrt{\frac{B}{m\gamma}} \quad (2.93)$$

is a characteristic length scale set by the material parameters of the interface. At length scales much smaller than l_c , attachment kinetics is the rate-limiting factor. In contrast, when the length scale largely exceeds l_c , diffusion along the tangential direction of the interface is the rate-limiting factor.

When the interface is highly mobile ($m \rightarrow \infty$), the effect of attachment kinetics can be neglected ($l_c \rightarrow 0$) and the interface dynamics are given by Eq. (2.84). When the surface diffusivity is comparably large ($B \rightarrow \infty$), so-called motion by the difference of mean curvature is retrieved ($l_c \rightarrow \infty$). Rätz et al. [47] showed that Eq. (2.92) can alternatively be expressed by the following two coupled second-order equations

$$v_n = \frac{B}{\gamma} \nabla_s^2 \mu \quad (2.94)$$

$$\mu = \mu_{\text{eq}} + \kappa\gamma + \frac{v_n}{m}. \quad (2.95)$$

2.4 Phase-field Models

Phase-field models are used particularly because they efficiently circumvent the complex task of continuously parameterizing and tracking a moving interface. In such a model, the evolution is governed by a spatially and temporally varying function and the interface is associated with a finite volumetric region where this function exhibits large gradients. This function, mostly denoted as $\phi(\mathbf{x}, t)$, is often referred to as a *phase field* or alternatively, as a so-called *order parameter*. While the former naming reflects its use to separate a domain into coexisting

thermodynamic phases, the latter is rooted in its original use to distinguish between an ordered (crystalline) and a disordered (liquid) phase in the context of solidification. The order parameter is dimensionless and tends towards a finite value far away from the interface which is associated with bulk material.

2.4.1 Two-Phase Models

In the most simplest case, a single (or scalar) order parameter is used to distinguish two separate phases. The construction of a phase-field model usually starts with the formulation of a free-energy functional F based on the order parameter in the domain Ω of volume V . In its simplest form it can be written as

$$F = \int_{\Omega} f(\phi) + a|\nabla\phi|^2 dV. \quad (2.96)$$

Here $f(\phi)$ is an energy density (in J/m^3) written as a function of ϕ that defines the potential energy landscape of the model and the second term is a gradient energy that can be scaled with a constant factor a (in J/m). The interplay of these two terms is crucial for a working phase-field model. The potential term defines minima to provide stable bulk states whereas the gradient energy penalizes sharp transitions between these degenerate states. Two important forms of $f(\phi)$ exist, the choice $f(\phi) \propto \phi^2(1-\phi)^2$ is called the double well potential, whereas $f(\phi) \propto \phi(1-\phi)$ is known as the obstacle potential⁴. Both forms are written such that $\phi = 0$ and $\phi = 1$ are the corresponding stable bulk states⁵.

Now that the energy functional is constructed, two main classes of phase-field models can be distinguished based on the way the evolution of the order parameter is postulated.

⁴ The additional Gibbs simplex constraint is omitted here for the sake of brevity.

⁵ Typical bulk values correspond either to -1 and 1 or to zero and 1 , respectively. While this is a matter of mathematical convenience, the latter formalism is easier to generalize to multiphase materials as will be shown in the following subsection. For this reason, the choice of zero and unity is mostly preferred in the current work.

2.4.1.1 Allen-Cahn Model

In phase-field models of Allen-Cahn type [10], the evolution of the order parameter is proportional to the functional derivative of the free energy F :

$$\varepsilon \frac{\partial \phi(\mathbf{x}, t)}{\partial t} = -m \frac{\delta F}{\delta \phi} = -m \left(\frac{df(\phi)}{d\phi} - 2a\nabla^2 \phi \right). \quad (2.97)$$

Here, m is a mobility parameter and has units of $\text{m}^4/(\text{Js})$ and $\varepsilon > 0$ is a parameter related to the interface thickness. A positive mobility is necessary for the evolution to be locally towards a minimum of the free energy.

2.4.1.2 Cahn-Hilliard Model

In phase-field models of Cahn-Hilliard type [9], the functional derivative is interpreted as a chemical potential

$$\mu = \frac{\delta F}{\delta \phi} = \frac{df(\phi)}{d\phi} - 2a\nabla^2 \phi \quad (2.98)$$

(here of unit J/m^3) which causes a flux density \mathbf{j} directed against the chemical potential gradient

$$\mathbf{j} = -M\nabla\mu \quad (2.99)$$

where the mobility $M > 0$ is the proportionality constant.

Based on this flux density, it is assumed that the order parameter behaves like a composition under constant molar volume (Eq. (2.27)) and is thus conserved leading to the balance equation

$$\frac{\partial \phi(\mathbf{x}, t)}{\partial t} = -\nabla \cdot \mathbf{j} = \nabla \cdot (M\nabla\mu) = M\nabla^2 \mu \quad (2.100)$$

where the last equality holds when M is simply a constant which corresponds to equal bulk diffusivities in both phases.

2.4.1.3 Equilibrium phase-field profiles

An interesting insight into the phase-field models at hand is to consider the equilibrium case for a planar interface $\partial\phi(x,t)/\partial t = \partial\phi(x,t)/\partial t = 0^6$. Here a one-dimensional treatment with the x -coordinate suffices.

It results in the condition

$$\frac{d^2\phi(x)}{dx^2} = \frac{1}{2a} \frac{df(\phi)}{d\phi} \quad (2.101)$$

which is an ordinary second-order differential equation for $\phi(x)$. It can be transformed into a first-order differential equation by multiplying with $\phi'(x)$ and performing integration by substitution to both sides of the equation. Assuming that at some point x_- one side of the bulk is reached, i.e. $\phi(x_-) = 0$ and $\phi'(x_-) = 0$ one obtains

$$\phi'(x) = \sqrt{\frac{f(\phi(x))}{a}} \quad (2.102)$$

if the potential vanishes in the bulk $f(0) = 0$ which holds both for well and obstacle potential. Additionally, the positive sign branch is selected to disregard negative values in the order parameter. This is a first-order separable differential equation. Dividing through the right-hand side and integrating by substitution yields

$$\int_{\frac{1}{2}}^{\phi(x)} \sqrt{\frac{a}{f(\phi(x))}} d\phi = x \quad (2.103)$$

⁶ Strictly speaking, for the Cahn-Hilliard model one would have to impose $\mu = 0$.

where the boundary condition $\phi(0) = 1/2$ has been applied. One obtains

$$x = \begin{cases} -\sqrt{\frac{a}{b}} \arcsin(1 - 2\phi(x)) & f(\phi) = b\phi(1 - \phi) \\ -2\sqrt{\frac{a}{b}} \operatorname{arctanh}(1 - 2\phi(x)) & f(\phi) = b\phi^2(1 - \phi)^2 \end{cases}. \quad (2.104)$$

Inverting this in favor of ϕ , the equilibrium order parameter profile is obtained as

$$\phi(x) = \begin{cases} \frac{1}{2} + \frac{1}{2} \sin\left(\sqrt{\frac{b}{a}}x\right) & f(\phi) = b\phi(1 - \phi) \\ \frac{1}{2} + \frac{1}{2} \tanh\left(\sqrt{\frac{b}{4a}}x\right) & f(\phi) = b\phi^2(1 - \phi)^2 \end{cases}. \quad (2.105)$$

Please note that the phase-field profiles for a moving interface correspond to the non-equilibrium case. Therefore, the phase-field profiles need not necessarily be equal to the equilibrium profiles. Chapter 4 addresses this point in detail and quantifies deviations from the equilibrium profiles.

Interface Thickness The equilibrium solutions are plotted in Fig. 2.7 as a function of the dimensionless coordinate $\sqrt{b/ax}$. It can be seen that for both potential formulations, the transition between the two bulk states occurs within a layer proportional to the length $\sqrt{a/b}$. Thus, the equilibrium interface thickness results from a competition of the magnitudes of the gradient and potential energy terms. Increasing the contribution of the potential term by increasing b leads to a lowering of the interfacial width, while the increase of the magnitude of the gradient term through an increased value of a facilitates the inverse.

If one defines the interface thickness as $\delta \equiv x_+ - x_-$, only the obstacle potential leads to a finite thickness of the interface. In contrast, the well potential approaches the values of 0 and 1 at $x_{\pm} = \pm\infty$. For the former, its value can be determined as $\delta = \sqrt{a/b}\pi$. To compare the apparent thicknesses of the two solutions, instead it is more meaningful to compare the slopes at the center of the interface $\phi = 1/2$. This can directly be obtained from Eq. (2.102) leading to $\phi'(0) = \sqrt{b}/(2\sqrt{a})$ and $\phi'(0) = \sqrt{b}/(4\sqrt{a})$ for the obstacle and well potential,

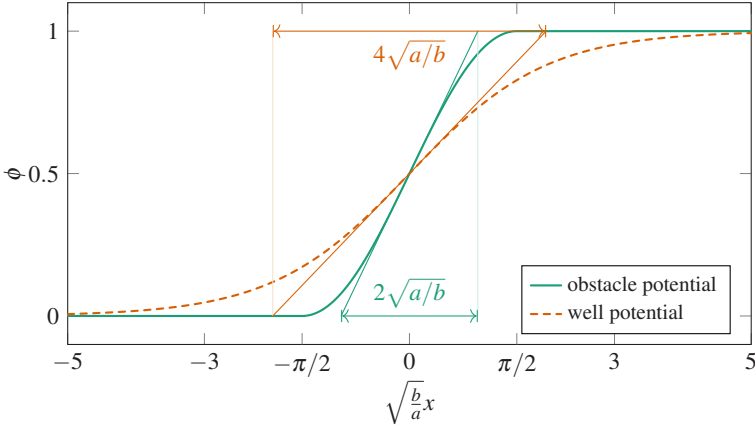


Figure 2.7: Equilibrium phase-field profiles for a planar interface in a two-phase model for both the obstacle and well potential. x is the signed distance from the location $\phi = 1/2$, whereas a and b are the prefactors of the gradient and potential term in the energy functional, respectively. The straight lines indicate the interface width derived from the slope at $x = 0$.

respectively. Thus, with this definition, the obstacle potential leads to half of the interface width compared to the well potential if all prefactors are chosen identically.

Interfacial Energy The interfacial energy σ of such a planar and equilibrated interface can be calculated as the excess free energy given through

$$\sigma = \int_{x_-}^{x_+} f(\phi(x)) + a(\phi'(x))^2 dx. \quad (2.106)$$

Making use of the first order ODE (Eq. (2.102)) one obtains

$$\sigma = \int_{x_-}^{x_+} 2f(\phi(x)) dx = 2 \int_{\phi(x_-)}^{\phi(x_+)} \frac{f(\phi(x))}{\phi'(x)} d\phi = 2\sqrt{a} \int_{\phi(x_-)}^{\phi(x_+)} \sqrt{f(\phi)} d\phi \quad (2.107)$$

Inserting a condition for the interfacial endpoint at the right end, i.e. $\phi(x_+) = 1$ and inserting $\phi(x_-) = 0$, one obtains

$$\sigma = \begin{cases} \frac{\pi}{4}\sqrt{ab} & f(\phi) = b\phi(1-\phi) \\ \frac{1}{3}\sqrt{ab} & f(\phi) = b\phi^2(1-\phi)^2 \end{cases} \quad (2.108)$$

which shows that the interfacial energy is proportional to the square-root of the product of the prefactors of both the gradient and potential term. Such a derivation can be found for instance in Plapp [48, cf. Eq. (15.28)]. With this result at hand, it is straightforward to re-express a and b in terms of σ and an interface thickness parameter ε , giving these prefactors a more physically sound meaning. For this, one has to choose $a \propto \sigma\varepsilon$ and $b \propto \sigma/\varepsilon$.

2.4.2 Multiphase-Field Models

Multiphase-field models extend the phase-field technique by replacing the scalar order parameter by a tuple $\phi = \{\phi_\alpha, \phi_\beta, \dots, \phi_N\}$ to describe an arbitrarily sized set of N phases. In these class of models, first introduced by Steinbach et al. [14], a sum constraint is imposed to ensure that the order parameter ϕ_α corresponding to phase α can be interpreted as a local volume fraction of this phase:

$$\sum_{\alpha=1}^N \phi_\alpha = 1. \quad (2.109)$$

A generalization of the gradient and potential terms to multiple phases is needed. The formulations in [14, 15, 17, 33, 49] express the free energy (or entropy) functional in terms of α - β combinations

$$\begin{aligned}
 F = \int_{\Omega} \sum_{\alpha=1}^N \sum_{\beta=\alpha+1}^N \gamma_{\alpha\beta} \left(\frac{16\mathcal{G}(\phi)}{\pi^2\varepsilon} \phi_{\alpha}\phi_{\beta} + \varepsilon|\mathbf{q}_{\alpha\beta}|^2 \right) \\
 + \sum_{\alpha=1}^N \sum_{\beta=\alpha+1}^N \sum_{\delta=\beta+1}^N \gamma_{\alpha\beta\delta} \phi_{\alpha}\phi_{\beta}\phi_{\delta} + \sum_{\alpha=1}^N h_{\alpha}(\phi) f_{\alpha} dV,
 \end{aligned} \tag{2.110}$$

and the additional bulk free energy densities f_{α} appear in Nestler et al. [17], Garcke et al. [33] and are interpolated by means of an interpolation function $h_{\alpha}(\phi)$ for each phase.

The interpolation function fulfills the condition

$$h_{\alpha}(\phi_{\alpha} = 1, \phi_{\beta \neq \alpha} = 0) = 1 \tag{2.111}$$

$$h_{\alpha}(\phi_{\alpha} = 0, \dots) = 0 \tag{2.112}$$

In Choudhury [50, Appendix C] it has been emphasized, that the sum constraint should also hold for the interpolation function, i.e.

$$\sum_{\alpha=1}^N h_{\alpha}(\phi) = 1, \tag{2.113}$$

which becomes important when $N > 2$. With this constraint in place, the last term in Eq. (2.110) becomes a weighted average of the bulk free energy densities. The Gibbs function

$$\mathcal{G}(\phi) = \begin{cases} 1 & \sum_{\alpha=1}^N \phi_{\alpha} = 1 \cap \phi_{\alpha} \geq 0 \forall 1 \leq \alpha \leq N \\ \infty & \text{else} \end{cases} \tag{2.114}$$

ensures that all order parameters remain within the following bounds

$$0 \leq \phi_\alpha \leq 1 \quad \forall 1 \leq \alpha \leq N. \quad (2.115)$$

The term $\phi_\alpha \phi_\beta$ reduces to $\phi(1 - \phi)$ in a two-phase model while $\mathbf{q}_{\alpha\beta} = \phi_\alpha \nabla \phi_\beta - \phi_\beta \nabla \phi_\alpha$ is a so-called generalized gradient vector, that replaces the gradient in the two-phase model and reduces to the gradient $\nabla \phi_\beta = -\nabla \phi_\alpha$ in a binary interface where $\phi_\alpha = 1 - \phi_\beta$ holds. Accordingly, the functional in Eq. (2.110) corresponds to the choice of prefactors $a = \gamma_{\alpha\beta} \varepsilon$ and $b = 16\gamma_{\alpha\beta}/(\pi^2 \varepsilon)$ in Eq. (2.96) for the gradient term and the obstacle potential, respectively. Thus, it can be seen that the interfacial energy is equally $\sigma = \pi/4 \sqrt{16\gamma_{\alpha\beta}^2/(\pi^2)} = \gamma_{\alpha\beta}$ which shows that $\gamma_{\alpha\beta}$ is the interfacial energy parameter for the interface between the α and the β phase. Similarly, the equilibrium interface thickness δ of a binary interface is given by $\delta = \pi \sqrt{\pi^2 \varepsilon^2 / (16)} = \pi^2 \varepsilon / 4$ and thus ε is a parameter that independently controls the interface width.

The additional triplet term scaled by $\gamma_{\alpha\beta\delta}$ is used to remove spurious third phases that may appear at triple or higher-order junctions (i.e. only relevant for $N > 2$). For more details, the interested reader is referred to Hötzer et al. [51].

Following the notation of Nestler et al. [17], the evolution equation for the N order parameters is commonly written as

$$\tau(\phi) \varepsilon \frac{\partial \phi_\alpha(\mathbf{x}, t)}{\partial t} = -\frac{\delta F}{\delta \phi_\alpha} - \lambda \quad (2.116)$$

where λ is a Lagrange multiplier to ensure the sum constraint (Eq. (2.109)). $\tau(\phi)$ is a relaxation time (the inverse of the mobility) and can be expressed by means of an arithmetic interpolation over the relaxation times of the binary interfaces

$$\tau(\phi) = \frac{\sum_{\alpha=1}^N \sum_{\beta=\alpha+1}^N \tau_{\alpha\beta} \phi_\alpha \phi_\beta}{\sum_{\alpha=1}^N \sum_{\beta=\alpha+1}^N \phi_\alpha \phi_\beta} \quad (2.117)$$

cf. e.g. Choudhury et al. [52]. The implications of the interpolation form (harmonic/arithmetic) was later discussed in detail in Enugala [53, Section 4.3.2] and it was shown that the arithmetic interpolation of the relaxation times can lead to pinning at junctions in practical simulations if $\tau_{\alpha\beta}$ are varying at order of magnitudes.

An alternate formulation of the evolution equation from Steinbach and Pezzolla [16] writes

$$\varepsilon \frac{\partial \phi_\alpha(\mathbf{x}, t)}{\partial t} = \frac{1}{\tilde{N}} \sum_{\beta=1}^N m_{\alpha\beta} \left(\frac{\delta F}{\delta \phi_\beta} - \frac{\delta F}{\delta \phi_\alpha} \right) \quad (2.118)$$

and avoids any interpolation of the mobilities or relaxation times by expressing it completely by means of binary mobilities $m_{\alpha\beta}$. In addition, it also gets rid of the Lagrange multiplier since the form implicitly ensures the sum constraint if the initial condition complies. Here \tilde{N} is the number of local active phases. Note that both formulations reduce to the two-phase Allen-Cahn model (Eq. (2.97)) in the binary ($N = 2$) case.

2.4.3 Models to Couple Diffusion and Phase Transformation

Historical Notes Up to this point, only model formulations that can treat either a two-phase or binary problem, as well as the multiphase case have been mentioned. In the past, a variety of phase-field formulations were established to study problems where the diffusion of a chemical species as well as the evolution of a non-conserved order parameter are coupled. Such problems usually arise in the solidification of an alloy, where the phase transformation from liquid to solid accompanies diffusion towards the solidifying front from the melt. Early attempts either assumed equal compositions of both the solid and the liquid in the interfacial region Wheeler et al. [54], or a constant partition coefficient was assumed Tiaden et al. [15]. For the former it has been shown by Kim et al. [55] that the assumption of equal compositions of both phases leads to a strong limitation in

the choice of interface width. This is rooted in an excess energy contribution to the interfacial energy σ which then also depends on the chemical contribution to the free-energy (for a review on the topic see Nestler and Choudhury [56]).

Kim-Kim-Suzuki and Eiken-Böttger-Steinbach Model The first approach to circumvent such problems was introduced by Kim et al. [55], where analogies between the sharp-interface laws of a pure material and an alloy were identified to establish the chemical potential as the intensive properties which is continuous across an interface (in contrast the composition usually shows a jump discontinuity). Their model for the first time introduces an explicit partitioning by phase-wise compositions c_α based on a local equilibrium condition of the following form

$$\mu = \frac{\partial f_\alpha(c_\alpha)}{\partial c_\alpha} = \frac{\partial f_\beta(c_\beta)}{\partial c_\beta}. \quad (2.119)$$

This condition ensures equal chemical potentials μ of both liquid and solid at each point in space. The composition was written as an interpolation between the liquid and solid compositions

$$c = h(\phi)c_\alpha + (1 - h(\phi))c_\beta \quad (2.120)$$

by means of the interpolation function $h(\phi)$ which depends on the order parameter ϕ . The evolution equations are derived in a non-variational way directly from a free-energy density of the form

$$f(c, \phi) = h(\phi)f_\alpha(c_\alpha) + (1 - h(\phi))f_\beta(c_\beta) + wg(\phi) \quad (2.121)$$

and read

$$\frac{\partial \phi(\mathbf{x}, t)}{\partial t} = M \left(\varepsilon^2 \nabla^2 \phi - \frac{\partial f(c, \phi)}{\partial \phi} \right) \quad (2.122)$$

$$\frac{\partial c(\mathbf{x}, t)}{\partial t} = \nabla \cdot \frac{D(\phi)}{\partial^2 f(c, \phi) / \partial c^2} \nabla \mu \quad (2.123)$$

where $g(\phi) = \phi^2(1 - \phi)^2$ is the double-well potential. Applying the chain rule yields

$$\frac{\partial f(c, \phi)}{\partial \phi} = h'(\phi) (f_\alpha(c_\alpha) - f_\beta(c_\beta) - \mu(c_\alpha - c_\beta)) + wg'(\phi) \quad (2.124)$$

and it can be seen that the driving force is given by the well-known double tangent construction. It is worth noting that this follows from the equilibrium condition (Eq. (2.119)) without imposing it from the start.

An almost identical model has been introduced later by Eiken et al. [18]. It generalizes the Kim-Kim Suzuki model to multiple phases (by employing Eq. (2.118) and using a multi-obstacle potential) and to multiple components. Also, it derives the governing equations from a free-energy functional that includes dependencies of the order parameters ϕ_α and the phase-inherent compositions c_α .

Grand-Potential Model The grand-potential model was derived independently by Plapp [19] and Choudhury and Nestler [20] with only minor differences: While Plapp proposed a two-phase model for the non-conserved order parameter using a double-well potential, the model of Choudhury et al. is based on the multi-phase framework and accordingly used an obstacle potential. Additionally, while Plapp proposed an antitrapping current in analogy to the dilute case [57], Choudhury et al. performed a thin-interface asymptotic analysis to calibrate the antitrapping current which enables to run simulations at vanishing kinetic coefficients even at large interface widths. This was previously only available for the solidification of dilute alloys [57, 58].

Instead of a free-energy functional, the model formulation starts with a grand potential functional, written as⁷

$$\Psi(\boldsymbol{\mu}, \phi) = \int_{\Omega} \sum_{\alpha=1}^N \sum_{\beta=\alpha+1}^N \gamma_{\alpha\beta} \left(\frac{16}{\pi^2 \varepsilon} \phi_{\alpha} \phi_{\beta} + \varepsilon |\mathbf{q}_{\alpha\beta}|^2 \right) + \psi(\boldsymbol{\mu}, \phi) dV. \quad (2.125)$$

It directly includes a dependence on the chemical potential tuple $\boldsymbol{\mu} = \{\mu_1, \dots, \mu_{K-1}\}$ for a multicomponent system of K components. The difference to the free-energy functional lies in the chemical contribution formulated as a grand-potential density

$$\psi(\boldsymbol{\mu}, \phi) = \sum_{\alpha=1}^N h_{\alpha}(\phi) \psi_{\alpha}(\boldsymbol{\mu}) \quad (2.126)$$

interpolated in terms of phase-inherent contributions

$$\psi_{\alpha}(\boldsymbol{\mu}) = f_{\alpha}(\mathbf{c}^{\alpha}(\boldsymbol{\mu})) - \sum_{i=1}^{K-1} \mu_i c_i^{\alpha}(\boldsymbol{\mu}) \quad (2.127)$$

which results in a driving force that can be graphically obtained by means of the double-tangent construction. Thus, in contrast to the Kim-Kim Suzuki model, the double tangent construction is assumed from the start instead of being obtained by means of the chain rule.

It is worth noting that by expressing the phase-wise composition tuple \mathbf{c}^{α} explicitly as a function of the chemical potential, its invertibility is directly assumed.

Furthermore, a quasi-equilibrium condition similar to the one in [18, 55] is imposed on the chemical potential

$$\frac{\partial f^{\alpha}(\mathbf{c}^{\alpha})}{\partial c_i^{\alpha}} = \frac{\partial f^{\beta}(\mathbf{c}^{\beta})}{\partial c_i^{\beta}} = \dots = \mu_i \quad \forall \{i, \alpha\}. \quad (2.128)$$

⁷ For the sake of brevity, the exposition here is limited to the multiphase formulation of Choudhury and Nestler [20].

By performing the derivative of $\Psi(\boldsymbol{\mu}, \phi)$ with respect to the chemical potential of the i 'th component μ_i , the equivalent of the partitioning in the Kim-Kim Suzuki model (Eq. (2.120)) results:

$$c_i(\boldsymbol{\mu}, \phi) = \sum_{\alpha=1}^N h_{\alpha}(\phi) c_i^{\alpha}(\boldsymbol{\mu}) \quad (2.129)$$

This rests on the thermodynamic relation $\partial\Psi(\boldsymbol{\mu}, \phi)/\partial\mu_i = -c_i$.

The evolution equation for the order parameters is formulated based on Eq. (2.116) and writes

$$\tau(\phi)\varepsilon \frac{\partial\phi_{\alpha}(\boldsymbol{x}, t)}{\partial t} = -\frac{\delta\Psi(\boldsymbol{\mu}, \phi)}{\delta\phi_{\alpha}} - \lambda \quad (2.130)$$

which shows that the bulk driving force is governed by the grand-potential densities Ψ_{α} instead of free-energy densities f_{α} .

In absence of any anti-trapping flux, the evolution of the i 'th composition is formulated as

$$\frac{\partial c_i(\boldsymbol{x}, t)}{\partial t} = \nabla \cdot \sum_{j=1}^{K-1} M_{ij}(\phi) \nabla \mu_j \quad (2.131)$$

where $M_{ij}(\phi)$ are the mobilities relating the flux density to the gradients in chemical potential. They are formulated as an interpolation of the phase-wise mobilities

$$M_{ij}(\phi) = \sum_{\alpha=1}^N h_{\alpha}(\phi) M_{ij}^{\alpha} \quad (2.132)$$

that are defined by means of a Darken relation Darken [59] to hold phase-wise diffusivities constant⁸

$$M_{ij}^\alpha \equiv D_{ij}^\alpha \frac{\partial c_i^\alpha(\boldsymbol{\mu})}{\partial \mu_j}. \quad (2.133)$$

The important feature of the grand-potential model is that an evolution equation for the chemical potential can be derived by applying the chain rule to Eq. (2.129). Accordingly, the evolution of the chemical potential is obtained by solving the following linear system of equations

$$\frac{\partial c_j(\boldsymbol{\mu}, \phi)}{\partial \mu_i} \frac{\partial \mu_i(\mathbf{x}, t)}{\partial t} = \frac{\partial c_j(\mathbf{x}, t)}{\partial t} - \sum_{\alpha=1}^N c_j^\alpha(\boldsymbol{\mu}) \frac{\partial h_\alpha(\mathbf{x}, t)}{\partial t} \quad (2.134)$$

written in Einstein notation for the $K - 1$ unknowns $\partial \mu_i(\mathbf{x}, t)/\partial t$.

It is worth stressing, that the results obtained from the grand-potential model in its simplest form (well-potential and two-phase, single component) and the Kim-Kim Suzuki model are identical. The differences are twofold: Firstly, the grand-potential model is directly derived from a grand-potential functional. Secondly, the evolution equation of the composition is replaced by an evolution equation of the chemical potential, which simplifies the numerical treatment.

2.4.4 Phase-Field Models for Surface Diffusion

Motivation All of the hitherto mentioned models incorporate bulk diffusion in such a way that a smooth interpolation between the corresponding bulk mobilities applies. This means that an additional surface flux is not incorporated into these models. The current subsection is meant to summarize the historical development of phase-field models for surface diffusion. The current subsection is based

⁸ This form seems to be meaningful only for pure diagonal entries in both D_{ij}^α and $\partial c_i^\alpha/\partial \mu_j$. It was generalized later in [60].

mostly on the exposition given in Hoffrogge et al. [24] but is written in a more explanatory way.

2.4.4.1 Cahn-Hilliard Based Two-Phase Models (Fourth order)

First ideas to incorporate an additional surface flux in phase-field models were formulated based on a mobility function which depends on the order parameter $M(\phi)$ in the Cahn-Hilliard model, i.e.

$$\frac{\partial \phi(\mathbf{x}, t)}{\partial t} = \nabla \cdot (M(\phi) \nabla \mu) \quad (2.135)$$

where the chemical potential is given by Eq. (2.98)). Such a form was first suggested in [46]. The idea is that $M(\phi)$ depends on the order parameter in such a way that the mobility vanishes in the bulk. Since μ includes the Laplacian of the order parameter and M is free of any gradients, the differential equation contains a fourth order spatial differential operator.

Most common formulations (e.g. [61–66]) employ well potential together with a quadratic mobility $M(\phi) \propto \phi(1 - \phi)$, while only few have used a biquadratic form $M(\phi) \propto \phi^2(1 - \phi)^2$ (e.g. [67]).

It is worth noting some subtleties in employing such mobility functions. In any case, the construction of the mobility function is motivated by the equilibrium phase-field profile for a flat interface (Eq. (2.105)) which tends to zero and unity in the bulk, respectively. This makes the mobility tending to zero at both sides which ensures that diffusion only occurs in within the interface. However, there is a shift of the chemical potential for a curved interface reflecting the Gibbs-Thomson effect and hence bulk compositions move slightly away from zero and unity for a well potential. While a biquadratic mobility remains positive by design, a quadratic mobility may lead to negative mobilities, which is thermodynamically inconsistent and causes instabilities [68]. To circumvent this, either the mobility function is forced to remain positive by truncation [61], or replaced by its absolute value [65, 68] (i.e. $M(\phi) \propto |\phi(1 - \phi)|$). Nevertheless, a remaining caveat is that

the mobility may still be positive in the bulk due to such shifts, leading to an unwanted additional bulk diffusion.

This has been the focus of the rigorous asymptotic treatments in [68–70]. They pointed out that the Cahn-Hilliard equation together with a well potential and a quadratic mobility does not lead to pure surface diffusion in the sharp interface limit but includes a nonlinear bulk contribution that scales with the curvature. For a biquadratic mobility, such a bulk diffusion term is not occurring in the sharp-interface limit, but appears as a first-order correction [70–72]. The problematic is twofold: Firstly, the Gibbs-Thomson shift of the bulk compositions compromises volume conservation and secondly, it leads to non-vanishing mobilities in the bulk.

An approach which effectively shuts out the Gibbs-Thomson shift in the bulk was first introduced by Rätz et al. [47] using an additional stabilizing function. While the evolution equation (Eq. (2.135)) remains unchanged, the chemical potential is defined by the following formula

$$g(\phi)\mu = \frac{\delta F}{\delta \phi} = \frac{df(\phi)}{d\phi} - 2a\nabla^2\phi \quad (2.136)$$

with the stabilizing function $g(\phi) \propto \phi^2(1 - \phi)^2$. It can be easily seen that a nonzero chemical potential does not anymore imply a significantly nonzero right-hand side when ϕ is near its equilibrium bulk values. This in turn means that in the bulk, where $|\nabla^2\phi| \rightarrow 0$, the term $f'(\phi)$ still remains very much near zero, keeping bulk compositions near zero and unity even for a curved interface. This implies, that an additional bulk flux is not occurring according to the form of the mobility function. This approach, also known as the *doubly degenerate* model referring to the degeneracy in both the mobility and the stabilizing function has been used in a variety of works [73–75]. It has been shown to be numerically more efficient [76, 77] and has been generalized and extended towards a variational form in the latter work.

2.4.4.2 Coupled Allen-Cahn and Cahn-Hilliard Models

In many cases, the coupled motion of an interphase boundary which evolves according to surface diffusion and migrating grain boundaries is of particular interest. Such problems have been often tackled by means of two types of coupled equations, one that evolves conservatively by means of the Cahn-Hilliard equation with a degenerate mobility and an Allen-Cahn non-conservative equation. The governing equations can be derived from a free-energy functional

$$F = \int_{\Omega} f(\phi, c) + a|\nabla c|^2 + \sum_{\alpha=1}^N a_{\alpha}|\nabla\phi_{\alpha}|^2 dV, \quad (2.137)$$

written in terms of a non-conserved order parameter tuple ϕ and a conserved order parameter c Wang [78], Moelans et al. [79]. $f(\phi, c)$ is an energy density which includes minimas for characteristic values of both ϕ_{α} and c . Similar forms of this model employing only a single non-conserved order parameter ϕ can be found in [80, 81]. The chemical potential is derived as in the Cahn-Hilliard model

$$\mu \equiv \frac{\delta F}{\delta c} = \frac{\partial f(\phi, c)}{\partial c} - 2a\nabla^2 c \quad (2.138)$$

and its gradient drives a flux for the evolution of the conserved order parameter:

$$\frac{\partial c(\mathbf{x}, t)}{\partial t} = \nabla \cdot (M(\phi, c)\nabla\mu) \quad (2.139)$$

Here the dependency of the mobility on both ϕ and c allows to separately adjust contributions along the free surface and the grain boundaries. The evolution equation of the non-conserved fields reads

$$\varepsilon \frac{\partial \phi_{\alpha}(\mathbf{x}, t)}{\partial t} = -m \frac{\delta F}{\delta \phi_{\alpha}} = m \left(2a_{\alpha} \nabla^2 \phi_{\alpha} - \frac{\partial f(\phi, c)}{\partial \phi_{\alpha}} \right) \quad (2.140)$$

in its simplest form, employing a constant mobility m .

2.4.4.3 Alternative Formulations

A formulation which is intrinsically different from the above mentioned formulations can be found for instance in Amirouche and Plapp [82]. The major difference of this model with respect to the Cahn-Hilliard based models is that the free-energy functional does not contain gradients in the concentration c and writes as

$$F = \int_{\Omega} \frac{H_c}{2} (c - g(\phi))^2 + H_p f_{\text{TW}}(\phi) + \sum_{\alpha=1}^3 a_{\alpha} |\nabla \phi_{\alpha}|^2 dV, \quad (2.141)$$

where the notation is adjusted to fit that of Eq. (2.137). In contrast, the definition of the chemical potential ($\mu \equiv \delta F / \delta c$) still holds and Eq. (2.139) remains invariant. The novelty is given by the term proportional to H_c which introduces a function $g(\phi)$ coupling the composition to the order parameter. The function f_{TW} is a triple-well to adjust the energy landscape for the three phases considered in that work ($N = 3$) which can be considered as a minor difference. The major difference, i.e. the missing gradient term, makes Eq. (2.139) a second order equation in terms of c , while the original coupled Allen-Cahn and Cahn-Hilliard model is of fourth-order regarding this variable. This seems to simplify the computational complexity of the model significantly. However, the authors of the work discussed several difficulties to relate the model to the existing sharp-interface theories.

A formulation which also leads to a second-order diffusion equation is given by the grand-potential model. Hötzer et al. [83] included an additional enhanced diffusion in the interfacial region by using pairwise terms of the form $\phi_{\alpha} \phi_{\beta}$ similar to those introduced in the Cahn-Hilliard based surface diffusion model. Although their work did not include an analytical calibration of the prefactors, they showed that the introduction of such terms seem to qualitatively reproduce the expected growth laws. The following chapter provides a model formulation following a similar spirit, but focuses on a more rigorous and quantitative incorporation of the surface diffusion terms closely related to the sharp-interface theories introduced earlier.

3 Multiphase-Field Model for Surface and Bulk Diffusion

My files are bursting with important material that I plan to include in the final, glorious, third edition of Volume 3, perhaps 17 years from now. But I must finish Volumes 4 and 5 first, and I do not want to delay their publication any more than absolutely necessary.

Knuth [84]

Remarks In order to develop a model well suited for the modeling of nickel coarsening at typical SOFC operating temperatures of 700 °C to 800 °C, a first literature review regarding volume and surface diffusion coefficients [85–90] revealed that the atomic transport of Ni is dominant along its free surface.

Therefore, a model needed to be developed that accurately handles surface diffusion phenomena. In addition, the model should be general enough to be applicable also to other materials and systems in order to ensure reusability and sustainability and enable future research perspectives. The grand-potential model [19, 20] constituted a promising choice since it was already applicable to multiphase and multicomponent systems. However, a term incorporating surface diffusivities was still missing in this model. The model modification and extension, first presented in [24] by the current author and coworkers, is recalled in the following. This publication also included asymptotic analysis of the pure surface diffusion case

and the governing rate constant for surface diffusion could successfully be derived and validated.

The model equations are briefly listed in the following. A systematic asymptotic treatise follows, concerning concomitant atom transport along interfaces and in the bulk, which was still lacking in the aforementioned work. To this end, a multiphase-field simulation study is conducted to benchmark the model in comparison to the analytical solution presented by Srinivasan and Trivedi [25]. This work combines two seminal works of Mullins ([42, 91]) where the pure surface and volume diffusion case were treated, respectively.

3.1 Model Formulation

The model formulation starts with the grand-potential functional according to [20]

$$\Psi(\phi, \nabla \phi, \mu) = \int_V f_{\text{int}}(\phi, \nabla \phi) + \psi(\phi, \mu) \, dV. \quad (3.1)$$

Here $\phi = \{\phi_\alpha, \phi_\beta, \dots, \phi_N\}$ is the order parameter tuple (dimensionless) for a set of N distinct phases and $\mu = \{\mu_1, \dots, \mu_{K-1}\}$ in J/m^3 is the set of independent diffusion (or chemical) potentials of the multicomponent system of K components.

The interfacial energy density

$$f_{\text{int}}(\phi, \nabla \phi) \equiv \sum_{\alpha=1}^N \sum_{\beta=\alpha+1}^N \gamma_{\alpha\beta} \left(\mathcal{G}(\phi) \frac{16\phi_\alpha \phi_\beta}{\pi^2 \varepsilon} - \varepsilon \nabla \phi_\alpha \cdot \nabla \phi_\beta \right) \quad (3.2)$$

comprises of a multiobstacle potential and a gradient term following [16] incorporating interface energies $\gamma_{\alpha\beta}$ in J/m^2 and fulfills the Gibbs constraint (Eq. (2.115)) through the Gibbs function (Eq. (2.114)).

The gradient term, a replacement for the norm of the generalized gradient vector $q_{\alpha\beta}$ according to [17], constitutes a minor difference to the original model formulation (Eq. (2.125)). In a recent work [92], coauthored by the current author, it could be shown to prevent the formation of spurious third phases which in turn improves the accuracy of the model in cases where unequal interfacial energies $\gamma_{\alpha\beta}$ exist. In this form, the model does not require the additional triplet term included in Eq. (2.110).

The grand-potential density $\psi(\phi, \mu)$ remains identical to Eq. (2.126) and the summation constraint (Eq. (2.113)), $\sum_{\alpha=1}^N h_{\alpha}(\phi) = 1$ is enforced on the interpolation functions.

The evolution equation of the phase-field is given by

$$\varepsilon \frac{\partial \phi_{\alpha}(\mathbf{x}, t)}{\partial t} = \frac{1}{\bar{N}} \sum_{\beta=1}^N m_{\alpha\beta} \left(\frac{\delta \Psi}{\delta \phi_{\beta}} - \frac{\delta \Psi}{\delta \phi_{\alpha}} \right) \quad (3.3)$$

in analogy to Eq. (2.118) which avoids an interpolation of the interface mobilities in contrast to the original work. This evolution equation is consistent with the sum constraint of the order parameters in Eq. (2.109) without introducing an additional Lagrange multiplier.

The major extension is formulated by modifying the evolution equation of the composition (Eq. (2.131)) which now reads

$$\frac{\partial c_i(\mathbf{x}, t)}{\partial t} = -\nabla \cdot \mathbf{j}_i \quad (3.4)$$

$$\mathbf{j}_i \equiv \mathbf{j}_i^b + \mathbf{j}_i^s \quad (3.5)$$

containing not only a bulk flux density \mathbf{j}_i^b but also an additional interface flux density \mathbf{j}_i^s . The evolution equations for the chemical potentials still hold (Eq. (2.134)).

The bulk flux density is chosen identical to the original formulation by interpolating the phase-inherent flux densities

$$\mathbf{j}_i^b \equiv \sum_{\alpha=1}^N h_{\alpha}(\phi) \mathbf{j}_i^{\alpha} \quad (3.6)$$

A minor generalization [60] may be applied by insisting on the following equality

$$\mathbf{j}_i^{\alpha} \equiv - \sum_{j=1}^{K-1} M_{ij}^{\alpha} \nabla \mu_j = - \sum_{j=1}^{K-1} D_{ij}^{\alpha} \nabla c_j^{\alpha} \quad (3.7)$$

where D_{ij}^{α} denote the phase-inherent interdiffusivities.

This condition yields a prescription by means of chain rule to relate the chemical mobilities to the interdiffusivities in each phase

$$M_{ij}^{\alpha} = \sum_{k=1}^{K-1} D_{ik}^{\alpha} \frac{\partial c_k^{\alpha}(\boldsymbol{\mu})}{\partial \mu_j} \quad (3.8)$$

using the Darken factors [59] $\partial c_k^{\alpha} / \partial \mu_j$.

The new interface flux density, postulated as

$$\mathbf{j}_i^s \equiv - \frac{1}{\varepsilon} \sum_{\alpha=1}^N \sum_{\beta=\alpha+1}^N \sum_{j=1}^{K-1} M_{ij}^{\alpha\beta}(\phi) \nabla \mu_j \quad (3.9)$$

$$M_{ij}^{\alpha\beta}(\phi) \equiv \bar{M}_{ij}^{\alpha\beta} g_{\alpha\beta}(\phi) \quad (3.10)$$

rests on a superposition of all possible binary interface contributions through interfacial chemical mobilities $\bar{M}_{ij}^{\alpha\beta}$ in $\text{m}^4/(\text{Js})$.

The inverse scaling with the interface width through the factor $1/\varepsilon$ is an important feature of the model. A preliminary argument is as follows: When the interface thickness is reduced, less material is contained in the interfacial region and thus, the total flux associated with the interface (excess flux density) would be reduced if the flux density were kept unchanged. Therefore, if the factor $1/\varepsilon$ were missing,

the interface kinetics would be largely dependent on the arbitrarily chosen interface thickness. This notion is also reflected in the following asymptotic treatment, since it makes the surface diffusion term dominant in the interfacial region as the interface thickness is reduced to zero. Note that the interface flux density j_i^s becomes singular for $\varepsilon \rightarrow 0$ which ensures that an excess term remains even for a vanishing interface thickness parameter.

An additional point worth noting is that a direct relation of the parameter $\bar{M}_{ij}^{\alpha\beta}$ to surface interdiffusivities is not possible without employing some sort of interpolation (involving at least the Darken factors). Moreover, since the compositions are usually subject to jumps at the interface and the thermodynamic properties of the phases in contact might be completely different, such a relation does not convey much meaningful information. Therefore, the relation to interface diffusivities is not performed for the general multicomponent case.

Instead, the model parameters $\bar{M}_{ij}^{\alpha\beta}$ can be used to individually control the rate at which atoms are transported along each $\alpha - \beta$ interface.

The dimensionless function $g_{\alpha\beta}$ is proposed as a generalization of the established two-phase formulations in the following multiphase form:

$$g_{\alpha\beta}(\phi) = \begin{cases} > 0 & \phi_\alpha > 0 \cap \phi_\beta > 0 \\ 0 & \phi_\alpha = 0 \cup \phi_\beta = 0 \end{cases}. \quad (3.11)$$

This ensures that the additional interface flux density is vanishing in the bulk.

A natural choice is

$$g_{\alpha\beta}(\phi) = \phi_\alpha^n \phi_\beta^n \quad (3.12)$$

with some exponent $n > 0$, $n \in \mathbb{R}$.

This completes the formulation of the grand-potential model with coupled interface and volume diffusion. The sharp-interface limit of the model is now to be determined analytically.

3.2 Sharp-Interface Limiting Behavior

Motivation In the current section, the governing laws of the grand-potential model including both surface and volume-diffusion are derived by performing asymptotic analysis. Asymptotic analysis is commonly conducted [12, 13, 93–95] to derive the sharp-interface limiting behavior of phase-field models. It therefore bridges the gap between the diffuse-interface formalism and the more broadly accepted notion of continuum descriptions, where singular surfaces separate distinct domains of varying properties. The asymptotic treatment helps to show, that the model is capable of recovering important physical aspects if the interface thickness were to vanish. In a numerical simulation, interface thickness must always be finite owing to the discretization which does not permit a discontinuous variation of the solution variable. In contrast, the asymptotic treatment is a purely analytical procedure and the sharp interface case can be approached as a limiting case. As such, the asymptotic treatment allows to rigorously validate a model that was initially constructed purely out of intuition.

The asymptotic derivation for the grand-potential model with pure volume diffusion was presented in [20]. The asymptotic analysis under pure surface diffusion was presented in [24] by the current author and coworkers. The current analysis is an extension of this derivation for combined surface and volume diffusion. For the derivation, a binary two-phase system is considered and therefore, composition subscripts i are omitted in the following and a single order parameter ϕ_α is considered. The derivation is also restricted to a two-dimensional setup.

3.2.1 Preliminaries

Governing Equations The governing equations for a two-phase binary system are given based on Eqs. (3.3) and (2.134). Accordingly, one obtains

$$\frac{\varepsilon}{m_{\alpha\beta}} \dot{\phi}_\alpha = \varepsilon \gamma_{\alpha\beta} \nabla^2 \phi_\alpha - \frac{8\gamma_{\alpha\beta}}{\varepsilon \pi^2} (1 - 2\phi_\alpha) - \frac{\psi_\alpha - \psi_\beta}{2} \frac{\partial h_\alpha}{\partial \phi_\alpha} \quad (3.13)$$

$$\frac{\partial c}{\partial \mu} \dot{\mu} = \nabla \cdot (M(\phi_\alpha) \nabla \mu) - (c^\alpha(\mu) - c^\beta(\mu)) \dot{h}_\alpha. \quad (3.14)$$

Here, according to Eq. (3.5) and in contrast to [24], the chemical mobility

$$M(\phi_\alpha, \mu) = \frac{M_s(\phi_\alpha)}{\varepsilon} + M_b(\phi_\alpha, \mu) \quad (3.15)$$

comprises of a surface

$$M_s(\phi_\alpha) = \bar{M}g(\phi_\alpha) \quad (3.16)$$

and bulk contribution

$$M_b(\phi_\alpha, \mu) = M_\alpha(\mu) h_\alpha(\phi_\alpha) + M_\beta(\mu) (1 - h_\alpha(\phi_\alpha)). \quad (3.17)$$

3.2.1.1 Solution in the Bulk

Order Parameter In a two-phase setup, there are two possible bulk regions satisfying $|\nabla \phi_\alpha| = 0$ and the Gibbs-simplex constraint (Eq. (2.115)). These are $\phi_\alpha = 0$ and $\phi_\alpha = 1$. Inserting these two constants into the governing equations yields two results, one for the order parameter and one for the chemical potential. For the phase-field equation (3.13), one obtains

$$\frac{\varepsilon}{m_{\alpha\beta}} \dot{\phi}_\alpha = -\frac{8\gamma_{\alpha\beta}}{\varepsilon \pi^2} (1 - 2\phi_\alpha) - \frac{\psi_\alpha - \psi_\beta}{2} \frac{\partial h_\alpha}{\partial \phi_\alpha} \quad (3.18)$$

which evaluates to

$$\frac{\varepsilon}{m_{\alpha\beta}}\dot{\phi}_\alpha = -\frac{8\gamma_{\alpha\beta}}{\varepsilon\pi^2} + \frac{\psi_\alpha - \psi_\beta}{2} \frac{\partial h_\alpha}{\partial \phi_\alpha} \Big|_{\phi_\alpha=0} \quad (3.19)$$

$$\frac{\varepsilon}{m_{\alpha\beta}}\dot{\phi}_\alpha = +\frac{8\gamma_{\alpha\beta}}{\varepsilon\pi^2} + \frac{\psi_\alpha - \psi_\beta}{2} \frac{\partial h_\alpha}{\partial \phi_\alpha} \Big|_{\phi_\alpha=1} \quad (3.20)$$

for $\phi_\alpha = 0$ and $\phi_\alpha = 1$ as initial condition, respectively. In the case that the derivative of the interpolation function vanishes at the respective bulk values, i.e. $\partial h_\alpha / \partial \phi_\alpha|_{\phi_\alpha \in \{0,1\}} = 0$, which is the case for most of the commonly employed interpolation functions (cf. the following Chapter 4) of order larger equal unity, we can omit the second term on the RHS. Then it is observed that $\dot{\phi}_\alpha < 0$ for $\phi_\alpha = 0$ and positive for $\phi_\alpha = 1$, given that all physical parameters mobility, interfacial energy and interface width are positive constants ($m_{\alpha\beta} > 0$, $\gamma_{\alpha\beta} > 0$ and $\varepsilon > 0$). In turn, in the very next moment, the Gibbs-simplex constraint would be violated. As this cannot be the case, $\dot{\phi}_\alpha = 0$ in the bulk since the Gibbs simplex is imposed here. We refer to this as *stable bulk states* since the evolution of the order parameter in the bulk cannot become a part of the interface globally and instantaneously. This is only possible in a special case when $\partial h_\alpha / \partial \phi_\alpha|_{\phi_\alpha \in \{0,1\}}$ evaluates to nonzero constants. Then, depending on the driving force $\psi_\alpha - \psi_\beta$, the bulk might become unstable when the sign of the right-hand side switches accordingly. However, as ε is reduced down to zero in the sharp-interface limit, the first term on the right hand side blows up and in turn dominates the right hand side for any finite driving force. Therefore, considerations have to be restricted to a region of small enough ε where stable bulk states can be maintained (which should be the case for reasonably large driving forces). For a more detailed exposition of the influence of large driving forces, the reader is referred to the next chapter (cf. Section 4.6.1).

Chemical Potential The governing equation for the chemical potential in the two bulk regions is obtained by inserting the bulk solution of the order parameter into Eq. (3.14)

$$\frac{\partial c^\alpha}{\partial \mu} \dot{\mu} = -\nabla \cdot \mathbf{j}^\alpha \text{ at } \phi_\alpha = 1 \quad (3.21)$$

$$\frac{\partial c^\beta}{\partial \mu} \dot{\mu} = -\nabla \cdot \mathbf{j}^\beta \text{ at } \phi_\alpha = 0, \quad (3.22)$$

taking into account Eq. (3.6), Eq. (2.129) as well as equations (2.111)-(2.112). Writing this in terms of the bulk compositions, one obtains the classical Fick's law of diffusion for a constant molar volume (Eq. (2.30))

$$\dot{c}^\alpha = \nabla \cdot (D^\alpha \nabla c^\alpha) \text{ at } \phi_\alpha = 1 \quad (3.23)$$

$$\dot{c}^\beta = \nabla \cdot (D^\beta \nabla c^\beta) \text{ at } \phi_\alpha = 0. \quad (3.24)$$

3.2.1.2 Moving Curvilinear Coordinates

The two partial differential equations (3.13) and (3.14) are written in terms of moving curvilinear coordinates, i.e. applying the surface parameterization introduced in Section 2.3.1. Since the current analysis is restricted to a two-dimensional problem, only a single surface parameter $s \equiv a_1$ needs to be considered. The subscript is also omitted for the tangential vector, i.e. $\mathbf{s} \equiv \mathbf{s}_1$. An arclength-parameterization is conducted which results in $|\mathbf{s}| = 1$. The spatial

differential operators are expressed in curvilinear coordinates according to [96] as

$$\nabla = n \frac{\partial}{\partial r} + s \frac{1}{1+r\kappa_0} \frac{\partial}{\partial s} \quad (3.25)$$

$$\begin{aligned} \nabla \cdot (a \nabla b) &= \frac{\partial}{\partial r} \left(a \frac{\partial b}{\partial r} \right) + \frac{1}{(1+r\kappa_0)^2} \frac{\partial}{\partial s} \left(a \frac{\partial b}{\partial s} \right) \\ &+ a \left(\frac{\kappa_0}{1+r\kappa_0} \frac{\partial b}{\partial r} - \frac{r \frac{\partial \kappa_0}{\partial s}}{(1+r\kappa_0)^3} \frac{\partial b}{\partial s} \right) \end{aligned} \quad (3.26)$$

$$\nabla^2 = \frac{\partial^2}{\partial r^2} + \frac{\kappa_0}{1+r\kappa_0} \frac{\partial}{\partial r} + \frac{1}{(1+r\kappa_0)^2} \frac{\partial^2}{\partial s^2} - \frac{r \frac{\partial \kappa_0}{\partial s}}{(1+r\kappa_0)^3} \frac{\partial}{\partial s}. \quad (3.27)$$

Here, $\kappa_0(s, t)$ is the signed curvature of the basesurface x_0 (Eq. (2.34)) and the scaling with r reflects how the curvature increases or decreases for surfaces of constant distance from the basesurface. As a sign convention, the curvature is positive if n points from the center of curvature to a point on the basesurface.

The time derivative is written in terms of the normal time derivative, i.e.

$$\dot{\phi}_\alpha = \overset{\square}{\phi}_\alpha - v_n \frac{\partial \phi_\alpha(r, s, t)}{\partial r} \quad (3.28)$$

$$\dot{\mu} = \overset{\square}{\mu} - v_n \frac{\partial \mu(r, s, t)}{\partial r} \quad (3.29)$$

which completes the coordinates transformation.

3.2.1.3 Moving Boundary Conditions

As the viewpoint of a moving coordinate system is established, it is now straightforward to apply appropriate boundary conditions. In the coordinate system at hand, they do not appear any different from a conventional boundary condition. However, in a fixed coordinate system they appear as moving in space. Thus, the movement of the coordinate surface is still a degree of freedom which is necessary to acquire any interesting result from the derivation.

Phasefield BCs In this spirit, it is assumed that the phase-field approaches the bulk values corresponding to the two phases α and β at signed distances $r = r_{\pm}$ with $r_- < 0$ and $r_+ > 0$. Without loss of generality the coordinate $r = 0$ corresponds to the $\phi_{\alpha} = 1/2$ contour by means of a boundary condition. By this specific choice, all properties of the basesurface such as its normal velocity v_n or its curvature κ_0 become properties of this contour. Thus they can be seen as important properties associated with the physical problem at hand. For instance, they may reflect the geometry and movement of a phase boundary in space that is parameterized by means of the order parameter.

The corresponding equations read

$$\phi_{\alpha}(0, s, t) = \frac{1}{2} \quad (3.30)$$

$$\phi_{\alpha}(r_+, s, t) = 0 \quad (3.31)$$

$$\phi_{\alpha}(r_-, s, t) = 1. \quad (3.32)$$

It is important to note, that r_{\pm} are not necessarily constants but may well be varying along the surface and with time, i.e. $r_{\pm} = r_{\pm}(s, t)$. Thus the current derivation does not a priori assume a uniform interface thickness or any symmetry of the order-parameter profile.

As it turns out, the above conditions are not sufficient to obtain a unique solution. Therefore, additional boundary conditions are imposed on the spatial derivative. It is assumed that the first derivative of the order parameter is continuous at the endpoints of the interface. Since in the bulk $|\nabla\phi_{\alpha}| = 0$ holds, the corresponding boundary condition writes

$$\left. \frac{\partial\phi_{\alpha}(r, s, t)}{\partial r} \right|_{r=r_{\pm}} = 0. \quad (3.33)$$

This assumption may also be justified by the Gibbs-simplex 2.115 which ensures that $\phi_{\alpha} = 0$ and $\phi_{\alpha} = 1$ are global minima and maxima of the order parameter function.

Chemical Potential BCs In contrast to the derivation for pure surface diffusion, given in [24], we assume continuity of the chemical potential at the interfacial endpoints.

$$\mu(r_{\pm}, s, t) = \mu_{\pm}. \quad (3.34)$$

Here μ_{\pm} denotes the limiting value of the chemical potential from the bulk at r_{\pm} .

This is justified due to the assumption of non-vanishing bulk diffusivities which should in turn remove any discontinuity instantaneously.

In order to derive appropriate boundary condition for the first derivative of the chemical potentials, the contours of the interfacial endpoints $r = r_{\pm}(s, t)$ are considered as a moving surface. Since the evolution equation of the composition in the current model (Eq. (3.4)) fulfills the species mass balance under constant molar volume (Eq. (2.27)), the corresponding interfacial balance can be deduced from Eq. (2.67).

According due to the continuity of the chemical potential, the left-hand side vanishes and thus

$$\mathbf{j}^{-} \cdot \mathbf{n}_{\pm}(s, t) = \mathbf{j}^{\alpha, -} \cdot \mathbf{n}_{\pm}(s, t) \quad (3.35)$$

$$\mathbf{j}^{+} \cdot \mathbf{n}_{\pm}(s, t) = \mathbf{j}^{\beta, +} \cdot \mathbf{n}_{\pm}(s, t) \quad (3.36)$$

results. Here \mathbf{j}^{\pm} denotes the flux density inside the interface as r_{\pm} is approached and $\mathbf{j}^{\alpha, -}$, $\mathbf{j}^{\beta, +}$ the corresponding bulk limits at either side. Note that, the normals $\mathbf{n}_{\pm}(s, t)$ on the $r_{\pm}(s, t)$ curves are not necessarily equal to $\mathbf{n}(s, t)$ since r_{\pm} might depend on the arclength s . However, since the chemical potential is a continuous function of arclength, and due to the aforementioned BC (Eq. (3.34)) as well as the continuity of the chemical mobilities, the tangential component of the flux

density must also be continuous across r_{\pm} . Therefore, continuity of the normal flux demands

$$\left(M \frac{\partial \mu(r, s, t)}{\partial r} \right) \Big|_{r=r_{\pm}} = -j_{n, \pm} \quad (3.37)$$

$$j_{n, +} \equiv \mathbf{j}^{\beta, +} \cdot \mathbf{n}(s, t) = -M^{\beta}(\mu_{+}) \nabla \mu_{+} \cdot \mathbf{n}(s, t) \quad (3.38)$$

$$j_{n, -} \equiv \mathbf{j}^{\alpha, -} \cdot \mathbf{n}(s, t) = -M^{\alpha}(\mu_{-}) \nabla \mu_{-} \cdot \mathbf{n}(s, t) \quad (3.39)$$

also with respect to the normal $\mathbf{n}(s, t)$ on the $\phi_{\alpha} = 1/2$ contour. Here $\nabla \mu_{\pm}$ indicates the bulk limit of the chemical potential gradient as r_{\pm} is approached.

3.2.1.4 Interface Width Expansion

Remarks As interface thickness is reduced, it is expected that the phasefield exhibits a growing magnitude of the gradient in the interfacial region to maintain the respective bulk values. Therefore, it is not meaningful to write the solution in terms of the radial distance r , as we expect it to become singular in terms of r . To obtain a useful set of mathematical equations, it is required to rescale the radial coordinate such that we zoom into the diffuse interface at a rate which keeps solutions regular as a vanishing thickness is approached. For that, the rescaled and dimensionless normal coordinate $\eta \equiv r/\varepsilon$ is introduced.

Additionally, as we expect the solution to approach a sharp-interface limit, Taylor expansion about $\varepsilon = 0$ of the differential equations is performed. Once this is done and assuming that such an expansion exists, it is sufficient to consider all terms of equal power with respect to ε and equate them. As we will see, this simplifies the partial differential equations drastically. It therefore replaces a hard problem, i.e. solving a partial differential equation being difficult or impossible to solve in general, into an infinite number of much simpler problems. And as we are interested in the sharp-interface limiting behavior only, there is no need to solve all of the simple problems but just the very first ones, already revealing the model behavior for vanishing small interface thickness.

Expanding Unknowns The unknowns of the differential equation at hand are the phasefield ϕ_α and the chemical potential μ . Additionally, the normal velocity v_n of the $\phi_\alpha = 1/2$ contour is unknown since in a fixed coordinate system it is a part of its partial time derivative $\dot{\phi}_\alpha$. Furthermore, the interfacial endpoints r^\pm are initially unknown.

Therefore, all these four quantities are written as expansions in terms of the interfacial width parameter ε :

$$\phi_\alpha(\eta, s, t) = \phi_\alpha^0(\eta, s, t) + \varepsilon\phi_\alpha^1(\eta, s, t) + \varepsilon^2\phi_\alpha^2(\eta, s, t) + \mathcal{O}(\varepsilon^3) \quad (3.40)$$

$$\mu(\eta, s, t) = \mu^0(\eta, s, t) + \varepsilon\mu^1(\eta, s, t) + \varepsilon^2\mu^2(\eta, s, t) + \mathcal{O}(\varepsilon^3) \quad (3.41)$$

$$v_n(s, t) = v_n^0(s, t) + \varepsilon v_n^1(s, t) + \varepsilon^2 v_n^2(s, t) + \mathcal{O}(\varepsilon^3) \quad (3.42)$$

$$\eta_\pm(s, t) = \eta_\pm^0(s, t) + \varepsilon\eta_\pm^1(s, t) + \varepsilon^2\eta_\pm^2(s, t) + \mathcal{O}(\varepsilon^3) \quad (3.43)$$

Expanding Functional Quantities Some quantities are functions of the above mentioned unknowns and are therefore expanded by means of chain rule. For instance, the chemical mobility expands as

$$M(\phi_\alpha, \mu) = \frac{1}{\varepsilon}M^0 + M^1 + \varepsilon M^2 + \mathcal{O}(\varepsilon^2) \quad (3.44)$$

$$M^0 = \bar{M}g(\phi_\alpha^0) \quad (3.45)$$

$$M^1 = \bar{M}g'(\phi_\alpha^0)\phi_\alpha^1 + M_b(\phi_\alpha^0, \mu^0) \quad (3.46)$$

$$M^2 = M_s^2 + M_b^2 \quad (3.47)$$

$$M_s^2 = \frac{1}{2} \left(\bar{M} \left(2\phi_\alpha^2 g'(\phi_\alpha^0) + g''(\phi_\alpha^0) (\phi_\alpha^1)^2 \right) \right) \quad (3.48)$$

$$M_b^2 = \mu^1 \left(M^{\alpha'}(\mu^0)h_\alpha(\phi_\alpha^0) + M^{\beta'}(\mu^0) (1 - h_\alpha(\phi_\alpha^0)) \right) + h'_\alpha(\phi_\alpha^0)\phi_\alpha^1 \left(M^\alpha(\mu^0) - M^\beta(\mu^0) \right). \quad (3.49)$$

Similarly, the interpolation function and its derivative

$$h_\alpha(\phi_\alpha) = h_\alpha^0 + \varepsilon h_\alpha^1 + \mathcal{O}(\varepsilon^2) = h_\alpha(\phi_\alpha^0) + \varepsilon h'_\alpha(\phi_\alpha^0) \phi_\alpha^1 + \mathcal{O}(\varepsilon^2) \quad (3.50)$$

$$h'_\alpha(\phi_\alpha) = h_\alpha'^0 + \varepsilon h_\alpha'^1 + \mathcal{O}(\varepsilon^2) = h'_\alpha(\phi_\alpha^0) + \varepsilon h''_\alpha(\phi_\alpha^0) \phi_\alpha^1 + \mathcal{O}(\varepsilon^2) \quad (3.51)$$

as well as chemical properties

$$\psi_\alpha(\mu) - \psi_\beta(\mu) = \psi_\alpha(\mu^0) - \psi_\beta(\mu^0) + \varepsilon \mu^1 \left(\psi'_\alpha(\mu^0) - \psi'_\beta(\mu^0) \right) + \mathcal{O}(\varepsilon^2) \quad (3.52)$$

$$c^\alpha(\mu) - c^\beta(\mu) = c^\alpha(\mu^0) - c^\beta(\mu^0) + \varepsilon \mu^1 \left(c^{\alpha'}(\mu^0) - c^{\beta'}(\mu^0) \right) + \mathcal{O}(\varepsilon^2) \quad (3.53)$$

can be expanded.

Expanding Differential Operators Since the spatial differential operators from Eqs. (3.26)-(3.27) itself include a dependency on ε , they are written in terms of η and an ε -expanded form, yielding

$$\nabla \cdot (a \nabla b) = \frac{1}{\varepsilon^2} \frac{\partial}{\partial \eta} \left(a \frac{\partial b}{\partial \eta} \right) + \frac{a \kappa_0}{\varepsilon} \frac{\partial b}{\partial \eta} - a \eta \kappa_0^2 \frac{\partial b}{\partial \eta} + \frac{\partial}{\partial s} \left(a \frac{\partial b}{\partial s} \right) + \mathcal{O}(\varepsilon) \quad (3.54)$$

$$\nabla^2 = \frac{1}{\varepsilon^2} \frac{\partial^2}{\partial \eta^2} + \frac{\kappa_0}{\varepsilon} \frac{\partial}{\partial \eta} - \eta \kappa_0^2 \frac{\partial}{\partial \eta} + \frac{\partial^2}{\partial s^2} + \mathcal{O}(\varepsilon). \quad (3.55)$$

Accordingly, the partial time derivative is expanded which gives

$$\dot{\phi} = -\frac{1}{\varepsilon} v_n^0 \frac{\partial \phi^0}{\partial \eta} - v_n^0 \frac{\partial \phi^1}{\partial \eta} - v_n^1 \frac{\partial \phi^0}{\partial \eta} + \bar{\phi}^0 + \mathcal{O}(\varepsilon). \quad (3.56)$$

Expanding Boundary Conditions The first boundary condition of the phasefield based on Eq. (3.30) can be written in expanded form as

$$\phi_{\alpha}^0(\eta = 0) = \frac{1}{2} \quad (3.57)$$

$$\phi_{\alpha}^n(\eta = 0) = 0 \quad \forall n > 0. \quad (3.58)$$

Incorporating the expansion of the interfacial endpoints from Eq. (3.43), as shown in [24], into the boundary condition of the phasefield (Eqs. (3.32)-(3.31)), one obtains the following equations for zeroth order

$$\phi_{\alpha}^0(\eta_{-}^0) = 1 \quad (3.59)$$

$$\phi_{\alpha}^0(\eta_{+}^0) = 0, \quad (3.60)$$

first order

$$\left. \frac{\partial \phi_{\alpha}^0(\eta)}{\partial \eta} \right|_{\eta_{\pm}^0} \eta_{\pm}^1 + \phi_{\alpha}^1(\eta_{\pm}^0) = 0, \quad (3.61)$$

and second order

$$\left. \frac{\partial^2 \phi_{\alpha}^0(\eta)}{\partial \eta^2} \right|_{\eta_{\pm}^0} (\eta_{\pm}^1)^2 + 2 \left. \frac{\partial \phi_{\alpha}^0(\eta)}{\partial \eta} \right|_{\eta_{\pm}^0} \eta_{\pm}^2 + 2 \left. \frac{\partial \phi_{\alpha}^1(\eta)}{\partial \eta} \right|_{\eta_{\pm}^0} \eta_{\pm}^1 + 2\phi_{\alpha}^2(\eta_{\pm}^0) = 0. \quad (3.62)$$

Analogously, the derivative boundary conditions from Eq. (3.33) require at lowest order that

$$\left. \frac{\partial \phi_{\alpha}^0}{\partial \eta} \right|_{\eta_{\pm}^0} = 0 \quad (3.63)$$

and at first order

$$\left. \frac{\partial^2 \phi_{\alpha}^0(\eta)}{\partial \eta^2} \right|_{\eta_{\pm}^0} \eta_{\pm}^1 + \left. \frac{\partial \phi_{\alpha}^1}{\partial \eta} \right|_{\eta_{\pm}^0} = 0, \quad (3.64)$$

as well as second order

$$\frac{\partial^3 \phi_\alpha^0(\eta)}{\partial \eta^3} \Big|_{\eta_\pm^0} (\eta_\pm^1)^2 + 2 \frac{\partial^2 \phi_\alpha^0(\eta)}{\partial \eta^2} \Big|_{\eta_\pm^0} \eta_\pm^2 + 2 \frac{\partial^2 \phi_\alpha^1(\eta)}{\partial \eta^2} \Big|_{\eta_\pm^0} \eta_\pm^1 + 2 \frac{\partial \phi_\alpha^2}{\partial \eta} \Big|_{\eta_\pm^0} = 0. \quad (3.65)$$

To account for the continuity of the chemical potential, firstly, the bulk limit is written in an expanded form

$$\mu_\pm = \mu_\pm^0 + \varepsilon \mu_\pm^1 + \varepsilon^2 \mu_\pm^2 + \mathcal{O}(\varepsilon^3) \quad (3.66)$$

which is equated with the the LHS of equation (3.34) and expanded to obtain

$$\mu_\pm^0 = \mu^0(\eta_\pm^0) \quad (3.67)$$

$$\mu_\pm^1 = \frac{\partial \mu^0(\eta)}{\partial \eta} \Big|_{\eta_\pm^0} \eta_\pm^1 + \mu^1(\eta_\pm^0) \quad (3.68)$$

for the lowest two orders.

The endpoint bulk flux is expanded

$$j_{n,\pm} = j_{n,\pm}^0 + \varepsilon j_{n,\pm}^1 + \varepsilon^2 j_{n,\pm}^2 + \mathcal{O}(\varepsilon^3) \quad (3.69)$$

and equated with the LHS of equation (3.38). Afterwards, to obtain a Taylor-expandable form in the zoomed coordinate η , both sides are multiplied with ε^2 to obtain

$$\left(\varepsilon M \frac{\partial \mu}{\partial \eta} \right) \Big|_{\eta=\eta_\pm} = -\varepsilon^2 j_{n,\pm}^0 + \mathcal{O}(\varepsilon^3). \quad (3.70)$$

To simplify the writeup, we first denote a negative rescaled flux as

$$J \equiv \varepsilon M \frac{\partial \mu}{\partial \eta} \quad (3.71)$$

which according to expansions (Eq. (3.41) and Eq. (3.45)) writes as

$$J = J^0 + \varepsilon J^1 + \varepsilon^2 J^2 + \mathcal{O}(\varepsilon^3) \quad (3.72)$$

$$J^0 \equiv M^0 \frac{\partial \mu^0}{\partial \eta} \quad (3.73)$$

$$J^1 \equiv M^1 \frac{\partial \mu^0}{\partial \eta} + M^0 \frac{\partial \mu^1}{\partial \eta} \quad (3.74)$$

$$J^2 \equiv M^2 \frac{\partial \mu^0}{\partial \eta} + M^1 \frac{\partial \mu^1}{\partial \eta} + M^0 \frac{\partial \mu^2}{\partial \eta}. \quad (3.75)$$

By incorporating the dependence of η_{\pm} on ε , one obtains

$$0 = J^0(\eta_{\pm}^0) \quad (3.76)$$

$$0 = \left. \frac{\partial J^0}{\partial \eta} \right|_{\eta_{\pm}^0} \eta_{\pm}^1 + J^1(\eta_{\pm}^0) \quad (3.77)$$

$$0 = \left. \frac{\partial^2 J^0}{\partial \eta^2} \right|_{\eta_{\pm}^0} (\eta_{\pm}^1)^2 + 2 \left. \frac{\partial J^0}{\partial \eta} \right|_{\eta_{\pm}^0} \eta_{\pm}^2 + 2 \left. \frac{\partial J^1}{\partial \eta} \right|_{\eta_{\pm}^0} \eta_{\pm}^1 + 2J^2(\eta_{\pm}^0) + 2j_{n,\pm}^0. \quad (3.78)$$

Evolution Equations Based on equation (3.13) and the expansions for the differential operators derived so far, the evolution equation for the phasefield in expanded form writes

$$\begin{aligned}
& \left(\frac{-v_n^0 - \varepsilon v_n^1}{m_{\alpha\beta} \gamma_{\alpha\beta}} - \kappa_0 \right) \left(\frac{\partial \phi_\alpha^0}{\partial \eta} + \varepsilon \frac{\partial \phi_\alpha^1}{\partial \eta} \right) + \varepsilon \eta \kappa_0^2 \frac{\partial \phi_\alpha^0}{\partial \eta} + \varepsilon \phi_\alpha^0 \\
&= \frac{1}{\varepsilon} \frac{\partial^2 \phi_\alpha^0}{\partial \eta^2} + \frac{\partial^2 \phi_\alpha^1}{\partial \eta^2} + \varepsilon \frac{\partial^2 \phi_\alpha^2}{\partial \eta^2} + \varepsilon \frac{\partial^2 \phi_\alpha^0}{\partial s^2} \\
&- \frac{8}{\pi^2} \left(\frac{1}{\varepsilon} - 2 \left(\frac{1}{\varepsilon} \phi_\alpha^0 + \phi_\alpha^1 + \varepsilon \phi_\alpha^2 \right) \right) \\
&- \frac{\Psi_\alpha(\mu^0) - \Psi_\beta(\mu^0)}{2\gamma_{\alpha\beta}} \left(h'_\alpha(\phi_\alpha^0) + \varepsilon h''_\alpha(\phi_\alpha^0) \phi_\alpha^1 \right) \\
&- \varepsilon \mu^1 h'_\alpha(\phi_\alpha^0) \frac{\Psi'_\alpha(\mu^0) - \Psi'_\beta(\mu^0)}{2\gamma_{\alpha\beta}} + \mathcal{O}(\varepsilon^2).
\end{aligned} \tag{3.79}$$

Additionally, the evolution equation for the chemical potential, expanded up to zero order writes as

$$\begin{aligned}
& \frac{1}{\varepsilon^3} \frac{\partial}{\partial \eta} \left((M^0 + \varepsilon M^1 + \varepsilon^2 M^2) \frac{\partial (\mu^0 + \varepsilon \mu^1 + \varepsilon^2 \mu^2)}{\partial \eta} \right) \\
&+ \frac{M^0 \kappa_0}{\varepsilon^2} \frac{\partial \mu^0}{\partial \eta} + \frac{M^0 \kappa_0}{\varepsilon} \frac{\partial \mu^1}{\partial \eta} + \frac{1}{\varepsilon} \frac{\partial}{\partial s} \left(M^0 \frac{\partial \mu^0}{\partial s} \right) \\
&+ \frac{M^1 \kappa_0 - M^0 \eta \kappa_0^2 + v_n^0 \partial c / \partial \mu |_{\phi_\alpha^0, \mu^0}}{\varepsilon} \frac{\partial \mu^0}{\partial \eta} \\
&+ \left(c^\alpha(\mu^0) - c^\beta(\mu^0) \right) \frac{v_n^0}{\varepsilon} \frac{\partial h_\alpha(\phi_\alpha^0)}{\partial \eta} + \mathcal{O}(1) = 0.
\end{aligned} \tag{3.80}$$

These two equations serve as a basis for the derivation performed order by order in the following section.

3.2.2 Derivation

3.2.2.1 Lowest Order Phase-Field Profile

Statement of the Differential Equation For the phase-field evolution, terms at the lowest order $1/\varepsilon$ are collected from equation (3.79) and hence

$$\frac{\partial^2 \phi_\alpha^0}{\partial \eta^2} + \frac{16}{\pi^2} \phi_\alpha^0 = \frac{8}{\pi^2}. \quad (3.81)$$

To obtain a unique solution, this differential equation with respect to η is subjected with the derived boundary conditions. For the current order, they read $\phi_\alpha^0(0) = 1/2$, $\phi_\alpha^0(\eta_-^0) = 1$, $\phi_\alpha^0(\eta_+^0) = 0$ (Eqs. (3.59)-(3.60)) as well as $\partial \phi_\alpha^0 / \partial \eta|_{\eta_\pm^0} = 0$ (Eq. (3.63)).

Solving the Equation The solution to the above differential equation satisfying $\phi_\alpha^0(0) = 1/2$ (which rules out a possible cosine term), reads

$$\phi_\alpha^0(\eta) = \frac{1}{2} + C_1 \sin\left(\frac{4}{\pi}\eta\right) \quad (3.82)$$

with a constant C_1 . At first sight, it is not clear at which point the interfacial endpoints are located, since $\phi_\alpha^0(\eta_-^0) = 1$ and $\phi_\alpha^0(\eta_+^0) = 0$ can hold at any point for arbitrary values of C_1 . For that, we turn our attention to the first derivative

$$\frac{\partial \phi_\alpha^0}{\partial \eta} = \frac{4C_1}{\pi} \cos\left(\frac{4}{\pi}\eta\right), \quad (3.83)$$

because the derivative BC $\partial \phi_\alpha^0 / \partial \eta|_{\eta_\pm^0} = 0$ demands roots of the above equations which is entirely independent of C_1 . The roots of the equation are periodically placed at $\pi^2/8 + n\pi^2/4$, $\forall n \in \mathbb{Z}$. Here, it is necessary to rule out some of the possibilities to obtain a unique solution for η_\pm^0 . To obtain only a single interface

with a monotonous ϕ_α^0 and demanding that $\eta_+^0 > 0$, the only choice that remains is that

$$\eta_\pm^0 = \pm \frac{\pi^2}{8}. \quad (3.84)$$

This means that in the sharp-interface limit, an interface thickness of $\varepsilon\pi^2/4$ independent of arclength and time is approached.

Now, the conditions $\phi_\alpha^0(\eta_-^0) = 1$ and $\phi_\alpha^0(\eta_+^0) = 0$ are satisfied if the constant $C_1 = -1/2$ and thus

$$\phi_\alpha^0(\eta) = \frac{1}{2} - \frac{1}{2} \sin\left(\frac{4}{\pi}\eta\right) \quad (3.85)$$

is the solution for the order parameter at lowest order.

Remarks Equation (3.85) is identical to the form usually obtained when finding an equilibrium solution for a planar interface, as done in [97, Section 3.1.3]. Therefore, the current analysis shows that the sinusoidal profile is the sharp-interface limiting interface profile also for a curved interface. It is no surprise, that this is also identical to [24, Eq. (68)] in the derivation with pure surface diffusion, as the chemical potential is not affecting the phase-field equation at lowest order. Another point worth mentioning is that ϕ_α^0 does neither depend on the arclength s or time t which in turn leads to $\partial\phi_\alpha^0/\partial s = 0$ and $\dot{\phi}_\alpha^0 = 0$ according to Eq. (2.61).

3.2.2.2 Lowest Order Chemical Potential

At lowest order in Eq. (3.80) only a single term exists, which reads

$$\frac{\partial}{\partial \eta} \left(M^0 \frac{\partial \mu^0}{\partial \eta} \right) = 0 \quad (3.86)$$

and is subject to the BCs $(M^0 \partial \mu^0 / \partial \eta)|_{\eta_{\pm}^0} = 0$ from Eq. (3.76). Integrated with respect to η from η_-^0 to η taking into account the BC, one obtains

$$M^0 \frac{\partial \mu^0}{\partial \eta} = 0, \quad (3.87)$$

satisfying also the other BC $(M^0 \partial \mu^0 / \partial \eta)|_{\eta_+^0} = 0$. Since $M^0(\eta) = \bar{M}g(\phi_\alpha^0)$ is a known function and according to the zeroth order phasefield, $M^0(\eta) > 0$ everywhere except at η_{\pm}^0 , it must be that

$$\frac{\partial \mu^0}{\partial \eta} = 0 \quad (3.88)$$

and hence $\mu^0 = \mu^0(s, t)$ is constant with respect to η . The continuity of the chemical potential at the endpoints (Eq. (3.67)) shows that in the sharp-interface limit,

$$\mu_+^0 = \mu_-^0 = \mu^0(s, t) \quad (3.89)$$

holds implying that the bulk chemical potential is continuous at the interface. As it turns out, the value of $\mu^0(s, t)$ is still unknown and needs to be fixed at higher orders.

3.2.2.3 Next to Lowest Order Phase-Field

Statement of the Differential Equation Collecting terms of order ε^0 in equation (3.79), the following differential equation results:

$$\frac{\partial^2 \phi_\alpha^1}{\partial \eta^2} + \frac{16}{\pi^2} \phi_\alpha^1 = \left(\frac{-v_n^0}{m_{\alpha\beta} \gamma_{\alpha\beta}} - \kappa_0 \right) \frac{\partial \phi_\alpha^0}{\partial \eta} + \frac{\psi_\alpha(\mu^0) - \psi_\beta(\mu^0)}{2\gamma_{\alpha\beta}} h'_\alpha(\phi_\alpha^0). \quad (3.90)$$

If the explicit form of $h'_\alpha(\phi_\alpha^0)$ was given, the dependence of the right-hand side on η would be completely known. To keep the analysis general, it is attempted to

solve the equation in an integral way such that important physical quantities can be deduced without having to explicitly give the formula for $\phi_\alpha^1(\eta)$.

Multiplication and Integration For that, Eq. (3.90) is multiplied by the known function $\partial\phi_\alpha^0/\partial\eta$ and integrated

$$\begin{aligned} \int_{\eta_-^0}^{\eta_+^0} \left(\frac{\partial^2 \phi_\alpha^1}{\partial \eta^2} + \frac{16}{\pi^2} \phi_\alpha^1 \right) \frac{\partial \phi_\alpha^0}{\partial \eta} d\eta = \\ \int_{\eta_-^0}^{\eta_+^0} \left(\frac{-v_n^0}{m_{\alpha\beta} \gamma_{\alpha\beta}} - \kappa_0 \right) \left(\frac{\partial \phi_\alpha^0}{\partial \eta} \right)^2 + \frac{\psi_\alpha(\mu^0) - \psi_\beta(\mu^0)}{2\gamma_{\alpha\beta}} h'_\alpha(\phi_\alpha^0) \frac{\partial \phi_\alpha^0}{\partial \eta} d\eta. \end{aligned} \quad (3.91)$$

To incorporate the boundary conditions for ϕ_α^1 and $\partial\phi_\alpha^1/\partial\eta$, the LHS is integrated by parts, which yields

$$\begin{aligned} \int_{\eta_-^0}^{\eta_+^0} \left(\frac{\partial^2 \phi_\alpha^1}{\partial \eta^2} + \frac{16}{\pi^2} \phi_\alpha^1 \right) \frac{\partial \phi_\alpha^0}{\partial \eta} d\eta = \left[\frac{\partial \phi_\alpha^1}{\partial \eta} \frac{\partial \phi_\alpha^0}{\partial \eta} \right]_{\eta_-^0}^{\eta_+^0} + \frac{16}{\pi^2} [\phi_\alpha^1 \phi_\alpha^0]_{\eta_-^0}^{\eta_+^0} \\ - \int_{\eta_-^0}^{\eta_+^0} \frac{\partial \phi_\alpha^1}{\partial \eta} \left(\frac{\partial^2 \phi_\alpha^0}{\partial \eta^2} + \frac{16}{\pi^2} \phi_\alpha^0 \right) d\eta. \end{aligned} \quad (3.92)$$

Repeating this procedure for the remaining integral, one obtains

$$\begin{aligned} \int_{\eta_-^0}^{\eta_+^0} \frac{\partial \phi_\alpha^1}{\partial \eta} \left(\frac{\partial^2 \phi_\alpha^0}{\partial \eta^2} + \frac{16}{\pi^2} \phi_\alpha^0 \right) d\eta = \left[\phi_\alpha^1 \left(\frac{\partial^2 \phi_\alpha^0}{\partial \eta^2} + \frac{16}{\pi^2} \phi_\alpha^0 \right) \right]_{\eta_-^0}^{\eta_+^0} \\ - \int_{\eta_-^0}^{\eta_+^0} \phi_\alpha^1 \left(\frac{\partial^3 \phi_\alpha^0}{\partial \eta^3} + \frac{16}{\pi^2} \frac{\partial \phi_\alpha^0}{\partial \eta} \right) d\eta. \end{aligned} \quad (3.93)$$

First it is noted, that the remaining integral vanishes since $0 = \partial^3 \phi_\alpha^0 / \partial \eta^3 + 16/\pi^2 \partial \phi_\alpha^0 / \partial \eta$ according to the differential equation for the zeroth order phase-field (Eq. (3.81)). Therefore one obtains the initial integral only in terms of the BCs for ϕ_α^1 and its first derivative as well as the known function ϕ_α^0 , i.e.

$$\int_{\eta_-^0}^{\eta_+^0} \left(\frac{\partial^2 \phi_\alpha^1}{\partial \eta^2} + \frac{16}{\pi^2} \phi_\alpha^1 \right) \frac{\partial \phi_\alpha^0}{\partial \eta} d\eta = \left[\frac{\partial \phi_\alpha^1}{\partial \eta} \frac{\partial \phi_\alpha^0}{\partial \eta} \right]_{\eta_-^0}^{\eta_+^0} - \left[\phi_\alpha^1 \frac{\partial^2 \phi_\alpha^0}{\partial \eta^2} \right]_{\eta_-^0}^{\eta_+^0}. \quad (3.94)$$

The first term on the RHS of the above equation vanishes since $\partial \phi_\alpha^0(\eta) / \partial \eta \big|_{\eta_\pm^0} = 0$ and from the BC of the phasefield at lowest order (Eq. (3.61)),

$$\phi_\alpha^1(\eta_\pm^0) = - \left. \frac{\partial \phi_\alpha^0(\eta)}{\partial \eta} \right|_{\eta_\pm^0} \eta_\pm^0 = 0 \quad (3.95)$$

and hence also the second term vanishes. Therefore, the left-hand side of Eq. (3.92) is identically zero.

For the right-hand side of Eq. (3.92), the first term can simply be integrated from the known solution

$$\int_{\eta_-^0}^{\eta_+^0} \left(\frac{\partial \phi_\alpha^0}{\partial \eta} \right)^2 d\eta = \frac{1}{2}, \quad (3.96)$$

whereas the second term can be deduced by means of integration by substitution

$$\int_{\eta_-^0}^{\eta_+^0} h'_\alpha(\phi_\alpha^0) \frac{\partial \phi_\alpha^0}{\partial \eta} d\eta = [h_\alpha(\phi_\alpha^0(\eta))]_{\eta_-^0}^{\eta_+^0} = h_\alpha(0) - h_\alpha(1) = -1 \quad (3.97)$$

taking into account the conditions imposed on the interpolation function through Eq. (2.111)-(2.112).

Gibbs-Thomson Condition The resulting equation turns out to be the Gibbs-Thomson effect relating the difference in grand-potential densities of the two phases to curvature

$$\psi_{\beta}(\mu^0) - \psi_{\alpha}(\mu^0) = \gamma_{\alpha\beta} \kappa_0 + \frac{v_n^0}{m_{\alpha\beta}}. \quad (3.98)$$

The additional kinetic term reflects the attachment kinetics due to a finite interface mobility $m_{\alpha\beta}$. An important special case pertains to grain boundaries, where the two grains at either side of the interface have identical chemical properties, i.e. $\psi_{\alpha}(\mu^0) = \psi_{\beta}(\mu^0)$. Then, the movement of the GB is governed by curvature, such that

$$v_n^0 = -m_{\alpha\beta} \gamma_{\alpha\beta} \kappa_0 \quad \text{for GBs} \quad (3.99)$$

holds. An interesting point is that in this case, the value of μ^0 is not affixed by the model equations.

In contrast, for chemically distinct phases, we may expand the grand-potential difference for small deviations from equilibrium as follows

$$\begin{aligned} \psi_{\alpha}(\mu^0) - \psi_{\beta}(\mu^0) &= \psi_{\alpha}(\mu_{\text{eq}}) - \psi_{\beta}(\mu_{\text{eq}}) \\ &+ (\mu^0 - \mu_{\text{eq}}) \left(c^{\beta}(\mu_{\text{eq}}) - c^{\alpha}(\mu_{\text{eq}}) \right) + \mathcal{O}((\mu^0 - \mu_{\text{eq}})^2) \end{aligned} \quad (3.100)$$

since $\psi'_{\alpha}(\mu) = -c^{\alpha}(\mu)$. Additionally, since $\psi_{\alpha}(\mu_{\text{eq}}) = \psi_{\beta}(\mu_{\text{eq}})$ per definition of μ_{eq} ,

$$\mu^0 - \mu_{\text{eq}} = \frac{\gamma_{\alpha\beta} \kappa_0 + \frac{v_n^0}{m_{\alpha\beta}}}{c^{\alpha}(\mu_{\text{eq}}) - c^{\beta}(\mu_{\text{eq}})} + \mathcal{O}((\mu^0 - \mu_{\text{eq}})^2) \quad (3.101)$$

holds. Therefore, the value of μ^0 is fixed depending on the curvature and the movement of the interface.

3.2.2.4 Next to Lowest Order Chemical Potential

Terms at order ε^{-2} are collected from Eq. (3.80) to obtain

$$\frac{\partial}{\partial \eta} \left(M^0 \frac{\partial \mu^1}{\partial \eta} \right) + \frac{\partial}{\partial \eta} \left(M^1 \frac{\partial \mu^0}{\partial \eta} \right) + M^0 \kappa_0 \frac{\partial \mu^0}{\partial \eta} = 0. \quad (3.102)$$

and since $\partial \mu^0 / \partial \eta = 0$, simplifies to

$$\frac{\partial}{\partial \eta} \left(M^0 \frac{\partial \mu^1}{\partial \eta} \right) = 0. \quad (3.103)$$

The flux BC from Eq. (3.77), simplifies to $J^1(\eta_{\pm}^0) = M^0 \partial \mu^1 / \partial \eta |_{\eta_{\pm}^0} = 0$ since $J^0 = 0$. Integrating from η_-^0 to η_+^0 and taking these conditions into account it results that

$$\frac{\partial \mu^1}{\partial \eta} = 0 \quad (3.104)$$

for the same reason as for the zero order chemical potential μ^0 .

3.2.2.5 Second Order Chemical Potential

The differential equation derived from Eq. (3.80) at order ε^{-1} is expressed as

$$\begin{aligned} 0 = & \frac{\partial}{\partial \eta} \left(M^0 \frac{\partial \mu^2}{\partial \eta} + M^1 \frac{\partial \mu^1}{\partial \eta} + M^2 \frac{\partial \mu^0}{\partial \eta} \right) + M^0 \kappa_0 \frac{\partial \mu^1}{\partial \eta} + M^0 \frac{\partial^2 \mu^0}{\partial s^2} \\ & + \frac{\partial M^0}{\partial s} \frac{\partial \mu^0}{\partial s} + \left(M^1 \kappa_0 - M^0 \eta \kappa_0^2 + v_n^0 \frac{\partial c}{\partial \mu} \Big|_{\phi_{\alpha}^0, \mu^0} \right) \frac{\partial \mu^0}{\partial \eta} \\ & + v_n^0 \left(c^{\alpha}(\mu^0) - c^{\beta}(\mu^0) \right) \frac{\partial h_{\alpha}(\phi_{\alpha}^0(\eta))}{\partial \eta}. \end{aligned} \quad (3.105)$$

Since $\partial\mu^0/\partial\eta = 0$ and $\partial\mu^1/\partial\eta = 0$ as well as $\partial M^0/\partial s = 0$ (since $\partial\phi_\alpha^0/\partial s = 0$) hold, the equation can be drastically simplified, resulting in

$$\frac{\partial}{\partial\eta} \left(M^0 \frac{\partial\mu^2}{\partial\eta} \right) = -M^0 \frac{\partial^2\mu^0}{\partial s^2} - \left(c^\alpha(\mu^0) - c^\beta(\mu^0) \right) v_n^0 \frac{\partial h_\alpha(\phi_\alpha^0(\eta))}{\partial\eta}. \quad (3.106)$$

Integrating with respect to the interval η_-^0 to η_+^0 gives

$$\left[M^0 \frac{\partial\mu^2}{\partial\eta} \right]_{\eta_-^0}^{\eta_+^0} = -\frac{\partial^2\mu^0}{\partial s^2} \int_{\eta_-^0}^{\eta_+^0} M^0 d\eta + v_n^0 \left(c^\alpha(\mu^0) - c^\beta(\mu^0) \right) \quad (3.107)$$

where the already known equation (3.97) has been utilized. The flux BC at second order, taking into account $J^0 = 0$ and $J^1 = 0$, yields $J^2(\eta_\pm^0) = \left(M^0 \frac{\partial\mu^2}{\partial\eta} \right) \Big|_{\eta_\pm^0} = -j_{n,\pm}^0$. Hence,

$$v_n^0 \left(c^\alpha(\mu^0) - c^\beta(\mu^0) \right) = \bar{M} I_g \frac{\partial^2\mu^0}{\partial s^2} + \left(j^\alpha - j^\beta \right) \cdot \mathbf{n} \quad (3.108)$$

is the governing law in the sharp-interface limit. $I_g \equiv \int_{\eta_-^0}^{\eta_+^0} g(\phi_\alpha^0) d\eta$ is the integral of the dimensionless surface diffusion function across the interface with respect to the rescaled normal coordinate η . Equation (3.108) is identical to the extended interfacial balance (Eq. (2.72)) where the density b corresponds to the composition c such that

$$b^- \rightarrow c^\alpha \quad (3.109)$$

$$b^+ \rightarrow c^\beta. \quad (3.110)$$

The excess surface flux density is given by replacing

$$j_{b,s} \rightarrow -\bar{M} I_g \nabla_s \mu \quad (3.111)$$

which is very much in the spirit of Mullins' surface-diffusion theory which defines an equation of equivalent form (Eq. (2.83)). Interestingly, the prefactor I_g has

a form equivalent to the excess surface flux density defined through Eq. (2.80). Additionally, a vanishing excess surface density

$$b_s \rightarrow 0 \quad (3.112)$$

is obtained which is in agreement with the same theory.

Table 3.1: Normal integral of the dimensionless surface diffusion function I_g for several choices of g [24, Table I]. $\Gamma(x)$ denotes the gamma function.

$g(\phi_\alpha)$	I_g
$\sqrt{\phi_\alpha(1-\phi_\alpha)}$	$\pi/4$
$\phi_\alpha(1-\phi_\alpha)$	$\pi^2/32$
$\phi_\alpha^2(1-\phi_\alpha)^2$	$3\pi^2/512$
$\phi_\alpha^n(1-\phi_\alpha)^n$	$\pi^{3/2}\Gamma(n+1/2)/(4^{n+1}\Gamma(n+1))$

The prefactor I_g is identical to the term obtained in the asymptotic treatment for pure surface diffusion [24, Table I] and is tabulated in Table 3.1 for functions of the form $\phi_\alpha^n(1-\phi_\alpha)^n$.

Comparing Eq. (3.108) with the evolution equation of the surface diffusion theory (Eq. (2.84)), the rate constant B is extracted by taking the limit of the bulk diffusivities as $D^\alpha = D^\beta \rightarrow 0$ which results in

$$B = \frac{\bar{M}I_g\gamma_{\alpha\beta}}{(c^\alpha(\mu_{\text{eq}}) - c^\beta(\mu_{\text{eq}}))^2} \quad (3.113)$$

taking into account Eq. (3.101) in the limit of infinite attachment kinetics ($m_{\alpha\beta} \rightarrow \infty$).

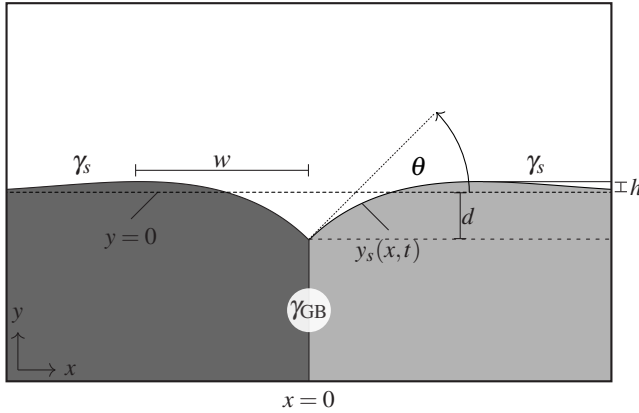


Figure 3.1: Sketch of a symmetric thermal groove and the corresponding quantities: Height h , depth d and width w of the groove. The groove geometry for the right-hand side is given by function $y_s(x,t)$ and the grain boundary is located at $x=0$. The original flat surface corresponds to $y=0$.

3.3 Thermal Grooving Study

Motivation Thermal grooving also known as grain-boundary grooving is a phenomenon occurring in polycrystalline materials at triple lines where a grain boundary intersects the free surface of the crystal. It is driven by the minimization of the grain-boundary energy by reducing its corresponding surface area. This results in a deepening at the triple junction which is due to mass transport away from the groove. Thermal grooving is a suitable benchmark case for the proposed multiphase-field model since at least three different grains or phases need to be distinguished. This is not possible with a simple two-phase model. Moreover, it is particularly well understood since analytical solutions are available for thermal grooving under a variety of transport mechanisms. The analytical solutions have been presented in two early works, [42] and [91], valid for pure surface diffusion and pure volume diffusion, respectively. Moreover, the solutions are valid in the so-called small-slope limit which corresponds to the case that the grain-boundary energy is much smaller than the energy of the free surface. A numerical

extension to finite surface slopes was presented in [98] for surface-diffusion governed grooving. For this case it could be demonstrated in a first work [24] that the current model is able to reproduce the more broadly applicable numerical solutions for finite slopes with a high level of accuracy. However, the combination of surface and volume diffusion was not included in the comparative study. Therefore, a demonstration of the accuracy of the current model for combined surface and volume diffusion is still missing. Although exact solutions for finite surface slopes are not available under the combined action of surface and volume diffusion to the best of the authors knowledge, a generalization of the analytical solutions by Mullins was presented in [25] for this case, valid for small slopes. Therefore, a comparison between the phase-field results and the sharp-interface solution is possible as long as small surface slopes can be maintained. The following study compares characteristic dimensions of the surface groove and the corresponding grooving kinetics between the developed multiphase-field model and the analytical solution presented in [25].

3.3.1 Sharp-Interface Solution

A sketch of a typical thermal groove is shown in Fig. 3.1, where a vertical grain boundary intersects the free surface at $x = 0$ corresponding to the root of the groove. A symmetry is assumed such that the groove has identical shapes for $x < 0$ and $x > 0$, corresponding to identical surface energies γ_s at each of the free surfaces. The grain-boundary energy is given by γ_{GB} . Due to the symmetry, the groove can be completely described by function $y_s(x, t)$ corresponding to the right-hand side of the groove. An equilibrium angle θ is assumed at $x = 0$ such that a constant slope m_0 results ($\partial y_s(x, t) / \partial x|_{x=0} = m_0 = \tan \theta$ holds).

The groove slope at the triple junction is given by [24, Eq. (127)]

$$m_0 = \left(4 \left(\frac{\gamma_s}{\gamma_{GB}} \right)^2 - 1 \right)^{-\frac{1}{2}} \quad (3.114)$$

in terms of the involved interfacial energies, known as Young's law.

There are three characteristic dimensions of the groove: A depth $d = -y_s(0, t)$ which corresponds to the deepening of the groove at the GB, a height h corresponding to the maximal elevation of the groove above the originally flat position $y = 0$ and a width w which is the x -coordinate of this maximum. These dimensions can be calculated as functions of time as soon as the solution to the function $y_s(x, t)$ is known.

The small-slope solution provided in [25] can be written as

$$y_s(x, t) = m_0(Bt)^{\frac{1}{4}} z_s(u(x, t), p(t)) \quad (3.115)$$

$$u(x, t) = \frac{x}{(Bt)^{\frac{1}{4}}} \quad (3.116)$$

including the rate constant B from Eq. (2.85). Moreover, $u(x, t)$ is a dimensionless rescaled x -coordinate, $z_s(u, p)$ is a dimensionless function to provide a rescaled y -coordinate of the groove and $p(t)$ is a dimensionless parameter given by

$$p(t) = \frac{A't^{\frac{1}{4}}}{B^{\frac{3}{4}}}. \quad (3.117)$$

It is a parameter indicating the relative contribution of volume diffusion with respect to surface diffusion. The rate constant for volume diffusion governed grooving is given by Eq. (A.13) as

$$A' \equiv \frac{Dc_0^m \gamma_s V_m^2}{RT}. \quad (3.118)$$

When $p = 0$, the surface geometry is completely determined by surface diffusion and becomes identical to the solution given in [42]. On the contrary, when p approaches ∞ , the groove shape is identical to the solution of [91]. Therefore, the groove growth is initially (at early times where $p(t) \ll 1$) dominated by surface diffusion and the relative contribution of volume diffusion increases with time

and becomes eventually dominant for late times where $p(t) \gg 1$. When p is in the order of unity, an interplay of both contribution governs the evolution.

For pure surface diffusion or pure volume diffusion, the groove shape evolves with time as a similarity solution. This means that all the dimensions of the groove remain identical up to a time-dependent scaling. For surface diffusion the scaling is given by an exponent of $1/4$, whereas for volume diffusion an exponent of $1/3$ is obtained. Therefore, a groove under pure surface diffusion doubles its size when the time is increased by a factor of sixteen, while for volume diffusion this factor is reduced to eight. For the combination of both effects, no constant exponent is maintained but the variation in the rescaled shape is incorporated through the extra dependence on the parameter p .

The dimensionless groove shape can be written as a Fourier-cosine transform in the following way

$$z_s(u, p) = \frac{2}{\pi} \int_0^\infty \frac{\exp(-k^4 - pk^3) - 1}{k^2} \cos(ku) dk. \quad (3.119)$$

For practical calculations, the Maclaurin series representation

$$z_s(u, p) = u + \frac{1}{2\pi} \sum_{k=0}^{\infty} a_k(p) u^{2k} \quad (3.120)$$

$$a_k(p) = \sum_{l=0}^{\infty} \frac{(-1)^{k+l}}{(2k)! l!} \Gamma\left(\frac{3l+2k-1}{4}\right) p^l \quad (3.121)$$

can be used by computing partial sums. Here $\Gamma(x)$ denotes the gamma function.

The corresponding rescaled groove geometries are depicted in Fig. 3.2. In the case of pure surface diffusion ($p = 0$) the groove assumes its global minimum at the root ($x = 0$) with a rescaled depth of about $z_s(0, 0) = -0.78$ and the function increases with increasing distance from the grain boundary. At $u \approx 2.3$, a maximum is reached with the height of $z_s \approx 0.19$. In addition, the curve assumes a local minimum between $5 < u < 6$ (a so-called dip) that has a relatively small magnitude but can be considered as a characteristic qualitative feature. As p

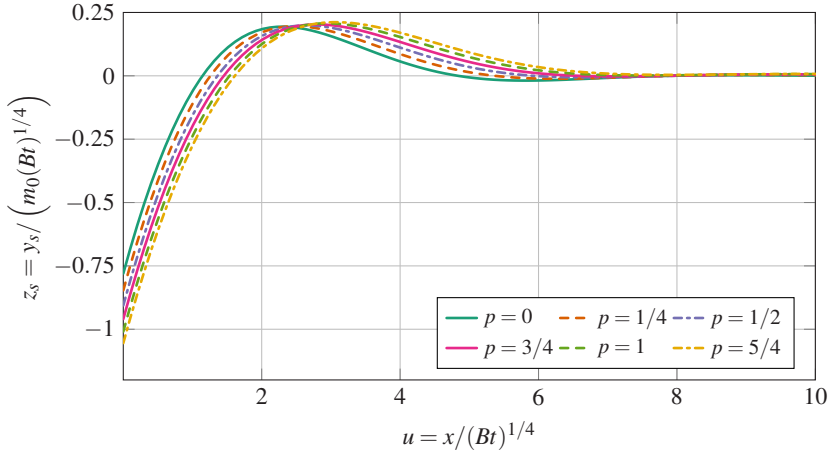


Figure 3.2: Small-slope sharp-interface solutions of the groove geometry in non-dimensional form $z_s(u, p)$ from [25], where the parameter p is varied. The contribution of volume diffusion relative to surface diffusion increases with p .

increases, the rescaled depth of the groove increases almost linearly with p such that at $p = 1$ the depth of the groove is approximately $z_s(0, 1) \approx -1$. Similarly, the distance of the grooves maximum from the GB increases with p , while the dimensionless height of the groove remains relatively constant (at $p = 1$, $z_s \approx 0.21$ at the maximum). In addition, the characteristic dip becomes less pronounced with increasing p and is absent for $p \geq 1$ such that the groove function remains positive for distances larger than its maximum location.

3.3.2 Phase-Field Simulation

In the following, a multiphase-field simulation is conducted for thermal grooving under combined surface and volume diffusion.

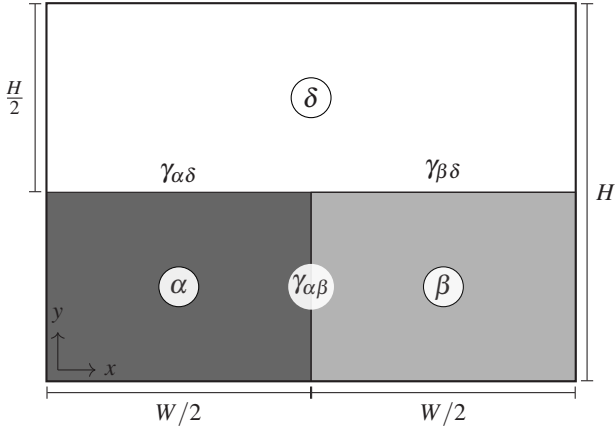


Figure 3.3: Two-dimensional simulation setup for the multiphase-field simulation of thermal grooving under a combination of surface and volume diffusion.

3.3.2.1 Simulation Setup

The simulation setup for the MPF simulation is sketched in Fig. 3.3. Three different order parameters ϕ_α , ϕ_β and ϕ_δ are considered (i.e. $N = 3$) and a single composition variable ($K = 2$) is utilized. The α and β phase correspond to two distinct grains with identical chemical properties and the δ phase corresponds to a solvent with a different equilibrium composition.

The domain has a total width of $W = 250u_l$ and a height of $H = 500u_l$ (u_l denotes an arbitrary length unit). The size of the domain is chosen firstly to keep enough space in the y -direction for the far composition field that develops due to volume diffusion and secondly to ensure that the groove surface remains flat far away from the grain boundary. The two grains are located on the bottom of the domain and are of equal size each covering half of the vertical and horizontal dimensions. Accordingly, the solvent covers the area with $y > H/2$.

Zero-Neumann boundary conditions are imposed on each order parameter such that $\nabla\phi_\alpha \cdot \mathbf{n} = 0 \forall \alpha \in \{\alpha, \beta, \delta\}$ for all boundaries. This ensures that firstly the grain boundary remains perpendicular to the bottom plane and secondly that

Table 3.2: Parameter set utilized for the simulations performed in the current work.

Parameter	Symbol	Value	Parameter	Symbol	Value
Equilibrium composition left	c_{eq}^{α}	1	Interface mobility left	$m_{\alpha\delta}$	$\frac{1u_l^4}{u_E u_t}$
Equilibrium composition right	c_{eq}^{β}	1	Interface mobility right	$m_{\beta\delta}$	$\frac{1u_l^4}{u_E u_t}$
Equilibrium composition solvent	c_{eq}^{δ}	0	Interface mobility (GB)	$m_{\alpha\beta}$	$\frac{1u_l^4}{u_E u_t}$
Interpolation function	h_{α}	ϕ_{α}	Surface energy (left)	$\gamma_{\alpha\delta}$	$\frac{1u_E}{u_l^2}$
Surface diff. function	$g_{\alpha\beta}$	$\frac{32\phi_{\alpha}\phi_{\beta}}{\pi^2}$	Surface energy (right)	$\gamma_{\beta\delta}$	$\frac{1u_E}{u_l^2}$
Surface diff. prefactor left	$\bar{M}^{\alpha\delta}$	$\frac{0.1u_l^6}{u_E u_t}$	Grain boundary energy	$\gamma_{\alpha\beta}$	$\frac{0.5u_E}{u_l^2}$
Surface diff. prefactor right	$\bar{M}^{\beta\delta}$	$\frac{0.1u_l^6}{u_E u_t}$	Thermodynamic prefactor	A	$\frac{20u_E}{u_l^2}$
GB diff. prefactor	$\bar{M}^{\alpha\beta}$	0	Interface thickness parameter	ε	$2u_l$
Bulk diffusivity	D	$\frac{0.2u_l^2}{u_t}$	Grid spacing	$\Delta x = \Delta y$	$\frac{u_l}{8}$

the groove surface approaches the side planes orthogonally. No-flux boundary conditions are imposed on the composition field at each boundary ensuring that no matter enters the domain. Therefore, the boundary conditions are chosen in order to approximate the infinite domain considered in the analytical solutions. Although an effect of the finite domain cannot fully be avoided, this strategy should minimize the influence of the finite domain on the simulation results.

3.3.2.2 Model Parameterization

Simple parabolic free-energy densities are assumed for each phase, such that $f_{\alpha}(c^{\alpha}) = A(c^{\alpha} - c_{\text{eq}}^{\alpha})^2 \forall \alpha \in \{\alpha, \beta, \delta\}$. The prefactor $A = 20u_E/(u_l^3)$ is chosen identical for all phases. For this choice of free energy, the chemical potential is derived as $\mu = f'_{\alpha}(c^{\alpha}) = 2A(c^{\alpha} - c_{\text{eq}}^{\alpha}) \forall \alpha \in \{\alpha, \beta, \delta\}$ and the composition of each phase can be written as $c^{\alpha} = c_{\text{eq}}^{\alpha} + \mu/(2A) \forall \alpha \in \{\alpha, \beta, \delta\}$. Therefore, the Darken

factors are all constant and identically $dc^\alpha/d\mu = 1/(2A) = 1/40u_l^3/u_E \forall \alpha \in \{\alpha, \beta, \delta\}$.

With this choice, c_{eq}^α is the flat-interface equilibrium composition of any phase α . The chemical potential corresponding to the flat-interface equilibrium is $\mu_{\text{eq}} = 0$. As initial condition, the chemical potential is set to this equilibrium value $\mu(\mathbf{x}, 0) = \mu_{\text{eq}}$ which corresponds to $c^\alpha(\mathbf{x}, 0) = c_{\text{eq}}^\alpha \forall \alpha \in \{\alpha, \beta, \delta\}$. This ensures that the far-field composition values of the analytical solution are met and that the chemical potential matches the equilibrium condition at the initial stage where flat interfaces exist. To keep the system as simple as possible, equal bulk diffusivities are assumed for all phases, i.e. $D = D_\alpha = D_\beta = D_\delta = 0.2u_l^2/u_t$. Furthermore, the surface diffusion prefactor for each side is chosen identical $\bar{M}^{\alpha\delta} = \bar{M}^{\beta\delta} = 0.1u_l^6/(u_E u_t)$ and a vanishing grain-boundary diffusion is assumed $\bar{M}^{\alpha\beta} = 0$. In combination with identical surface energies ($\gamma_s = \gamma_{\alpha\delta} = \gamma_{\beta\delta} = 1u_E/u_l^2$) for each grain this ensures that the groove develops in a symmetric manner. The grain-boundary energy is set to half the value of the surface ($\gamma_{\alpha\beta} = \gamma_{\text{GB}} = \gamma_s/2$) in order to remain close enough to the small-slope limit but still allow a measurable evolution of the groove. This choice yields a slope of $m_0 = 1/\sqrt{15} \approx 0.26$ by means of Eq. (3.114) which corresponds to an angle $\theta \approx 14.5^\circ$. All model parameters are summarized in Table 3.2.

Of particular importance are the rate constants appearing in the sharp-interface solution presented above. The rate constant for surface diffusion is given by Eq. (3.113) and its value can be computed by inserting the values from Table 3.2. Since the current choice of surface diffusion function satisfies $I_g = 1$ and the equilibrium compositions are either unity or zero, it results $B = 0.1u_l^4/u_t$ from $\bar{M}^{\alpha\delta}/\bar{M}^{\beta\delta}$ and $\gamma_{\alpha\delta}/\gamma_{\beta\delta}$ for each surface.

In order to obtain an equation for the volume diffusion rate constant A' , a derivation is presented in Appendix A.1. The corresponding resulting expression for the current setup reads

$$A' = \frac{(D^\alpha + D^\delta) \gamma_{\alpha\delta}}{2A (c_{\text{eq}}^\alpha - c_{\text{eq}}^\delta)^2} = 0.01 \frac{u_l^3}{u_t}. \quad (3.122)$$

3.3.2.3 Simulation Results

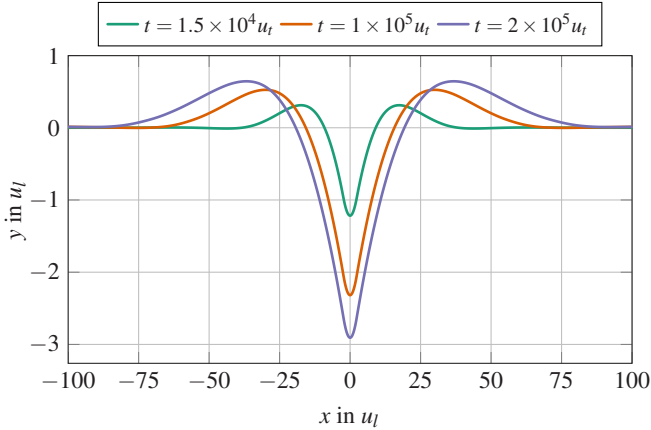


Figure 3.4: Evolution of the thermal groove evaluated by means of the $\phi_\delta = 1/2$ contour under combined surface and volume diffusion in the MPF simulation. Three consecutive snapshots are shown corresponding to an early time $t = 1.5 \times 10^4 u_t$, an intermediate time $t = 1 \times 10^5 u_t$ and the final state $t = 2 \times 10^5 u_t$.

Groove Evolution The evolution of the groove in the MPF simulation is calculated by taking the $\phi_\delta = 1/2$ contour and is shown in Fig. 3.4 for three distinct snapshots corresponding to an early time (7.5% of total simulation time), intermediate time (50% of simulation time) and the final state. Please note that the y-coordinate spans a much smaller range than the x-coordinate which corresponds to an overall shallow geometry of the groove. It is clear that this is caused by the small slope of the groove and indicates that the approximation applied in the analytical solution is reasonably valid. Overall, the groove shows the same qualitative characteristics as the analytical solution: Deepening occurs at the GB ($x = 0$) and the maximum of the groove shifts away from the root. In the initial period of time the growth is very fast, since after a comparably small timespan of $t = 1.5 \times 10^4 u_t$, the groove already reaches almost half of the dimensions observed after an order of magnitude larger timespan in the final state. This seems to align well with the expected power-law growth of a relatively small exponent in the

order of $1/4 \rightarrow 1/3$. The groove also shows the expected symmetry, since the shape for $x < 0$ is a mirrored picture of the groove corresponding to the right-hand grain ($x > 0$).

A clear discrepancy to the analytical shape is the blunt at the root which is originated from the interface of finite thickness inherent to the PF model. Therefore, it can be considered as an artifact of practical PF simulations.

Growth Dynamics In order to investigate the dynamics of the groove in a more quantitative fashion, the height h , width w and depth d are determined from the simulation (see Fig. 3.1 for their definition). These quantities are also available from the analytical solution as a function of time and are therefore suitable for a quantitative comparison. While the determination of the height and width is straightforward by locating the grooves maximum, the depth of the groove is not directly available due to the mentioned blunt which is expected to lead to a clear underestimation of the depth. In order to obtain a more accurate value for the depth, sixth-order polynomials are fitted to the groove curve up to its maximum and evaluated at $x = 0$ which corresponds to an extrapolation of the groove surface towards the GB. This method has also been used in the first study on surface-diffusion governed grooving [24]. In the fit, points near the GB ($|x| < 1.1 \varepsilon \pi^2 / 8$) are excluded from the fit. The chosen value corresponds to half of the interface width of the sinusoidal interface profile plus ten percent which is chosen due to the nonzero slope of the groove.

The growth kinetics of these characteristic dimensions are summarized in Fig. 3.5. In addition to the curves extracted from the simulation, analytical solutions corresponding to the pure surface diffusion case [42], pure volume diffusion case [91] and the general solution [25] applicable to the current simulation parameter set are shown. All curves show the same qualitative behavior, i.e. an initially rapid growth that decays strongly with time. In general, the analytical growth kinetics taking both surface and volume diffusion into account are faster compared to either effect in insulation. This is expected since the consideration of an additional mass transfer mechanism should facilitate the growth of the groove. However, the

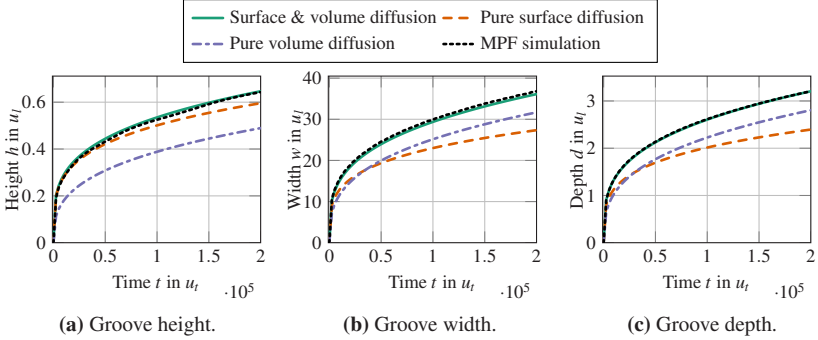


Figure 3.5: Growth kinetics of characteristic groove dimensions in the MPF model: Height h (a), width w (b) and depth d (c). Additionally, the analytical growth kinetics corresponding to pure surface diffusion with rate constant B [42], corresponding to pure volume diffusion with rate constant A' as well as the analytical solution including both effects concomitantly [25] are shown.

dimensions of each case are not simply additive which means that a preliminary estimation of the grooving kinetics from the solutions provided in [42] and [91] is not straightforward.

In general, the MPF simulation matches best the solution considering both effects [25]. Furthermore, an overall very well match is achieved. This shows that the MPF model is capable of quantitatively handling a combination of surface and volume diffusion. The relative error taking the L^2 -norm is calculated for each quantity by means of the formula

$$L_{\text{rel}}^2(f) = \sqrt{\left(\int_{t=0}^{t_{\text{end}}} (f_{\text{MPF}}(t) - f_{\text{SI}}(t))^2 dt \right) / \left(\int_{t=0}^{t_{\text{end}}} f_{\text{SI}}^2(t) dt \right)} \quad (3.123)$$

where f_{MPF} denotes the dimension corresponding to the MPF simulation and f_{SI} is the sharp-interface solution from [25], t_{end} is the total simulation time ($2 \times 10^5 u_t$). It results $L_{\text{rel}}^2(w) \approx 2\%$, $L_{\text{rel}}^2(h) \approx 2\%$ and $L_{\text{rel}}^2(d) \approx 0.4\%$ which demonstrates the high accuracy obtained.

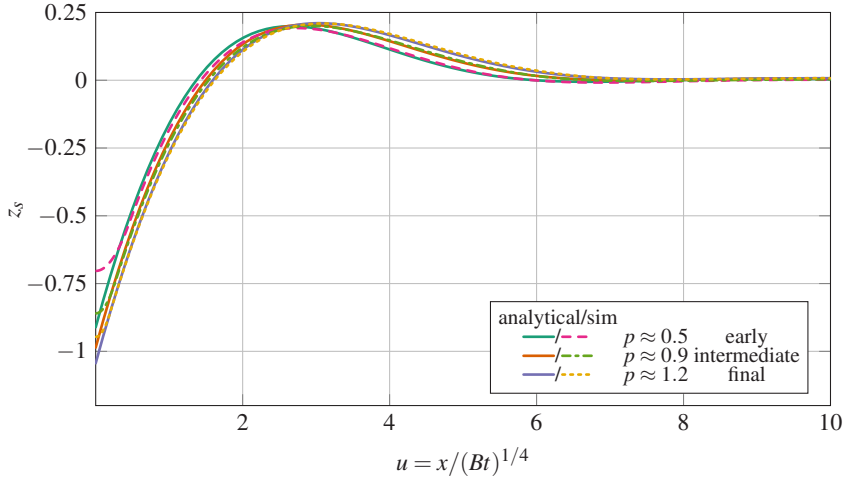


Figure 3.6: Comparison of rescaled groove geometries from the analytical solution [25] and the MPF simulation at three different times. Early time corresponds to $t = 7.5 \times 10^3 u_t$ and $p = 0.523$, intermediate state corresponds to $t = 6 \times 10^4 u_t$ and $p = 0.880$ and the final time corresponds to $t = 2 \times 10^5 u_t$ and $p = 1.189$.

Groove Geometries In order to compare the groove geometries of the sharp-interface solution and the numerical MPF simulation in a more thorough form, $\phi_\delta = 1/2$ contours are rescaled into the coordinate system (u, z) at three selected snapshots. For the comparison, the calculation of the parameter p is needed. Since the simulation snapshots are discretely placed at a time spacing of $\Delta t = 2.5 \times 10^3 u_t$, the first simulation frame corresponds to $p \approx 0.4$ and the final simulation frame ($t = 2 \times 10^5 u_t$) corresponds to $p \approx 1.2$. This firstly means that the simulation has been performed in the regime where both surface and volume diffusion contributions are relevant and secondly that the regime where p is small is not available from the simulation. Please also note that even if more simulation frames were written out, the initial period of time where the groove has a very small dimension is not well resolved by the discrete simulation grid due to its small slope. Furthermore, in the surface-diffusion dominant regime $p \ll 1$, the groove has a size smaller than the interfacial thickness which clearly shows that the current parameterization of the model does not permit accurate

solutions at these length scales. Therefore, the region of interest for the current simulation corresponds to $0.5 < p < 1.2$. It is stressed that a different parameterization of the model with a smaller bulk diffusivity would allow investigating the surface-diffusion dominant regime, since the values of p corresponding to the same simulation times are modified accordingly.

Fig. 3.6 contains the rescaled groove geometries of both the MPF simulation and the analytical solution at times $t = 7.5 \times 10^3 u_t$, $t = 6 \times 10^4 u_t$ and the final state $t = 2 \times 10^5 u_t$ corresponding to $p \approx 0.5$, $p \approx 0.9$ and $p \approx 1.2$. It is observed that the blunt near the root due to the finite interface thickness causes a significant deviation from the analytical solution only when the groove has a relatively small dimension, i.e at early times where p is small. Apart from the blunt, the deviation of the simulation and analytical solution is most apparent for u smaller than the (rescaled) width of the groove. In general, the disappearance of the dip at the tail of the groove is recovered as p increases by the simulation. Therefore, the qualitative characteristics of the change in the groove geometry which is due to the increasing dominance of volume diffusion as p increases, can be reproduced.

The overall L^2 relative error of the MPF and SI solution is calculated by means of the formula

$$L_{\text{rel}}^2(f, p) \equiv \frac{\sqrt{\int_{u=u_{\min}}^{10} (f_{\text{MPF}}(u, p) - f_{\text{SI}}(u, p))^2 du}}{\sqrt{\int_{u=u_{\min}}^{10} f_{\text{SI}}^2(u, p) du}} \quad (3.124)$$

$$u_{\min} \equiv u(1.1 \frac{\epsilon \pi^2}{8}, t) \quad (3.125)$$

where u_{\min} disregards the triple junction region. It results $L_{\text{rel}}^2(z_s, 0.5) \approx 8\%$, $L_{\text{rel}}^2(z_s, 0.9) \approx 4\%$ and $L_{\text{rel}}^2(z_s, 1.2) \approx 2\%$ for increasing simulation times. Therefore, the deviation of the curves decreases with time.

In order to check whether the magnitude of the difference might be explained by the limitation of the small-slope approximation, the L^2 relative error of the numerical finite slope solution [98] and the small-slope approximant [42] is calculated. Although these solutions correspond to the pure surface diffusion case,

the deviation can be considered as an estimate for the admissible deviation for the current study. At the current value of m_0 this results in about 2% of relative error. Therefore, the solution at late times can be considered as an exact match. However, at early times additional error sources are contributing to the mismatch.

Error sources attributed to the phase-field model may be explained by its nonzero interface thickness: While the asymptotic analysis presented in the previous section showed that the phase-field model at hand converges towards the sharp-interface problem when ε tends to zero, practical simulations are always performed at finite interface widths. It is clear that there exist interface-thickness dependent terms which were not investigated in the sharp-interface limit. Accordingly, it is expected that the deviations caused by these terms are most relevant when the groove has a small size relative to the interface width. In addition it seems that the nonzero grain-boundary thickness causes a slight shift of the groove away from the GB. This would also explain a time-dependent error since the width of the GB becomes less relevant as the groove widens. These points might partially explain the mismatch at early times, but the following point may hint at an additional error source rooted in the limitations of the sharp-interface solution.

It is worth re-examining the additional assumptions introduced in [91] for the volume-diffusion case (cf. Appendix A.1). Not only a vanishing slope of the groove was assumed, but also a fully developed concentration field which means that a transient in the bulk concentration field is neglected. In contrast, the multiphase-field simulation starts with a constant chemical potential field and thus, the composition field in the bulk is not divergenceless in general. Mullins [91] considered the assumption of a vanishing divergence of the concentration to be valid when the width of the groove satisfies the following condition $2wD/A' \geq 10^3$. For the current simulation setup, estimating $w \approx 2.5(Bt)^{1/4}$ one finds that $2wD/A' = 100(Bt)^{1/4}/u_l$. This yields the condition $(Bt)^{1/4} \geq 10u_l$ or $t \geq 10^5 u_l$ and thus, the condition is not satisfied for early times where $p < 1$. This corresponds to one half of the total simulation time. Therefore, an additional contribution to the temporally decaying deviations can reasonably be attributed to

the limitations of the sharp-interface solution due to the assumption of a quasi steady-state concentration field. In order to estimate the magnitude of this error, an additional simulation was performed including only the early time result ($t = 7.5 \times 10^3 u_t$) with a higher diffusivity of $D = 1.0u_l^2/u_t$ and an adjusted thermodynamic prefactor $A = 100u_E/u_l^3$ in order to ensure the same rate constant A' . A relative error of $L_{\text{rel}}^2(z_s, 0.5) \approx 6\%$ is obtained. This shows that the steady-state assumption is responsible for about a quarter of the error at early time.

Chemical Potential In the asymptotic treatment the chemical potential becomes a constant function with respect to the interface normal direction in the sharp (and thin) interface limit. It is worth checking whether the predictions of the analytic treatment valid for small interface thicknesses are recovered in the simulation. Fig. 3.7 shows the chemical potential field after half of the simulation time in the vicinity of the groove root. First of all, it is apparent that the chemical potential has a characteristic far-field character since even far away from the groove, a non-vanishing chemical potential established. In addition, the chemical potential approximately shows a symmetry with respect to the y -axis which is in-line with the applied small-slope approximation (cf. Appendix A.1). The iso-value contours of the chemical potential at different levels reveal the orientation of the chemical potential gradients since they are always orthogonally related. It is observed that within the interface region where $0 < \phi_\delta < 1$, the iso-contours are almost perfectly aligned with the surface normal. This means that the gradient in the normal direction is negligible and hence, a constant chemical potential in the interfacial region is maintained. In addition, the ϕ_δ profile is indistinguishable from the sinusoidal sharp-interface profile. Therefore, the result seems to suggest that the simulation is overall performed at least near the sharp-interface limit.

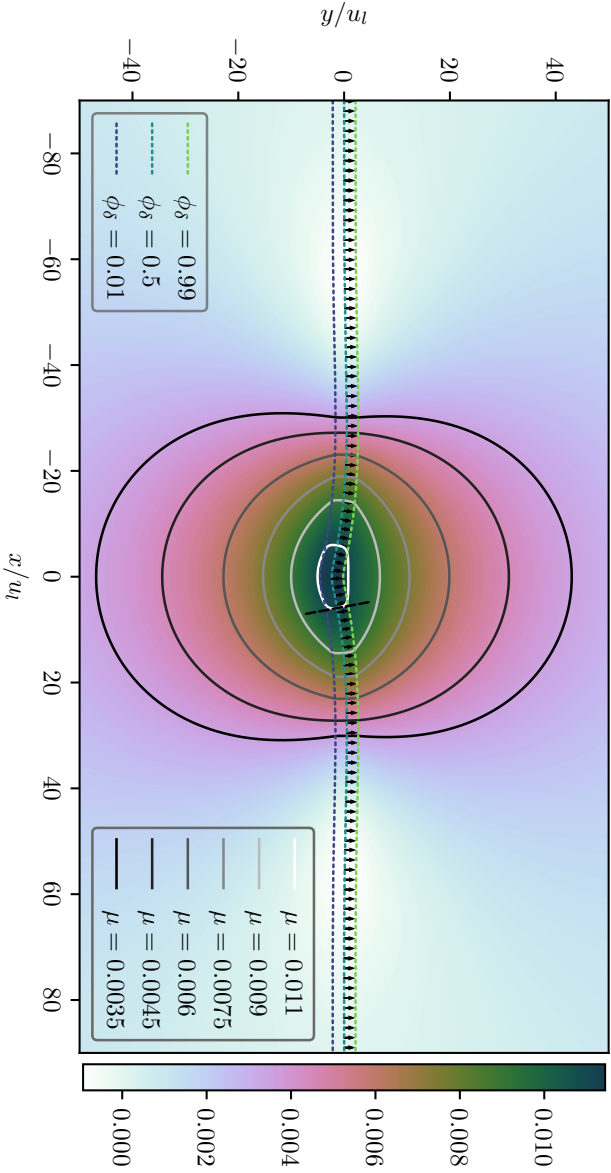


Figure 3.7: Chemical potential field $\mu(x, t)$ (its unit u_E/u_i^2 is omitted) at half the simulation time ($t = 10^5 u_i$) in the vicinity of the grain boundary ($x = 0$). Contours of constant chemical potential are shown representing the orientation of the chemical potential gradients. Dotted lines are iso-contours of the order parameter ϕ_δ to indicate the surface location and thickness. Arrows indicate normals on the $\phi_\delta = 1/2$ contour and the black dashed line is a normal cross-section of the interface.

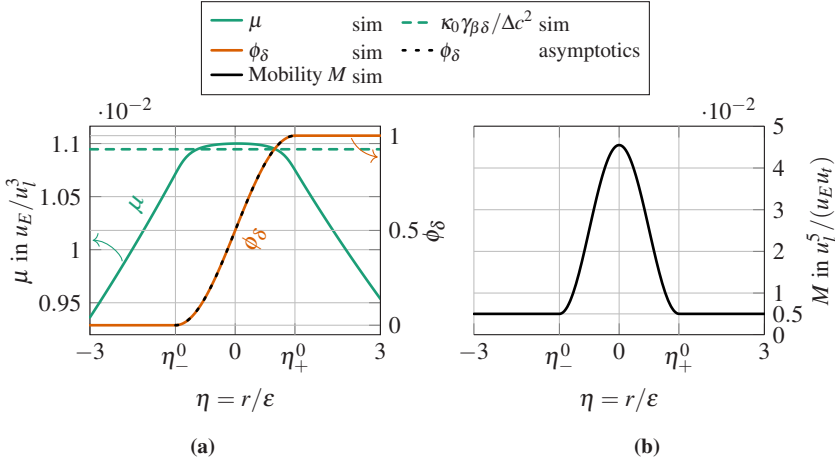


Figure 3.8: Chemical potential μ , order parameter ϕ_δ (both (a)) and chemical mobility (b) of the MPF simulation in normal direction at a point close to the triple-junction region (dashed line in Fig. 3.7). The time corresponds to $t = 10^5 u_t$. Corresponding quantities from the asymptotic derivation are additionally shown. The mobility is calculated as $M = \bar{M}^{\beta\delta} g_{\beta\delta}(\phi) / \varepsilon + M_\beta \phi_\beta + M_\delta \phi_\delta$.

Only in a region very near the groove root, a slightly curved iso-contour is found ($\mu = 0.011$ contour in Fig. 3.7). This means that the chemical potential is also slightly varying in the normal direction. In this regard, chemical potential, order parameter of the solvent ϕ_δ and the corresponding chemical mobility are plotted as a function of the dimensionless normal coordinate $\eta = r/\varepsilon$ in Fig. 3.8. It is seen that the chemical potential is a continuous function which approaches the interface with a well defined slope which in turn causes a non-constant chemical potential near the ends of the interface η_\pm^0 . However, in an interval near the $\phi_\delta = 1/2$ contour, i.e. the center of the interface, the chemical potential is virtually constant. It is worth noting that the maximal relative variation of the chemical potential in the normal direction is small (about 3%) and can thus be considered insignificant. Moreover, by applying a local quadratic fit to the $\phi_\delta = 1/2$ contour to calculate its curvature κ_0 , it is found that the chemical potential function is on average very closely resembling the Gibbs-Thomson relation of the asymptotic treatment through Eq. (3.101) (the

deviation at $r = 0$ is approximately $+0.5\%$ and roughly -2% at $r = \varepsilon\eta_{\pm}^0$. In order to explain the deviation from the constant chemical potential, it is worth considering the variation of the chemical mobility in the normal direction (Fig. 3.8b). The mobility, which is symmetric with respect to $r = 0$ varies from the bulk value of $M(r < \varepsilon\eta_{-}^0) = M_{\beta} = Ddc^{\beta}/d\mu = 0.005u_1^5/(u_E u_t)$ towards a maximum at $r = 0$ until the δ -phase is approached with the identical value of $M(r > \varepsilon\eta_{+}^0) = M_{\delta} = M_{\beta}$. For the current choice of ε , the mobility in the center of the interface is given by $M(r = 0) = M_{\beta} + 8\bar{M}^{\beta\delta}/(\pi^2\varepsilon) \approx 0.0455u_1^5/(u_E u_t)$ since the $\phi_{\beta}\phi_{\delta}$ term evaluates to $1/4$. Thus, the chemical mobility in the interface is roughly an order of magnitude larger than the bulk mobility and is maximal at its center. This means that gradients of the chemical potential in the interfacial region are most dominantly suppressed in the center of the interface. It is important to note that as ε is reduced, $M(\eta_{-}^0 < \eta < \eta_{+}^0)$ increases by the same factor and in the limit $\varepsilon \rightarrow 0$ an infinitely large mobility in the interface results everywhere even near the endpoints η_{\pm}^0 . Accordingly, it is expected that the remaining chemical potential gradients in the normal direction can be removed by reducing the interface thickness (which is actually what the asymptotic derivation showed more formally). A quantity which can be considered as a heuristic to assess the deviation from the sharp-interface limit can be deduced along these lines. It is demanded that the following conditions are fulfilled for each $\alpha\beta$ -interface: $M(\phi_{\alpha} = 1/2, \phi_{\beta} = 1/2)/M_{\alpha} \gg 1$ and $M(\phi_{\alpha} = 1/2, \phi_{\beta} = 1/2)/M_{\beta} \gg 1$. In other words, the local value of the chemical mobility in the center of the interface is much larger than the bulk mobility of any adjacent phase. If this is ensured, an almost constant mobility in normal direction can be expected.

3.4 Conclusion

In the current chapter, a multiphase-field model for a combination of surface and bulk diffusion in multicomponent systems is presented. This model was first published and analyzed for the case of vanishing bulk diffusivities in [24], but a rigorous analysis and validation of concomitant surface and bulk diffusion was

still missing. Within this chapter, asymptotic analysis is conducted for a combination of surface and volume diffusion in this model. It is shown that the model recovers the extended interfacial balance with an excess surface flux accounting for the additional interface diffusion in tangential direction when the interface thickness vanishes. The chemical potential, which becomes a constant function in normal direction in this limit, fulfills the Gibbs-Thomson condition with a term reflecting attachment kinetics at the interface. In addition to the analytical treatment, a simulation study of thermal grooving is conducted to compare the simulation result with an analytical solution valid in the so-called small-slope approximation. The simulation and analytical results show a very good quantitative agreement, with respect to both the grooving kinetics and the geometry of the groove at various times. In addition it is shown that the chemical potential is in fact approximately constant within the interface in this study. Remaining small deviations from the ideal sharp-interface limiting behavior are discussed and a heuristic condition is proposed to deduce regions where the model ensures an almost constant chemical potential in normal direction.

4 Regarding the Choice of Interpolation Function

When you learn mathematics, whether in books or in lectures, you generally only see the end product – very polished, clever and elegant presentations of a mathematical topic.

However, the process of discovering new mathematics is much messier, full of the pursuit of directions which were naïve, fruitless or uninteresting.

Terry Tao “Ask yourself dumb questions – and answer them!”

4.1 Introduction

4.1.1 Motivation

A core element in a phase-field model is the interpolation function used to incorporate bulk driving forces. This function for instance can be of mechanical or chemical type. The name *interpolation* refers to the notion that the densities of extensive quantities in the smoothed out interfacial region have a contribution calculated as a weighted average of the respective bulk energy densities. The

interpolation function for a two-phase model $h_\alpha(\phi_\alpha)$ is constructed to fulfill the criteria $h_\alpha(0) = 0$ and $h_\alpha(1) = 1$ (see e.g. [17, p. 2]). This ensures that the free-energy densities of each phase are approached in the bulk. As an additional constraint, a vanishing derivative of the interpolation $h'_\alpha(\phi_\alpha) = 0$ is often demanded for the bulk states $\phi_\alpha = 0$ and $\phi_\alpha = 1$. For a well-type potential this ensures that the bulk states constitute equilibrium points of the partial differential equation, i.e. lead to $\partial\phi_\alpha/\partial t = 0$ when $\phi_\alpha = 0$ or $\phi_\alpha = 1$ and $\nabla^2\phi_\alpha = 0$ (cf. [6, p. 171]).

Karma [13] imposed a symmetry condition on the interpolation function of the order parameter $\varphi = 2\phi_\alpha - 1$, when $\varphi = \pm 1$ represent bulk states. This means that both phases are treated symmetrically (in the current notation expressed as $h_\alpha(\phi_\alpha) = 1 - h_\alpha(1 - \phi_\alpha)$).

While all of the above conditions may be satisfied by a whole class of interpolation functions, it is currently unclear, which of the available interpolation functions is more accurately describing the physical problem at hand. Some light has been shed on this problem in a review article Steinbach [7, Appendices A.1 and A.2]. Here specific choices of interpolation functions were highlighted. They lead to travelling-wave solutions identical to the well-known equilibrium solutions (tanh or sin profiles, for both well-type and obstacle-type potentials, respectively) for driving forces of arbitrary magnitude. For obstacle potentials such a form of interpolation function was first appearing in the antisymmetric approximation presented in [18]. Nevertheless, it is still unclear if either at all or up to which extent the more established forms of interpolation functions deviate therefrom. It would be important to figure out which of the conditions usually imposed on interpolation functions are really crucial and which of them are not. This clarification is one aim of the current chapter.

In various works [12, 13, 20, 94], thin-interface limits of phasefield models are commonly derived to show that the governing equations of the phase-field model recover the sharp-interface laws up to first order corrections in the interface thickness. By this method, the accuracy of phase-field models for solidification could be significantly improved. The derivation of the thin-interface limit is based on

a Maclaurin expansion of the time-dependent partial differential equations with respect to the interfacial thickness that is truncated after first order. So far, higher order corrections are usually not discussed. It is however clear that the expansion has higher order terms whose influence on the simulation results remains completely hidden. The original asymptotic derivation in [93, cf. e.g. Eq. (62)] considered a first-order correction in the interface velocity. Although the derivations in [12, 13] are based thereon, this term was dropped in these works without discussing its limitations. In this regard, the work of Almgren [94] is worth mentioning since it included first-order corrections in the interface velocity.

To be more rigorous and thorough in the following treatments, the role of the interface velocity corrections is explicitly outlined by considering higher-order corrections v_2 , v_3 and so forth. As such, the current chapter is meant to generalize the derivations for higher orders, but in contrast to the work of Karma and co-workers, an obstacle-type potential is studied. Although the asymptotic treatment has recently been advanced for well-potentials in [99, 100] – by either studying early time regimes or by considering triple-junction dynamics – such a procedure is so far not available for obstacle-type models.

On the one hand, the treatment of an obstacle potential complicates the derivation, since piecewise order parameter functions are obtained as a result rooted in the Gibbs-simplex used to hold the order parameter function within meaningful bounds. Therefore, the standard matched asymptotic expansion which is based on limits towards infinity cannot be used. On the other hand, once the asymptotic method has been adjusted for these type of models following first ideas in Hof-frogge et al. [24], the analytical structure of the corresponding ODEs that appear at each order seem not be too demanding and can often be solved exactly.

The current chapter presents a framework to generalize the asymptotic treatment for obstacle potentials to arbitrary orders and a computer algebra system is utilized to perform the tedious and lengthy derivations.

Table 4.1: Considered interpolation functions and corresponding derivatives. Two common choices for order parameters are considered: ϕ_α ranges from 0 to 1, whereas $\varphi = 2\phi_\alpha - 1$ ranges from -1 to 1 in the interfacial region.

Symbol	$h_\alpha(\phi_\alpha)$	$h'_\alpha(\phi_\alpha)$	$h(\varphi)$	$h'(\varphi)$
h_0	ϕ_α	1	$\frac{\varphi+1}{2}$	$\frac{1}{2}$
h_1	$\phi_\alpha^2(3 - 2\phi_\alpha)$	$6\phi_\alpha(1 - \phi_\alpha)$	$\frac{(2-\varphi)(\varphi+1)^2}{4}$	$\frac{3}{4}(1 - \varphi^2)$
h_2	$\phi_\alpha^3(6\phi_\alpha^2 - 15\phi_\alpha + 10)$	$30\phi_\alpha^2(1 - \phi_\alpha)^2$	$\frac{(8-9\varphi+3\varphi^2)(\varphi+1)^3}{16}$	$\frac{15}{16}(1 - \varphi^2)^2$
h_d	$\frac{1}{2} + \frac{1}{\pi} \operatorname{asin}(2\phi_\alpha - 1)$ $+ \frac{2}{\pi} \sqrt{\phi_\alpha(1 - \phi_\alpha)}$ $(2\phi_\alpha - 1)$	$\frac{8}{\pi} \sqrt{\phi_\alpha(1 - \phi_\alpha)}$	$\frac{1}{2} + \frac{1}{\pi} \operatorname{asin}(\varphi)$ $+ \frac{\varphi}{\pi} \sqrt{1 - \varphi^2}$	$\frac{2}{\pi} \sqrt{1 - \varphi^2}$

4.1.2 Considered Interpolation Functions

The considered interpolation functions $h(\varphi) = h_\alpha(\phi_\alpha)$ and the corresponding derivatives that enter the evolution equations are listed in Table 4.1 both in terms of an order parameter ranging from zero to unity (ϕ_α) or one that ranges from -1 to 1 ($\varphi = 2\phi_\alpha - 1$). The interpolation functions written as h_n with some integer n are simple polynomials of ϕ_α or φ . Moreover, they lead to $h'_\alpha(\phi_\alpha) \propto (\phi_\alpha(1 - \phi_\alpha))^n$ (or, equivalently to $h'(\varphi) \propto (1 - \varphi^2)^n$), where the prefactor ensures that the interpolation function recovers the constraints $h_\alpha(0) = 0$ and $h_\alpha(1) = 1$. In contrast, h_d is an interpolation function that has a more complex form. Nevertheless, in comparison with h_n , it leads to a similar form of the derivative $h'_\alpha(\phi_\alpha)$, where n is replaced by the non-integer power $1/2$.

All interpolation functions satisfy the symmetry $h_\alpha(1/2 + \phi_\alpha) = 1 - h_\alpha(1/2 - \phi_\alpha)$, or in terms of φ : $h(\varphi) = 1 - h(-\varphi)$. The interpolation functions can also be distinguished in terms of their bulk behavior by considering the first and second derivatives $h'_\alpha(0)$, and $h''_\alpha(0)$. For $n > 0$ (i.e. excluding h_0), all interpolation functions satisfy $h'_\alpha(0) = 0$. The second derivative $h''_\alpha(0)$ is zero for h_0 and h_2 , assumes a finite value of 6 for h_1 and tends to infinity for h_d .

In phase-field models employing a well-potential, h_1 is used for instance in [101]. In obstacle-potential models, h_0 has been used e.g. in [18], h_1 was used in [102, 103] and h_2 has been applied in [104, 105] without providing a reasoning to

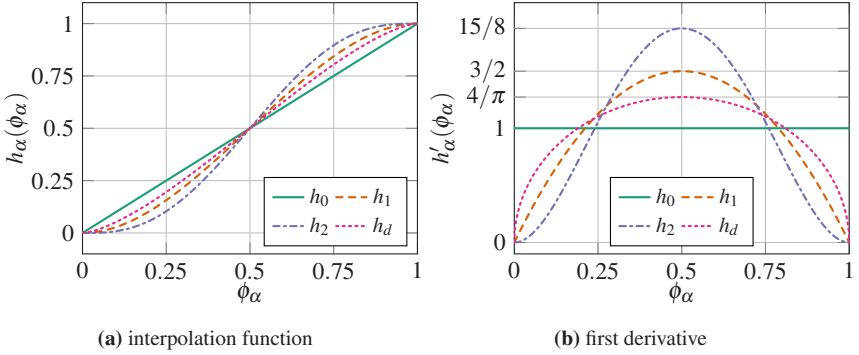


Figure 4.1: Different choices of interpolation functions a and their corresponding derivatives b that enter the evolution equation of the order parameter.

explain why one of the above formulations is chosen. The following analysis is meant to shed some light on the intricacies and subtleties between the different interpolation functions in obstacle-type models.

4.2 Problem Formulation

4.2.1 Statement of the PDE for a Two-Phase System

The free-energy functional for a two-phase system with constant bulk free energy densities f_α (in J/m^3) writes as

$$F = \int_V \gamma \left(\frac{16}{\pi^2 \varepsilon} \phi_\alpha (1 - \phi_\alpha) + \varepsilon |\nabla \phi_\alpha|^2 \right) + h_\alpha(\phi_\alpha) f_\alpha + f_\beta (1 - h_\alpha(\phi_\alpha)) dV \quad (4.1)$$

where $h_\alpha(\phi_\alpha)$ is the interpolation function which satisfies the criteria $h_\alpha(0) = 0$ and $h_\alpha(1) = 1$, γ is the interfacial energy parameter in J/m^2 , ε is the interface

thickness controlling parameter in m. Based on the functional above, the evolution equation for the order parameter is formulated as

$$\frac{\partial \phi_\alpha(\mathbf{x}, t)}{\partial t} = -\frac{m}{2\varepsilon} \frac{\delta F}{\delta \phi_\alpha} = \frac{m}{\varepsilon} \left(\frac{8\gamma}{\pi^2 \varepsilon} (2\phi_\alpha - 1) + \varepsilon \gamma \nabla^2 \phi_\alpha + \frac{h'_\alpha(\phi_\alpha)}{2} \Delta f \right) \quad (4.2)$$

by introducing the mobility parameter m in $\text{m}^4/(\text{J}\cdot\text{s})$ and the driving force is given as $\Delta f \equiv f_\beta - f_\alpha$. The above equation is a partial differential equation for ϕ_α .

4.2.2 Transformation to an Ordinary Differential Equation

One-dimensional Travelling Wave Ansatz It is expected, that due to the presence of a bulk driving force difference Δf , a time-invariant movement of the interface results. Furthermore, neglecting the effect of curvature, a one-dimensional setup (x -coordinate) is considered. Therefore, the following travelling-wave ansatz for the evolution of the phase-field

$$\phi_\alpha(\mathbf{x}, t) = \phi_\alpha(u(t)) \quad (4.3)$$

$$u(t) = x - x_0(t) \quad (4.4)$$

$$\frac{dx_0}{dt} = v \quad (4.5)$$

is used, introducing the moving reference location x_0 and interface velocity v (in m/s). Applying the chain rule which yields $\partial \phi_\alpha(\mathbf{x}, t)/\partial t = -v d\phi_\alpha/du$ one obtains an *ordinary* differential equation (ODE) in the moving coordinate u

$$\frac{8\gamma}{\pi^2 \varepsilon} (2\phi_\alpha(u) - 1) + \varepsilon \gamma \frac{d^2 \phi_\alpha(u)}{du^2} + \frac{v\varepsilon}{m} \frac{d\phi_\alpha}{du} + \frac{h'_\alpha(\phi_\alpha(u))}{2} \Delta f = 0 \quad (4.6)$$

for the phasefield.

Boundary Conditions In order to obtain unique solutions to the differential equation, boundary conditions are needed. First it is assumed, that the bulk is approached at either side of the interface, i.e.

$$\phi_\alpha(u_-) = 1 \quad (4.7)$$

$$\phi_\alpha(u_+) = 0 \quad (4.8)$$

for some finite locations u_- and u_+ and an ordering is assumed such that $u_+ > u_-$. The interface thickness is denoted as $\delta = u_+ - u_-$.

Additionally, it is assumed that the first derivative of the order parameter is continuous at the interfacial endpoints, i.e.

$$\left. \frac{\partial \phi_\alpha}{\partial u} \right|_{u_\pm} = 0 \quad (4.9)$$

holds.

Gibbs Constraint Additionally, since ϕ_α represents the local volume fraction of phase α , the Gibbs constraint

$$0 < \phi_\alpha < 1 \quad \forall u_- < u < u_+ \quad (4.10)$$

is enforced.

Interfacial Energy In a one-dimensional system, the interfacial energy σ for a two-phase system is defined as the integral of the potential and gradient term, as follows

$$\sigma \equiv \int_{u_-}^{u_+} \gamma \left(\frac{16}{\pi^2 \varepsilon} \phi_\alpha(u)(1 - \phi_\alpha(u)) + \varepsilon \left(\frac{d\phi_\alpha(u)}{du} \right)^2 \right) du. \quad (4.11)$$

Note that this is just one possible definition rooted in the way the free-energy functional is constructed by introducing the notion of the interfacial energy parameter γ in Eq. (4.1). Another point of view is obtained by following the notion of the Gibbs dividing surface (cf. Sec. 2.3.4). In the current context where f_α and f_β are constants this means that the location of the dividing surface, denoted here as u_0 is given by calculating the excess energy through

$$\int_{u_-}^{u_+} \gamma \left(\frac{16}{\pi^2 \varepsilon} \phi_\alpha(u)(1 - \phi_\alpha(u)) + \varepsilon \left(\frac{d\phi_\alpha(u)}{du} \right)^2 \right) + h_\alpha(\phi_\alpha) f_\alpha + f_\beta(1 - h_\alpha(\phi_\alpha)) du = \sigma + f_\alpha(u_0 - u_-) + f_\beta(u_+ - u_0) \quad (4.12)$$

which implies, according to the definition in Eq. (4.11) that the location of the Gibbs dividing surface corresponding to σ has to be chosen as

$$u_0 = u_- + \int_{u_-}^{u_+} h_\alpha(\phi_\alpha(u)) du. \quad (4.13)$$

This does not necessarily equal the natural contour, i.e. $\phi_\alpha(u_0) = 1/2$ might not be fulfilled. However, if $h_\alpha(\phi_\alpha)$ is bound between 0 and 1 which is the case for all common interpolation functions and since Eq. (4.10) holds, $u_- \leq u_0 \leq u_+$ is always fulfilled which means that the Gibbs dividing surface is located somewhere inside the interfacial region. This fact justifies the definition through Eq. (4.11).

4.2.3 Non-Dimensionalization

Dimensionless Spatial Coordinate At this point, a lot of physical constants remain in equation (4.6). It is therefore convenient (but not necessary) to non-dimensionalize the equation to simplify the mathematical treatment. The dimensionless coordinate

$$\eta \equiv \frac{4u}{\pi \varepsilon} \quad (4.14)$$

and rescaled order parameter

$$\varphi \equiv 2\phi_\alpha - 1 \quad (4.15)$$

as well the interpolation function

$$h(\varphi) = h_\alpha \left(\frac{\varphi(\eta) + 1}{2} \right) \quad (4.16)$$

$$h'(\varphi) = \frac{1}{2} h'_\alpha \left(\frac{\varphi(\eta) + 1}{2} \right) \quad (4.17)$$

are introduced. The interpolation function satisfies $h(-1) = 0$ and $h(1) = 1$, since $\varphi = \pm 1$ correspond to the bulk states $\phi_\alpha = 0$ and $\phi_\alpha = 1$. Moreover, $d^n \phi_\alpha(u)/du^n = (1/2)(4/(\pi\varepsilon))^n d^n \varphi(\eta)/d\eta^n$ holds for $n > 0$ and a relatively simple form of equation (4.6) is obtained:

$$\varphi(\eta) + \frac{d^2 \varphi(\eta)}{d\eta^2} + \frac{\pi v \varepsilon}{4\gamma m} \frac{d\varphi(\eta)}{d\eta} + \frac{\pi^2 \varepsilon \Delta f}{16\gamma} 2h'(\varphi) = 0 \quad (4.18)$$

Now all terms in the above equation are dimensionless.

Dimensionless Driving Force and Velocity An interesting fact is that there are two lengths involved, namely $\gamma m/v$ and $\gamma/\Delta f$ that relate to the chosen interface thickness parameter ε . A possible choice which only includes known input parameters, in contrast to the unknown velocity v , is to define the dimensionless interface width as

$$\tilde{\varepsilon} \equiv \frac{\pi^2 \varepsilon \Delta f}{16\gamma} \quad (4.19)$$

which might also be regarded as a dimensionless driving force.

To compare the interface velocity with the sharp-interface relation from Eq. (2.91), a dimensionless interface velocity is defined as

$$\tilde{v} \equiv \frac{v}{m\Delta f} \quad (4.20)$$

and in case the sharp-interface relation holds, $\tilde{v} = 1$.

Dimensionless Interfacial Energy The dimensionless interfacial energy $\tilde{\sigma}$ is defined as the ratio of the actual interfacial energy σ and the interfacial energy parameter γ based on Eq. (4.11). Inserting the identities $\phi_\alpha(1 - \phi_\alpha) = (1 - \varphi^2)/4$ and $d\phi_\alpha(u)/du = 2d\varphi(\eta)/d\eta/(\pi\varepsilon)$, one obtains

$$\tilde{\sigma} \equiv \frac{\sigma}{\gamma} = \frac{1}{\pi} \int_{\eta_-}^{\eta_+} 1 - (\varphi(\eta))^2 + \left(\frac{d\varphi(\eta)}{d\eta} \right)^2 d\eta. \quad (4.21)$$

Due to the Gibbs-constraint (Eq. (4.10)), and since $\eta_+ > \eta_-$, the interfacial energy is always positive, i.e. $\tilde{\sigma} > 0$.

Final Set of Equations Inserting the above quantities into the ODE, one obtains a remarkably simple form of the differential equation

$$\varphi(\eta) + \frac{d^2\varphi(\eta)}{d\eta^2} + \frac{4\tilde{\varepsilon}\tilde{v}}{\pi} \frac{d\varphi(\eta)}{d\eta} + 2\tilde{\varepsilon}h'(\varphi) = 0 \quad (4.22)$$

$$\varphi(\eta_\pm) = \mp 1 \quad (4.23)$$

$$\left. \frac{d\varphi(\eta)}{d\eta} \right|_{\eta_\pm} = 0 \quad (4.24)$$

$$|\varphi(\eta)| < 1 \quad \forall \eta_- < \eta < \eta_+ \quad (4.25)$$

with corresponding boundary conditions (Eqs. (4.7)-(4.9)) and the Gibbs constraint, where $\eta_\pm = 4u_\pm/(\pi\varepsilon)$ and the ordering $\eta_+ > \eta_-$ applies. The dimensionless interface thickness is denoted as $\tilde{\delta} = \eta_+ - \eta_-$. Note that η_\pm are unknowns

and remain part of the problem. Moreover, the prescription through Eqs. (4.22)-(4.25) does not yield a unique solution $\varphi(\eta)$. This can be seen by the following argument: Suppose a solution $\varphi(\eta)$ satisfying all equations above exists, then a shifted variant $\varphi_s(\eta) = \varphi(\eta + K)$ with some constant K also completely satisfies the same equations with shifted endpoints $\eta_{s,\pm} = \eta_{\pm} - K$. Therefore it is possible to remove this ambiguity for instance by demanding that either one of η_{\pm} be zero or by setting $\varphi(0) = 0$. Appropriate reshifting may be done to obtain more convenient forms of the solutions.

4.3 Exact Solutions

4.3.1 General Properties

4.3.1.1 Positivity of the Interface Velocity

Suppose that a solution satisfying Eqs. (4.22)-(4.25) exists, then one may multiply the ODE with $d\varphi(\eta)/d\eta$ and integrate from η_- to η_+ , resulting in

$$\int_{\eta_-}^{\eta_+} \varphi(\eta) \frac{d\varphi(\eta)}{d\eta} d\eta + \int_{\eta_-}^{\eta_+} \frac{d^2\varphi(\eta)}{d\eta^2} \frac{d\varphi(\eta)}{d\eta} d\eta + \frac{4\tilde{\varepsilon}\tilde{\nu}}{\pi} \int_{\eta_-}^{\eta_+} \left(\frac{d\varphi(\eta)}{d\eta} \right)^2 d\eta + 2\tilde{\varepsilon} \int_{\eta_-}^{\eta_+} h'(\varphi) \frac{d\varphi(\eta)}{d\eta} d\eta = 0. \quad (4.26)$$

The last integral can be integrated by substitution and is identically $h(\varphi(\eta_+)) - h(\varphi(\eta_-)) = h(-1) - h(1) = -1$ according to the order parameter BCs (Eq. (4.23)). The first term is integrated by parts, raising $d\varphi(\eta)/d\eta$ which yields

$$2 \int_{\eta_-}^{\eta_+} \varphi(\eta) \frac{d\varphi(\eta)}{d\eta} d\eta = \left[(\varphi(\eta))^2 \right]_{\eta_-}^{\eta_+} = 0 \quad (4.27)$$

applying the same BCs. The second term is different only in a higher degree of differentiation, and is therefore integrated by parts by raising $d^2\varphi(\eta)/d\eta^2$, yielding

$$2 \int_{\eta_-}^{\eta_+} \frac{d^2\varphi(\eta)}{d\eta^2} \frac{d\varphi(\eta)}{d\eta} d\eta = \left[\left(\frac{d\varphi(\eta)}{d\eta} \right)^2 \right]_{\eta_-}^{\eta_+} = 0 \quad (4.28)$$

according to the differential BCs (Eq. (4.24)). Therefore, the first two terms can be neglected and one finds after trivial manipulations and dividing through $\tilde{\epsilon}$

$$\tilde{\nu} = \frac{\pi/2}{\int_{\eta_-}^{\eta_+} \left(\frac{d\varphi(\eta)}{d\eta} \right)^2 d\eta}. \quad (4.29)$$

Thus, $\tilde{\nu}$ can be determined from the solution to the ODE and is not a free parameter. Furthermore, an important property is the positivity $\tilde{\nu} > 0$ since $\eta_+ > \eta_-$. This means that the interface moves towards a lowering of the total free energy, which in some sense resembles the second law of thermodynamics. It is stressed that $h(0) = 0$ and $h(1) = 1$ are the only constraints required from the interpolation function to yield this property. Thus, this result holds independent of the choice of herein discussed interpolation functions.

Note however, that the ODE itself is a function of $\tilde{\epsilon}$ and $\tilde{\nu}$ and thus the solution and as well $\int_{\eta_-}^{\eta_+} \left(\frac{d\varphi(\eta)}{d\eta} \right)^2 d\eta$ may vary with $\tilde{\epsilon}$ and $\tilde{\nu}$. It follows that Eq. (4.29) may be a (nonlinear) relation between $\tilde{\nu}$ and $\tilde{\epsilon}$ that needs to be inverted to obtain $\tilde{\nu}(\tilde{\epsilon})$.

4.3.1.2 Exploiting the Symmetry of the Interpolation Function

Symmetry of the Interface Velocity It is assumed that Eq. (4.29) can be inverted and a unique relation $\tilde{\nu}(\tilde{\epsilon})$ is obtained. This, in particular means that Eqs. (4.22)-(4.25) can only be satisfied for a single value of $\tilde{\nu}$ for each choice of driving force, i.e. $\tilde{\epsilon}$.

For further analysis, it is necessary to use a more rigorous notation¹ for the solution by letting

$$\varphi(\eta) = \varphi(\tilde{\varepsilon}, \eta) \quad (4.30)$$

be the solution to Eqs. (4.22)-(4.25) for $\tilde{\varepsilon}$.

Commonly, a phase-field model should be designed such that identical results are obtained independent of the order of labeling of the phases (here α and β). In view of the other phase (here β), any driving force is identical in magnitude but has opposite sign. Therefore, it is interesting to study the solution $\bar{\varphi}(\eta)$ satisfying the same equations for a driving force in the opposite direction but equal magnitude, i.e.

$$\bar{\varphi}(\eta) = \varphi(-\tilde{\varepsilon}, \eta). \quad (4.31)$$

For this, the following ODE needs to be fulfilled:

$$\bar{\varphi}(\eta) + \frac{d^2 \bar{\varphi}(\eta)}{d\eta^2} - \frac{4\tilde{\varepsilon}\tilde{v}(-\tilde{\varepsilon})}{\pi} \frac{d\bar{\varphi}(\eta)}{d\eta} - 2\tilde{\varepsilon}h'(\bar{\varphi}) = 0 \quad (4.32)$$

One may try the solution $\bar{\varphi}(\eta) = -\varphi(-\eta)$ which, by construction, satisfies $\bar{\varphi}(-\eta_+) = -\varphi(\eta_+) = 1$ and $\bar{\varphi}(-\eta_-) = -\varphi(\eta_-) = -1$. Thus, all BCs defined through Eqs. (4.23)-(4.24) are satisfied at the points $\bar{\eta}_- = -\eta_+$ and $\bar{\eta}_+ = -\eta_-$ with the correct ordering $\bar{\eta}_- < \bar{\eta}_+$.

¹ In the initial problem formulation through Eqs. (4.22)-(4.25), the dimensionless driving force is treated just as a constant. However, since the ODE changes as $\tilde{\varepsilon}$ is varied, this implies that φ changes with $\tilde{\varepsilon}$ as well. In most of the current chapter, the shorthand notation $\varphi(\eta)$ is used for the sake of brevity, keeping in mind that a more rigorous form would be $\varphi(\tilde{\varepsilon}, \eta)$ and the ordinary derivatives have to be replaced with partial derivatives.

It remains to show that Eq. (4.32) is satisfied. Inserting the trial solution into the left-hand side of the ODE, one obtains

$$-\varphi(-\eta) - \frac{d^2\varphi(\eta)}{d\eta^2} \Big|_{-\eta} - \frac{4\tilde{\varepsilon}\tilde{v}(-\tilde{\varepsilon})}{\pi} \frac{d\varphi(\eta)}{d\eta} \Big|_{-\eta} - 2\tilde{\varepsilon}h'(-\varphi(-\eta)) = 0. \quad (4.33)$$

The first two terms can be replaced according to the ODE for φ which yields

$$(\tilde{v}(\tilde{\varepsilon}) - \tilde{v}(-\tilde{\varepsilon})) \frac{4\tilde{\varepsilon}}{\pi} \frac{d\varphi(\eta)}{d\eta} \Big|_{-\eta} + 2\tilde{\varepsilon}(h'(\varphi(-\eta)) - h'(-\varphi(-\eta))) = 0. \quad (4.34)$$

If $h'(\varphi)$ is an even function, i.e. $h'(\varphi) = h'(-\varphi)$, the last term vanishes and hence the problem given by Eqs. (4.22)-(4.24) for $-\tilde{\varepsilon}$ is satisfied by $\bar{\varphi}(\eta)$ if the dimensionless velocity is chosen as $\tilde{v}(-\tilde{\varepsilon}) = \tilde{v}(\tilde{\varepsilon})$. According to the assumption of a unique relation of $\tilde{v}(\tilde{\varepsilon})$, this means that $\tilde{v}(\tilde{\varepsilon})$ is an even function.

In this case

$$\varphi(-\tilde{\varepsilon}, \eta) = -\varphi(\tilde{\varepsilon}, -\eta) \quad (4.35)$$

solves the ODE.

It is stressed that this holds only if $h'(\varphi) = h'(-\varphi)$, and taking into account that $h(-1) = 0$ and $h(1) = 1$, this implies that the interpolation function has to be symmetric, or more precisely $h(\varphi) = 1 - h(-\varphi)$ and $h_\alpha(1/2 + \varphi) = 1 - h_\alpha(1/2 - \varphi)$ according to Eq. (4.16).

Symmetry of the Interface Thickness The choice of solution implies that the interface thickness is even, since $\tilde{\delta}(-\tilde{\varepsilon}) = \bar{\eta}_+ - \bar{\eta}_- = \tilde{\delta}(\tilde{\varepsilon})$.

Symmetry of the Interfacial Energy Moreover, since $\bar{\varphi}^2(\eta) = \varphi^2(-\eta)$ and $\bar{\varphi}'(\eta) = \varphi'(-\eta)$ it follows according to Eq. (4.21) that the dimensionless interfacial energy also possesses an even symmetry with respect to the driving force, i.e. $\tilde{\sigma}(\tilde{\varepsilon}) = \tilde{\sigma}(-\tilde{\varepsilon})$.

Symmetry of the Maclaurin Coefficients of the Order Parameter In section 4.4, approximate asymptotic solutions are derived relying on a Maclaurin expansion of the order parameter $\varphi(\tilde{\varepsilon}, \eta)$. Please note that Eq. (4.35) can be made to comply with the shift constraint $\varphi(\tilde{\varepsilon}, 0) = 0$, which is enforced in the same section. In other words, when $\varphi(0) = 0$ also $\bar{\varphi}(0) = -\varphi(-0) = 0$ is ensured. Now, one can determine the Maclaurin coefficients in the usual way

$$\varphi_n(\eta) = \frac{1}{n!} \left. \frac{\partial^n \varphi(\tilde{\varepsilon}, \eta)}{\partial \tilde{\varepsilon}^n} \right|_{\tilde{\varepsilon}=0}. \quad (4.36)$$

This identity can be used for differentiating Eq. (4.35) n times yielding

$$(-1)^n \varphi_n(\eta) = -\varphi_n(-\eta) \quad (4.37)$$

after applying the chain rule n times to the left-hand side. This equality can be written in a more instructive form

$$\varphi_n(\eta) = \begin{cases} -\varphi_n(-\eta) & \text{even } n \\ \varphi_n(-\eta) & \text{odd } n \end{cases}, \quad (4.38)$$

revealing an interesting and quite satisfactory pattern: $\varphi_n(\eta)$ is an odd function if n is even and vice versa.

4.3.2 Solution for h_0

In the general case, Eq. (4.22) is a nonlinear second order ODE, where the non-linearity stems from the derivative of the interpolation function $h'(\varphi)$. Thus, the ODE cannot be exactly solved for arbitrary interpolation functions. However, for the special choice h_0 , an exact solution is possible, because $h'(\varphi)$ is simply a constant. The considered ODE is

$$\varphi(\eta) + \frac{d^2 \varphi(\eta)}{d\eta^2} + \frac{4\tilde{\varepsilon}\tilde{\nu}}{\pi} \frac{d\varphi(\eta)}{d\eta} + \tilde{\varepsilon} = 0. \quad (4.39)$$

which can be solved by performing the Laplace transform. The choice $\eta_- = 0$ helps applying the BCs as initial conditions ($\varphi(0) = 1$ and $\varphi'(0) = 0$) therein.

Let $a \equiv 2\tilde{\varepsilon}\tilde{\nu}/\pi$ and $s \equiv \sqrt{a^2 - 1}$, then the obtained solution reads

$$\varphi(\eta) = \frac{1 + \tilde{\varepsilon}}{2} \exp(-a\eta) \left(\left(1 + \frac{a}{s}\right) \exp(s\eta) + \left(1 - \frac{a}{s}\right) \exp(-s\eta) \right) - \tilde{\varepsilon} \quad (4.40)$$

$$\varphi'(\eta) = \frac{1 + \tilde{\varepsilon}}{2s} \exp(-a\eta) (\exp(-s\eta) - \exp(s\eta)). \quad (4.41)$$

Thus $s \neq 0$ needs to be fulfilled if $\tilde{\varepsilon} \neq -1$. Now it is necessary to ensure that $\varphi'(\eta_+) = 0$ for some $\eta_+ > 0$. So either $\exp(-a\eta_+) = 0$ or $\exp(-s\eta) - \exp(s\eta) = 0$. Since $a \in \mathbb{R}$, the former can only be satisfied for $a > 0$ and $\eta_+ \rightarrow \infty$, which is excluded as a possibility since it is demanded that η_+ and η_- be finite. If $s \in \mathbb{R}$, the latter can only be satisfied at $\eta_+ = 0$ and hence, no solution exists in this case that satisfies $\eta_+ > \eta_-$. So the only possibility left is that $s \in \mathbb{C}$ and $\text{Im}(s) \neq 0$. Since $s = \sqrt{a^2 - 1}$ and $a \in \mathbb{R}$ this implies that $a^2 < 1$ and $s = i\sqrt{1 - a^2}$, i is the imaginary unit and $\sqrt{1 - a^2} \in \mathbb{R}$, furthermore $\text{Im}(s) > 0$. According to Euler's formula and since \sin is an odd and \cos is an even function it follows

$$\exp(\pm s\eta) = \cos\left(\sqrt{1 - a^2}\eta\right) \pm i \sin\left(\sqrt{1 - a^2}\eta\right) \quad (4.42)$$

$$\exp(s\eta) + \exp(-s\eta) = 2 \cos\left(\sqrt{1 - a^2}\eta\right) \quad (4.43)$$

$$\exp(s\eta) - \exp(-s\eta) = 2i \sin\left(\sqrt{1 - a^2}\eta\right) \quad (4.44)$$

and accordingly

$$\varphi(\eta) = (1 + \tilde{\varepsilon}) \exp(-a\eta) \left(\cos\left(\sqrt{1 - a^2}\eta\right) + \frac{a}{\sqrt{1 - a^2}} \sin\left(\sqrt{1 - a^2}\eta\right) \right) - \tilde{\varepsilon} \quad (4.45)$$

$$\varphi'(\eta) = -\frac{1 + \tilde{\varepsilon}}{\sqrt{1 - a^2}} \exp(-a\eta) \sin\left(\sqrt{1 - a^2}\eta\right). \quad (4.46)$$

Possible endpoints need to fulfill $\varphi'(\eta_+) = 0$ according to the derivative BCs (Eq. (4.24)). This is fulfilled when $\sqrt{1-a^2}\eta_+ = n\pi$, $n \in \mathbb{Z}$. To ensure $\eta_+ > 0$, $\eta_+ = n\pi/\sqrt{1-a^2}$ with $n \in \mathbb{N}$. Furthermore, Eq. (4.23) demands that $\varphi(\eta_+) = -1$ is satisfied. This is the case if $(-1)^n(1+\tilde{\varepsilon})\exp\left(-an\pi/\sqrt{1-a^2}\right) - \tilde{\varepsilon} = -1$ which is a relation between the interface velocity (through a) and the driving force (through $\tilde{\varepsilon}$). Since $a \in \mathbb{R}$, and $a^2 < 1$, the exponential term is positive and hence, solutions only exist if $|\tilde{\varepsilon}| < 1$ for odd n and $|\tilde{\varepsilon}| > 1$ for even n .

A remaining problem is the non-uniqueness of the solution since it is not clear which n should be picked. This can be resolved by considering the Gibbs constraint (Eq. (4.25)). Since $\varphi'(\eta_k) = 0$ provides possible extrema locations $\eta_k = k\pi/\sqrt{1-a^2}$ between η_- and η_+ , where $0 < k < n$ with $k \in \mathbb{N}$, it is sufficient to consider $|\varphi(\eta_k)| < 1 \forall k$. For $n = 1$ there exists no such k , and accordingly, the Gibbs-constraint is fulfilled. Then $\varphi(\eta)$ is a monotonous function in the interval $\eta_- \leq \eta \leq \eta_+$. For odd $n \geq 3$ there are at least a single odd and an even k and it turns out, that at least one of them does not comply with the Gibbs constraint (i.e. the order parameter overshoots or undershoots the physically valid range). For even n there is at least a single odd k with $|\varphi(\eta_k)| \geq 1$ and therefore, the only valid choice is $n = 1$. This implies that no solution exists for $|\tilde{\varepsilon}| \geq 1$.

The main result of the current analysis are the dimensionless interface thickness and interface velocity as a function of dimensionless drivingforce $\tilde{\varepsilon}$.

$$\tilde{\delta}(\tilde{\varepsilon}) = \eta_+(\tilde{\varepsilon}) = \sqrt{\pi^2 + \ln^2\left(\frac{1+\tilde{\varepsilon}}{1-\tilde{\varepsilon}}\right)} \quad (4.47)$$

$$\tilde{v}(\tilde{\varepsilon}) = \frac{\pi a(\tilde{\varepsilon})}{2\tilde{\varepsilon}} = \frac{\pi \ln\left(\frac{1+\tilde{\varepsilon}}{1-\tilde{\varepsilon}}\right)}{2\tilde{\varepsilon} \tilde{\delta}(\tilde{\varepsilon})} \quad (4.48)$$

Additionally, the interfacial energy σ can be derived as

$$\tilde{\sigma}(\tilde{\varepsilon}) = \frac{1}{\pi} \left(\frac{4\tilde{\varepsilon} \ln\left(\frac{1+\tilde{\varepsilon}}{1-\tilde{\varepsilon}}\right)}{\tilde{\delta}(\tilde{\varepsilon})} + (1-\tilde{\varepsilon}^2) \tilde{\delta}(\tilde{\varepsilon}) \right). \quad (4.49)$$

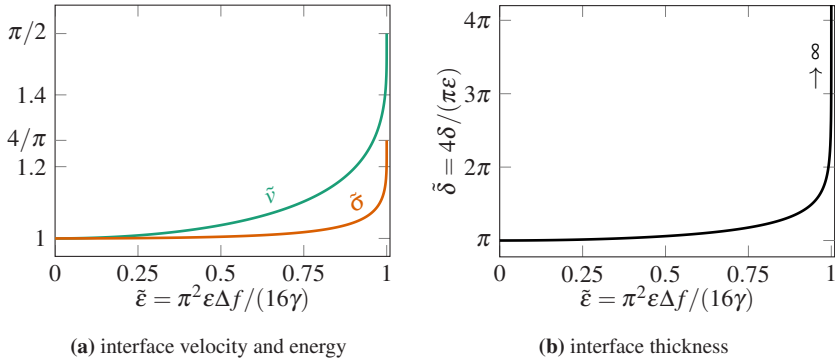


Figure 4.2: Dimensionless interface velocity \tilde{v} and interfacial energy $\tilde{\sigma}$ (a) as well as dimensionless interface thickness $\tilde{\delta}$ (b) as a function of the dimensionless driving force $\tilde{\varepsilon}$ in the range $0 < \tilde{\varepsilon} < 1$ for the interpolation function h_0 . \tilde{v} and $\tilde{\sigma}$ tend to $\pi/2$ and $4/\pi$ for $\tilde{\varepsilon} \rightarrow 1$, respectively, whereas the interfacial thickness tends to infinity. No solution exists for $|\tilde{\varepsilon}| \geq 1$.

It is easy to see, that all three quantities are even functions of $\tilde{\varepsilon}$, i.e. $\tilde{\delta}(\tilde{\varepsilon}) = \tilde{\delta}(-\tilde{\varepsilon})$, $\tilde{v}(\tilde{\varepsilon}) = \tilde{v}(-\tilde{\varepsilon})$ and $\tilde{\sigma}(\tilde{\varepsilon}) = \tilde{\sigma}(-\tilde{\varepsilon})$ hold. This can be traced back to the symmetry of the interpolation function (cf. section 4.3.1.2). Therefore, it is sufficient to discuss the behavior for positive $\tilde{\varepsilon}$ of these three quantities, which are plotted in Fig. 4.2. First of all, the sharp interface limit corresponds to $\tilde{\varepsilon} \rightarrow 0$. In this limit, $\tilde{v} \rightarrow 1$ and $\tilde{\sigma} \rightarrow 1$ which means that the sharp-interface relation $v = m\Delta f$ (Eq. (2.91)) is recovered and also the interfacial energy σ tends to the prescribed interfacial energy parameter γ . As can be seen in Fig. 4.2a, for larger driving forces however, the interface moves faster than demanded by the physical law. The deviation increases with increasing $\tilde{\varepsilon}$ and shows a very high slope as $\tilde{\varepsilon}$ approaches unity. Finally $\tilde{v}(1) = \pi/2$, i.e. a maximal acceleration of about 60% is reached. Therefore, the simulation result deviates significantly from the expected governing law. The behavior of the interfacial energy is qualitatively similar but since $\tilde{\sigma}(1) = 4/\pi$, it deviates less significantly (at max about 30%) from the sharp-interface value.

The interfacial thickness $\tilde{\delta}$, shown as a function of $\tilde{\varepsilon}$ in Fig. 4.2b approaches the conventional interface thickness of $\delta = \pi^2 \varepsilon / 4$ for vanishing driving forces which

similarly as for \tilde{v} and $\tilde{\sigma}$ constitutes its minimum. $\tilde{\delta}$ remains near this value for the interval $0 < \tilde{\epsilon} < 1/2$ but increases significantly afterwards which corresponds to an artificial thickening of the interfacial region. Furthermore, in contrast to \tilde{v} and $\tilde{\sigma}$ no finite limit is reached for $\tilde{\epsilon} \rightarrow 1$, but rather $\tilde{\delta} \rightarrow \infty$. This shows why no solution exists for $|\tilde{\epsilon}| \geq 1$, the interfacial thickness is out of any bounds and is therefore untractable. The no-solution means that the interface is not able to reach a travelling-wave form for $|\tilde{\epsilon}| \geq 1$. Therefore, the obvious conjecture is that a transient solution exists which never reaches a steady state.

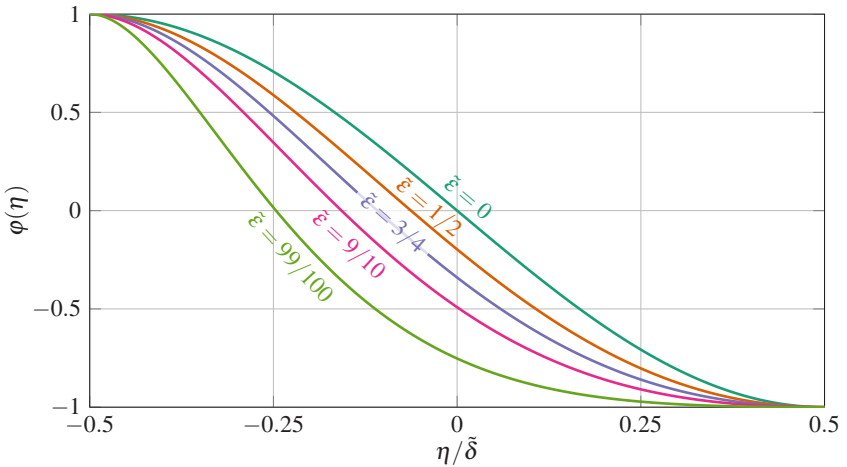


Figure 4.3: Rescaled order parameter $\varphi(\eta)$ in terms of the dimensionless moving coordinate η for various choices of $\tilde{\epsilon}$. The increase in dimensionless interfacial thickness $\tilde{\delta}$ with $\tilde{\epsilon}$ is compensated by an appropriate scaling of the horizontal axis.

Finally, the order parameter function $\varphi(\eta)$ is presented in a shifted form (i.e. replacing $\varphi(\eta)$ with $\varphi(\eta + \eta_+/2)$) and writes

$$\varphi(\eta) = \left(\frac{1 - \tilde{\epsilon}}{1 + \tilde{\epsilon}} \right)^{\frac{\eta}{\tilde{\delta}(\tilde{\epsilon})}} \sqrt{1 - \tilde{\epsilon}^2} \left(\frac{\ln \left(\frac{1 + \tilde{\epsilon}}{1 - \tilde{\epsilon}} \right)}{\pi} \cos \left(\frac{\pi \eta}{\tilde{\delta}(\tilde{\epsilon})} \right) - \sin \left(\frac{\pi \eta}{\tilde{\delta}(\tilde{\epsilon})} \right) \right) - \tilde{\epsilon}. \quad (4.50)$$

The shift has been introduced in order to make the symmetry with respect to the sign of $\tilde{\varepsilon}$ more apparent. The shifted endpoints now correspond to $\eta_{\pm} = \pm\tilde{\delta}/2$. In this form, Eq. (4.50) reduces in the sharp-interface limit ($\tilde{\varepsilon} \rightarrow 0$) to the well-known sinusoidal solution $\varphi(\eta) = -\sin(\eta)$. The order parameter profile $\varphi(\eta)$ is plotted for various values of $\tilde{\varepsilon} > 0$ in Fig. 4.3 as a function of $\eta/\tilde{\delta}$. It can be seen that the initially ($\tilde{\varepsilon} = 0$) odd function $\varphi(\eta)$ is distorted for finite $\tilde{\varepsilon}$ and thereby loses the symmetry. The deviation increases as $\tilde{\varepsilon}$ comes closer to unity. Near the right endpoint $\eta/\tilde{\delta} = 1/2$, a flat valley is formed, that extends over a wider interval as $\tilde{\varepsilon}$ increases.

This completes the presentation of the solution for h_0 which is of closed form.

4.3.3 Solution for h_d

The solution for h_d has to fulfill the following ODE

$$\varphi(\eta) + \frac{d^2\varphi(\eta)}{d\eta^2} + \frac{4\tilde{\varepsilon}\tilde{\nu}}{\pi} \frac{d\varphi(\eta)}{d\eta} + \frac{4\tilde{\varepsilon}}{\pi} \sqrt{1 - \varphi^2(\eta)} = 0. \quad (4.51)$$

The solution is simply found by inserting the known equilibrium solution $\varphi(\eta) = -\sin(\eta)$ in analogy to [7] satisfying the BCs (Eqs. (4.23)-(4.24)) at $\eta_{\pm} = \pm\pi/2$ and the Gibbs constraint (Eq. (4.25)). Then, the first two terms vanish and one obtains

$$-\frac{4\tilde{\varepsilon}\tilde{\nu}}{\pi} \cos(\eta) + \frac{4\tilde{\varepsilon}}{\pi} |\cos(\eta)| = 0. \quad (4.52)$$

Since $\cos(\eta) \geq 0$ for $-\pi/2 \leq \eta \leq \pi/2$, it follows that the ODE is fulfilled when

$$\tilde{\nu} = 1 \quad (4.53)$$

independent of $\tilde{\varepsilon}$. Moreover, evaluating equation (4.21), one obtains

$$\tilde{\sigma} = 1. \quad (4.54)$$

Thus, this interpolation function exactly recovers all physics for a planar interface. This is the important feature of this interpolation function and explains why it is used more frequently recently.

4.4 Approximate Asymptotic Solutions

4.4.1 Solution Framework

The asymptotic expansion employed here is an extension of the derivation in the previous chapter to arbitrary orders. However, for the one-dimensional treatment in the current chapter, the curvature influence can be neglected.

It is worth recalling how the expansion in the interface thickness parameter ε worked. To obtain equations at each order it was important to expand all (possibly nonlinear) dependencies on ε in the form of a polynomial in order to correctly compute the limit $\varepsilon \rightarrow 0$ at each order and match terms of equal power. By performing the limiting process, all other quantities were assumed to remain constant, i.e. independent of ε such as the interfacial energy parameter γ or the curvature. In the current chapter this means that an expansion in ε is identical to an expansion in $\tilde{\varepsilon}$, because the driving force Δf and γ are simply constants and an expansion in terms of $\tilde{\varepsilon}$ can be easily rewritten as an expansion in terms of ε by including these constants².

Expanding Unknowns Therefore, the solution to the ordinary differential equation (4.22) is assumed to be Maclaurin-expandable as follows:

$$\varphi(\eta) = \sum_{n=0}^{\infty} \tilde{\varepsilon}^n \varphi_n(\eta) \quad (4.55)$$

² Although using asymptotic expansions would be more rigorous, for the sake of readability, the more established notion of Taylor series is used.

Here, $\varphi_n(\eta)$ is simply the n th Taylor coefficient of $\varphi(\eta)$ and $\varphi_0(\eta)$ corresponds to the sharp-interface limiting solution.

This expansion implies an expansion of the dimensionless interfacial energy $\tilde{\sigma}$

$$\tilde{\sigma} = \sum_{n=0}^{\infty} \tilde{\epsilon}^n \tilde{\sigma}_n \quad (4.56)$$

where the coefficients $\tilde{\sigma}_n$ can be determined from Eq. (4.21).

The exact solutions derived so far showed that the interface velocity may vary as a function of dimensionless interface width $\tilde{\epsilon}$. Accordingly, the ansatz

$$\tilde{v} = \sum_{n=0}^{\infty} \tilde{\epsilon}^n \tilde{v}_n \quad (4.57)$$

is chosen. The same has to be done for the interfacial endpoints

$$\eta_{\pm} = \sum_{n=0}^{\infty} \tilde{\epsilon}^n \eta_{\pm}^n \quad (4.58)$$

where the superscript n in η_{\pm}^n simply acts as a label. From the expansion of dimensionless interface thickness

$$\tilde{\delta} = \sum_{n=0}^{\infty} \tilde{\epsilon}^n \tilde{\delta}_n = \sum_{n=0}^{\infty} \tilde{\epsilon}^n (\eta_+^n - \eta_-^n) \quad (4.59)$$

the coefficients are related as $\tilde{\delta}_n = \eta_+^n - \eta_-^n$.

ODEs at Each Order Now as the expanded forms are written down, it is necessary to insert them into the ODE (Eq. (4.22)) which yields

$$\begin{aligned} & \sum_{n=0}^{\infty} \tilde{\varepsilon}^n \left(\varphi_n(\eta) + \frac{d^2 \varphi_n(\eta)}{d\eta^2} \right) \\ & + \frac{4\tilde{\varepsilon} \sum_{n=0}^{\infty} \tilde{\varepsilon}^n \tilde{\nu}_n}{\pi} \sum_{n=0}^{\infty} \tilde{\varepsilon}^n \frac{d\varphi_n(\eta)}{d\eta} + 2\tilde{\varepsilon} h' \left(\sum_{n=0}^{\infty} \tilde{\varepsilon}^n \varphi_n(\eta) \right) = 0. \end{aligned} \quad (4.60)$$

Let L denote the left-hand side of the above equation, then differential equations at each order of $\tilde{\varepsilon}$ can now be obtained by demanding that the ODE has to hold for arbitrary $\tilde{\varepsilon}$ which results in the following recipe

$$\lim_{\tilde{\varepsilon} \rightarrow 0} \frac{\partial^n L}{\partial \tilde{\varepsilon}^n} = 0. \quad (4.61)$$

At lowest order, this leads to

$$\varphi_0(\eta) + \frac{d^2 \varphi_0(\eta)}{d\eta^2} = 0 \quad (4.62)$$

which is a linear second order differential equation for φ_0 . At first and second order, one obtains

$$\varphi_1(\eta) + \frac{d^2 \varphi_1(\eta)}{d\eta^2} = -\frac{4\tilde{\nu}_0}{\pi} \frac{d\varphi_0(\eta)}{d\eta} - 2h'(\varphi_0(\eta)) \quad (4.63)$$

$$\varphi_2(\eta) + \frac{d^2 \varphi_2(\eta)}{d\eta^2} = -\frac{4}{\pi} \left(\tilde{\nu}_0 \frac{d\varphi_1(\eta)}{d\eta} + \tilde{\nu}_1 \frac{d\varphi_0(\eta)}{d\eta} \right) - 2\varphi_1(\eta) h''(\varphi_0(\eta)). \quad (4.64)$$

Note that the right-hand side for the ODE of order n is a known function of η once the ODEs of orders $0, \dots, n-1$ have been successfully solved. Therefore, it is already apparent, that the nonlinearity in the original ODE could efficiently be removed by replacing it with an infinite number of linear ODEs each for the Taylor coefficient of the order parameter φ_n . Differential equations at higher

orders can be obtained in the same way but become lengthy and are thus omitted here.

Expanding Boundary Conditions The expansion of the boundary conditions is analogous to Sec. 3.2.1.4. Eqs. (4.23)-(4.24) rewritten in the expanded form and again demanding to hold for arbitrary $\tilde{\epsilon}$ yields

$$\lim_{\tilde{\epsilon} \rightarrow 0} \frac{\partial^n}{\partial \tilde{\epsilon}^n} \varphi \left(\sum_{n=0}^{\infty} \tilde{\epsilon}^n \eta_{\pm}^n \right) = \begin{cases} \mp 1 & n = 0 \\ 0 & n \geq 1 \end{cases} \quad (4.65)$$

$$\lim_{\tilde{\epsilon} \rightarrow 0} \frac{\partial^n}{\partial \tilde{\epsilon}^n} \varphi' \left(\sum_{n=0}^{\infty} \tilde{\epsilon}^n \eta_{\pm}^n \right) = 0. \quad (4.66)$$

Both equations are identical in the sense that all require the application of the generalization of the chain rule to n -th order. This relation is known as Faà di Bruno's formula. For the first few orders, it can be performed manually, but becomes tedious for higher orders as more and more terms accumulate.

One obtains

$$\varphi_0(\eta_{\pm}^0) = \mp 1 \quad (4.67)$$

$$\varphi'_0(\eta_{\pm}^0) = 0 \quad (4.68)$$

$$\varphi_1(\eta_{\pm}^0) = -\varphi'_0(\eta_{\pm}^0) \eta_{\pm}^1 \quad (4.69)$$

$$\varphi'_1(\eta_{\pm}^0) = -\varphi''_0(\eta_{\pm}^0) \eta_{\pm}^1 \quad (4.70)$$

$$\varphi_2(\eta_{\pm}^0) = -\frac{1}{2} \varphi''_0(\eta_{\pm}^0) (\eta_{\pm}^1)^2 - \varphi'_0(\eta_{\pm}^0) \eta_{\pm}^2 - \varphi'_1(\eta_{\pm}^0) \eta_{\pm}^1 \quad (4.71)$$

$$\varphi'_2(\eta_{\pm}^0) = -\frac{1}{2} \varphi'''_0(\eta_{\pm}^0) (\eta_{\pm}^1)^2 - \varphi''_0(\eta_{\pm}^0) \eta_{\pm}^2 - \varphi''_1(\eta_{\pm}^0) \eta_{\pm}^1 \quad (4.72)$$

and so forth. Interestingly, this provides boundary conditions for each φ_n at the zeroth order endpoints η_{\pm}^0 which underlines their importance.

Additional Shift Condition As mentioned earlier, the obtained solution is unique only up to a shift in η . Therefore an additional shift condition $\varphi(0) = 0$ is imposed for the current section. This results in

$$\varphi_n(0) = 0 \quad \forall n. \quad (4.73)$$

It is important to guarantee that the location $\eta = 0$ is part of the interfacial region by demanding that $\eta_- < 0 < \eta_+$. If this was not the case, it might be that the solution, as an analytical continuation, is artificially constraint in regions which belong to the bulk. Note that the boundary conditions (Eq. (4.23)) together with the intermediate-value theorem ensure that a point exists in between η_- and η_+ where $\varphi = 0$. Thus, the above condition can be imposed without loss of generality.

Remark Regarding the Gibbs-Constraint Unfortunately, there is no straightforward way to ensure that the Gibbs-simplex (Eq. (4.25)) is fulfilled by the expanded form without knowing all of the infinite number of Taylor coefficients φ_n . Therefore, the current strategy is that Eq. (4.25) is imposed on the zeroth-order $\varphi_0(\eta)$ by demanding that the Gibbs simplex must be fulfilled in the sharp interface limit. From there on, it can only be hoped that the expansion yields solutions that smoothly follow the right branch of the solution which ensures Eq. (4.25).

4.4.2 Solution at Low Orders

The relations obtained in the previous subsection are now applied to solve for the first few orders to obtain some insights that hold for large classes of interpolation functions. The goal is to identify certain conditions that must be met by the interpolation function to obtain certain properties of e.g. the interface velocity. Furthermore, the herein developed solutions show how one can proceed at higher orders.

4.4.2.1 Lowest Order Solution

The solution to Eq. (4.62) satisfying Eq. (4.73) reads $\varphi_0(\eta) = A \sin(\eta)$ with some prefactor A . Eq. (4.68) is evaluated to obtain the lowest order interfacial endpoints as $\eta_{\pm}^0 = \pi/2 + n\pi$ for some $n \in \mathbb{Z}$. The shift-constraint demands that $\eta_-^0 < 0 < \eta_+^0$. Therefore, $\eta_-^0 = \pi/2 - n\pi$ with $n \in \mathbb{N}$ and $\varphi_0(\eta_-^0) = (-1)^n A = 1$ which implies $A = (-1)^n$. If $n > 1$, the Gibbs simplex cannot be fulfilled since there exists a point $\eta_k = \pi/2 - k\pi$ with $0 < k < n$, $k \in \mathbb{N}$, where $|\varphi_0(\eta_k)| = 1$. Accordingly, $\eta_-^0 = -\pi/2$ which implies

$$\varphi_0(\eta) = -\sin(\eta) \quad (4.74)$$

and the only choice for η_+^0 that ensures the Gibbs simplex is $\eta_+^0 = \pi/2$. This result holds independent of the choice of interpolation function.

4.4.2.2 Integral Properties

Motivation The solution for φ_n , $n > 0$ (cf. Eqs. (4.63)-(4.64)) depend on the form of interpolation function, e.g. $h'(\varphi)$, $h''(\varphi)$ and so forth. Therefore, the solution cannot be presented without solving each of the interpolation functions separately. However, one can approach the ODE and integrate it to obtain some properties that hold without detailed knowledge over the order-parameter function.

Generalized Integration Since it appears that the differential operator for φ_n in Eq. (4.61) is always the same, one can in analogy to Eq. (3.91), multiply the ODE with $d\varphi_0/d\eta$ and integrate within the lowest order endpoints to obtain for the LHS:

$$\int_{\eta_-^0}^{\eta_+^0} \frac{d\varphi_0(\eta)}{d\eta} \left(\varphi_n(\eta) + \frac{d^2\varphi_n(\eta)}{d\eta^2} \right) d\eta = [\varphi_n'(\eta)\varphi_0'(\eta)]_{\eta_-^0}^{\eta_+^0} + [\varphi_n(\eta)\varphi_0(\eta)]_{\eta_-^0}^{\eta_+^0} \quad (4.75)$$

where the zero order ODE has been used to cancel the remaining integral from the partial integration. Incorporating Eqs. (4.67)-(4.68) it follows

$$\int_{\eta_-^0}^{\eta_+^0} \frac{d\varphi_0(\eta)}{d\eta} \left(\varphi_n(\eta) + \frac{d^2\varphi_n(\eta)}{d\eta^2} \right) d\eta = -(\varphi_n(\eta_+^0) + \varphi_n(\eta_-^0)). \quad (4.76)$$

Sharp-Interface Velocity In order to derive the value of the sharp-interface velocity \tilde{v}_0 , Eq. (4.63) is multiplied by $d\varphi_0(\eta)/d\eta$ and integrated using the relation from Eq. (4.76). By applying the BC from Eq. (4.69), one obtains

$$0 = \frac{4\tilde{v}_0}{\pi} \int_{\eta_-^0}^{\eta_+^0} \left(\frac{d\varphi_0(\eta)}{d\eta} \right)^2 d\eta + 2 \int_{\eta_-^0}^{\eta_+^0} h'(\varphi_0(\eta)) \frac{d\varphi_0(\eta)}{d\eta} d\eta \quad (4.77)$$

The first integral on the RHS can be integrated from the known solution given by Eq. (4.74) and is equally $\pi/2$. The second integral can be performed by substitution and is thus equal to $h(-1) - h(1)$ which is identically -1 due to the interpolation constraint. It follows that the sharp-interface limiting velocity recovers the physical law, i.e.

$$\tilde{v}_0 = 1 \quad (4.78)$$

which holds independent of the choice of interpolation function.

Thin-Interface Velocity The first-order correction to the interface velocity is given by \tilde{v}_1 . In analogy to the previous step, its value is derived by multiplying the second order ODE (Eq. (4.64)) with $d\varphi_0(\eta)/d\eta$ and subsequent integration.

Incorporating the BCs from Eq. (4.71) into the LHS given by Eq. (4.76), one obtains

$$\begin{aligned} \frac{1}{2} \left[\left(\frac{d\varphi_1(\eta)}{d\eta} \right)^2 \right]_{\eta_-^0}^{\eta_+^0} &= \frac{4}{\pi} \int_{\eta_-^0}^{\eta_+^0} \frac{d\varphi_0(\eta)}{d\eta} \frac{d\varphi_1(\eta)}{d\eta} d\eta + 2\tilde{v}_1 + \\ &2 \int_{\eta_-^0}^{\eta_+^0} \varphi_1(\eta) h''(\varphi_0(\eta)) \frac{d\varphi_0(\eta)}{d\eta} d\eta. \end{aligned} \quad (4.79)$$

The last integral on the RHS can be integrated by parts by raising $h''(\varphi_0(\eta))\varphi_1'(\eta)$ to $h'(\varphi_0(\eta))$ and incorporating the BC from Eq. (4.69). To evaluate the remaining integral $\int_{\eta_-^0}^{\eta_+^0} h'(\varphi_0)\varphi_1'(\eta) d\eta$, one has to express $h'(\varphi_0(\eta))$ in terms of φ_1 by rearranging the ODE for φ_1 (Eq. (4.63)). Then, two terms can be integrated by substitution and one of them vanishes by making use of the vanishing value of φ_1 at η_{\pm}^0 . The other term cancels the LHS of equation (4.79). Finally, \tilde{v}_1 can be expressed as

$$\tilde{v}_1 = -\frac{4}{\pi} \int_{\eta_-^0}^{\eta_+^0} \frac{d\varphi_0(\eta)}{d\eta} \frac{d\varphi_1(\eta)}{d\eta} d\eta. \quad (4.80)$$

Interestingly, this result can also be obtained by expanding the more general equation (4.29) using Leibniz rule. Unfortunately it seems that no progress could be made since $\varphi_1(\eta)$ is unknown.

Some progress can be made by redoing the integration from the previous paragraph but changing the bounds of integration from 0 to η_{\pm}^0 . Then, the integration of the LHS of Eq. (4.63) is given by

$$\int_0^{\eta_{\pm}^0} \frac{d\varphi_0(\eta)}{d\eta} \left(\varphi_1(\eta) + \frac{d^2\varphi_1(\eta)}{d\eta^2} \right) d\eta = \varphi_1'(0) \quad (4.81)$$

which follows from the BCs (Eqs. (4.68)-(4.69)), the shift-constraint (Eq. (4.73)) as well as the zero-order ODE (Eq. (4.62)). The corresponding RHS is given by

$$-\frac{4}{\pi} \int_0^{\eta_{\pm}^0} \left(\frac{d\varphi_0(\eta)}{d\eta} \right)^2 d\eta - 2 \int_0^{\eta_{\pm}^0} h'(\varphi_0(\eta)) \frac{d\varphi_0(\eta)}{d\eta} d\eta = 2h(0) - 1. \quad (4.82)$$

Here, the first integral is simply found by Eq. (4.74) as $\pm\pi/4$ and the second integral has been performed by substitution. Equating LHS and RHS yields

$$\varphi_1'(0) = 2h(0) - 1. \quad (4.83)$$

For the special case of an even symmetry of $h'(\varphi)$, $h(0) = 1/2$ and thus

$$\varphi_1'(0) = 0. \quad (4.84)$$

Based on this result, the implications of the even nature of $h'(\varphi)$ can be exploited more thoroughly. Accordingly, note that the RHS in Eq. (4.63) becomes an even function with respect to η . This implies that its odd coefficients in a Maclaurin series with respect to η are zero. When the ODE is seen as a recurrence relation for the Maclaurin coefficients of φ_1 , one can state by differentiating Eq. (4.63) $2n + 1$ times ($n \in \mathbb{Z}, n \geq 0$) that

$$\left. \frac{d^{2n+3}\varphi_1(\eta)}{d\eta^{2n+3}} \right|_{\eta=0} = - \left. \frac{d^{2n+1}\varphi_1(\eta)}{d\eta^{2n+1}} \right|_{\eta=0} \quad (4.85)$$

which means that by induction

$$\left. \frac{d^{2n+1}\varphi_1(\eta)}{d\eta^{2n+1}} \right|_{\eta=0} = (-1)^n \varphi_1'(0) = 0, \quad (4.86)$$

where the last equality follows from Eq. (4.84). This result is remarkable, as it shows that $\varphi_1(\eta)$ is an even function. Thus, the more general result shown

in Eq. (4.38) is rediscovered. Furthermore, this is enough to conclude that the interface velocity is first-order accurately recovered, i.e.

$$\tilde{v}_1 = 0 \quad (4.87)$$

by evaluating the integral in Eq. (4.80). It is stressed that this follows from the symmetry of the interpolation function.

Thin-Interface Thickness It is worth multiplying the ODE for φ_1 with a different test function, namely $\varphi_0''(\eta)$, before integration. In analogy with the steps to derive Eq. (4.76) (performing partial integration and using Eq. (4.62)) yields

$$\eta_+^1 - \eta_-^1 = \frac{4}{\pi} \int_{\eta_-^0}^{\eta_+^0} \frac{d\varphi_0(\eta)}{d\eta} \frac{d^2\varphi_0(\eta)}{d\eta^2} d\eta + 2 \int_{\eta_-^0}^{\eta_+^0} h'(\varphi_0(\eta)) \frac{d^2\varphi_0(\eta)}{d\eta^2} d\eta. \quad (4.88)$$

Here, BCs from Eqs. (4.67)-(4.70) have been used. If $h'(\varphi_0)$ is an even function and since $\varphi_0(\eta)$ is odd, the right-hand side vanishes and thus

$$\tilde{\delta}_1 = \eta_+^1 - \eta_-^1 = 0, \quad (4.89)$$

i.e. the interface thickness is first-order constant.

Summary This completes the derivation exploiting certain properties of the interpolation function $h(\varphi)$. To summarize, it was shown that the interpolation constraint $h(1) = 1$ and $h(-1) = 0$ is sufficient to warrant that the interface velocity is given by $v_0 = m\Delta f$ in the sharp-interface limit. Furthermore, it was shown that if the interpolation function is symmetric, i.e. $h(\varphi) = 1 - h(-\varphi)$ this result keeps holding considering first-order corrections in the driving force. Since the property $h(\varphi) = 1 - h(-\varphi)$ is fulfilled by all interpolation functions commonly used in phase-field models of the obstacle type (cf. Table 4.1), this is a quite

general result. Interestingly, in this case, also the interface thickness remains unchanged incorporating first-order corrections.

4.4.3 Solution at Higher Orders

Motivation It turned out, that for the first two orders, all interpolation functions lead to an identical model behavior. On the one hand, it shows that the design of the interpolation functions has been performed with a portion of foresightedness. On the other hand, it is a bit disappointing that so far no subtleties could be identified to explain differences between the interpolation functions regarding the effort to derive the results from the previous section. In order to extract useful information at higher orders, the most straightforward approach is to solve the corresponding ODEs for the order parameter, i.e. derive explicit functions $\varphi_n(\eta)$, $n > 1$. As this is a tedious task to do manually, a significant effort has been put into automating the procedure using modern computer algebra systems. The software *Wolfram Mathematica 13.1* is being used to perform the following derivations.

Solution Algorithm The solution procedure can be described as an algorithm in pseudo-code and is shown in Listing 4.1.

Listing 4.1: Asymptotic solution procedure for higher orders

Prescribe $\varphi_0(\eta) = -\sin(\eta)$ from Eq. (4.74).

Set $\eta_{\pm}^0 = \pm\pi/2$.

for $n \in \{1, \dots, N\}$ **do**

Solve $\varphi_n(\eta)$ from Eq. (4.61) subject to BC $\varphi_n(0) = 0$ from Eq. (4.23) and BC from Eq. (4.65) at order n and at η_+^0 .

Determine the interfacial velocity coefficient \tilde{v}_{n-1} by evaluating the solution φ_n through BC Eq. (4.65) at order n and at η_-^0 .

Insert the value of \tilde{v}_{n-1} into the solution to $\varphi_n(\eta)$.

Determine interfacial endpoints η_{\pm}^n by evaluating BCs from Eq. (4.66) at order n .

Determine interfacial energy coefficients $\tilde{\sigma}_n$ by expanding Eq. (4.21) according to Eq. (4.56) at current order.

end

The lowest order phase-field profile can be solved manually, as given by Eq. (4.74) which also leads to $\eta_{\pm}^0 = \pm\pi/2$. Alternatively, this result can be re-obtained by the computer algebra system by subjecting it with appropriate assumptions. The main part of the algorithm consists of a loop which iterates over the orders n from 1 to N in increasing order, where N is the maximal order considered. The maximal order was chosen as 11 since solutions at high orders become very time consuming. Within the loop, the first step is to derive $\varphi_n(\eta)$ subject to two boundary conditions in order to obtain a unique result. The solution $\varphi_n(\eta)$ contains \tilde{v}_{n-1} as a free parameter that is determined in a next step by incorporating an additional boundary condition. Accordingly, there is no need to determine it by integration, as done manually. This was only necessary because the exact form of $\varphi_n(\eta)$ could not be derived without selecting one of the h -variants.

After inserting the determined interface-velocity coefficient into the solution $\varphi_n(\eta)$, the interfacial endpoint coefficients η_{\pm}^n can be similarly determined by evaluating additional boundary conditions. As a last step, the dimensionless interfacial energy coefficient at order n can be determined from Eq. (4.21) and Eq. (4.56).

Once the computer algebra system has successfully completed the algorithm, the phase-field equations $\varphi_n(\eta) \forall 0 \leq n \leq N$ and the interfacial velocity coefficients $\tilde{v}_n(\eta) \forall 0 \leq n \leq N-1$ as well as the interfacial endpoint corrections $\eta_{\pm}^n \forall 0 \leq n \leq N$ are readily available in symbolic (and thus exact) form. This makes this methodology so valuable.

Derived Order-Parameter Profiles The resulting order-parameter functions are tabulated in Table 4.2 for the first order and in Table 4.3 for the second order.

Table 4.2: First order correction to the phase-field profile $\varphi_1(\eta)$ for all common interpolation functions used in PF-models of the obstacle type.

h -Type	$\varphi_1(\eta)$
h_0	$\frac{2\eta \sin(\eta)}{\pi} + \cos(\eta) - 1$
h_1	$\frac{2\eta \sin(\eta)}{\pi} + \frac{\cos(\eta)}{2} + \frac{\cos(2\eta)}{4} - \frac{3}{4}$
h_2	$\frac{2\eta \sin(\eta)}{\pi} + \frac{3\cos(\eta)}{8} + \frac{5\cos(2\eta)}{16} + \frac{\cos(4\eta)}{64} - \frac{45}{64}$
h_d	0

Table 4.3: Second order correction to the phase-field profile $\varphi_2(\eta)$ for all common interpolation functions used in PF-models of the obstacle type.

h -Type	$\varphi_2(\eta)$
h_0	$\frac{(2-2\pi+\pi^2-2\pi^2)\sin(\eta)+2(1-\pi)\eta\cos(\eta)}{\pi^2}$
h_1	$\frac{(107\pi^2-64\pi+128-128\eta^2)\sin(\eta)}{64\pi^2} + \frac{(32-16\pi-21\pi^2)\eta\cos(\eta)}{16\pi^2}$ $-\frac{3}{\pi}\eta + \left(\frac{1}{4} + \frac{2}{3\pi}\right)\sin(2\eta) + \frac{3}{64}\sin(3\eta) - \frac{\eta\cos(2\eta)}{\pi}$
h_2	$\frac{(32768(1-\eta^2)+23393\pi^2-12288\pi)\sin(\eta)}{16384\pi^2} - \frac{15}{8\pi}\eta$ $+\frac{(4096-1536\pi-1365\pi^2)\eta\cos(\eta)}{2048\pi^2} + \left(\frac{15}{64} - \frac{5}{6\pi}\right)\sin(2\eta) - \frac{1065\sin(3\eta)}{8192}$ $+\left(\frac{3}{128} + \frac{1}{20\pi}\right)\sin(4\eta) + \frac{105\sin(5\eta)}{8192} + \frac{5\sin(7\eta)}{16384} - \frac{\eta\cos(4\eta)}{8\pi}$
h_d	0

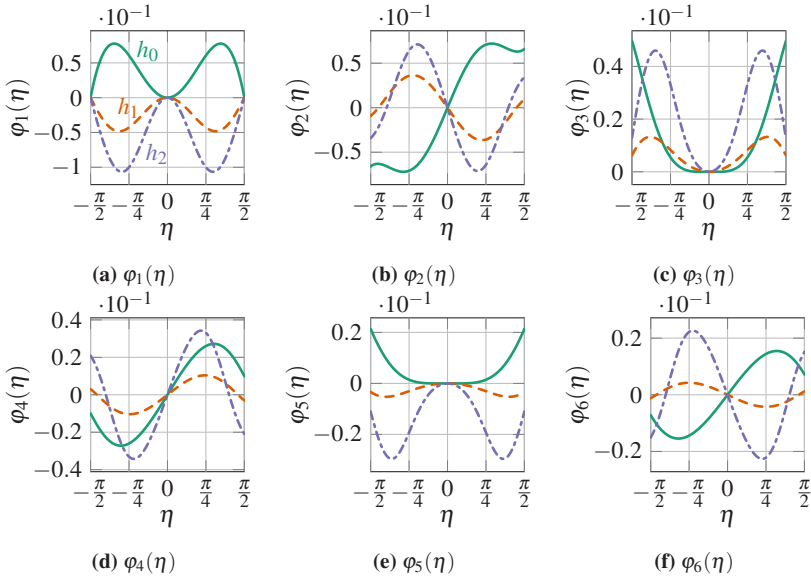


Figure 4.4: The first six corrections $\varphi_n(\eta)$, $1 \leq n \leq 6$ to the interface profile as a function of the rescaled interface normal coordinate η . Three different interpolation functions h_0 (solid), h_1 (dashed) and h_2 (dashdotted) are shown. The order increases from (a) to (f).

Firstly, it is apparent that all interpolation functions lead to even functions $\varphi_1(\eta)$ and odd functions $\varphi_2(\eta)$. For the first order, this resembles the derivation of the previous section shown in Eq. (4.86). The first two orders suggest that this pattern might continue for higher orders. It can be proven, that this holds indeed true for symmetric interpolation functions (i.e. $\varphi_n(\eta)$ is an even function if n is odd and vice versa) – see section 4.3.1.2. In accordance with the exact solution for h_d , all corrections $\varphi_n(\eta) = 0$ for $n \geq 1$. The solutions for integer-power interpolation function h_n can be written as a sum of products of polynomials in η and trigonometric functions of the form $\sin(z\eta)$ and $\cos(z\eta)$ with some integer $z \in \mathbb{Z}$. In general, the higher the exponent n in h_n , the more terms appear. For instance, the second-order correction $\varphi_2(\eta)$ for h_2 comprises of sixteen different terms and is thus already difficult to tabulate. As the number of terms increases with order, solutions at orders $n > 2$ in $\varphi_n(\eta)$ – although available – are not listed herein for the sake of brevity. However, the functions $\varphi_1(\eta)$ to $\varphi_6(\eta)$ are plotted

in the range $-\pi/2 \leq \eta \leq \pi/2$ in Fig. 4.4. This figure highlights the rich variety of functions obtained by performing higher-order asymptotics. For instance, the even and odd symmetry of the functions can be observed visually by mirroring the functions about the plane $\eta = 0$.

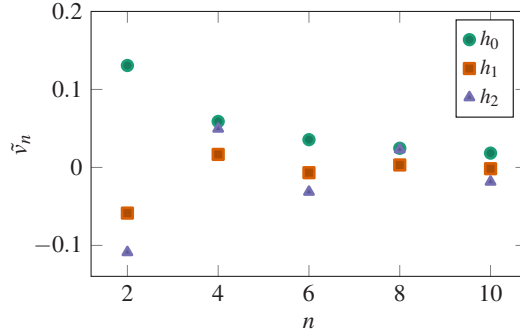


Figure 4.5: Even interface velocity coefficients \tilde{v}_n for three different interpolation functions of integer type.

Derived Interface Velocities In deriving the interface velocity coefficients \tilde{v}_n through the presented algorithm for the first eleven orders, it is seen that all odd coefficients vanish (independent of the choice of interpolation function). This is in line with the derivation performed earlier for the general case (cf. section 4.3.1.2). Therefore, it is sufficient to take even powers into account. Table 4.4 tabulates all even interface velocity coefficients.

Additionally, these coefficients are plotted against the order n in Fig. 4.5. It can be seen that for h_0 all coefficients are positive and decaying with order. This means that for this interpolation function, the interface velocity is monotonously increasing with the magnitude of the driving force. This is no surprise since the velocity coefficients can alternatively be derived as the Maclaurin coefficients of the exact solution derived earlier (Eq. (4.48)). As this check has explicitly been performed, it shows that the current expansion works correctly and is able to reproduce exact solutions successfully. The same is true for the special case of

Table 4.4: Dimensionless interface velocity coefficients up to order ten for all common interpolation functions. Results are given in symbolic form except lengthy expression which are shown as numerical values accurate to 14 significant digits. The odd coefficients are equally zero for all interpolation functions.

Symbol	h_0	h_1	h_2	h_d
\tilde{v}_0	1	1	1	1
\tilde{v}_2	$\frac{1}{3} - \frac{2}{\pi^2}$	$\frac{83}{96} - \frac{82}{9\pi^2}$	$\frac{24263}{24576} - \frac{2434}{225\pi^2}$	0
\tilde{v}_4	$\frac{1}{5} - \frac{2}{\pi^2} + \frac{6}{\pi^4}$	$-\frac{6793}{2560} + \frac{234479}{21600\pi^2} + \frac{4130}{27\pi^4}$	$-\frac{1164005201}{335544320} + \frac{179711871821}{5245599744\pi^2} + \frac{25942}{5625\pi^4}$	0
\tilde{v}_6	$\frac{1}{7} - \frac{28}{15\pi^2} + \frac{10}{\pi^4} - \frac{20}{\pi^6}$	$\frac{13847837}{2293760} - \frac{358602673}{14515200\pi^2} - \frac{151322221}{4860000\pi^4} - \frac{83612}{27\pi^6}$	-0.031353620256855	0
\tilde{v}_8	0.024574396386496	0.0031878895228450	0.023020558168523	0
\tilde{v}_{10}	0.018351125315404	-0.0016441767901692	-0.018405432524639	0

h_d , where all coefficients in the current framework are zero for positive orders. In contrast, for the interpolation functions where no exact solution is known, namely h_1 and h_2 , coefficients have alternating signs that also decay in magnitude. Thus, a clear trend cannot be deduced only from the sign of the coefficients. The first non-zero correction \tilde{v}_2 is negative, which indicates that for small driving forces, the interface moves more slowly than expected from the physical law. Since the magnitude of the coefficients are smaller for h_1 compared to h_2 it seems that the former choice produces results closer to this law.

Derived Interface Thicknesses In the same fashion as the interface velocity coefficients, the interfacial thickness coefficients $\tilde{\delta}_n$ are non-vanishing only for even powers. This is another consequence of the symmetry of the interpolation function (cf. section 4.3.1.2). The values of the interface thickness coefficients corresponding to even powers are tabulated in Table 4.5. The lowest order coefficient $\tilde{\delta}_0$ is equal among all interpolation functions which reflects the identical sharp-interface limiting profile $\varphi_0(\eta)$. Figure 4.6 reveals the same qualitative pattern for $\tilde{\delta}_n$ compared with the velocity coefficients \tilde{v}_n : For h_0 all coefficients are positive and decaying, whereas for h_1 and h_2 , alternating signs are observed. This means that h_0 leads to an increasing thickness with driving force that was already

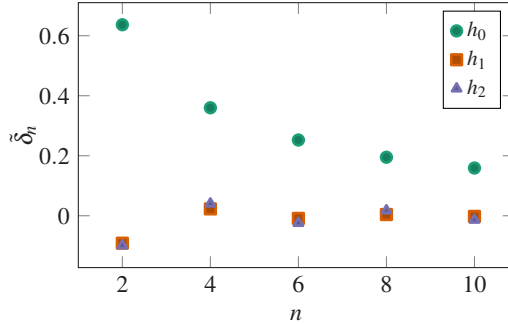


Figure 4.6: Even interface thickness coefficients $\tilde{\delta}_n$ for three different interpolation functions of integer type.

discovered earlier (cf. Eq. (4.47)). In general, the magnitude of the coefficients of h_0 are much larger compared to either h_1 or h_2 . Comparing the latter two shows that the coefficient h_1 are smaller in magnitude compared to h_2 , indicating that the interface thickness is less perturbed for h_1 . The negativity of $\tilde{\delta}_2$ in both cases shows that these interpolation functions tend to a sharpening of the interface as a first correction.

Table 4.5: Dimensionless interface thickness coefficients up to order ten for all common interpolation functions. Results are given in symbolic form except lengthy expression which are shown as numerical values accurate to 14 significant digits. The odd coefficients are equally zero for all interpolation functions.

Symbol	h_0	h_1	h_2	h_d
$\tilde{\delta}_0$	π	π	π	π
$\tilde{\delta}_2$	$\frac{2}{\pi}$	$\frac{38}{3\pi} - \frac{21\pi}{16}$	$\frac{94}{15\pi} - \frac{1365\pi}{2048}$	0
$\tilde{\delta}_4$	$\frac{4}{3\pi} - \frac{2}{\pi^3}$	$-\frac{2422}{27\pi^3} - \frac{8567}{720\pi} + \frac{2185\pi}{1024}$	$\frac{1572898}{3375\pi^3} + \frac{876077341}{28385280\pi} - \frac{265037755\pi}{33554432}$	0
$\tilde{\delta}_6$	$\frac{46}{45\pi} - \frac{8}{3\pi^3} + \frac{4}{\pi^5}$	$\frac{318092}{243\pi^5} - \frac{40640209}{54000\pi^3} - \frac{1112521}{46080\pi} + \frac{432929\pi}{49152}$	-0.024325894233315	0
$\tilde{\delta}_8$	0.19500067118787	0.0040557348420294	0.017427708396088	0
$\tilde{\delta}_{10}$	0.15912944627703	-0.0020566481533696	-0.013722716819636	0

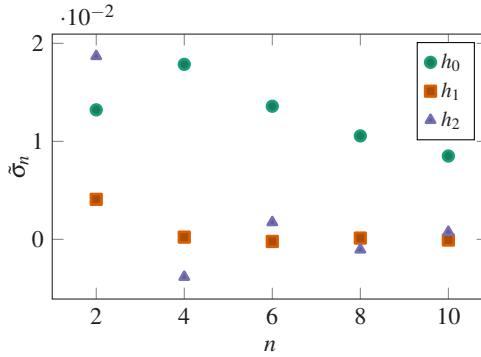


Figure 4.7: Even interface energy coefficients $\tilde{\sigma}_n$ for three different interpolation functions of integer type.

Derived Interfacial Energies By considering the dimensionless interfacial energy $\tilde{\sigma}$ as a Maclaurin series with respect to the driving force $\tilde{\epsilon}$, once again only even coefficients are relevant, as proven in section 4.3.1.2. The corresponding values are tabulated in Table 4.4.

The plot shown in Fig. 4.7 reveals a different pattern compared to the two quantities discussed in the two previous paragraphs. In particular, the first non-vanishing correction $\tilde{\sigma}_2$ is positive for all interpolation functions. This means that the sharp-interface solution φ_0 corresponds to a minimum in the interfacial energy function. This is at the heart of variational calculus which demands that the ODE for φ_0 , namely Eq. (4.62), minimizes the free-energy functional given by Eq. (4.1) in the absence of driving forces, i.e. $f_\alpha = f_\beta = 0$, which then is nothing but the definition for σ . The value of $\tilde{\sigma}_2$ shows that for small perturbations, h_1 remains closest to the physical law, followed by h_0 and h_2 . Apart from this very first correction, the pattern of the coefficients is qualitatively identical to that of the other quantities $\tilde{\nu}$ and $\tilde{\delta}$ in the sense that the coefficients for h_0 are positive and decaying and both h_1 and h_2 have coefficients of alternating signs. Also the magnitudes relate as before.

Table 4.6: Dimensionless interfacial energy coefficients up to order ten for all common interpolation functions. Results are given in symbolic form except lengthy expression which are shown as numerical values accurate to 14 significant digits. The odd coefficients are equally zero for all interpolation functions.

Symbol	h_0	h_1	h_2	h_d
$\tilde{\sigma}_0$	1	1	1	1
$\tilde{\sigma}_2$	$\frac{10}{\pi^2} - 1$	$\frac{14}{3\pi^2} - \frac{15}{32}$	$\frac{18}{5\pi^2} - \frac{2835}{8192}$	0
$\tilde{\sigma}_4$	$\frac{2}{\pi^2} - \frac{18}{\pi^4}$	$-\frac{5729}{1024} + \frac{13370}{27\pi^4} + \frac{1817}{360\pi^2}$	$-\frac{424758505}{33554432} - \frac{276638}{375\pi^4} + \frac{4407630973}{22077440\pi^2}$	0
$\tilde{\sigma}_6$	$\frac{52}{\pi^6} - \frac{50}{3\pi^4} + \frac{58}{45\pi^2}$	$\frac{54781219}{983040} - \frac{7361284}{243\pi^6} + \frac{87947393}{27000\pi^4} - \frac{131107427}{230400\pi^2}$	0.0017364639640677	0
$\tilde{\sigma}_8$	0.010553941380702	0.00012769279975424	-0.0010521810743562	0
$\tilde{\sigma}_{10}$	0.0085010899147613	-0.000072938112294313	0.0007415407539526	0

4.4.4 Summation Strategy

Limitations of Maclaurin Series As a lot of Maclaurin coefficients regarding several quantities are now known, one might think that it is straightforward to obtain meaningful information by simply constructing the approximation corresponding to some quantity $a(\tilde{\epsilon})$ as a partial sum

$$P_N(a, \tilde{\epsilon}) \equiv \sum_{n=0}^N a_n \tilde{\epsilon}^n, \quad (4.90)$$

where the coefficients a_n are fixed by demanding that the derivatives at $x = 0$ are equal up to order N , i.e. $\partial^n P_N / \partial x^n|_{x=0} = \partial^n a / \partial x^n|_{x=0} \forall 0 \leq n \leq N$.

However, as it turned out, this seems to give awkward results that do not comply with some of the general bounds derived (e.g. the positivity of the dimensionless velocity is not fulfilled) for large arguments (e.g. $\tilde{\epsilon} > 1$).

It seems that a common problem with the summation of Taylor series is encountered, namely the limited radius of convergence. A typical example is the Maclaurin series for $f(x) = 1/(1+x)$ which writes as

$$P_N(f, x) = \sum_{n=0}^N (-1)^n x^n. \quad (4.91)$$

This series has a radius of convergence equal to 1 and trying to evaluate its value at $x = 1$, which is equally $1/2$, results in values of alternating signs crucially determined by the choice of N .

$$P_N(f, x) = 1 - 1 + 1 - 1 + \dots = \begin{cases} 1 & N \text{ even} \\ 0 & N \text{ odd} \end{cases} \quad (4.92)$$

Thus, the result does not get closer to the correct value by incorporating an increasing number of coefficients. More drastically, for arguments larger than 1 something quite remarkable happens: The more coefficients one incorporates, the farther away is the result from the actual value. This is a serious concern because it means that all the effort so far to derive more and more coefficients (which was a hard task) is completely worthless.

Padé Summation Fortunately, this troublesome situation can be improved by using a different summation strategy, i.e. using a different prescription to incorporate the Maclaurin coefficients. In the field of perturbation theory, divergent series are commonly encountered and, as shown in [106], a versatile method to obtain more accurate approximations is by means of Padé summation. Padé approximants are a generalization of Taylor approximation to rational functions and can be written as

$$P_M^N(a, x) \equiv \frac{\sum_{n=0}^N P_n x^n}{\sum_{n=0}^M Q_n x^n}, \quad (4.93)$$

where p_n and q_n are the Padé coefficients corresponding to the numerator and denominator, respectively. Two orders of the approximant, namely N and M have to be prescribed, the special case $M = 0$ corresponds to the Maclaurin series. In analogy to the way the Maclaurin coefficients are fixed, p_n and q_n are uniquely³ determined by insisting that the Maclaurin coefficients of both the approximation and the exact function are identical up to order $M + N$, i.e. $\partial^n P_M^N / \partial x^n \big|_{x=0} = \partial^n a / \partial x^n \big|_{x=0} \forall 0 \leq n \leq M + N$.

The superiority of Padé approximants is best apparent for the simple example above ($f(x) = 1/(1+x)$). Any Padé approximant with $M > 0$ exactly recovers the function.

Stieltjes-like Behavior As outlined in [106, Ch. 8.4] Padé summation is discussed with respect to Stieltjes-functions, where they demonstrate some interesting properties namely the diagonal and the first off-diagonal Padé approximants monotonically decrease and increase, respectively for real and positive arguments, i.e.

$$P_{N+1}^{N+1}(f, x) \leq P_N^N(f, x) \quad \forall x \in \mathbb{R}, x > 0 \quad (4.94)$$

$$P_{N+2}^{N+1}(f, x) \geq P_{N+1}^N(f, x) \quad \forall x \in \mathbb{R}, x > 0 \quad (4.95)$$

cf. [106, Eq. 8.6.6] and assuming that they converge to the same limit, i.e. $\lim_{N \rightarrow \infty} P_N^N(f, x) = \lim_{N \rightarrow \infty} P_{N+1}^N(f, x)$ provide error bounds on $f(x)$:

$$P_{N+1}^N(f, x) \leq f(x) \leq P_N^N(f, x). \quad (4.96)$$

Moreover, for this special class of functions, all poles of $P_N^N(f, x)$ and $P_{N+1}^N(f, x)$ lie on the negative real axis.

³ One degree of freedom can be removed by demanding that $q_0 = 1$. This always works when the Maclaurin expansion to $a(x)$ exists. Then $N + 1$ unknown coefficients for the numerator and M unknowns for the denominator remain, thus in total $M + N + 1$ unknowns.

The conditions given by Eqs. (4.94)-(4.95) and the location of the poles can be tested for the derived coefficients. In the current work, a function is denoted as *Stieltjes-like* if these conditions are satisfied.

For h_1 and h_2 , in performing these checks on the approximants for $\tilde{\nu}$, $\tilde{\delta}$ and $\tilde{\sigma}$, it turned out that at least for $\tilde{\nu}$ and $\tilde{\delta}$, all conditions are fulfilled if one constructs the approximant with respect to $\tilde{\varepsilon}^2$, exploiting the even nature proven in section 4.3.1.2. Thus it seems, that $\tilde{\nu}$ and $\tilde{\delta}$ behave Stieltjes-like with respect to $\tilde{\varepsilon}^2$.

Although $\tilde{\sigma}$ seems not to be exactly Stieltjes, the error bounds (Eq. (4.96)) are exploited for all three scalar quantities by calculating an average as

$$f(\tilde{\varepsilon}^2) \approx \frac{1}{2} (P_N^N(f, \tilde{\varepsilon}^2) + P_{N+1}^N(f, \tilde{\varepsilon}^2)), \quad (4.97)$$

where f is one of $\tilde{\nu}$, $\tilde{\delta}$ and $\tilde{\sigma}$. This approximation is used in the following numerical comparison and completes the analytical treatments.

4.5 Numerical Comparison

Preface After the analytical derivations are thoroughly presented, it is now required to relate them to the numerical results obtained in a typical phase-field simulation. The main question to be addressed is whether the derived equations are able to explain deviations between the simulation results where all parameters are kept identical except the choice of interpolation function.

It is worth stressing that a numerical study of the problem without the previous analytical derivations can become cumbersome. First note that the model contains five model parameters: m , f_α , f_β , γ and ε . This corresponds to a five parameter space which requires a large number of simulations in order to fully cover all the possible combinations. The performed non-dimensionalization revealed that the parameter space can be reduced to a single non-dimensional driving force $\tilde{\varepsilon}$.

This clearly simplifies the comparison since it reduces the computational effort tremendously.

The following study can be considered as a cross-validation: If any one of either the numerical or analytical solutions are erroneous, it is expected that a mismatch can be observed. On the contrary, if a good match is observed, this would increase the confidence in both the analytical and numerical solutions.

4.5.1 Setup and Parameterization

Table 4.7: Parameter set used for the driving force simulations in terms of the model units for length u_l , energy u_E and time u_t . A range of possible dimensionless drivingforces $\tilde{\epsilon}$ is set through f_β .

Parameter	Symbol	Value
Interface Width	ϵ	$4u_l$
Interfacial Energy	γ	$3\frac{u_E}{u_t^2}$
Interface Mobility	m	$\frac{1}{2}\frac{u_l^4}{u_E u_t}$
Grid Spacing	Δx	$0.125u_l$
Energy density α -phase	f_α	0
Energy density β -phase	f_β	> 0 , varying

For the simulations, a one-dimensional setup is considered in order to match the flat-interface analytical treatment. A thin layer of α -phase is applied on the left-hand side of the simulation domain by setting $\phi_\alpha = 1$, the remaining domain is filled with a β -phase by setting $\phi_\alpha = 0$ in order to ensure the same ordering as imposed in the analytics through BCs in Eqs. (4.7)-(4.8). The initial condition corresponds to a sharp interface between the two phases. In the simulations, the full partial differential equation is solved, i.e. Eq. (4.2), using a forward Euler timestepping and using second-order accurate finite differences. This means that a travelling-wave solution is not imposed from the outset. Since the initial condition

is not appearing in the travelling-wave form assumed in the previous section, one has to ensure that any initial transient building up the interface profile can be neglected. This is done by setting the runtime of the simulations significantly larger than the diffusion time ($m\gamma$ is essentially a diffusivity) in Eq. (4.2) through $t \geq 100 \varepsilon^2 / (m\gamma)$. Velocities v are computed by comparing interface locations by means of $\phi_\alpha = 0.5$ contours at an early and a late time. The interface width δ is deduced by extrapolating within the interfacial region towards the bulk to obtain locations x_\pm where $\partial\phi_\alpha/\partial x = 0$ is fulfilled. In order to exclude discretization issues as a possible source of error, a relatively fine resolution of the interface is maintained by choosing $\varepsilon/\Delta x = 32$.

The parameterization of the model is presented in Table 4.7. Interface width, energy and mobility are assigned values near but not identical to 1 in order to make sure that all nonlinearities in the parameters are correctly captured. The energy density for the alpha phase is assigned a vanishing value and the driving force Δf is controlled by varying f_β . Values of f_β are chosen in a range such that both relatively small and large dimensionless driving forces are covered, i.e. $0 < \tilde{\varepsilon} \leq 10$. The size of the domain is dynamically adjusted for each driving force to ensure that the interface is not hitting the end of the domain during runtime (a maximal interface velocity of $v = 2m\Delta f$ is assumed for that). At the end of the domain, zero-Neumann boundary conditions are applied.

4.5.2 Results

4.5.2.1 Order Parameter Profile

To check whether the derivation is able to quantify the distortion of the interface at a finite driving force, order parameter functions φ are plotted in terms of the rescaled moving coordinate at a dimensionless driving force of $\tilde{\varepsilon} = 3/4$ in Fig. 4.8. It can be seen, that independent of the choice of interpolation function, the analytical and numerical solutions are indistinguishable which corresponds to an exact match. It is stressed that although the numerical solution is a piecewise

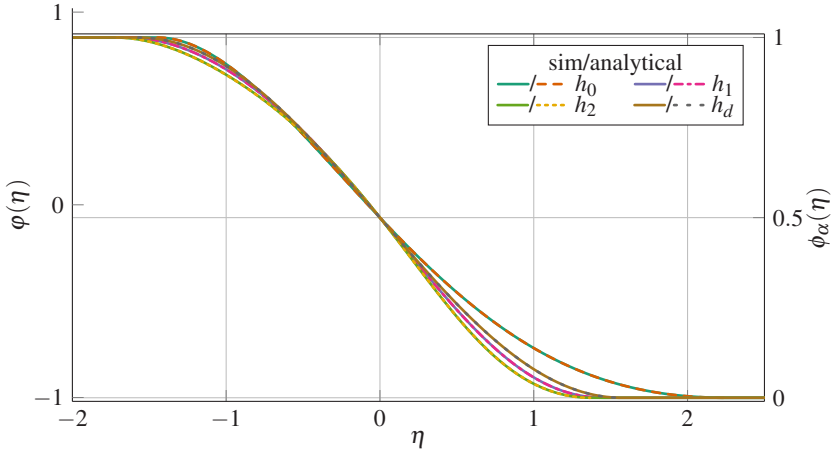


Figure 4.8: Rescaled order parameter $\varphi(\eta)$ obtained from the numerical simulation (solid lines) and the analytical treatments (dashed lines) at a dimensionless driving force of $\tilde{\varepsilon} = 3/4$ for all studied interpolation functions. Within the interfacial region, the analytical and numerical results are indistinguishable. The exact analytical solution for h_0 is shifted such that $\varphi(0) = 0$. For the interpolation functions h_1 and h_2 , Maclaurin partial sums $P_{11}(\varphi, \tilde{\varepsilon})$ are utilized in the analytical case.

function which has discontinuous second derivatives, the first derivative at the interfacial endpoints always seemingly remains continuous. This justifies the assumption needed to obtain interfacial endpoints in the analytical treatment. To make the comparison, it is important to truncate the analytical solutions at $\eta = \eta_{\pm}$, since the values of φ evaluated at $\eta > \eta_+$ or $\eta < \eta_-$ are only the analytical continuation of the interfacial profile in the bulk. For the asymptotic analytical solutions (applicable for h_1 and h_2) it is worth noting that deviations for larger dimensionless driving forces are expected, since simple Maclaurin partial sums $P_{11}(\varphi, \tilde{\varepsilon})$ are used. Although the deviation might be reduced by using Padé approximants, it is a considerable effort since the construction of the approximant has to be performed for each η . For this reason, why no further considerations have been performed at higher $\tilde{\varepsilon}$.

Instead, the scalar quantities, namely interface velocity v , interface thickness δ as well as interfacial energy σ are compared for a small and large driving-force

regime in the following. This tremendously reduces the effort while there is still provided enough information to assess differences between the analytical and the numerical results.

4.5.2.2 Interface Velocities

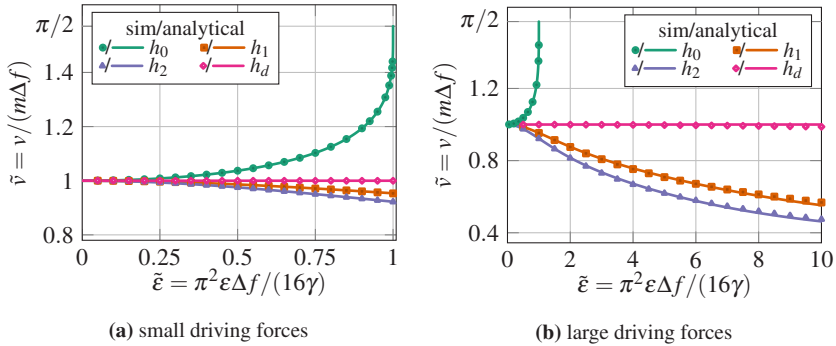


Figure 4.9: Comparison between dimensionless interface velocity obtained from the analytic treatment and numerical simulations in the small (a) and large driving-force regime (b). Solid lines correspond to the analytics, either exact (for h_0 and h_d) or in terms of Padé approximants $1/2 (P_2^2(\tilde{v}, \tilde{\epsilon}^2) + P_3^2(\tilde{v}, \tilde{\epsilon}^2))$ (for h_1 and h_2). Symbols represent the numerical solutions.

Dimensionless interface velocities corresponding to the simulation and analytics are plotted in Fig. 4.9 for both a small and large-driving-force regime, characterized by $\tilde{\epsilon} < 1$ and $\tilde{\epsilon} < 10$, respectively. In general, the match between the analytic results and the numerical simulations is remarkable. This is in particular true for the small-driving force regime. In the numerical simulations, the behavior of the interpolation function h_0 is very well reproduced. For $\tilde{\epsilon} > 1$, the simulations with h_0 showed an immediate transformation towards the α -phase, i.e. $\phi_\alpha = 1$ everywhere in the domain at the final time step. Thus, no finite interface velocity could be deduced and hence, the points are missing in the plots. This seems to reflect the non-existence of a travelling-wave solution derived earlier. For h_1 and h_2 , the numerical results show slowly decaying velocities that are significantly below

the sharp-interface limit $\tilde{v} = 1$ only for large driving forces. They also remain positive, as predicted by the analytics. The Padé approximants used to describe the analytical relation for \tilde{v} for these two choices reproduce the numerical results extremely well, except for very small deviations at large driving forces ($\tilde{\varepsilon} > 5$) that may either be rooted in the limited order of the approximant or in remaining numerical uncertainties.

The latter is likely explaining a small mismatch for h_d in the same regime which is of a similar magnitude. Here, the interface velocity in fact remains independent on $\tilde{\varepsilon}$, which is the superior feature of this interpolation function.

4.5.2.3 Interface Thickness

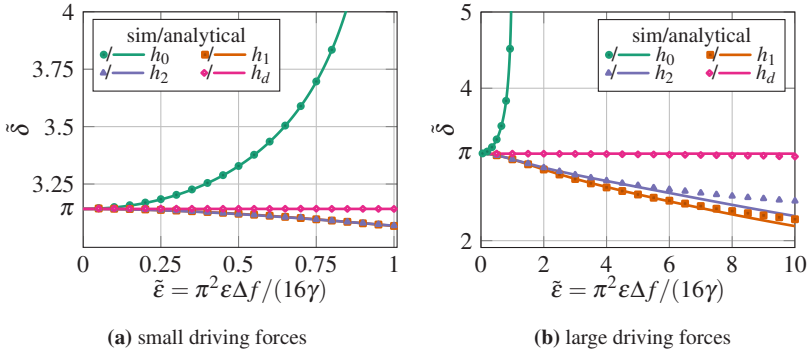


Figure 4.10: Comparison between dimensionless interface width obtained from the analytic treatment and numerical simulations in the small (a) and large driving-force regime (b). Solid lines correspond to the analytics, either exact (for h_0 and h_d) or in terms of Padé approximants $1/2 \left(P_2^2(\tilde{\delta}, \tilde{\varepsilon}^2) + P_3^2(\tilde{\delta}, \tilde{\varepsilon}^2) \right)$ (for h_1 and h_2). Symbols represent the numerical solutions.

For the interface thickness, the corresponding comparisons are shown in Fig. 4.10 in the same two driving force regimes. In general, the match is remarkable, but not as striking as for the interface velocities. While the exact solutions for h_0 and h_d can be nearly exactly reproduced, the Padé-approximated choices h_1 and h_2 show slight deviations in the large-interface regime which increase with $\tilde{\varepsilon}$.

Therefore, it is concluded that this is a remaining limitation of the limited order of the approximants. The qualitative behavior of the interface thickness function is similar as for \tilde{v} for these two cases, namely slowly decaying with increasing driving forces. However, the order is reversed, in contrast to the interface velocity (where h_1 remained closer to \tilde{v}_0), namely the deviation from the sharp-interface limit is slightly larger for h_1 for most of the interval $0 < \tilde{\epsilon} < 10$, compared to h_2 , although this is not apparent from the values of the coefficients alone. This fact highlights the counterintuitive behavior of diverging Maclaurin series and demonstrates the power of Padé approximation in unraveling the underlying functional dependence.

4.5.2.4 Interfacial Energy

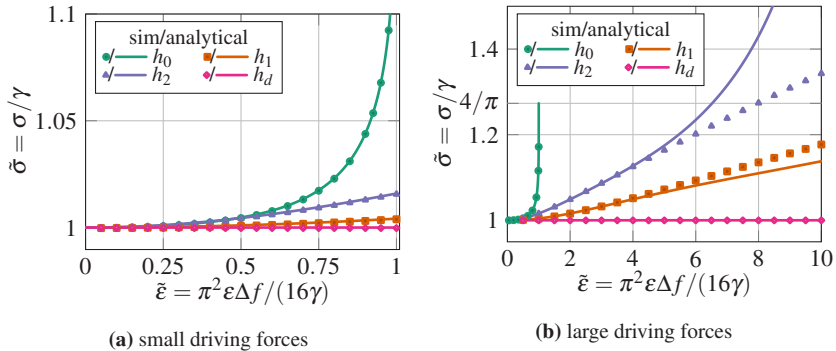


Figure 4.11: Comparison between dimensionless interfacial energies obtained from the analytic treatment and numerical simulations in the small (a) and large driving-force regime (b). Solid lines correspond to the analytics, either exact (for h_0 and h_d) or in terms of Padé approximants $1/2(P_2^2(\tilde{\sigma}, \tilde{\epsilon}^2) + P_3^2(\tilde{\sigma}, \tilde{\epsilon}^2))$ (for h_1 and h_2). Symbols represent the numerical solutions.

The comparison for the interfacial energies is presented in Fig. 4.11 which completes the numerical studies. For the small interface regime in Fig. 4.11a, an excellent match is found. In general, the interfacial energies are increasing with driving force. The deviation is negligible for h_d , and among those that deviate,

smallest for h_1 , followed by h_2 and h_0 in increasing order, respectively. Thus, the qualitative behavior is completely different from the previous two quantities. Moreover, the numerical results seem to show that the functional dependence of $\tilde{\sigma}(\tilde{\epsilon})$ for h_1 and h_2 are asymptotic to a linear function with positive slope for large driving forces (see Fig. 4.11b). The Padé approximants, which are significantly deviating from this behavior for $\tilde{\epsilon} > 5$ especially for h_2 , are seemingly not effective in approximating such a behavior very well.

4.6 Discussion

4.6.1 Origin of No-Solutions

In the analytical derivation for h_0 , it was found that travelling solutions are existing only if $|\tilde{\epsilon}| < 1$. This poses a severe limitation to the application of this interpolation function. Although the non-existence of travelling-wave solution does not necessarily imply that the partial differential equation has no solution, numerical experiments showed that at $|\tilde{\epsilon}| > 1$, a rapid transient phase transformation occurs including intractable interface widths. Accordingly, it seems important to ensure that travelling-wave solutions exist for arbitrary $|\tilde{\epsilon}|$. While a complete proof for arbitrary interpolation functions might be too involved, the following argument provides a necessary condition for the existence of travelling-wave solutions for planar interfaces.

For this, take a look at the ODE and corresponding boundary conditions given through equations (4.22)-(4.25). The trick is to evaluate the ODE at η_{\pm} by inserting the boundary conditions $\varphi(\eta_{\pm}) = \mp 1$ and $\varphi'(\eta_{\pm}) = 0$. It is somewhat surprising, but without solving the ODE for arbitrary η , one obtains the second derivative at the endpoints

$$\varphi''(\eta_{\pm}) = \pm 1 - 2\tilde{\epsilon}h'(\mp 1) \quad (4.98)$$

only in terms of the derivative of the interpolation function evaluated at the bulk values $h'(\mp 1)$ (which is a known value). Now, in order to ensure the Gibbs-constraint (Eq. (4.25)) it is important that $\varphi(\eta_-) = 1$ and $\varphi(\eta_+) = -1$ are a local maximum and minimum, respectively. Thus, since a necessary condition $\varphi'(\eta_{\pm}) = 0$ is already satisfied, additional requirements are $\varphi''(\eta_-) \leq 0$ and $\varphi''(\eta_+) \geq 0$. It follows that

$$\tilde{\epsilon} h'(-1) \leq \frac{1}{2} \quad (4.99)$$

$$\tilde{\epsilon} h'(1) \geq -\frac{1}{2} \quad (4.100)$$

have to be fulfilled. For $h'(\pm 1) = 0$, this is always fulfilled, but for non-vanishing derivatives, one obtains a restriction on $\tilde{\epsilon}$ that reads

$$-\frac{1}{2h'(1)} \leq \tilde{\epsilon} \leq \frac{1}{2h'(-1)}. \quad (4.101)$$

For h_0 , since $h'_0(\varphi) = 1/2$ this exactly yields the found restriction $|\tilde{\epsilon}| \leq 1$. This result shows that a vanishing derivative of the interpolation function at the bulk values $h'(\pm 1) = 0$ is a necessary condition for the existence of travelling wave solutions for arbitrary driving forces. As this is ensured by all interpolation functions studied herein that are different from h_0 , this is a possible explanation why they performed much superior.

Note that this condition is not restricted to interpolation functions: Any additional term that does not vanish as the bulk is approached may lead to non-existence of travelling wave solutions. In designing new models with an increasing number of terms, it is important to be aware of this result.

4.6.2 Separation of Numerical and Analytical Errors

In the comparative study, numerical and analytical solutions were found to show a good agreement. One might think that the current analytical treatment might not

reveal much interesting news, since the obtained relations could be alternatively obtained in a purely numerical study. While this is true to some extent, there are usually certain pitfalls that one has to face. One of these is related to the inaccuracies of numerical schemes. Such a phenomenon is observed for instance in the case when h_0 was used near $\tilde{\varepsilon} = 1$ and at a lower resolution Δx : The dimensionless interface velocity seemed to deviate less significantly from its expected value of 1, i.e. numerical and analytical errors canceled to some extent which would have led to a completely wrong conclusion.

Therefore, in order to study the same phenomenon numerically, it would be necessary to perform extensive grid convergence studies, largely increasing the effort to obtain useful information. More drastically, even if one performs such a costly procedure, it may occur that convergence towards the exact solution is not at all guaranteed [53, Ch. 4].

Accordingly, the current analytical results can serve as a benchmark to assess the accuracy of a given numerical scheme.

4.6.3 Remaining Challenges

In the current chapter it has been shown that higher order asymptotics are capable of extracting a considerable amount of information about the nonlinear model behavior, that is usually completely inaccessible. However, there are certain simplifications employed that helped keeping the effort to an absolute minimum. To mention the first one, a travelling wave solution was assumed, which completely removed the time derivative from the problem. This is possible, since a planar interface was studied and all quantities remained time-invariant such as the driving force. In a realistic scenario, the interface boundary is curved and may be subject to driving forces that vary with time as a complex microstructure is swept by the boundary. These effects can all be considered, as shown in the previous chapter, however, automating the procedure with a computer algebra system might not be as straightforward, as performed herein.

Nevertheless, many available asymptotic treatments such as the one presented by Choudhury and Nestler [20], are also restricted to a flat interface and do only consider thin-interface corrections. However, in contrast to the current chapter, a system of two coupled equations has been studied. In order to derive higher order corrections for such problems one has to include additional boundary conditions at the interfacial endpoints in the current framework in order to match with the outer unknowns. For the phasefield, the outer value is simply constant, but for any other field such as the composition, this is not the case, complicating the procedure accordingly.

Another point worth noting is that for certain models such as the surface diffusion model studied by the current author in Hoffrogge et al. [24] or in the previous chapter, the second order chemical potential blows up as the interfacial endpoints are approached. It is still necessary to regularize this phenomenon in order to obtain tractable limits in a possibly more involved matching procedure. Once this problem has been solved, higher order asymptotics can also be employed for such more complex models revealing nonlinear intricacies.

4.7 Conclusion and Outlook

In the current chapter, analytical solutions are presented for all common interpolation functions used in phase-field models of obstacle type for a flat-interface subject to a constant driving force. The influence of the interpolation function on the simulation results could be successfully quantified by means of the derived formulas. While exact solutions are derived only for two special interpolation functions, the general nonlinear equations are solved employing Maclaurin expansions in the interface width. The solutions are presented up to eleventh order using a computer algebra system, largely extending the common treatments that consider first-order corrections at maximum. It is shown that the interface velocity is varying with the interface thickness parameter, which is usually neglected in most of the available derivations. It could be proven that for a planar interface,

the first-order velocity vanishes if the interpolation function satisfies a certain symmetry, which applies to all common interpolation functions.

A numerical comparison is employed for both a small driving force and a large driving force regime, revealing mostly excellent agreements between the analytics and simulations. Padé approximants are established as a suitable tool to incorporate Maclaurin coefficients, improving the convergence in contrast to Taylor partial sums. By this method, the analytical results match well also in the regime far away from the sharp interface limit with only a few exceptions.

In a future work, the current framework might be applied to modern model extensions, such as the mechanical jump conditions introduced in [22], highlighting their computational advantage, although the sharp-interface limit is likely identical with more traditional formulations.

5 Nickel Coarsening in SOFC Anodes

Since all models are wrong the scientist must be alert to what is importantly wrong. It is inappropriate to be concerned about mice when there are tigers abroad.

Box [107]

The current chapter aims to provide insights into the coarsening mechanism responsible for the degradation of SOFC anodes by means of multi-phase field simulations of both artificially created and experimentally reconstructed anode microstructures. For this, the extended multiphase-field model presented in the previous chapter is utilized. Numerous simulations of nickel coarsening in Ni-YSZ SOFC anodes are performed and characteristic microstructural properties are extracted from the simulation results. After the working principle of SOFCs is briefly outlined, the analysis tools are described and validated which are used for the extraction of these microstructural properties. Subsequently, the multiphase-field simulation studies are presented. The chapter concludes with a summary of the findings.

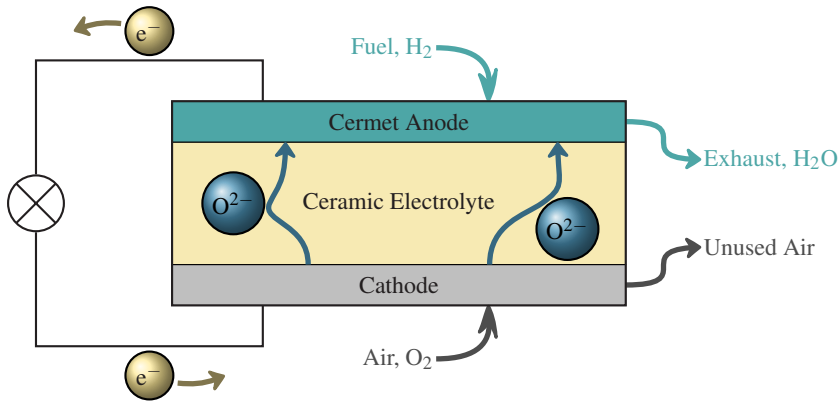


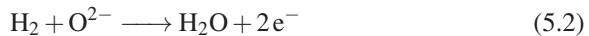
Figure 5.1: Sketch of the electrochemical processes occurring in a solid-oxide fuel cell (SOFC).

5.1 Working Principle of SOFCs

An SOF cell is schematically depicted in Fig. 5.1. In the cathode (bottom), oxygen ions are formed by the reaction of electrons with oxygen:



These oxygen ions are diffusing through the solid electrolyte and react with the fuel gas (here hydrogen) at the anode side by means of the reaction



to generate electrons and exhaust gas (here gaseous H_2O). The electrons which move back to the cathode side are used to power a load.

A microstructural view of the anode functional layer, where the fuel gas reaction takes place, is shown in Fig. 5.2. The anode layer comprises of a porous metal-ceramic compound usually made of yttria-stabilized zirconia (YSZ) as the ion conductor, nickel (Ni) as the electron conductor and pores which are used for gas transport.

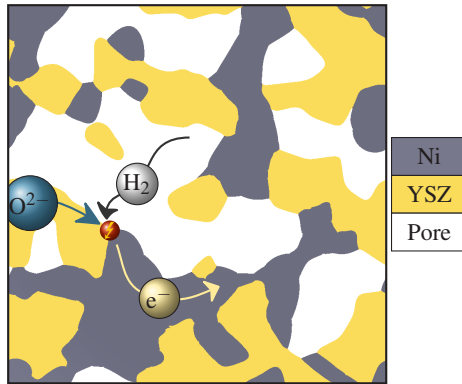


Figure 5.2: Schematic microstructural view on the transport processes occurring in the porous anode functional layer of an SOFC. Oxygen ions diffuse through the ion conducting phase (here YSZ), electrons are transported through the metallic phase (here nickel). Hydrogen and steam (not shown) are transported through the pores. The fuel-gas reaction takes place at the triple-phase boundary (ξ -symbol).

Since the fuel gas reaction in equation (5.2) involves a total of four reactants and products, the following transport processes are identified for a working SOFC anode:

1. Transport of hydrogen through the pores towards the reaction site
2. Transport of oxygen ions from the electrolyte towards the reaction site
3. Transport of steam through the pores away from the reaction site towards the outlet
4. Transport of electrons away from the reaction site to the load

Based on these transport processes, it is clear that the reaction can only take place at the triple-phase boundary where all of the three phases are in contact. As a high number of reaction sites is required for an efficient operation of the SOF cell, and since the triple-phase boundary corresponds to triple lines in three dimensions, the corresponding quantity is referred to as the triple-phase boundary length. A detailed definition of triple-phase boundary length is provided in section 5.2.2.

In addition, an efficient transport of each of the reactants and reaction products listed above is needed to achieve a good performance of the SOF cell. To quantify the transport efficiency in each of the phases, a so-called tortuosity is utilized in the current chapter. Details regarding the calculation of tortuosities are given in section 5.2.1.

5.2 Analysis Tools

5.2.1 Tortuosity Calculation

5.2.1.1 Preliminaries

Tortuosity is a quantity that can be used to assess the efficiency of transport through a certain phase or material Joos et al. [108], Joos [109]. Its name refers to the tortuous nature of transport pathways that occur in percolated microstructures. The tortuosity is calculated by measuring the electrical resistance of a certain phase in the microstructure when a voltage is applied, assuming a constant electrical conductivity within the phase.

Underlying Assumptions To derive the equation needed to solve, one begins with Maxwell's equations for electrostatics [37, Eq. (4.5),(4.6),(4.27)]

$$\nabla \cdot \mathbf{E} = \frac{q}{\epsilon_0} \quad (5.3)$$

$$\mathbf{E} = -\nabla U \quad (5.4)$$

where \mathbf{E} is the electric field in V/m, U is the electric potential in V, q denotes the charge density in C/m³ and ϵ_0 in F/m is the permittivity of free space. This equation follows from electrodynamics assuming a steady state of the electric and magnetic field ($\partial \mathbf{E} / \partial t = \mathbf{0}$ and $\partial \mathbf{B} / \partial t = \mathbf{0}$, \mathbf{B} denotes magnetic field).

Let Ω_α denote the domain occupied by phase α , then Ohm's law [110, p. 296] is assumed therein (i.e. $\forall \mathbf{x} \in \Omega_\alpha$) as constitutive relation for the electric flux density:

$$\mathbf{j}_{\text{el}} = \sigma_{\text{el}} \mathbf{E} = -\sigma_{\text{el}} \nabla U. \quad (5.5)$$

Here, σ_{el} is the electric conductivity in S/m and the last equality follows from Eq. (5.4). Assuming a constant value of σ_{el} , one obtains from the balance of electric charges (Eq. (2.33)) and a steady state assumption for the charge density ($\partial q / \partial t = 0$) that

$$\nabla^2 U = 0 \quad \forall \mathbf{x} \in \Omega_\alpha \quad (5.6)$$

has to hold. Therefore, Laplace equation is obtained in the steady state for the electrostatic potential U .

Note that, instead of starting with electrostatics, the same field equation as for U can be obtained for other transport phenomena. E.g. this Laplace equation is obtained for the velocity potential in irrotational flow, or for the concentration field assuming a constant diffusivity (cf. Eq. (2.28)). In these cases, the electric current density is replaced by momentum $\rho \mathbf{v}$ or the species flux density \mathbf{j}_i^m , respectively. The same applies to heat conduction (Fourier's law) for a constant thermal conductivity assuming a steady-state solution of the temperature field (then temperature T replaces U). Thus, the tortuosity is a general quantity characterizing transport phenomena not restricted to electric currents.

Boundary Conditions To solve the Laplace equation uniquely, boundary conditions are needed. In order to enforce a nonzero current through the structure, a voltage difference $\Delta U = 1 \text{ V}$ is applied between two opposite sides of the microstructure. This corresponds to boundary conditions $U(\mathbf{x} \in d\Omega_-) = 0$ and $U(\mathbf{x} \in d\Omega_+) = 1 \text{ V}$, where $d\Omega_\pm$ are the domain boundaries perpendicular to the d -coordinate. When the microstructure has periodic boundaries, all other flat sides of the simulation domain are treated periodically, otherwise, a vanishing

electric flux density is applied which corresponds to zero-Neumann boundary conditions

$$\nabla U \cdot \mathbf{n} = 0 \quad \forall \mathbf{x} \in d\Omega \setminus (d\Omega_- \cup d\Omega_+). \quad (5.7)$$

In addition, when a specific phase is considered, the interfaces between distinct phases are treated as isolating boundaries, i.e.

$$\nabla U \cdot \mathbf{n}_\alpha = 0 \quad \forall \mathbf{x} \in (d\Omega_\alpha \setminus (d\Omega_- \cup d\Omega_+)) \quad (5.8)$$

where \mathbf{n}_α is the normal on the surface of phase α .

Definition Once the solution to the Laplace equation (Eq. (5.6)) under the above boundary condition is known, the total electric current that enters the domain can be calculated as

$$I_{\alpha,d} \equiv - \int_{d\Omega_+} \mathbf{j}_{\text{el}} \cdot \mathbf{e}_d \, dA = - \int_{d\Omega_-} \mathbf{j}_{\text{el}} \cdot \mathbf{e}_d \, dA \quad (5.9)$$

where the equality follows from the Laplace equation in combination with the boundary condition and reflects that the currents entering and leaving the domain must equal each other. Here, the unit vector \mathbf{e}_d is the Cartesian base vector pointing towards increasing d .

Based on the calculated current, the tortuosity in direction d is then defined by the relation

$$\tau_{\alpha,d} \equiv \frac{j_{\alpha,d}^{\text{ideal}}}{I_{\alpha,d}} \quad (5.10)$$

where $I_{\alpha,d}^{\text{ideal}}$ is a current related to an ideally conducting structure. The ideally conducting structure corresponds to the case when the electric current is unidirectional due to channels of constant thickness aligned along the d -direction. In this case U is a linear function

$$U(\mathbf{x}) = U_- + \frac{(U_+ - U_-)d}{L_d} \quad (5.11)$$

and one gets for the ideal current the relation

$$I_{\alpha,d}^{\text{ideal}} = \frac{\sigma_{\text{el}} \Delta U X_{\alpha} V}{L_d^2} \quad (5.12)$$

where X_{α} is the volume fraction of phase α . L_d is the length of the domain in the d -direction and V its volume.

In the current work, tortuosities are measured in all three sample directions x , y and z . Accordingly, the mean tortuosity

$$\tau_{\alpha} \equiv \frac{1}{3} (\tau_{\alpha,x} + \tau_{\alpha,y} + \tau_{\alpha,z}) \quad (5.13)$$

is used in conjunction with the standard deviation

$$\Delta\tau_{\alpha} \equiv \sqrt{\frac{1}{3} \sum_{d \in \{x,y,z\}} (\tau_{\alpha,d} - \tau_{\alpha})^2}. \quad (5.14)$$

Subsequently, $\tau_{\alpha} \pm \Delta\tau_{\alpha}$ is shown in the form of error bars in several plots.

5.2.1.2 Validation

The tortuosity tool is implemented in the C programming language as a part of the PACE3D in-house software. It uses finite differences on an equidistant grid and solves the Laplace equation with a matrix-free conjugate-gradient (CG) method. In order to validate the solver, it is compared with the open-source finite-element software DEALII [111].

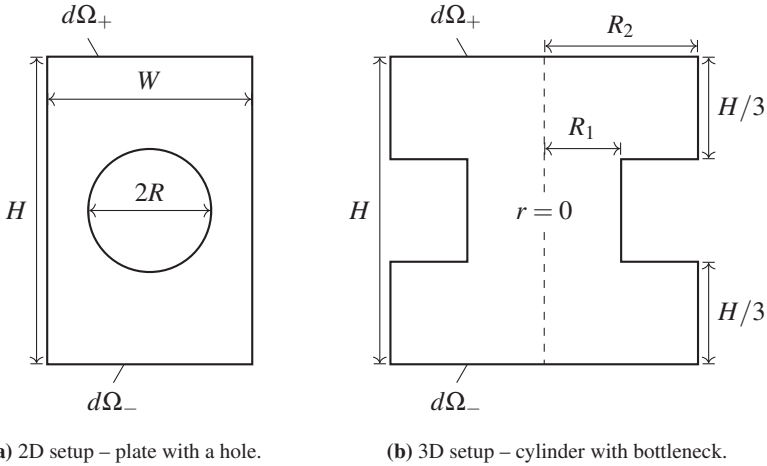


Figure 5.3: Geometries used for the validation of the tortuosity tool. Dirichlet boundary conditions are applied on the top and bottom plane ($U = 1 \forall \mathbf{x} \in d\Omega_+$ and $U = 0 \forall \mathbf{x} \in d\Omega_-$), whereas the other boundaries are treated as isolating.

Considered geometries The comparison is performed both for a two-dimensional and a three-dimensional setup (see Fig. 5.3). For the 2D setup, a plate with a hole is used, as sketched in Fig. 5.3a. Here, the ratio of the hole radius to the width of the plate $2R/W$ is varied while the ratio of height to width is kept at a constant $H/W = 3/2$. The 3D setup comprises of a cylindrical shape with a bottleneck (Fig. 5.3b). Here, the ratio of the neck radius to the outer radius R_1/R_2 is varied while the ratio of the outer radius to the height of the object is kept at $R_2/H = 1/2$. The height of upper and lower segment, as well as the height of the neck are chosen identically $H/3$.

High resolution results Results for the 2D-setup obtained by the PACE3D solver at a high resolution are shown in Fig. 5.4 for various hole radii along with the obtained tortuosities. It can be seen that the tortuosities increase from the ideal case of a plate without a hole ($R = 0$) with increasing hole radius. Due to the Neumann boundary conditions, the corresponding electric streamlines (lines

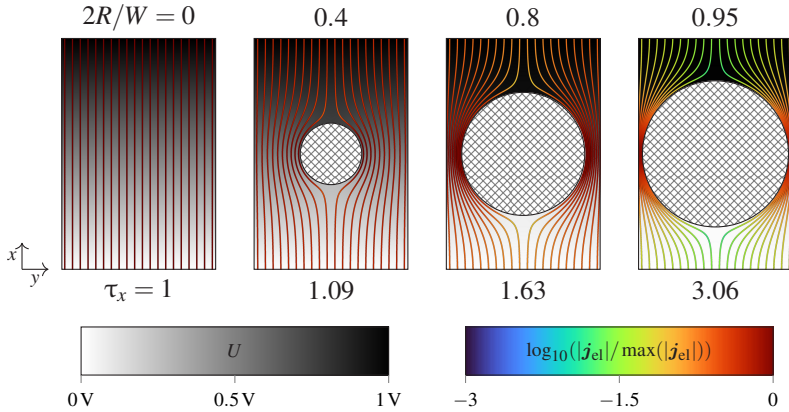


Figure 5.4: Solutions to the Laplace equation obtained by means of the in-house tortuosity solver for a plate with a hole of varying radius. The streamlines (lines parallel to \hat{j}_{e1}) are colored according to the magnitude of the current density. The electrostatic potential is additionally shown in the background in grayscale. The corresponding ratios of the radius of the hole to the width of the plate are shown above, whereas the obtained tortuosities are shown below.

parallel to \hat{j}_{e1}) are forced towards the side of the plate and thus exhibit an elongated pathlength as compared to the ideal case. Within the narrow channel at the side, the magnitude of the electric flux density assumes its maximum which can be seen from the coloring scheme. This effect is enhanced when the radius of the inner circle approaches half the width of the plate.

Results corresponding to the 3D-setup are shown in Fig. 5.5 for varying neck radii. Here, the ideal geometry corresponds to a pure cylinder, where again the value of $\tau_x = 1$ is reached. Geometries with decreasing neck diameters lead to increasing tortuosities, while the streamlines are forced towards the narrow channel in the center. Compared to the two-dimensional setup, the tortuosities are seemingly more sensitive to the variation of the neck diameter, as their magnitude is generally higher when compared with the 2D-setup.

To see whether all these results can be reproduced with the finite-element solver, the tortuosities of both solvers are plotted as a function of the hole ratio $2R/W$ and the neck ratio R_1/R_2 for the 2D and 3D-solver in Fig. 5.6a and Fig. 5.6b,

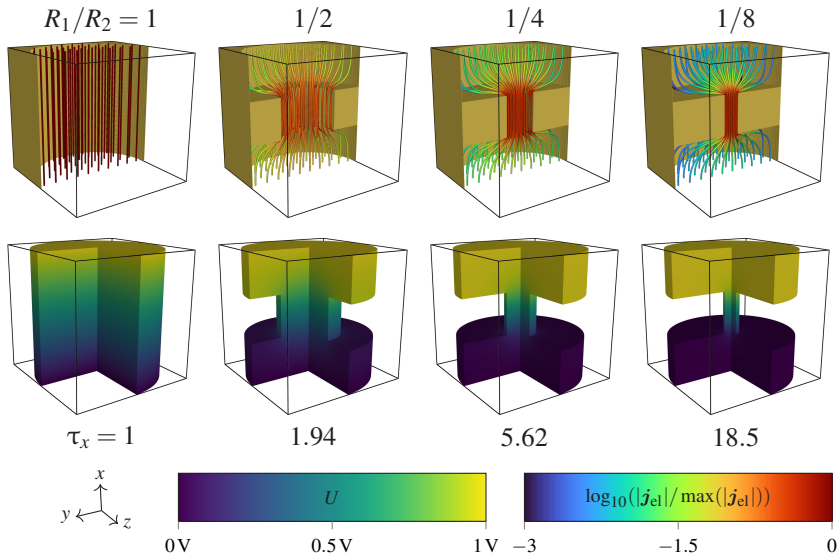


Figure 5.5: Solutions to the Laplace equation obtained by means of the in-house tortuosity solver for a cylinder with a neck. The streamlines (lines parallel to \mathbf{j}_{el}) are colored according to the magnitude of the current density. The electrostatic potential is additionally shown below. The corresponding ratios of the radius of the neck to the outer radius are shown at the top, whereas the obtained tortuosities are shown on the bottom.

respectively. It can be seen, that the match between the developed PACE3D-solver and the FEM solver is remarkably good for a wide range of possible geometries, both in 2D and 3D.

Grid Convergence The accuracy of the obtained tortuosity values depends on the resolution of the underlying grid. Fig. 5.7 shows the tortuosities obtained for three different geometries for each of the two used setups as the resolution of the grid is varied. In general, it can be seen that the DEALII-solver converges rapidly to a unique value. Therefore, the finest result (number of refinements equal 3) is used as a reference for the in-house solver and is additionally shown as a gray horizontal line. The corresponding relative errors in percent are tabulated in Table 5.1 and Table 5.2. The tortuosities obtained from the PACE3D tool with

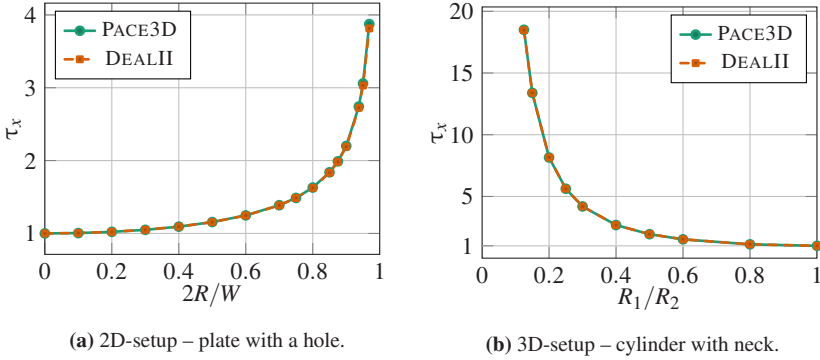


Figure 5.6: Comparison between tortuosities obtained with the developed PACE3D tool and the FEM software DEALII for two-dimensional (a) and three-dimensional (b) geometries.

Table 5.1: Relative errors $e_{\text{rel}} = (\tau_x - \tau_x^{\text{fine}}) / \tau_x^{\text{fine}}$ in percent for various refinement steps of the 2D plate at three selected hole radii. τ_x^{fine} refers to the tortuosity value obtained by the DEALII solver at the finest resolution and N_{ref} denotes the number of refinements.

e_{rel}	$2R/W$	PACE3D			DEALII		
		0.5	0.75	0.9	0.5	0.75	0.9
$N_{\text{ref}} = 0$		8.2	-0.88	∞	-0.34	-1.3	-4.4
1		4.1	1.3	-9.8	-0.090	-0.33	-1.2
2		1.5	8.2	20	-0.019	-0.069	-0.24
3		-0.31	1.0	2.6	0 (ref)	0 (ref)	0 (ref)
4		-0.18	1.1	4.2			
5		0.35	0.58	0.94			
6		0.16	0.43	1.4			
7		0.060	0.089	0.46			

equidistant grids converge to the same value, with an accuracy of less than a percent at a high resolution, but require more refinements to achieve the same level of accuracy compared with the FEM solver.

For the plate with a hole, cf. Fig. 5.7a and Table 5.1, the convergence of the values obtained with the PACE3D tool is enhanced when the hole has a relatively small

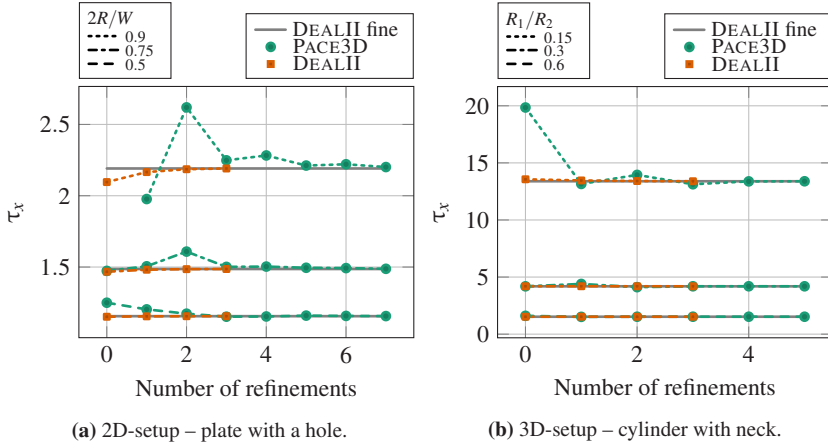


Figure 5.7: Tortuosities at different grid refinement levels for both the PACE3D tool and the FEM software DEALII for two-dimensional (a) and three-dimensional (b) geometries.

radius. A similar observation can be made for the cylindrical setup (Fig. 5.7b and Table 5.2), where high tortuosities (implying a thin neck) are less accurately recovered at coarse grids.

Table 5.2: Relative errors $e_{\text{rel}} = (\tau_x - \tau_x^{\text{fine}}) / \tau_x^{\text{fine}}$ in percent for various refinement steps of the 3D cylinder at three selected neck radii. τ_x^{fine} refers to the tortuosity value obtained by the DEALII solver at the finest resolution and N_{ref} denotes the number of refinements.

e_{rel}	R_1/R_2	PACE3D			DEALII		
		0.15	0.3	0.6	0.15	0.3	0.6
N_{ref}							
	0	48	-0.041	5.2	1.3	0.10	-0.074
	1	-1.8	5.0	-0.75	0.52	0.17	0.063
	2	4.2	-1.8	-0.030	0.16	0.070	0.034
	3	-2.0	0.063	0.14	0 (ref)	0 (ref)	0 (ref)
	4	-0.080	0.098	0.081			
	5	-0.010	0.033	-0.010			

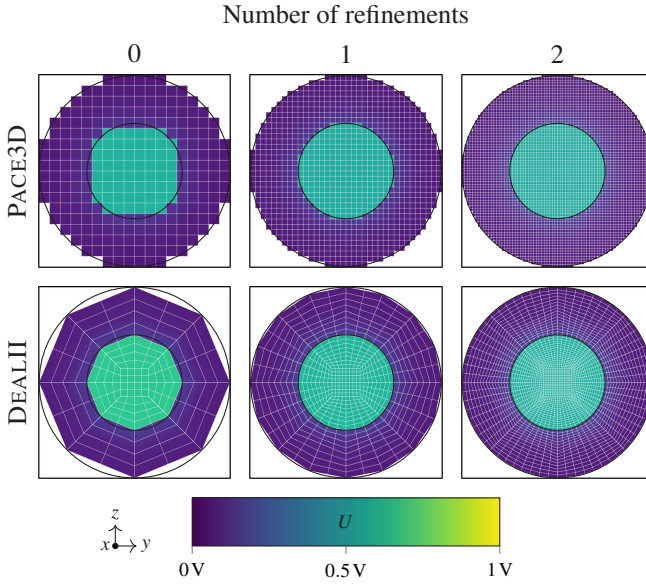


Figure 5.8: Three consecutively refined grids in a top view at $x = H/2$ of the cylinder with neck for $R_1 = R_2/2$. The top row shows the equidistant grid used in the in-house tool, whereas the bottom row shows the finite elements used in the FEM solver. Circles are additionally shown to illustrate the exact shape of the cylindrical segments.

The reason can be identified from the different shapes of the grids for each type of solver, shown in Fig. 5.8. The DEALII solver uses an irregular mesh which is capable of approximating spherical shapes more accurately at a comparatively small number of elements. In contrast, for the equidistant grid employed in the PACE3D tool, it is clear that the neck is represented only by a very low number of cells if its radius is small, which explains the behavior observed in Fig. 5.7.

While the convergence is superior for the FEM solver, the PACE3D tool can still yield accurate results. Additionally, it provides some advantages over the FEM solver. In this regard, the practical experiments show that the in-house solver is computationally advantageous since the usage of the equidistant grid and the finite-difference implementation requires less sophisticated algorithms compared to the finite-element method. In addition, the complex meshes used by

the DEALII-software are not as easily constructed for complex microstructures. In contrast, the PACE3D tool is tailored for voxel data which is widely available both from microscopy or the multiphase-field method. For this reason, the PACE3D tool is used for all the following studies.

5.2.2 Triplephase-Boundary Detection

5.2.2.1 Preliminaries

Voxel datasets are commonly available from microscopy or the multiphase-field method such that each voxel is mapped to a certain phase or material. One can identify voxels based on their neighboring cells when at least three different phases are present in the neighborhood. The obtained subset of voxels still represents a volumetric region belonging to the vicinity of the triple-phase boundary. The current subsection describes the tool developed within the PACE3D framework to convert this volumetric information into a network of curved line segments which enables an accurate determination of triple-phase boundary lengths¹.

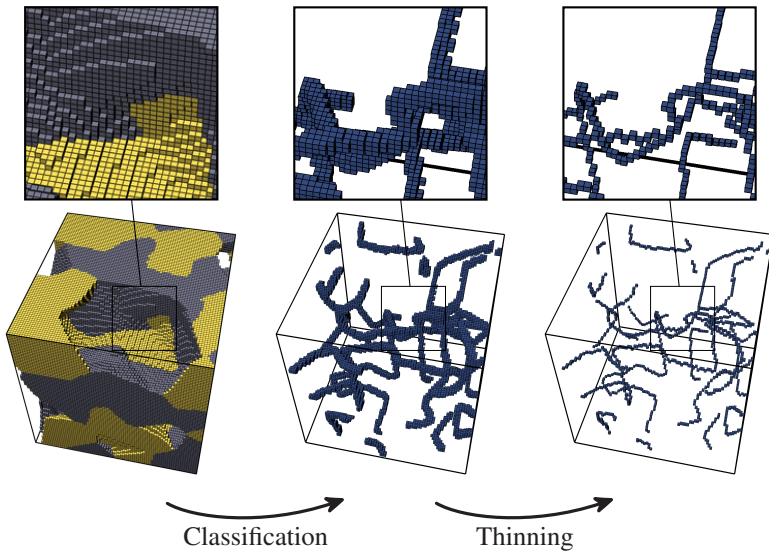


Figure 5.9: Skeletonization procedure for the detection of the triplephase-boundary for a three-phase system (each phase different color, one phase is shown transparent). Triple-junction voxels are first extracted to channels of a non-vanishing thickness (left to center) and then thinned (center to right).

5.2.2.2 Developed Algorithm

Listing 5.1: Algorithm for the detection of the triple-phase boundary network.

```
foreach voxel in dataset do  
    number = the number of distinct phases within the  $3 \times 3 \times 3$  neighborhood  
    result[voxel] = 1 if number  $\geq$  3 else 0  
end  
skeleton = Skeletonization according to [113] on result  
Create graph with node positions corresponding to the centers all active voxels in  
    skeleton.  
Establish edges between the nodes in graph by subsequently:  
    1. Connecting nodes via voxel faces.  
    2. Connecting nodes via voxel edges if no connection via at most two edges exists.  
    3. Connecting nodes via voxel vertices if no connection via three edges exists.  
Perform a smoothing of graph according to Eq. (5.15) for several iterations.  
Remove spurious short loops and end segments in graph
```

The developed algorithm for the triple-phase boundary detection is listed in Listing 5.1. The first step is the classification of voxels through a neighborhood test. An example dataset comprising of three phases is shown in Fig. 5.9.

After the classification step, interconnected channels of a thickness of several voxels remain. In order to avoid spurious contributions from the nonzero thickness, it is necessary to reduce the thickness of these channels. In the field of image processing, such a procedure is known as *skeletonization* and efficient algorithms exist. For the current work, the algorithm according to Palàgyi and Kuba [113] is selected and implemented within the in-house software toolchain. This algorithm ensures that the topology (i.e. interconnectivity of the line segments) remains conserved. For the example dataset, the corresponding skeleton is shown on the right-hand side of Fig. 5.9.

¹ Alternative methods that directly work on the voxel data exist, see for instance [112]. The current algorithm, which is suitable for an arbitrary number of phases, might be extended with a modified version of such methods in the future as well.

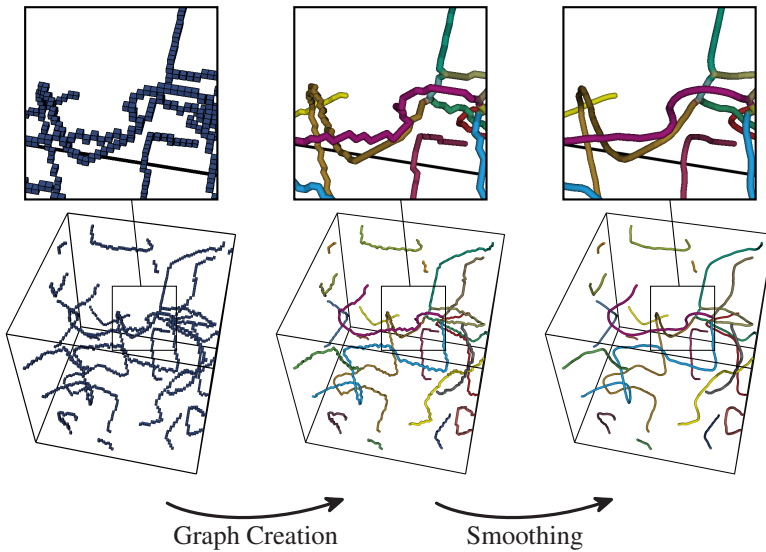


Figure 5.10: Conversion of the thinned voxel skeleton to curved line segments within the three-phase boundary detection algorithm. Firstly, the voxel centers are connected by straight lines (left to center) and then smoothed by the prescription given in Eq. (5.15).

In the next step, an undirected graph is constructed by connecting the voxel centers of neighboring voxels with straight lines. The construction proceeds as follows: First, lines are drawn between voxels that are connected via faces. Afterwards, connections via edges are established if the two voxels are not yet connected via two faces. Thirdly, vertex-connected cells are directly connected if a connection is not yet existing via at max three straight segments. Additionally, artifacts such as short line segments and short loops can be detected and are accordingly removed.

The resulting line network includes individual segments that can be distinguished and separately colored. For the example dataset, such a resulting line network is depicted in the center of Fig. 5.10.

While this is already close to the initial goal, a zoomed inset reveals a spurious roughness of the graph which originates from the finite grid spacing. It is clear

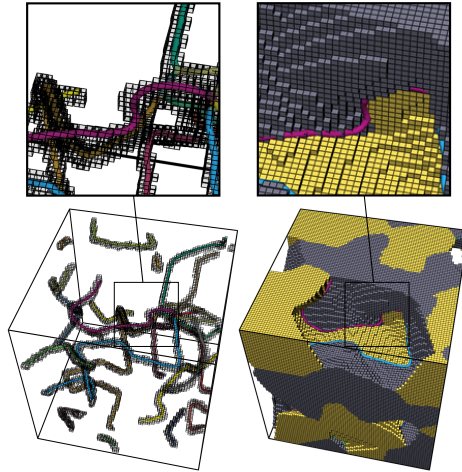


Figure 5.11: Overlay of the initial classified channels with the detected and smoothed TPB (left). Input raw data with one phase removed and the corresponding smoothed TPB network (right).

that this overestimates the length of the graph and the length becomes sensitive to the resolution (i.e. finer grids may lead to a pronounced roughness and thus to a significant overestimation of the line length).

Therefore, an additional smoothing step is performed, where the vertices of the lines are moved towards their center of curvature. The direction (unit vector \mathbf{n} , pointing towards the center of curvature) and magnitude of curvature κ are approximated from three consecutive line vertices. The smoothing operation at each iteration can be expressed as

$$\mathbf{x}_{i+1} = \mathbf{x}_i + a\kappa^2\mathbf{n} \quad (5.15)$$

where \mathbf{x}_i denotes the position of a curve vertex at the i 'th smoothing step and the factor κ^2 is chosen such that highly curved regions are more strongly smoothed compared to nearly straight segments. a is a user-defined smoothing factor which can be used to control the amount of smoothing together with the number of iterations. Vertices belonging to segment joints are kept unchanged during the

smoothing step. For the example dataset, the resulting smoothed graph is shown on the right-hand side of Fig. 5.10.

The final line network for the example dataset is shown in conjunction with the input voxel data in Fig. 5.11. It can be seen that the resulting network approximates the three-phase boundary quite well since it remains within the initially classified channels (left-hand side of this figure).

5.2.3 Particle Size Distributions

5.2.3.1 Preliminaries

For the quantification of nickel coarsening, a particle size distribution is to be determined from the microstructure. However, a typical structure does not comprise solely of disconnected individual particles but rather an interconnected network of particles of varying sizes. Thus, the determination of a classical particle size distribution is not easily possible. Münch and Holzer [114] presented an algorithm which delivers a well-defined particle size distribution even for network-like or porous structures. This algorithm is based on Euclidean distance transforms, similar as the method proposed by Ender [115, p.98]. In contrast to the latter alternate, it avoids a user-defined threshold radius, and is thus more easily reproducible and directly provides a continuously varying particle size distribution. Due to these advantages, this algorithm is selected for implementation within the PACE3D toolchain. The algorithm is briefly described in the following.

5.2.3.2 Definition

The working principle of the algorithm to determine the continuous particle-size distribution (PSD) is schematically shown in Fig. 5.12. The domain corresponding to a certain phase is filled with overlapping spheres of a particular radius r . It is observed that only a subvolume $V_{\alpha}^{\text{fill}}(r)$ corresponding to the union of all such spheres can be filled. This procedure is repeated by increasing the radius until

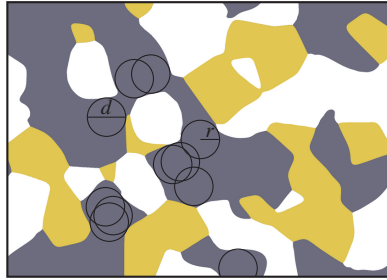


Figure 5.12: Schematic highlighting the determination of the continuous particle-size distribution by means of overlapping spheres of a certain radius r or diameter d . Each phase is shown with a different color. The phase under consideration corresponds to a shade of gray.

eventually no sphere can be placed within the domain without touching the phase boundary. This radius may be denoted as r_{\max} . The continuous PSD is defined as the ratio of the filled volume divided by the total volume of the phase:

$$\text{PSD}_{\alpha}(r) \equiv \frac{V_{\alpha}^{\text{fill}}(r)}{V_{\alpha}} \quad (5.16)$$

For a vanishing radius, all fine features can be filled and hence $\text{PSD}_{\alpha}(0) = 1$. The maximal feature size is reached when $\text{PSD}_{\alpha}(r_{\max}) = 0$. It is usually suitable to define a mean particle radius r_{50} or diameter d_{50} by demanding that $\text{PSD}_{\alpha}(r_{50}) = 1/2$ and $d_{50} = 2r_{50}$.

5.2.3.3 Validation

The continuous PSD algorithm has been implemented in the PACE3D toolchain making use of the Euclidean distance transform algorithm according to Saito and Toriwaki [116]. The Euclidean distance transform implementation has been extended for periodic boundary conditions and is validated by comparing it with the Matlab[®] function *bwdist*.

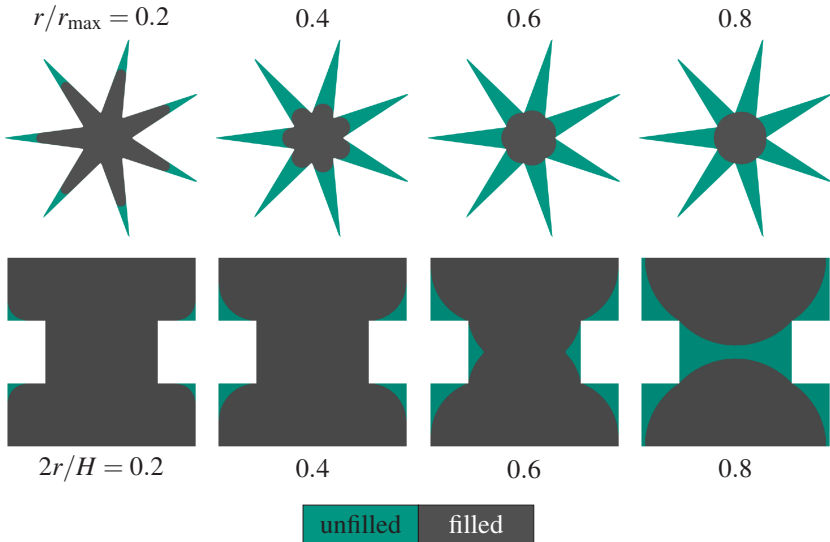


Figure 5.13: Filled volumes detected during the PSD calculation for a 2D and 3D geometry at varying radii. The top row shows the two-dimensional star-like shape from [114]. The bottom row shows axial cross sections of the cylinder with neck at $R_1/R_2 = 0.6$.

In addition to the underlying distance transforms, the validation of the PSD calculation requires well-defined geometries as no reference implementation is available. In the following, two example geometries are considered: A star-like shape which was presented in graphical form in the original paper of Münch and Holzer [114] in conjunction with a plot of the corresponding continuous PSD. Secondly, simple geometrical arguments are given to derive an analytical equation for the continuous PSD of a cylinder with neck (already presented in subsection 5.2.1). The derivation is outlined in Appendix A.2.

Fig. 5.13 shows the filled volumes obtained by the implemented tool for both the 2D and 3D geometries as the radius is varied. It can be seen that the numerical calculations can very well reproduce the expected circular or spherical segments and a decrease of the filled volume with an increase of the radius.

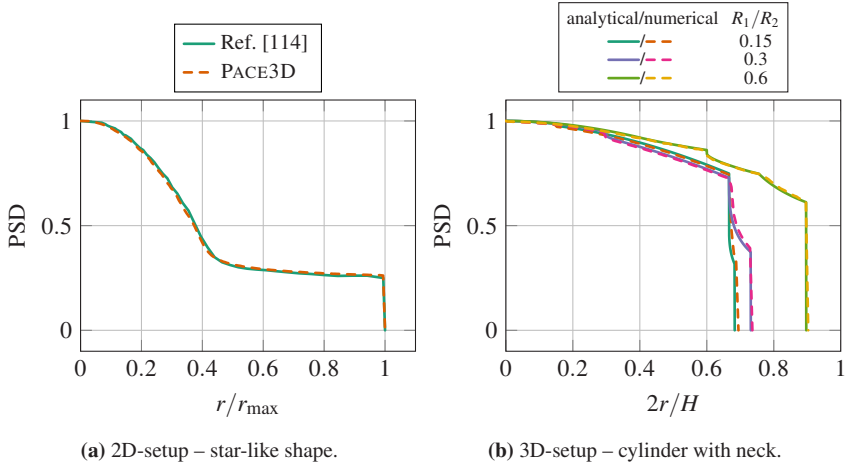


Figure 5.14: Plots of the continuous particle-size distribution for well-defined 2D and 3D geometries. PSDs calculated in [114] and by the PACE3D implementation are shown for the star-like shape in (a). Numerical calculations of PSDs for cylinder with necks of varying radii are shown in (b) in conjunction with the analytic equations derived (Eqs. (A.25)- (A.33)).

Fig. 5.14 compares the corresponding obtained PSD functions of the PACE3D tool and the literature as well as the analytical derivations according to Eqs. (A.25)- (A.33) for a number of neck radii. It can be seen that the match is overall very good. The remaining differences in Fig. 5.14b are due to discretization errors. In summary, very good agreement is found in both example cases and thus the PSD tool is successfully validated.

5.3 Simulation Studies

In the following, simulation studies employing the developed multiphase-field model (Section 3.1) are presented. This section contains two parts: First, a large number of simulations are performed using Voronoi-type artificially generated AFL microstructures as initial condition (Section 5.3.2). Here, the influence of a variation in the YSZ microstructure and a modification of nickel content is

analyzed. This study includes statistical analysis regarding correlations between the input parameters and microstructural properties.

An additional study is conducted using an experimental FIB-SEM reconstructed microstructure as reference for analyzing the influence of an increase in nickel content (Section 5.3.3). Differences and similarities between the results from the Voronoi structures and the experimentally-based structures are discussed.

Furthermore, the relation of the simulation results to the anode performance and degradation is established based on an existing transmission-line model in section 5.4.

5.3.1 Model Setup

For the modeling of nickel coarsening in the AFL, the model as described in Section 3.1 is employed. Three distinct order parameters ($N = 3$) are utilized $\phi = \{\phi_{\text{Ni}}, \phi_{\text{YSZ}}, \phi_{\text{Pore}}\}$ to distinguish between the metallic nickel phase, the zirconia structure and the voids. Two composition variables c_{Ni} and c_{YSZ} implying $K = 3$ are introduced to allow the species transport of each substance. Nickel redistribution is assumed to be governed by diffusion along its surface only, hence its evolution can be written as

$$\frac{\partial c_{\text{Ni}}(\mathbf{x}, t)}{\partial t} = \nabla \cdot \left(\frac{32M_{\text{Ni}}^{\text{NiPore}}}{\pi^2 \varepsilon} \phi_{\text{Ni}} \phi_{\text{Pore}} \nabla \mu_{\text{Ni}} \right) \quad (5.17)$$

and the YSZ is assumed invariant

$$\frac{\partial c_{\text{YSZ}}(\mathbf{x}, t)}{\partial t} = 0. \quad (5.18)$$

which is motivated from experiments [117, 118].

According to equation (5.17), the nickel flux density is given by

$$\mathbf{j}_{\text{Ni}} = - \frac{32M_{\text{Ni}}^{\text{NiPore}}}{\pi^2 \varepsilon} \phi_{\text{Ni}} \phi_{\text{Pore}} \nabla \mu_{\text{Ni}} \quad (5.19)$$

which corresponds to the choice of

$$g_{\text{NiPore}}(\phi) = \frac{32}{\pi^2} \phi_{\text{Ni}} \phi_{\text{Pore}} \quad (5.20)$$

in Eq. (3.10) with prefactor $\bar{M} = M_{\text{Ni}}^{\text{NiPore}}$. Taking the results from Table 3.1, one finds that for this specific choice, $I_g = 1$ is obtained. Therefore, the rate constant for surface diffusion of the nickel surface B is given according to Eq. 3.113 as

$$B = \frac{M_{\text{Ni}}^{\text{NiPore}} \gamma_{\text{NiPore}}}{\left(c_{\text{Ni,eq}}^{\text{Ni}} - c_{\text{Ni,eq}}^{\text{Pore}}\right)^2}, \quad (5.21)$$

where $c_{\text{Ni,eq}}^{\text{Ni}}$ and $c_{\text{Ni,eq}}^{\text{Pore}}$ denote the model-specific Ni-equilibrium compositions of the nickel and the pore phase, respectively.

In order to capture the correct real-life microstructural kinetics, it is crucial to equate this rate constant to the one measured in experiments. In this regard, Eq. (2.85) is recalled here

$$B = \frac{V_m D_s \delta_s \gamma}{RT} \quad (5.22)$$

including the physical interface thickness $\delta_s \equiv V_m \rho_s$.

Therefore, the calibration of the model yields the chemical mobility prefactor

$$M_{\text{Ni}}^{\text{NiPore}} = \frac{V_m D_s \delta_s \left(c_{\text{Ni,eq}}^{\text{Ni}} - c_{\text{Ni,eq}}^{\text{Pore}}\right)^2}{RT} \quad (5.23)$$

in terms of measurable quantities. This is the relation provided in Hoffrogge et al. [119, Eq. (13)]. Please note, that $\gamma = \gamma_{\text{NiPore}}$ is needed for this equation to hold. Therefore, it is important to set the model parameter γ_{NiPore} equal to that of the surface energy of nickel.

The free-energy densities for each phase α are assumed as simple parabolas of the form:

$$f_\alpha(c_{\text{Ni}}^\alpha, c_{\text{YSZ}}^\alpha) = A_{\text{Ni}} \left(c_{\text{Ni}}^\alpha - c_{\text{Ni,eq}}^\alpha \right)^2 + A_{\text{YSZ}} \left(c_{\text{YSZ}}^\alpha - c_{\text{YSZ,eq}}^\alpha \right)^2. \quad (5.24)$$

Here, the equilibrium compositions $c_{i,\text{eq}}^\alpha$ are so chosen such that the composition is relatively high when α corresponds to the component i and low when the opposite is true. The following values are chosen: $c_{i \neq \alpha}^\alpha = 0.1$ and $c_{i=\alpha}^\alpha = 0.9$ where $i \in \{\text{Ni}, \text{YSZ}\}$ and $\alpha \in \{\text{Ni}, \text{YSZ}, \text{Pore}\}$. By this one achieves a clear separation of the phases and an overall sufficient volume conservation of each phase given sufficiently large prefactors A_i .

All simulations are performed at a temperature of $T = 750^\circ\text{C}$ and the molar volume of nickel is $V_m = 6.59 \times 10^{-6} \text{ m}^3/\text{mol}$. The surface diffusivity is taken from recent measurements obtained by means of grain-boundary grooving experiments [120, 121] at the same temperature. Since the surface diffusivity varied strongly depending on the orientation of the surface, it is assumed that the isotropic value D_s inherent to the current model corresponds to the surface orientation with the lowest diffusivity. This is considered reasonable because first of all, the slow $\{100\}$ -surfaces occupy a significant portion of the surface in the equilibrium crystal shape (also known as Wulff shape) [122, 123]. Furthermore, in order for an overall change in morphology, diffusion needs to occur along all surfaces concomitantly. Hence it is expected that these surface are the rate-limiting factor. Therefore, the four values in [120, Figure S3.2] near $\{100\}$ -surfaces are collected to obtain an average of $D_s \delta_s = 3.75 \times 10^{-22} \text{ m}^3/\text{s}$. Accordingly, one obtains

$$M_{\text{Ni}}^{\text{NiPore}} = 1.86 \times 10^{-31} \text{ m}^6/(\text{J s}). \quad (5.25)$$

This finalizes the calibration of the surface-diffusion kinetics of the model.

5.3.2 Voronoi Structures

5.3.2.1 Simulation Setup

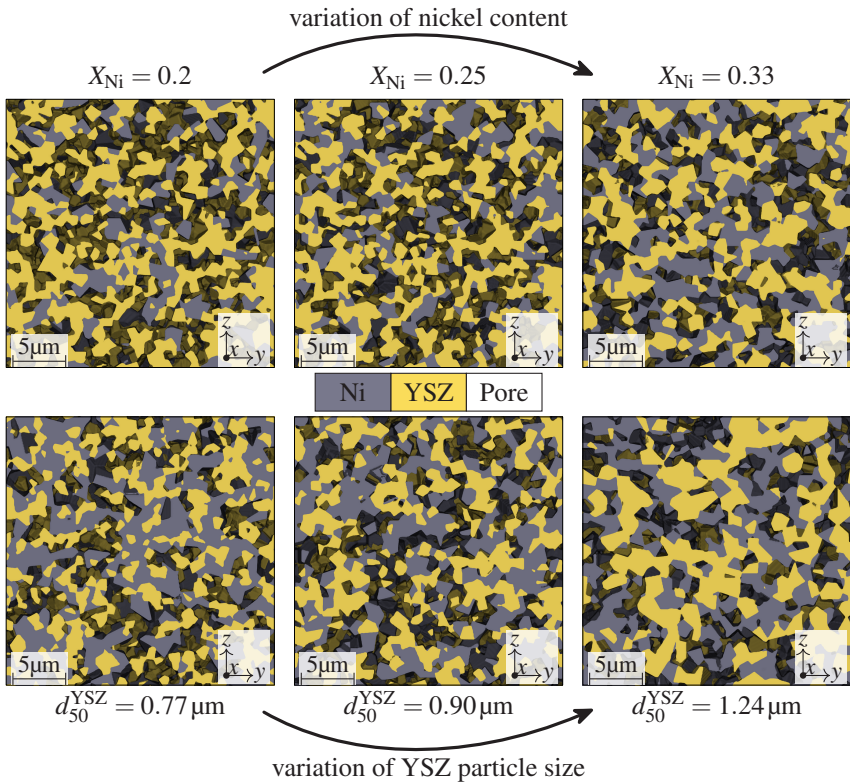


Figure 5.15: Two-dimensional cross-sections of the Voronoi-constructed anode structures. The top row highlights a variation in nickel content and the bottom row illustrates a variation in the mean particle size of the YSZ network at constant $X_{Ni} = 33\%$.

For a systematic study of a variation in the microstructural properties, artificial three-dimensional structures have been generated based on the well-known

Voronoi method². The spatial discretization corresponds to an equidistant Cartesian grid. The height, width and depth of the structure are chosen all equal to 25 μm and the resolution of the structure is equally $400 \times 400 \times 400$ grid cells. The structures are periodic with respect to all three spatial directions and periodic boundary conditions are also enforced for all solution variables during the simulations.

As a first step, a YSZ skeleton is constructed to decompose the whole domain into YSZ and non-YSZ by a single Voronoi diagram. Here, the ratio of the number of cells assigned to YSZ is set according to the desired volume fraction of YSZ. The total number of seeds has been varied by which a modification of the YSZ particle size can be accomplished. In a next step, Voronoi seeds are placed into the domain corresponding to non-YSZ and distributed among the nickel and pore phase according to their predefined volume fractions. Here, the total number of seeds is manipulated until a desired initial particle size d_{50} of nickel is reached. To study the influence of the YSZ particle size independently, this particle size is held constant among the various structures corresponding to a certain volume fraction of nickel.

Volume fractions of nickel of $X_{\text{Ni}} = 0.2$, $X_{\text{Ni}} = 0.25$ and $X_{\text{Ni}} = 0.33$ have been considered and a set of six different YSZ particle sizes are generated for each case. This results in a total number of eighteen different structures. The volume fraction of the pore phase is maintained equal to that of the YSZ phase for each structure. Periodic boundary conditions are chosen to minimize the influence of the finite size of the simulation domain. Cross-sections of a subset of the initial structures are shown in Fig. 5.15.

An analysis of the structure yields PSDs of the initial state shown exemplarily in Fig. 5.16 for $X_{\text{Ni}} = 0.33$. It can be seen in Fig. 5.16a that although the nickel particles are completely randomly placed and their locations are not identical among the structures with varying YSZ particle sizes, their initial continuous

² Generation of the structures and performing of the corresponding simulations was done in a Master's thesis by Fengcheng Cai [124], conceptualized and supervised by the current author.

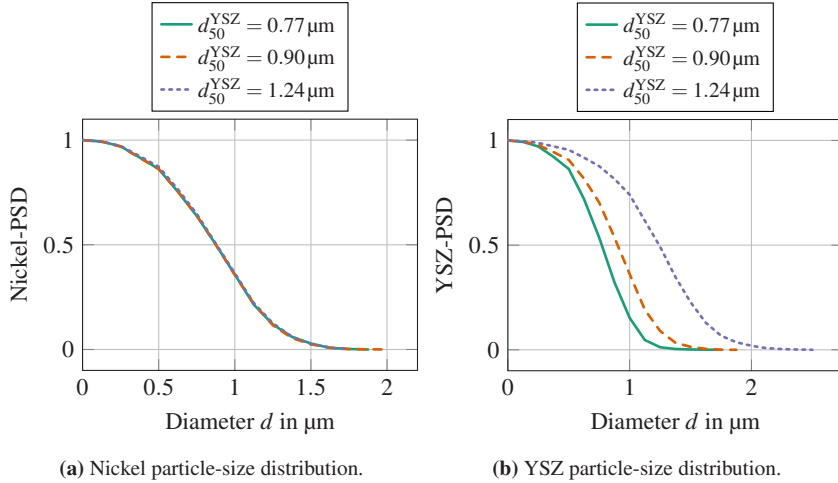


Figure 5.16: Initial particle size distributions of Voronoi-based structures at a variation of YSZ particle diameter and at constant $X_{\text{Ni}} = 33\%$. The continuous PSD of the nickel phase is shown in (a) which shows negligible changes. The change in mean YSZ diameter is reflected in a clear shift of the corresponding PSD (b).

PSDs are indistinguishable. This shows that the mean particle size of nickel could successfully be held constant. In addition, the similarity of the PSDs implies that differences in the coarsening evolution observed in the simulations can reasonably be attributed to the difference in YSZ particle size. In contrast to the PSD of nickel, the corresponding YSZ particle size distributions shown in Fig. 5.16b are shifted towards larger particle sizes, as desired.

5.3.2.2 Model Parameters

The utilized model parameters are tabulated in Table 5.3. All model parameters are expressed in a model unit system. Here u_l denotes the unit of length, u_E the unit of energy and u_t the time unit. The length unit is set by the resolution of $\Delta x = 62.5 \text{ nm}$. As already mentioned earlier, the mobility parameter $M_{\text{Ni}}^{\text{NiPore}}$ is set in order to capture the measured surface diffusivity. The surface energy of nickel is set to $\gamma_{\text{NiPore}} = 2.29 \text{ J/m}^2$ according to [125, Fig. 1. (a)]. All other

Table 5.3: Parameter set utilized for the MPF simulations based on the artificially constructed Voronoi AFL-microstructures. The model unit system is given by $u_E = 8.95 \times 10^{-15}$ J, $u_t = 3.58$ s and $u_l = 62.5$ nm.

Parameter	Symbol	Value (model units)	Value (SI units)
Ni-surface chem. mobility	$M_{\text{Ni}}^{\text{NiPore}}$	$0.1 u_l^6 / (u_E u_t)$	$1.86 \times 10^{-31} \frac{\text{m}^6}{\text{J s}}$
Interfacial energy Ni-Pore	γ_{NiPore}	$1.0 u_E / u_l^2$	$2.29 \frac{\text{J}}{\text{m}^2}$
Interfacial energy Ni-YSZ	γ_{NiYSZ}	$1.0 u_E / u_l^2$	$2.29 \frac{\text{J}}{\text{m}^2}$
Interfacial energy Pore-YSZ	γ_{PoreYSZ}	$1.0 u_E / u_l^2$	$2.29 \frac{\text{J}}{\text{m}^2}$
Interface mobility Ni-Pore	m_{NiPore}	$0.1 u_l^4 / (u_E u_t)$	$4.76 \times 10^{-17} \frac{\text{m}^4}{\text{J s}}$
Interface mobility Ni-YSZ	m_{NiYSZ}	$0.1 u_l^4 / (u_E u_t)$	$4.76 \times 10^{-17} \frac{\text{m}^4}{\text{J s}}$
Interface mobility Pore-YSZ	m_{PoreYSZ}	$0.1 u_l^4 / (u_E u_t)$	$4.76 \times 10^{-17} \frac{\text{m}^4}{\text{J s}}$
Interface width parameter	ε	$2.0 u_l$	125 nm
Grid spacing	$\Delta x = \Delta y = \Delta z$	$1.0 u_l$	62.5 nm
Thermodynamic pref. Nickel	A_{Ni}	$5 u_E / u_l^3$	$1.83 \times 10^8 \frac{\text{J}}{\text{m}^3}$
Thermodynamic pref. YSZ	A_{YSZ}	$50 u_E / u_l^3$	$1.83 \times 10^9 \frac{\text{J}}{\text{m}^3}$

interfacial energies are set to the same value, which means that a 90° wetting angle is assumed between the YSZ substrate and the nickel particles. This choice may underestimate the coarsening kinetics compared to realistic wetting angles in Ni-YSZ anodes [119]. However, since the evolution of the triple-phase boundary length was found to be invariant under a change in wetting angle, the following simulations still provide reasonably valid outcomes. The only quantities which are significantly changed by a modified wetting angle is the tortuosity τ_{Ni} and the active fraction of TPB length. Since the current study focuses on a mutually comparison of different microstructures, it is thought that although the quantitative outcome might be modified under a slight change in wetting angle, the relative influence of the microstructure properties remains mostly unchanged.

The mobilities $m_{\alpha\beta}$ are not governing significantly the simulation but are chosen in such a way that attachment kinetics is subdominant and to avoid any pinning effects. The characteristic length for attachment kinetics can be computed from Eq. (2.93). For the current parameter set, one obtains $B = 0.15625 u_l^4 / u_t$ according to Eq. (5.21) and taking m_{NiPore} into account $l_c = 1.25 u_l$ holds. Since this value is much smaller than the interface thickness $\pi^2 \varepsilon / 4 \approx 5 u_l$, the length scale

where attachment kinetics are relevant is not resolved in the current simulation. Therefore, the simulations are performed near infinite attachment kinetics which means that surface diffusion is the sole mechanism driving nickel coarsening. This implies $|v_n| \ll |m_{\alpha\beta} \kappa \gamma|$ which inserted into Eq. (3.98) results in

$$|\Delta f| \ll |\gamma_{\alpha\beta} \kappa| \quad (5.26)$$

where $\Delta f \equiv \psi_\beta - \psi_\alpha - \gamma_{\alpha\beta} \kappa$ is the total driving force acting on the interface.

The interpolation function is chosen as $h_\alpha = \phi_\alpha$. Based on the insights from the previous chapter, it is important to ensure that one operates near the sharp-interface limit by $|\tilde{\epsilon}| \ll 1$. To see that this follows from the relation in Eq. (5.26), one has to insert it into the definition for the dimensionless driving force. This yields

$$|\tilde{\epsilon}| = \frac{\pi^2 \epsilon |\Delta f|}{16 \gamma} \ll \frac{\pi^2}{16} \epsilon \kappa \quad (5.27)$$

Writing this in terms of the interfacial thickness $\delta = \pi^2 \epsilon / 4$ of the equilibrium sinusoidal profile, and estimating a maximal mean curvature by a sphere of radius R as $|\kappa_{\max}| = 2/R$, one obtains

$$|\tilde{\epsilon}| \ll \frac{\delta}{2R}. \quad (5.28)$$

In order to resolve a particle properly, it is demanded that $R > \delta/2$ and hence one obtains

$$|\tilde{\epsilon}| \ll 1 \quad (5.29)$$

as the sought relation which guarantees small driving forces. This is only an estimate assuming that the curvature driving force is included through h_α . For a more rigorous derivation, one has to solve the higher order corrections of the phase-field profile including curvature terms. In this regard, the interested reader is referred to Hoffrogge et al. [24, Sec. 2.G].

5.3.2.3 Results and Discussion

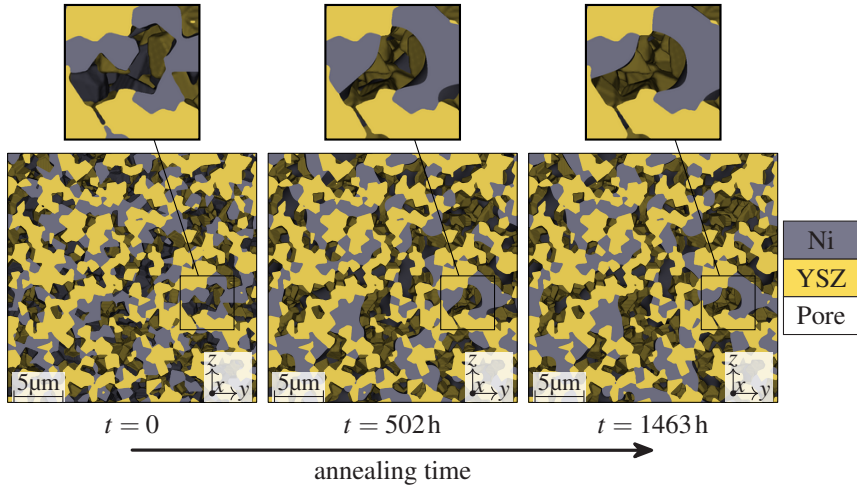


Figure 5.17: Two-dimensional cross-section of the evolution of the microstructure at $X_{\text{Ni}} = 25\%$ and $d_{50}^{\text{YSZ}} = 0.92\mu\text{m}$.

Microstructure Evolution A typical evolution of the anode microstructure is shown in Fig. 5.17. It can be seen that the nickel particles, which initially are dominated by planar faces due to the Voronoi tessellation, agglomerate quickly by forming smooth surfaces. The microstructural evolution seems to occur predominantly at early times less than 500h of annealing at $T = 750^\circ\text{C}$. During the simulated annealing, the YSZ structure remains invariant. In some areas the nickel particles are encapsulated by the YSZ network which poses a constraint on their further evolution. It is clear that this is rooted in the fact that self-diffusion of nickel is limited along the free nickel surface in the model. Thus, the first visual impressions suggest that the nickel particle evolution is strongly influenced by the characteristics of the YSZ phase.

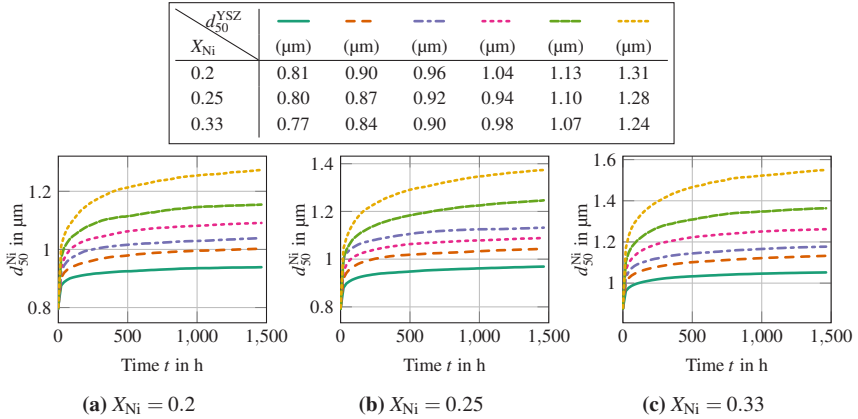


Figure 5.18: Evolution of the mean nickel diameter with time for MPF simulations of artificially generated SOFC-anode structures at three different nickel content of 20 % (a), 25 % (b) and 33 % (c). For each nickel content, six different simulations are shown where the mean YSZ particle diameter increases from --- to --- .

Particle-size Evolution To test this hypothesis, quantitative analysis by means of the continuous PSD of the nickel phase is conducted to derive the evolution of the mean nickel diameter shown in Fig. 5.18. Here, simulations corresponding to different volume fractions of nickel are shown in three separate figures, while the variation of YSZ particle size can be deduced from the line style of each plot. First of all, it can be seen that as a commonality among all the different microstructures, the mean nickel diameter increases as a function of time. Generally, the coarsening rates (i.e. slopes of the $d_{50}^{Ni}(t)$ curves) are very high in the first few hundred hours. At later times, the rate at which the nickel diameter increases is significantly lower. This is in-line with the qualitative impression gained from the micrographs shown in Fig. 5.17.

Additionally, each plot shows a clear correlation between the mean YSZ particle diameter and the particle size evolution. Here, irrespective of the nickel content, nickel coarsening is enhanced when the YSZ network comprises of larger particles. This is true with only one exception for $X_{Ni} = 0.25$ (Fig. 5.18b) where the order is exchanged between $d_{50}^{YSZ} = 0.92 \mu\text{m}$ (---) and $0.94 \mu\text{m}$ (---). It is expected that this is due to the small difference of the particle size between the two

microstructures and remaining uncertainties or inaccuracies as well as statistical error due to the finite size of the simulation domains. Relating nickel diameters from the finest and the coarsest YSZ structure, the relative increase is +36%, +42% and +47% for increasing nickel content. Therefore, the effect of the YSZ diameter on the particle diameter is significant and increases slightly with nickel content. This supports the visually motivated hypothesis of a strong influence of the YSZ network on the microstructural evolution.

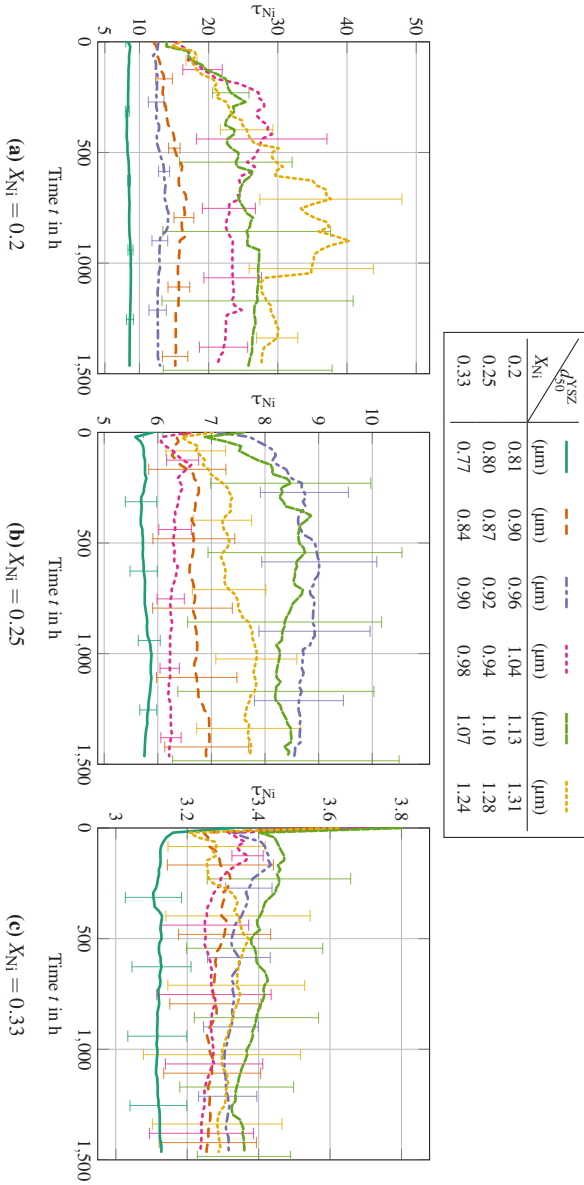


Figure 5.19: Evolution of the nickel tortuosity with time for MPF simulations of artificially generated SOFC-anode structures at three different nickel content of 20 % (a), 25 % (b) and 33 % (c). For each nickel content, six different simulations are shown where the mean YSZ particle diameter increases from — to - - -.

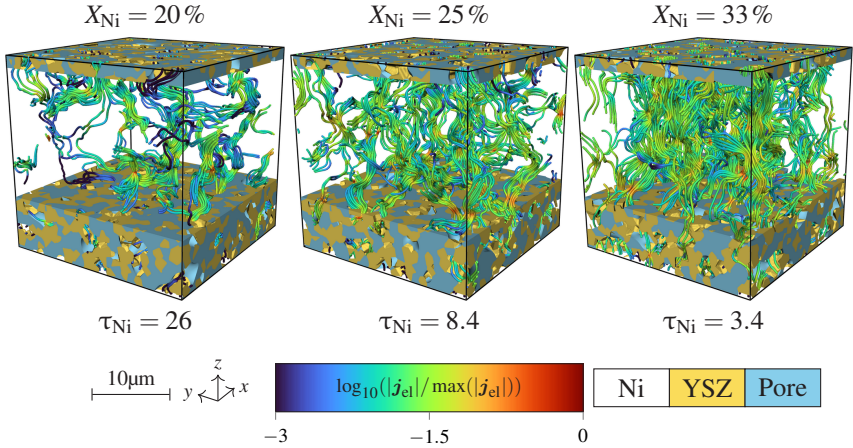


Figure 5.20: Streamlines of the electric current (lines parallel to \mathbf{j}_{el}) in the tortuosity calculation for generated SOFC-anode structures at varying nickel content (increasing from left to right). All results correspond to the final state ($t = 1463\text{h}$) of simulations shown as --- in Fig. 5.19. The streamlines are colored according to the magnitude of the current density. The corresponding volume fractions of nickel are shown at the top, whereas the obtained tortuosities are shown on the bottom.


Tortuosity Evolution While the knowledge of particle-size evolution is useful to gain a first understanding of the microstructural dynamics, it is not clear how it relates to the key microstructural parameters with respect to the performance of the anode. One such parameter is the tortuosity of the nickel phase. It is expected that when the nickel tortuosity is high, since this corresponds to an inefficient electric conduction, the formation of local electrochemically inactive regions becomes more likely.

Fig 5.19 shows the evolution of the nickel tortuosity for all generated structures, grouped with respect to the nickel content. The occasionally shown error bars represent the standard deviation obtained from the tortuosity values in each sample direction. First of all, it is directly apparent that the nickel tortuosity is strongly determined by the nickel content. For a nickel content of 20%, tortuosities range roughly from a value of $\tau_{Ni} = 10$ to 40, for $X_{Ni} = 25\%$ from $\tau_{Ni} = 5$ to 10, and for

$X_{Ni} = 33\%$ in the range $\tau_{Ni} = 3$ to 4. Therefore, a high nickel content improves the percolation of the nickel phase significantly.

When the nickel content is low (i.e. $X_{Ni} = 20\%$, Fig. 5.19a), a significant increase in tortuosity with increasing mean YSZ diameter is observed. In this case, not only the magnitude of the tortuosity but also its relative increase with time seem to be correlated to the fineness of the YSZ structure in such a way that finer YSZ structures lead to a stabilization of τ_{Ni} . For higher nickel content (Fig. 5.19b-Fig. 5.19c), the correlation is significantly weaker and a decrease in YSZ particle size does not necessarily lead to a lowering in τ_{Ni} or its relative increase with time. For the structures with the largest amount of nickel of 33% (Fig. 5.19c), the tortuosity value is almost invariant in time taking into account the scatter observed for varying sample directions.

The results suggest that at high nickel content, nickel conduction is sufficiently warranted such that the constraints imposed by the YSZ structure become unimportant for maintaining a good percolation of the nickel phase. In contrast, when manufacturing constraints do not permit large nickel content for any possible reason, an alternative route to ensure a good percolation of nickel is to maintain a sufficiently fine YSZ structure.

An additional observation can be made regarding the magnitude of the directional deviations in τ_{Ni} : When τ_{Ni} is high, the errors are usually large as well. To gain an understanding of all these peculiarities, the corresponding streamlines for the tortuosity calculation in the z -direction are shown in Fig. 5.20 for the final state of the simulations shown as  in Fig. 5.19 ($d_{50}^{YSZ} = 1.13, 1.10$ and 1.07 for increasing nickel content, respectively). It can be seen that when the nickel content is low (implying high tortuosity), only a low number of transport pathways govern the electric current through the structure. This means that the statistics underlying the value of $\tau_{Ni,d}$ in any given direction d is low, explaining the large scatter encountered. In contrast, when the tortuosity is low, the number of transport pathways is tremendous and the simulation domain can be considered as statistically representative. It is stressed that this is a feature solely caused by the limited size of the simulation domain and thus a microscale-phenomenon not

apparent in macroscopic measurements of the same material. This shows that in a microscale setup it is important to make measurements of the tortuosities in different directions in order to be capable of assessing the reliability of the calculated tortuosity values.

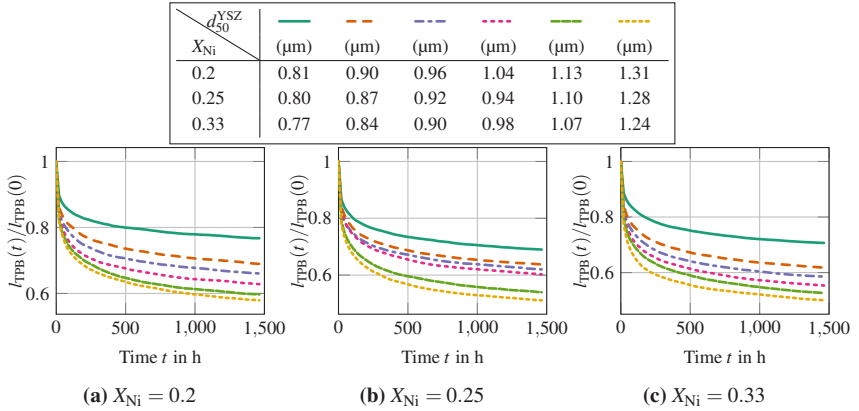


Figure 5.21: Evolution of the relative triple-phase boundary length with time for MPF simulations of artificially generated SOFC-anode structures at three different nickel content of 20 % (a), 25 % (b) and 33 % (c). For each nickel content, six different simulations are shown where the mean YSZ particle diameter increases from — to - - -.

Table 5.4: Initial TPB lengths ($l_{TPB}(0)$) corresponding to the evolution shown in Fig. 5.21. The coloring and linestyles are such that the mean YSZ particle diameter increases from — to - - - (from left to right).

X_{Ni}	—	- -	- - -	· · ·	- - -	- - -
	($1/\mu\text{m}^2$)	($1/\mu\text{m}^2$)	($1/\mu\text{m}^2$)	($1/\mu\text{m}^2$)	($1/\mu\text{m}^2$)	($1/\mu\text{m}^2$)
0.2	0.76	0.90	0.92	0.91	0.88	0.80
0.25	1.04	1.09	1.07	1.10	1.03	0.93
0.33	1.05	1.12	1.10	1.10	1.03	0.94

Triple-phase Boundary Length Evolution A reduction in triple-phase boundary is typically considered as a major cause for degradation as it corresponds to a reduced number of available reaction sites in the anode. For each nickel content, calculating the l_{TPB} of the initial structures reveals that these are subject to variations even though the initial nickel particle sizes are held constant. This complicates the comparison and hence, this quantity has been normalized with respect to the initial TPB length of each structure. The corresponding relative TPBL ($l_{\text{TPB}}(t)/l_{\text{TPB}}(0)$) is shown in Fig. 5.21 as a function of time for each of the simulations. For the sake of completeness, the corresponding initial TPB lengths are tabulated in Table 5.4.

In general it can be observed that the TPBL evolution is qualitatively inversely related to the temporal behavior of the mean nickel diameter. In particular, a decrease of TPBL with time is observed that is rapid at early times. Over the simulation time of about 1500h, l_{TPB} reduces by at least 20% and thus, the reduction in TPB length is significant. A clear influence of the YSZ particle size is obtained independent of the nickel content: All of the curves are ordered such that finer YSZ particle sizes correspond to a less pronounced relative decay of l_{TPB} . This means that fine YSZ particles promote a stabilization of the TPB length and hence a less pronounced degradation of the anode material is expected.

Only a fraction of the total TPB length is relevant for the electrochemical performance of the anode material. When any of the particles (Ni/YSZ/pore) is disconnected from its network, the fuel gas reaction (Eq. (5.2)) cannot take place at the corresponding TPB line segments. Therefore, in addition to a reduction in total TPB, the breakup or coalescence of particles during the coarsening process may alter the active fraction of the TPB. Fig. 5.22 shows the active fraction of the TPB ($l_{\text{ATPB}}/l_{\text{TPB}}$) in percent as a function of time for the simulations at varying nickel content and YSZ particle size.

First of all, a clear influence of the nickel content is apparent. When the nickel content is high ($X_{\text{Ni}} = 0.33$, Fig. 5.22c), almost the entire TPB is connected ($l_{\text{ATPB}}/l_{\text{TPB}} > 0.9$) and fluctuations with time can be considered as almost insignificant (the active fraction drops only slightly). For a nickel content of 25%,

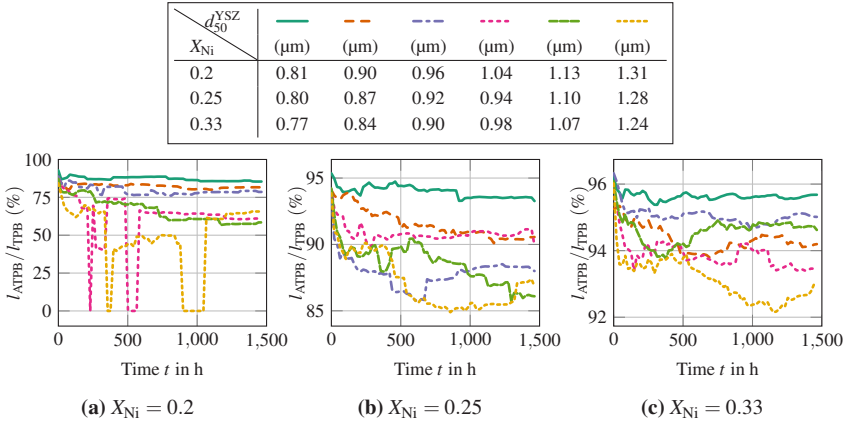


Figure 5.22: Evolution of the relative triple-phase boundary length with time for MPF simulations of artificially generated SOFC-anode structures at three different nickel content of 20% (a), 25% (b) and 33% (c). For each nickel content, six different simulations are shown where the mean YSZ particle diameter increases from — to - - -.

the active fraction of the TPB shows a clear negative trend with time and features a clearly discontinuous behavior. For this case, the active fraction of the TPB varies roughly between 80% and 95%. Here, smaller YSZ particle sizes seem to have a positive effect on the active fraction of the TPB, although the correspondence is not as clear as for the temporal behavior of the total TPB length. When the nickel content is low (20%), in certain cases mostly corresponding to large YSZ particle sizes a fatal drop to a vanishing active TPB may occur. Despite the low nickel content, when the YSZ particle size is small, such drops in TPB can be avoided and a high fraction of more than 75% can be sustained.

This means that at high nickel content, the YSZ structure is only relevant for ensuring a small decay of l_{TPB} with time. However, when the nickel content is low, significant portions of the TPB may become isolated during operation of the SOFC and then a fine YSZ network may help to mitigate this phenomenon.

Correlation Analysis The simulation studies performed so far deliver a tremendous amount of information. Each simulation corresponds to about seventy

temporal snapshots at which data about each quantity (i.e. mean nickel diameter d_{50}^{Ni} , nickel tortuosity τ_{Ni} , l_{TPB} , ...) are available. Collecting all simulation snapshots of the eighteen simulations, an ensemble of more than one thousand data points are available for all of these quantities. Therefore, the obtained data are suitable for a statistical analysis.

The advantage of a statistical analysis is that noise and discontinuous variation in certain quantities owing to the finite size of the simulation domain can (at least to some extent) efficiently be removed. In addition, the vast amount of data can be compressed to a much lower number of quantities containing the essential correlations between various parameters.

As input (or prescribed) parameters, the nickel content X_{Ni} and YSZ particle size d_{50}^{YSZ} are considered. The question is how strong these are correlated to the measured microstructural parameters.

To quantify the correlation, Spearman correlation coefficients are determined. The Spearman correlation coefficient $p(a, b)$ between two quantities a and b and their corresponding data pairs $\{(a_1, b_1), \dots, (a_N, b_N)\}$ is given as

$$p(a, b) \equiv \frac{\sum_{i=1}^N (n_i^a - \bar{n}^a)(n_i^b - \bar{n}^b)}{\sqrt{\sum_{i=1}^N (n_i^a - \bar{n}^a)^2} \sqrt{\sum_{i=1}^N (n_i^b - \bar{n}^b)^2}} \quad (5.30)$$

$$\bar{n}^a \equiv \frac{1}{N} \sum_{i=1}^N n_i^a \quad (5.31)$$

where n_i^a is the rank corresponding to a_i obtained by sorting the entries a_i in increasing order (equal values are assigned the average of their integer rank). p is dimensionless and always ranges between -1 and 1 , where $p = 1$ corresponds to a perfect positive correlation (if a increases, so does b) and -1 to a perfect negative correlation (if a increases, b decreases) between the two quantities. When $p = 0$, the two quantities are uncorrelated.

Table 5.5: Spearman correlation coefficients for the MPF simulation studies of nickel coarsening in artificially generated SOFC anode structures.

		<i>b</i>				
X_{Ni}		d_{50}^{Ni}	τ_{Ni}	l_{TPB}	l_{ATPB}	l_{ATPB}/l_{TPB}
$p(d_{50}^{YSZ}, b)$	0.2	0.92	0.83	-0.60	-0.78	-0.86
	0.25	0.87	0.50	-0.78	-0.80	-0.72
	0.33	0.93	0.33	-0.83	-0.84	-0.70
$p(X_{Ni}, b)$	all	0.44	-0.93	0.31	0.57	0.90

In the current analysis, all available data pairs are collected together. Since the data points are distributed equidistant in time, the obtained correlations can be considered as an average over the total simulation time of roughly $1500h^3$.

The calculated correlation coefficients are tabulated in Table 5.5. It can be seen that independent of the volume fraction, the mean nickel diameter d_{50}^{Ni} almost always increases with d_{50}^{YSZ} since the corresponding correlation coefficients are about 0.9. The correlation analysis also supports the visual impression of a decreasing positive correlation between d_{50}^{YSZ} and the nickel tortuosity as the nickel content increases. When the nickel content is low, this correlation is quite strong ($p(d_{50}^{YSZ}, \tau_{Ni}) \approx 0.83$). l_{TPB} is negatively correlated to the mean YSZ diameter but the correlation is not always very strong. However, the correlation of d_{50}^{YSZ} to the active TPB length l_{ATPB} is also negative but stronger. This is rooted in a strong negative correlation to the active fraction of the TPB (l_{ATPB}/l_{TPB}).

Furthermore, the correlation analysis shows that the influence of the nickel content is strongest with respect to the nickel tortuosity. Here, a negative coefficient of more than 0.9 means that the tortuosity is almost entirely determined by the nickel content. All other correlations with respect to X_{Ni} are much weaker except the active fraction of TPB length (l_{ATPB}/l_{TPB}). The coefficient has the opposite sign

³ It can be considered corresponding to the case that someone randomly picks a sample with lacking knowledge of the annealing time and sole access to the value of X_{Ni} and/or d_{50}^{YSZ} .

which seems to suggest that the active ratio of TPB is somehow inversely related to the nickel tortuosity. This is in fact what one would expect as the isolation of nickel particles should result in an increase of the nickel tortuosity.

5.3.3 Experimentally-Based Structures

Motivation The hitherto performed simulation studies on artificial generated Voronoi structures provide first insights on the microstructural evolution in the anode functional layer. It is clear that real anode microstructures can only roughly be approximated by such idealized geometries. Therefore, it is interesting to perform coarsening simulations using experimentally reconstructed structures as initial condition.

Focused ion beam (FIB) milling [126] is commonly combined with scanning electron microscopy (SEM) [127, 128] to enable a detailed three-dimensional reconstruction of multiphase materials on the microscale. Resolutions down to 5 nm can be reached.

FIB-SEM technique is widely applied for the reconstruction of SOFC materials and has also been conducted in a joint research project for the reconstruction of the SOFC-anode functional layer [118, 129, 130]. The corresponding reconstructed volume has been used in a first multiphase-field simulation study [119], where the simulations were performed with the herein presented model by the current author. Here, a variation in the wettability of Ni on YSZ was studied to span a range of possible operation conditions. It was found that the wetting condition influences the coarsening behavior decisively and that an improper wetting of nickel on YSZ increases both the coarsening rate $d_{50}^{Ni}(t)$ and the loss in active TPB length. Therefore, a high wettability is desired in order to reduce the degradation of the anode functional layer. However, changing the wetting conditions is not easily possible without changing the composition of the underlying materials.

Alternate routes must be taken in order to mitigate the degradation in the AFL. A possible solution suggested by the coarsening behavior of the artificial Voronoi

structures is to increase the nickel content. It is of interest whether this trend observed for the artificial structures is also present for more realistic structures. Therefore, based on the original FIB-SEM reconstructed anode structure, structures are generated with increased amount of nickel. The modification is done by a small dilation of the nickel particles towards the pore phase, while the YSZ structure is held invariant. This ensures that an influence of the YSZ structure, which was found to be quite significant, can be excluded as a possible source to modify coarsening dynamics.

5.3.3.1 Simulation Setup

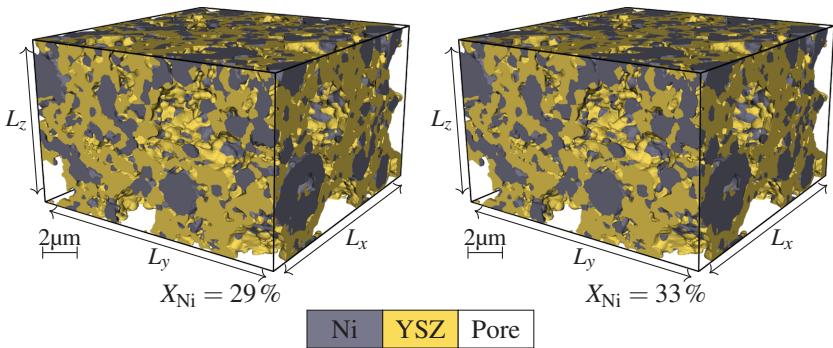


Figure 5.23: Initial anode structures with increased nickel content based on the FIB-SEM reconstructed structure from [119].

The two modified anode structures are shown in Fig. 5.23 and correspond to $X_{Ni} = 29\%$ and $X_{Ni} = 33\%$, respectively, whereas the original structure contained only 25% of nickel. Each structure has dimensions of $L_x = L_y = 15\mu\text{m}$ and the layer height is given by $L_z = 9.2\mu\text{m}$. At first sight, the structures seem to look almost identical owing to the way additional nickel is added at its surface.

Visualizing the microstructure by a cross section at $z = L/2$ (Fig. 5.24), one can identify the differences between the structures which are reflected in enlarged

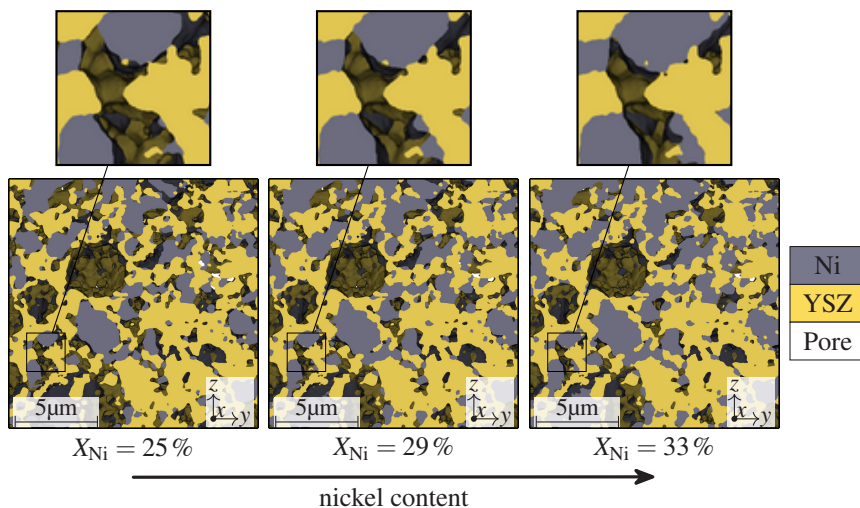


Figure 5.24: Cross-sections of the initial anode microstructures for the multiphase-field simulation studies at varying nickel content. The original FIB-SEM reconstructed microstructure is shown left, and structures of increasing nickel content are shown in the center and right, respectively.

nickel particles. It can be seen that the overall morphology of the nickel particles is preserved. The fine YSZ network is completely kept unmodified, as desired. The microstructural features of the structure are clearly different from the structures generated by means of the Voronoi method. The pore phase is finely dispersed but additionally comprises of large abnormal crater-like voids with an almost spherical shape. From the three-dimensional picture (Fig. 5.23) it is deduced that similar holes are nearly entirely filled with nickel. However, most nickel particles are distributed between the YSZ and pore phase with no clear correlation.

The phase-field model is identically chosen as in the case of the Voronoi-based structures, i.e. two compositions Ni and YSZ are chosen and three order parameters are used. For the simulation, no-flux boundary conditions are imposed on each chemical potential ($\nabla\mu_i \cdot \mathbf{n} = 0$) at the outer boundaries, leading to a

Table 5.6: Parameter set utilized for the MPF simulations based on the experimental FIB-SEM microstructures. The model unit system is given by $u_E = 1.43 \times 10^{-15}$ J, $u_t = 9.2 \times 10^{-2}$ s and $u_l = 25$ nm.

Parameter	Symbol	Value (model units)	Value (SI units)
Ni-surface chem. mobility	$M_{\text{Ni}}^{\text{NiPore}}$	$0.1 u_l^6 / (u_E u_t)$	$1.86 \times 10^{-31} \frac{\text{m}^6}{\text{J s}}$
Interfacial energy Ni-Pore	γ_{NiPore}	$1.0 u_E / u_l^2$	$2.29 \frac{\text{J}}{\text{m}^2}$
Interfacial energy Ni-YSZ	γ_{NiYSZ}	$1.25 u_E / u_l^2$	$2.87 \frac{\text{J}}{\text{m}^2}$
Interfacial energy Pore-YSZ	γ_{PoreYSZ}	$1.0 u_E / u_l^2$	$2.29 \frac{\text{J}}{\text{m}^2}$
Interface mobility Ni-Pore	m_{NiPore}	$0.1 u_l^4 / (u_E u_t)$	$2.97 \times 10^{-16} \frac{\text{m}^4}{\text{J s}}$
Interface mobility Ni-YSZ	m_{NiYSZ}	$1.0 u_l^4 / (u_E u_t)$	$2.97 \times 10^{-15} \frac{\text{m}^4}{\text{J s}}$
Interface mobility Pore-YSZ	m_{PoreYSZ}	$1.0 u_l^4 / (u_E u_t)$	$2.97 \times 10^{-15} \frac{\text{m}^4}{\text{J s}}$
Interface width parameter	ε	$2.0 u_l$	50 nm
Grid spacing	$\Delta x = \Delta y = \Delta z$	$1.0 u_l$	25 nm
Thermodynamic pref. Nickel	A_{Ni}	$5 u_E / u_l^3$	$4.58 \times 10^8 \frac{\text{J}}{\text{m}^3}$
Thermodynamic pref. YSZ	A_{YSZ}	$50 u_E / u_l^3$	$4.58 \times 10^9 \frac{\text{J}}{\text{m}^3}$

vanishing influx of matter into the system. For the order parameters, zero Neumann boundary conditions are imposed ($\nabla \phi_\alpha \cdot \mathbf{n} = 0$). This leads to a 90° angle between the surface of each phase and the boundary.

5.3.3.2 Model Parameters

The model parameters in the model unit system are chosen almost identical to the case of the Voronoi-based structures (Table 5.3) and are tabulated in Table 5.6. The major difference lies in the higher resolution in SI units of 25 nm. This results in modified SI values of the thermodynamic prefactors A_i and the interface mobilities $m_{\alpha\beta}$ which is needed in order to compensate for the higher curvatures that can be resolved. In addition, the wetting angle of Ni on YSZ is modified towards a more realistic value by adjusting γ_{NiYSZ} and is given by $\theta = 104^\circ$ (cf. [119]). Very importantly, the interfacial energy of the nickel surface γ_{NiPore} and the surface chemical mobility of nickel remain unchanged. This means that the kinetics are still governed by the experimentally obtained surface diffusivity and the surface energy (cf. Section 5.3.1).

5.3.3.3 Results and Discussion

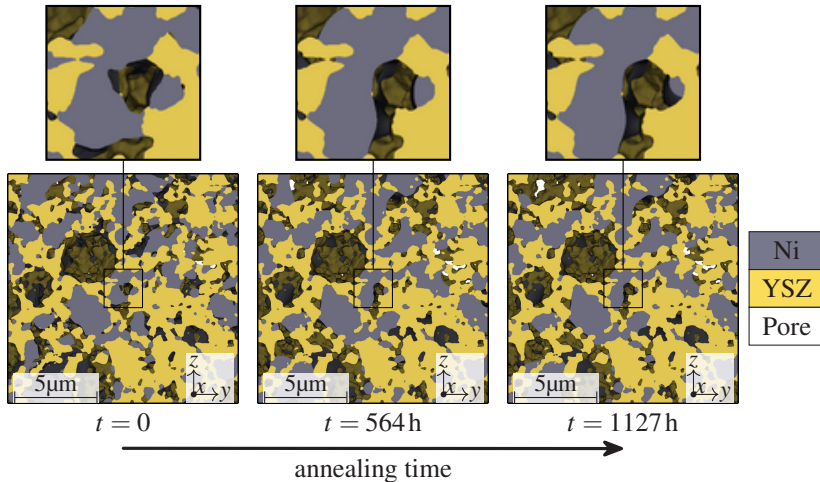


Figure 5.25: Cross-sections of the anode microstructure at $X_{\text{Ni}} = 29\%$ at initial (left), intermediate (center) and final state (right).

Microstructure Evolution The evolution of the microstructure is exemplarily shown for the intermediate case of $X_{\text{Ni}} = 29\%$ as a 2D-cross section in Fig. 5.25. It can be observed that most of the particles reach a virtually invariant shape after roughly 500h of annealing time (cf. inset in the figure). Only relatively large nickel particles show a significant change in morphology at late times. This is qualitatively consistent with the coarsening dynamics observed in the artificially constructed Voronoi structures.

Evolution of Ni Particle Size A more quantitative measure for the microstructural dynamics is given by the nickel particle size evolution shown in Fig. 5.26 for all three Ni-YSZ structures. It can be seen that the mean nickel diameter increases in the initial period of time relatively quickly and slows significantly down for times more than 500 h. This feature becomes slightly more

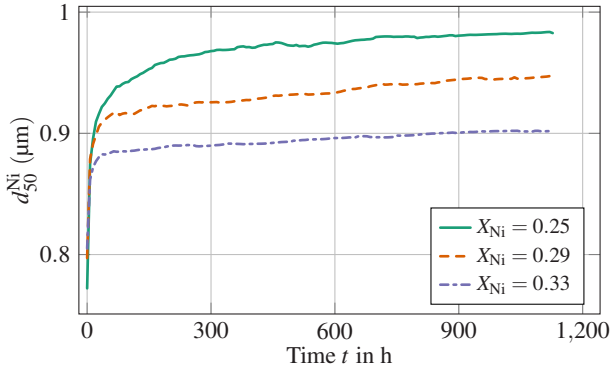


Figure 5.26: Mean nickel diameter evolution for experimentally-based SOFC anodes for a variation in nickel content.

pronounced as the amount of nickel is increased (for $X_{Ni} = 0.33$, the curve is almost discontinuous corresponding to a very rapid initial growth and a subdominant late-time coarsening). It is worth noting that even though the initial particle size increases slightly with nickel content, Ni particles have a smaller average size at late times for higher nickel content. While the former clearly corresponds to the way nickel was added at its free surface, the latter shows that at high nickel content further growth is prohibited. Although the decrease in nickel size with nickel content is in the order of maximal 10% in the studied range of compositions, such a negative correlation of the particle size to nickel content was not observed in the Voronoi-based structures (cf. Table 5.5). A possible explanation might be given based on the differences in composition: While in the Voronoi-based study, YSZ and pore phase are assigned equal amounts, contrarily, in the current study, YSZ content is held constant. This means that as nickel content is increased in the current treatment, the YSZ content increases relative to the porosity. Therefore, a low porosity (or high solid content) counteracts the coarsening of nickel which is likely due to the encapsulation of particles in the fine YSZ network.

Tortuosity Evolution The evolution of nickel tortuosity is shown for the three structures in Fig. 5.27. It can be seen that the nickel tortuosity is strongly

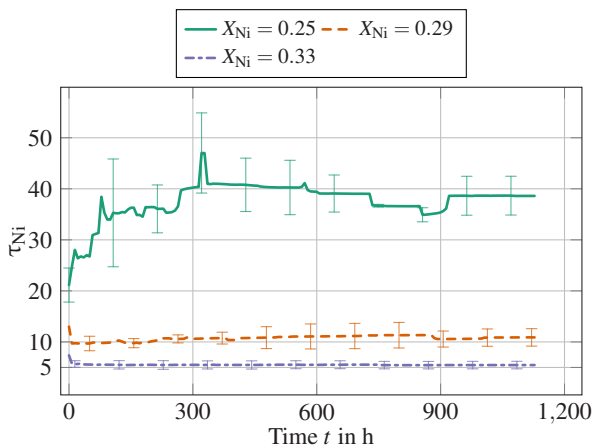


Figure 5.27: Tortuosity evolution of the nickel phase for experimentally-based SOFC anodes for a variation in nickel content.

dependent on the nickel content. At low nickel content the nickel tortuosity increases significantly from roughly 20 to 40 in total, i.e. a nearly doubling of the tortuosity value is observed during the total simulation time of 1127 h. In contrast, when the nickel content is higher, the tortuosity of Ni is significantly lower and shows a qualitative different behavior over time. The tortuosity curve for the intermediate case $X_{\text{Ni}} = 0.29$, which is initially already lower than that of the experimental structure, shows a drop at early time and increases only slowly and insignificantly over time such that a tortuosity value near roughly 10 can be maintained during the whole simulation. Qualitatively similar is the behavior of the structure with the highest amount of nickel, i.e. $X_{\text{Ni}} = 0.33$. Here, the tortuosity of nickel can be maintained at a level half as high, i.e. $\tau_{\text{Ni}} \approx 5$ is achieved.

The clear negative correlation of tortuosity to nickel content is consistent with the findings obtained by means of the artificially generated Voronoi structures (see Table 5.5 and Fig. 5.19). Therefore, a quite pervasive observation is that a slight increase in nickel content can strongly stabilize electron conduction and improve the percolation in the nickel phase even over long operating times. Nevertheless,

the tortuosity values obtained are significantly higher than those of the Voronoi structures at the same nickel content (compare e.g. Fig. 5.19c with $X_{\text{Ni}} = 0.33$ in Fig. 5.27). This seems to be related to the microstructural differences between the idealized Voronoi geometries and the experimental structures.

The Voronoi structures likely comprise of a more uniform distribution of particle sizes due to the randomized placement of particles compared to the experimentally-based structure which contains a few large abnormal nickel clusters. It is sought that these large particles consume significant amounts of nickel without being necessarily well connected and thus promote the formation of bottlenecks and isolated nickel regions. Another point worth mentioning is the lower wettability of nickel on YSZ assumed for the experimentally-based structures, which can drastically increase tortuosity values as shown in [119]. Nevertheless, comparing the FIB-SEM reconstructed structure at $X_{\text{Ni}} = 0.25$ from this work at $\theta = 90^\circ$, the corresponding tortuosities in the Voronoi-based structures (with the same wetting angle) are still at least a factor of two lower. This seems to suggest that a uniform distribution of nickel is a desired property to improve the percolation of the microstructure.

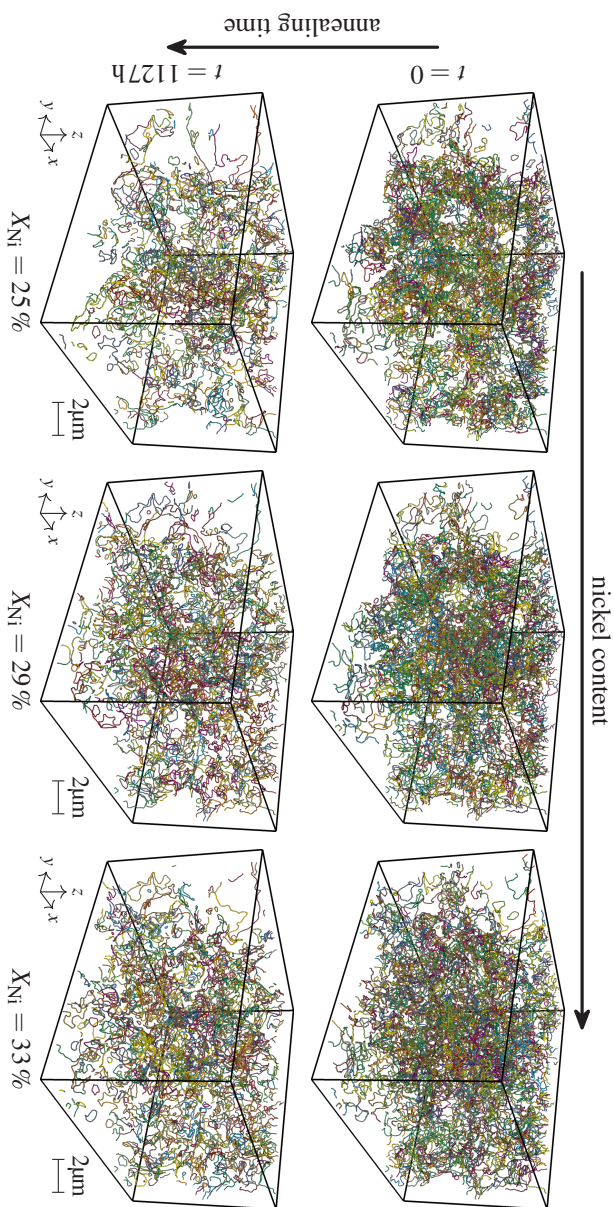


Figure 5.28: Active triple-phase boundary (corresponding to t_{ATPB}) at initial (top row) and final (bottom row) stages of the MPF simulations. The nickel content increases from left to right. Each TPB segment is assigned a different color.

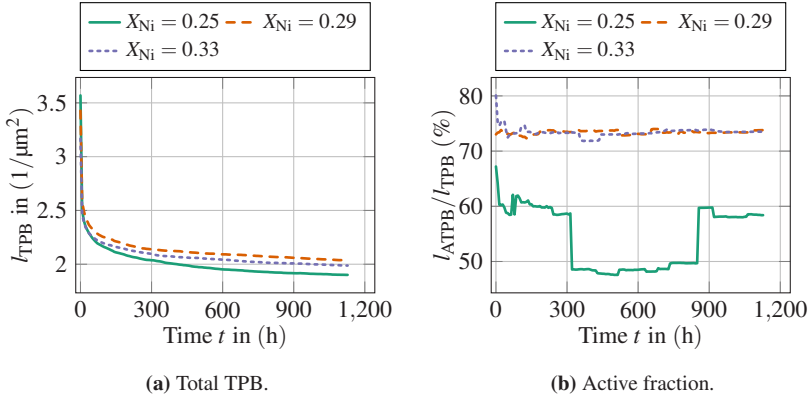


Figure 5.29: Triple-phase boundary evolution for experimentally-based SOFC anodes for a variation in nickel content. The evolution of the total TPB length is shown in (a) and the active fraction evolution is shown in (b).

Triple-phase Boundary Evolution Fig. 5.29 shows the evolution of the TPB length and its active fraction during the simulation run. A significant reduction in TPB length is observed in all three cases during the annealing (Fig. 5.29a). The reduction in l_{TPB} occurs mainly in the first few hundred hours of annealing time and the final amount of TPB is almost invariant under a modification of Ni volume fractions.

However, it is stressed that the initial TPB length is not identical among the three cases but reduces slightly with nickel content. Therefore, an increased nickel content might lead to an initially reduced TPB length which is however compensated by a lower relative decrease with time. A clearer picture is obtained by considering the active fraction of the TPB (Fig. 5.29b). While the active percent can be maintained at an identical and almost constant level of roughly 75% for the structures with $X_{Ni} \geq 0.29$, at low nickel content, the active ratio is significantly reduced. The corresponding large differences in l_{ATPB} are also clearly visible by visualizing the corresponding line network (Fig. 5.28). It can be seen that the active TPB comprises of a complex interconnected network of line segments. Moreover, it can be seen that the length is clearly reduced after the total simulation time and that more line segments remain at high nickel content.

A point worth mentioning is that the curve in Fig. 5.29b for $X_{\text{Ni}} = 25\%$ drops below 50% after three hundred hours of coarsening. This drop in active percent is caused by a sudden breakup of a large nickel particle within the microstructure [119, Fig. 6] and is therefore caused by an insufficient percolation of the nickel phase. Although this drop is reversed after 800h of annealing, it shows the susceptibility of the material at low nickel content to small local perturbations imposed by coarsening. This positive correlation of the active fraction to nickel content is also backed by the preliminary studies on Voronoi-based microstructures (Table 5.5). However, active percents close to 90%, as observed in the Voronoi-based systems (cf. Fig. 5.22b-Fig. 5.22c), cannot be reached for the experimentally-based microstructures. This means that the percolation in the idealized structures is more optimal but likely difficult to reach in any real microstructure without a significant change in the manufacturing conditions. Moreover, the simulations for the experimental structures show that after a certain nickel content is exceeded, the active fraction cannot necessarily be further increased. This was not occurring in the Voronoi structures. This shows that the Voronoi method cannot capture certain peculiarities in the microstructure of a real anode. In this regard, more advanced techniques are promising (cf. e.g. Westhoff et al. [131]) that allow a higher degree of freedom for the generation of electrode microstructures.

5.4 Relation to Performance

The rich variety of obtained microstructural parameters which are available as a time series, are suitable input for microstructural based electrode models such as a simplified transmission-line model (TLM) according to Dierickx et al. [132]. Therefore, the multiphase-field simulations deliver valuable data for an estimation of the performance of the anode.

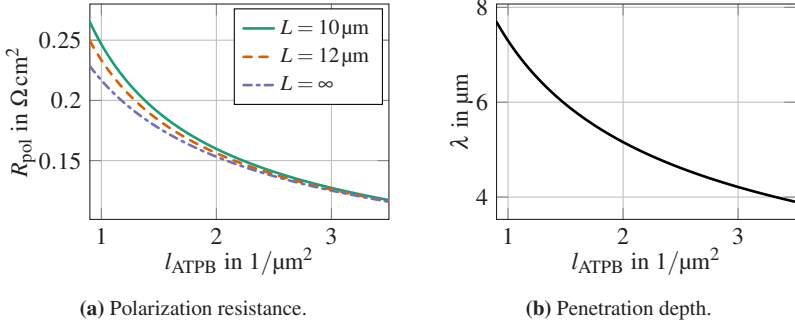


Figure 5.30: Relation of the active triple-phase boundary length l_{ATPB} to polarization resistance R_{pol} (a) for the experimentally-based structures (Eq. (5.36)). The AFL thickness is varied from $L = 10 \mu\text{m}$ to ∞ in order to analyze its effect on the polarization resistance, all other microstructural properties held constant. The increasing importance of L at low l_{ATPB} are due to a concomitant increase in the electrochemically active AFL thickness (b).

The derivation of the TLM is outlined in Appendix A.3 to give the equation defining the TLM which can be written as an impedance (Eq. (A.56))

$$Z_{\text{TLM}} = \sqrt{\zeta} \chi_1 \coth \left(\sqrt{\frac{\chi_1}{\zeta}} L \right) \quad (5.32)$$

with the ionic specific resistance $\chi_1 \equiv 1/(\sigma_{\text{ion,eff}}A)$ in Ω/m and reaction-related impedance $\zeta \equiv z_{\text{LSR}}/(l_{\text{ATPB}}A)$ in Ω/m . Here A denotes the electrode area, L the thickness of the AFL, $\sigma_{\text{ion,eff}}$ is the effective ionic conductivity in S/m and z_{LSR} in Ω/m is an impedance specific to the active TPB length.

The effective ionic conductivity is given by the relation

$$\sigma_{\text{ion,eff}} = \frac{X_{\text{YSZ}} \sigma_{\text{ion}}}{\tau_{\text{YSZ}}} \quad (5.33)$$

in terms of the intrinsic ionic conductivity σ_{ion} (a material constant) [132, Eq. (6)-(7)].

The reaction-related complex impedance is modeled by an RQ-element

$$z_{\text{LSR}}(\omega) \equiv \frac{\text{LSR}_{\text{CT}}}{1 + (j\omega\tau_{\text{CT}})^n} \quad (5.34)$$

which makes this quantity dependent on the frequency ω in $1/\text{s}$ (j is the imaginary unit) and includes a charge-transfer resistance LSR_{CT} in Ωm and a (mean) relaxation time τ_{CT} in s combined with an exponent $0 < n < 1$ to allow a smooth distribution of relaxation times.

This model could successfully fitted to experimental electrochemical impedance spectroscopy (EIS) data of Ni-YSZ anodes and thus, the model parameters such as LSR_{CT} can be experimentally determined. This means that the model provides a microstructure-property linkage relating the microstructural parameters to the macroscopically measurable electrochemical performance of the anode.

The electrochemical losses in the Ni-YSZ anode can be expressed in terms of the polarization resistance defined as

$$R_{\text{pol}} \equiv AZ_{\text{TLM}}^{\text{Re}}(\omega = 0) - A \lim_{\omega \rightarrow \infty} Z_{\text{TLM}}^{\text{Re}}(\omega) = AZ_{\text{TLM}}^{\text{Re}}(\omega = 0) \quad (5.35)$$

with $Z_{\text{TLM}}^{\text{Re}} \equiv \text{Re}(Z_{\text{TLM}})$ and the last equality holds since $\lim_{\omega \rightarrow \infty} \text{Re}(Z_{\text{TLM}}(\omega)) = 0$ for this type of TLM. It follows that

$$R_{\text{pol}} = \sqrt{\frac{\text{LSR}_{\text{CT}}}{l_{\text{ATPB}} \sigma_{\text{ion,eff}}}} \coth\left(\frac{L}{\lambda}\right) \quad (5.36)$$

$$\lambda \equiv \sqrt{\frac{\sigma_{\text{ion,eff}} \text{LSR}_{\text{CT}}}{l_{\text{ATPB}}}}, \quad (5.37)$$

where λ is a so-called penetration depth. The thickness of the electrochemical active zone in the AFL is roughly 2λ since $\coth(2) = 1.04 \approx 1$.

One can insert the material constants from [119], i.e. $\text{LSR}_{\text{CT}} = 158.14 \Omega\text{m}$, layer thickness $L = 10 \mu\text{m}$ and $\sigma_{\text{ion}} = 2.84 \text{S/m}$. Furthermore, since X_{YSZ} and τ_{YSZ} are

time-invariant quantities, R_{pol} varies with time solely due to a change in active TPB length.

Fig. 5.30 shows the relation between polarization resistance and active TPB length for the experimentally-based anodes (i.e. $X_{\text{YSZ}} = 0.32$ and $\tau_{\text{YSZ}} = 2.7$) as well as the corresponding effective AFL thickness. It is seen that the polarization resistance for the experimentally based samples ranges in between $0.12 \Omega \text{cm}^2$ and $0.25 \Omega \text{cm}^2$ as well as being a monotonously decreasing function of l_{ATPB} . This means that a reduction in l_{ATPB} is directly related to an increase in polarization resistance and thus a decrease in performance results. The preliminary analysis shows that the TLM is a viable tool to quantify the influence of the coarsening kinetics obtained in the MPF model to a degradation of the anode material. This technique has been used in a first collaborative work [119] and can be applied to the herein presented data in the same straightforward manner to derive the temporal evolution of R_{pol} ⁴.

Furthermore, by means of the transmission-line model, it is possible to analyze the influence of the AFL thickness on the polarization resistance. The additional curves included in Fig. 5.30a show that when coarsening leads to a low l_{ATPB} (i.e. low nickel content and late times), the increase in polarization resistance can be partially compensated by increasing the AFL thickness. This is due to an increase of the active AFL thickness λ at low l_{ATPB} (cf. Fig. 5.30b).

Therefore, even if a change in composition is impossible, using the combination of MPF simulations and the TLM, one can suggest an optimized layer thickness to mitigate degradation of the anode.

⁴ A publication along these lines is prepared for publication.

5.5 Conclusion

In the current chapter, multiphase-field simulation studies of nickel coarsening in Ni-YSZ solid-oxide fuel cell anodes are performed at typical operating conditions of $T = 750^\circ$ and over a total annealing time of more than thousand hours. Voronoi-based artificially generated as well as experimentally-based structures are considered.

The large number of Voronoi-based structures cover a range of YSZ particle sizes and nickel content to analyze their effect on the microstructural evolution. In the study, which is also accompanied by statistical analysis, it is observed that a fine YSZ network reduces the magnitude of nickel coarsening and a high nickel content is vital for a sufficient percolation of the nickel phase. Although nickel coarsening is always accompanied with a reduction in triple-phase boundary length over time, a fine YSZ network is efficient in minimizing this effect. Furthermore, a good percolation of nickel (which corresponds to a low tortuosity), can only be achieved when its content is sufficiently high. If this is not the case, isolated nickel particles lead to a lowering of the active fraction of the TPB which might occasionally lead to a local dysfunction of the AFL.

The influence of an increased nickel content in the experimentally-based structures similarly leads to a drastic improvement in the percolation of the nickel phase. The simulations suggest that an amount of about 30% of nickel seems to be an optimal choice since a further increase in nickel content did not yield a further increase in the active TPB length.

The obtained microstructural time-series data can be used in an existing transmission-line model to obtain a quantitative relation to the polarization resistance of the anode functional layer. The analysis gives a nonlinear monotonous relation between the polarization resistance and the active TPB length and shows that the reduction in I_{ATPB} observed is the main driver for a degradation of the anode material. Based on the TLM an optimized AFL layer thickness for low nickel content is suggested to improve the performance of the anode after long operating times.

In summary, this chapter shows that the combination of multiphase-field simulations and application of a transmission-line model is a promising toolchain to obtain in-depth knowledge of the underlying microstructural mechanisms and their effect on the electrochemical performance of the anode.

6 Conclusion

6.1 Summary

The current work provides interesting insights into degradation phenomena in solid-oxide fuel cells at the microscale and in addition delivers so far unavailable analytical insights into certain ingredients in state-of-the art phase-field models. Multiphase-field simulation studies on nickel coarsening in SOFC anodes have been successfully conducted in three dimensions and on realistic time scales of more than thousand hours of operation providing a very high level of detail.

To achieve a quantitative interpretation of the simulations, the developed model has been carefully validated, firstly analytically using a technique called asymptotic analysis. This derivation delivered the sharp-interface limit of the model for the general case of a combination of surface and volume diffusion. The recovered law is consistent with an extended balance of chemical species accounting for an excess surface flux reflecting the additional interface diffusion term. An additional numerical validation study on thermal grooving under both surface and volume diffusion showed that the analytically derived physical law is applicable to practical simulations since the simulation results matched very well with an analytical solution to this problem. This marks the first achievement of the current thesis.

In addition to the sharp-interface limit of the presented multiphase-field model, high-order analytical derivations are performed to unravel the implications of a choice of interpolation functions in phase-field models of obstacle type. Since the different interpolation functions are not distinguishable by state-of-the art

thin-interface asymptotics, this theoretical study provides for the first time quantitative predictions regarding the nonlinear model behavior for large driving forces which occur far away from the sharp-interface limit. The match of the obtained travelling-wave solutions with one-dimensional numerical solutions are overall excellent. These results provide an estimate which warrants operation in the small driving force regime in the subsequent three-dimensional simulation studies for anode degradation. More importantly, the travelling-wave solutions can be used to gain a deep and sound analytical understanding of the limitations of current phase-field model formulations.

The simulation studies on SOFC anode degradation explore the influence of variations in nickel content and overall microstructural configuration on key microstructural properties as they evolve with time. The simulations not only deliver the evolution of the three-dimensional microstructure graphs with time but also quantitative data due to the implementation and utilization of advanced microstructure analysis tools. The simulations show that the degradation in the anode functional layer is related to a fast coarsening at early times that reduces the triple-phase boundary length significantly. In addition, certain microstructural conditions could be identified that either promote degradation or can help to mitigate it. Therefore, the gained insights are valuable in order to accompany material design decisions aimed at an improvement of the functional material of state-of-the-art Ni-YSZ anodes.

6.2 Outlook

In the course of the generation of this work, a lot of effort has been put into keeping the developed methods and tools as general as possible to facilitate reusability and expandability.

For instance, the multiphase-field model extension allows arbitrary combinations of volume and interface diffusion and thus can be applied to a vast range of

materials such as multicomponent metallic alloys. The model can also easily be modified to allow an investigation of modern Ni-GDC SOFC anode structures.

In addition, the microstructure analysis tools developed are available within the PACE3D framework and thus can be directly applied to materials with similar microstructures, such as porous battery electrode materials or nanoporous battery cathode particles. Another application regards to membrane structures used in medical lateral flow tests [133].

The high-order asymptotic treatment, applied herein to analyze the role of driving forces to great detail, can be applied to more complex models in the future, quantifying their higher order terms. It is thought that this method has great potential to improve the accuracy of phase-field models in the future because it makes the unintuitive interplay of nonlinear terms in the model visible and may enable removal of spurious terms.

A Appendix

A.1 Rate Constant for Volume Diffusion

Underlying Assumptions Let the surface between a solid and a solvent be parameterized by a function $y = y_s(x, t)$ where x is the distance from a vertically aligned grain boundary ($x = 0$) and y is the vertical coordinate.

In addition, the following assumptions are employed in [91]:

1. The surface energy γ_s is isotropic, i.e. independent of the orientation of the surface.
2. Diffusion in the solid is negligible and the diffusivity in the solvent is given by D .
3. The concentration field $c^m(x, y, t)$ in the solvent, which is in contact with the solid from above ($y > y_s(x, t)$), is steady state, i.e. divergenceless ($\nabla^2 c^m = 0$).
4. The surface is nearly flat, implying a relatively small slope $|\partial y_s / \partial x| \ll 1$.
 - a) The surface concentration can be evaluated at $y = 0$, i.e. is given by $c^m(x, 0, t)$.
 - b) The curvature of the surface is given by $\kappa_s(x, t) \approx -\partial^2 y_s(x, t) / \partial x^2$.
 - c) The normal vector points towards increasing y .
 - i. The normal velocity of the surface is given by $v_n(x) \approx \partial y_s(x, t) / \partial t$.

- ii. The gradient of the concentration normal to the surface is given by $\nabla c^m \cdot \mathbf{n} \approx \partial c^m(x, y, t) / \partial y|_{y=0}$.

Corresponding Balance Law The starting point in Mullins' theory for bulk (or volume) diffusion governed thermal grooving is the Gibbs-Thomson effect in terms of a shift of the concentration at the interface due to its curvature [91, Eq. 4]:

$$c^m(x, 0, t) = c_0^m \left(1 + \frac{\gamma_s V_m}{RT} \kappa_s(x, t) \right) \quad (\text{A.1})$$

Here c_0^m is the concentration in equilibrium with a planar surface, γ_s the interfacial energy of the free surface, V_m denotes molar volume and R and T are the ideal gas constant and temperature, respectively. All of these quantities are assumed to be constants.

An additional statement relates the motion of the surface function to the influx of material from the solvent

$$\frac{\partial y_s(x, t)}{\partial t} = V_m D \left. \frac{\partial c^m(x, y, t)}{\partial y} \right|_{y=0}. \quad (\text{A.2})$$

From the above listed assumptions it is clear that this is the small-slope approximated version of the following formulas

$$v_n = -V_m \mathbf{j}^m \cdot \mathbf{n} \quad (\text{A.3})$$

$$\mathbf{j}^m = -D \nabla c^m \quad (\text{A.4})$$

It is easy to see that this is equivalent to the standard interfacial balance (Eq. (2.67)) under the following assignments:

$$b^+ \rightarrow 0 \quad (\text{A.5})$$

$$b^- \rightarrow \frac{1}{V_m} \quad (\text{A.6})$$

$$j_b^+ \rightarrow j^m \quad (\text{A.7})$$

$$j_b^- \rightarrow \mathbf{0} \quad (\text{A.8})$$

Thus, the balance corresponds to a binary system where the composition in the solid is assumed to be a constant of unity $c_1^- = 1$ and the composition in the solvent to be negligibly small. In addition, a vanishing flux density in the solid is assumed.

Rate Constant In order to derive the rate constant as Mullins did, first the solution to the Laplace equation subject to the boundary condition Eq. (A.1) is stated in form of a Fourier transformation (Eq. 5 therein):

$$c^m(x, y, t) = c_0^m + c_0^m \frac{\gamma_s V_m}{RT} \frac{2}{\pi} \int_0^\infty \cos(\omega x) e^{-\omega y} K(\omega, t) d\omega \quad (\text{A.9})$$

$$K(\omega, t) \equiv \int_0^\infty \kappa_s(x, t) \cos(\omega x) dx \quad (\text{A.10})$$

By differentiating Eq. (A.2) twice with respect to x

$$\frac{\partial \kappa_s(x, t)}{\partial t} = -DV_m \frac{\partial^2}{\partial x^2} \frac{\partial c^m(x, y, t)}{\partial y} \Big|_{y=0} \quad (\text{A.11})$$

and inserting the solution for $c(x, y, t)$, one obtains

$$\frac{\partial \kappa_s(x, t)}{\partial t} = -\frac{Dc_0^m \gamma_s V_m^2}{RT} \frac{2}{\pi} \int_0^\infty \omega^3 \cos(\omega x) K(\omega, t) d\omega \quad (\text{A.12})$$

which is equivalent to [91, Eq. 7] up to a change in sign¹. The contained prefactor

$$A' \equiv \frac{Dc_0^m \gamma_s V_m^2}{RT} \quad (\text{A.13})$$

is the rate constant in m³/s for volume diffusion governed grooving appearing in the solutions for $y_s(x, t)$ provided by Mullins.

Relation to the PF Model The corresponding rate constant in the phase-field model at hand can be obtained by analogy from the sharp-interface limiting equations. A binary two-phase system is considered where α and β phase are the phases below and above the surface, respectively.

Therefore, in the sharp-interface representation one may write:

$$c(x, y, t) = \begin{cases} c^\alpha(x, y, t) = c^\alpha(\mu(x, y, t)) & y < 0 \\ c^\beta(x, y, t) = c^\beta(\mu(x, y, t)) & y > 0 \end{cases} \quad (\text{A.14})$$

An equivalent expression to Eq. (A.1) can be obtained as a first correction by expanding c^α from equilibrium:

$$c^\alpha(\mu) \approx c^\alpha(\mu_{\text{eq}}) + \left. \frac{dc^\alpha(\mu)}{d\mu} \right|_{\mu_{\text{eq}}} (\mu - \mu_{\text{eq}}) \quad \alpha \in \{\alpha, \beta\} \quad (\text{A.15})$$

The next step is to insert Eq. (3.101) which yields

$$c^\alpha(\mu(x, 0, t)) \approx c^\alpha(\mu_{\text{eq}}) + \left. \frac{dc^\alpha(\mu)}{d\mu} \right|_{\mu_{\text{eq}}} \frac{\gamma_{\alpha\beta} \kappa_s(x, t)}{c^\alpha(\mu_{\text{eq}}) - c^\beta(\mu_{\text{eq}})} \quad \alpha \in \{\alpha, \beta\} \quad (\text{A.16})$$

the composition for each phase at the interface under the assumption that attachment kinetics can be neglected.

¹ Based on Eq. A3 in Mullins' work it can be shown that Eq. 7 has a wrong sign.

The bulk flux in each phase is given by

$$\mathbf{j}^\alpha = -D^\alpha \nabla c^\alpha \quad \alpha \in \{\alpha, \beta\} \quad (\text{A.17})$$

From the governing law of the phase-field model (Eq. (3.108)), neglecting the additional surface contribution and under the assumption that the composition shifts are small, one obtains

$$v_n^0 (c^\alpha(\mu_{\text{eq}}) - c^\beta(\mu_{\text{eq}})) = (\mathbf{j}^\alpha - \mathbf{j}^\beta) \cdot \mathbf{n} \quad (\text{A.18})$$

and hence the corresponding small-slope approximated version reads

$$\frac{\partial y_s(x, t)}{\partial t} (c^\alpha(\mu_{\text{eq}}) - c^\beta(\mu_{\text{eq}})) = D^\beta \frac{\partial c^\beta(x, y, t)}{\partial y} \Big|_{y=0} - D^\alpha \frac{\partial c^\alpha(x, y, t)}{\partial y} \Big|_{y=0} \quad (\text{A.19})$$

Assuming that Laplace equation holds for c^α and c^β in their respective subdomains, in analogy to Eq. (A.10), one obtains

$$c^\alpha(x, y, t) = c^\alpha(\mu_{\text{eq}}) + \frac{dc^\alpha(\mu)}{d\mu} \Big|_{\mu_{\text{eq}}} \frac{\gamma_{\alpha\beta}}{c^\alpha(\mu_{\text{eq}}) - c^\beta(\mu_{\text{eq}})} \times \left(\frac{2}{\pi} \int_0^\infty \cos(\omega x) e^{\omega y} K(\omega, t) d\omega \right) \quad (\text{A.20})$$

$$c^\beta(x, y, t) = c^\beta(\mu_{\text{eq}}) + \frac{dc^\beta(\mu)}{d\mu} \Big|_{\mu_{\text{eq}}} \frac{\gamma_{\alpha\beta}}{c^\alpha(\mu_{\text{eq}}) - c^\beta(\mu_{\text{eq}})} \times \left(\frac{2}{\pi} \int_0^\infty \cos(\omega x) e^{-\omega y} K(\omega, t) d\omega \right) \quad (\text{A.21})$$

taking into account the boundary condition (Eq. (A.16)) and the far-field limits ($\lim_{y \rightarrow \infty} c^\beta(x, y, t) = c^\beta(\mu_{\text{eq}})$ and $\lim_{y \rightarrow -\infty} c^\alpha(x, y, t) = c^\alpha(\mu_{\text{eq}})$).

Differentiating Eq. (A.19) twice with respect to x yields

$$\frac{\partial \kappa_s(x, t)}{\partial t} = - \frac{(M_{\text{eq}}^\alpha + M_{\text{eq}}^\beta) \gamma_{\alpha\beta}}{(c^\alpha(\mu_{\text{eq}}) - c^\beta(\mu_{\text{eq}}))^2} \frac{2}{\pi} \int_0^\infty \omega^3 \cos(\omega x) K(\omega, t) d\omega \quad (\text{A.22})$$

$$M_{\text{eq}}^\alpha \equiv D^\alpha \left. \frac{dc^\alpha(\mu)}{d\mu} \right|_{\mu_{\text{eq}}} \quad \alpha \in \{\alpha, \beta\} \quad (\text{A.23})$$

Therefore, the rate constant for volume diffusion in the PF model at hand is given by

$$A' = \frac{(M_{\text{eq}}^\alpha + M_{\text{eq}}^\beta) \gamma_{\alpha\beta}}{(c^\alpha(\mu_{\text{eq}}) - c^\beta(\mu_{\text{eq}}))^2} \quad (\text{A.24})$$

which is the final result.

A.2 Derivation of PSD for Cylinder with Neck

A schematic of the cylinder with neck and the included spherical shapes are shown in Fig. A.1.

Firstly, the volume which can be filled with a sphere of certain radius r can be expressed as a solid of revolution:

$$V_\alpha^{\text{fill}}(r) = 2\pi \int_0^{H/2} R^2(r, h) dh \quad (\text{A.25})$$

where $R(r, h)$ is the maximal radius corresponding the envelope of all overlapping spheres that fit into the cylinder with neck. h is the vertical coordinate and the symmetry of the cylinder at $h = H/2$ is exploited.

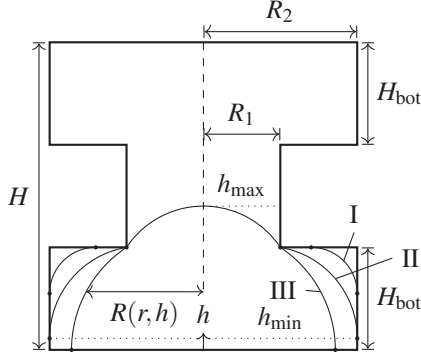


Figure A.1: Schematic for the derivation of the continuous PSD for a cylinder with neck. Note that the top and bottom plane are removed as a boundary condition and the center of the spheres are forced to remain within the domain. The volume that can be filled with overlapping spheres of radius r is given by the solid of revolution with $R(r, h)$. Roman numbers depict the different regimes considered for the bottom part of the cylinder.

The spherical shapes leave circular traces in the cylindrical coordinate system, such that

$$R(r, h) = \begin{cases} 0 & h > h_{\max}(r) \cap r \geq R_1 \\ R_1 & h > h_{\max}(r) \cap r < R_1 \\ R_0(r, h) + \sqrt{r^2 - (h - h_0(r, h))^2} & h_{\min} < h < h_{\max} \\ R_2 & h < h_{\min}(r) \end{cases} \quad (\text{A.26})$$

where cutoffs h_{\min} and h_{\max} are taken according to Fig. A.1.

The location of a sphere's centroid is given as

$$R_0(r, h) = \begin{cases} R_0^{\text{bot}}(r) & h < H_{\text{bot}} \\ R_0^{\text{neck}}(r) & h \geq H_{\text{bot}} \end{cases} \quad (\text{A.27})$$

distinguishing the bottom and neck part of the cylinder.

Similarly the vertical location of the sphere's midpoint is given as

$$h_0(r, h) = \begin{cases} h_0^{\text{bot}}(r) & h < H_{\text{bot}} \\ h_0^{\text{neck}}(r) & h \geq H_{\text{bot}} \end{cases}. \quad (\text{A.28})$$

Then $h_{\min}(r) = h_0^{\text{bot}}(r)$.

For the neck, the centroid location is given as

$$h_0^{\text{neck}}(r) = H_{\text{bot}} - \sqrt{r^2 - R_1^2} \quad r > R_1 \quad (\text{A.29})$$

$$R_0^{\text{neck}}(r) = 0 \quad (\text{A.30})$$

and the cutoff reads

$$h_{\max} = \begin{cases} h_0^{\text{neck}}(r) + r & r > R_1 \\ H_{\text{bot}} & r \leq R_1 \end{cases} \quad (\text{A.31})$$

according to the radial symmetry and the intersection with the corner at $h = H_{\text{bot}}$ and $R = R_1$.

For the bottom part of the cylinder, three regimes can be distinguished as shown in Fig. A.1:

- I. A sphere touches both the hull of the cylinder and the horizontal plane when $r \leq H_{\text{bot}}$ and $r \leq R_2 - R_1$.
- II. A sphere touches the hull of the cylinder and intersects with a corner at $h = H_{\text{bot}}$ and $R = R_1$ when $r > R_2 - R_1$ and $h_0 > 0$.
- III. A spheres centroid is located on the bottom plane ($h_0 = 0$) and interects the corner at $h = H_{\text{bot}}$ and $R = R_1$.

Additional constraints apply to keep the sphere center located within the cylinder. The corresponding solutions for h_0 and R_0 write

$$h_0^{\text{bot}}(r) = \begin{cases} H_{\text{bot}} - r & r < R_2 - R_1 \cap r < H_{\text{bot}} \\ H_{\text{bot}} - \sqrt{2(R_2 - R_1)r - (R_2 - R_1)^2} & r \geq R_2 - R_1 \cap h_0^{\text{bot}} > 0 \\ 0 & r > H_{\text{bot}} \cap R_0^{\text{bot}} > 0 \end{cases} \quad (\text{A.32})$$

and

$$R_0^{\text{bot}}(r) = \begin{cases} R_2 - r & r < R_2 - R_1 \cap r < H_{\text{bot}} \\ R_2 - r & r \geq R_2 - R_1 \cap h_0^{\text{bot}} > 0 \\ R_1 - \sqrt{r^2 - H_{\text{bot}}^2} & r > H_{\text{bot}} \cap R_0^{\text{bot}} > 0 \end{cases} \quad (\text{A.33})$$

where the last condition is only evaluated when the other two are not fulfilled in each case. If none of the conditions are satisfied, or $R_0 + r > R_2$, then $V(r) = 0$. This completes the analytical solution for the continuous PSD for a cylinder with neck.

A.3 Transmission-Line Model

The utilized transmission-line model can be drawn as an equivalent circuit with impedance Z_{TLM} as shown in Fig. A.2a. The circuit network underlying the transmission-line model is illustrated in Fig. A.2b. For an overview regarding the equations of such a type of transmission-line model see [134]. The derivation of the equation impedance Z_{TLM} is outlined below for the special case of an Ni-YSZ anode according to [132].

The anode functional layer of thickness L is represented with a single x -coordinate, where $x = 0$ corresponds to the plane in contact with the electrolyte and $x = L$ is the free surface of the anode functional layer where electric contact is established. The functional layer is subdivided into N segments.

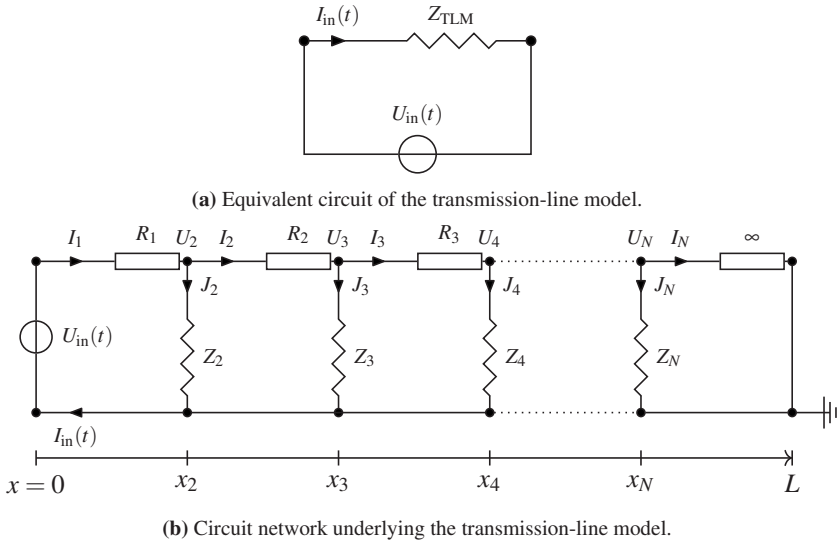


Figure A.2: Electric circuits representing the transmission-line model: Equivalent circuit element (a) and underlying circuit network (b).

The electrically conducting phase (Ni) is assumed to be an ideal conductor and hence is modeled with a vanishing ohmic resistance (bottom row in Fig. A.2b). The ion conductor in each segment i is modeled with an ohmic resistance R_i and the reaction occurring at the three-phase boundary is modeled with an impedance Z_i .

The impedance of the TLM is given by Ohm's law by relating the input voltage and the total current entering the TLM:

$$Z_{\text{TLM}} \equiv \frac{U_{\text{in}}(t)}{I_{\text{in}}(t)} \tag{A.34}$$

In order to obtain an equation related to the circuit elements of the TLM, the following equations hold for each segment $i \in \{1, \dots, N - 1\}$:

$$U_i - U_{i+1} = R_i I_i \quad \text{Ohm's law in YSZ} \quad (\text{A.35})$$

$$I_i - I_{i+1} = J_{i+1} \quad \text{Kirchhoff's law YSZ/TPB} \quad (\text{A.36})$$

$$Z_{i+1} J_{i+1} = U_{i+1} \quad \text{Ohm's law at TPB} \quad (\text{A.37})$$

for the voltages U_i , currents I_i and impedances Z_i .

Additionally, the following boundary conditions apply

$$U_1 = U_{\text{in}}(t) \quad (\text{A.38})$$

$$I_1 = I_{\text{in}}(t) \quad (\text{A.39})$$

$$I_N = 0 \quad (\text{A.40})$$

where the last equation means that a vanishing ion flux is assumed at the free surface (equivalent to $R_N = \infty$).

This is a linear system of $3N - 1$ equations that can be solved exactly for the unknowns $U_{1\dots N}$, $I_{1\dots N}$ and $J_{2\dots N}$. The solution for Z_{TLM} then depends on the number of segments N and becomes tedious to solve as N becomes large.

However, keeping in mind that this is just a discrete representation of the electrode layer, one may associate positions with each of the nodes in the network and interpret each segment given by functions

$$U_i = U(x_i) \quad (\text{A.41})$$

$$I_i = I(x_i) \quad (\text{A.42})$$

$$J_i = J(x_i) \quad (\text{A.43})$$

$$R_i = R(x_i) \quad (\text{A.44})$$

$$Z_i = Z(x_i) \quad (\text{A.45})$$

that depend on the layer depth x .

Placing the segments at equidistant positions, such that $x_1 = 0$ and $x_i = (i + 1)\Delta x$ as well as $\Delta x = L/(N + 2)$, one obtains

$$U(x) - U(x + \Delta x) = R(x)I(x) \quad (\text{A.46})$$

$$I(x) - I(x + \Delta x) = \frac{U(x + \Delta x)}{Z(x + \Delta x)}. \quad (\text{A.47})$$

Let A be the area of the anode orthogonal to the x -direction. It is expected that if the electrode is sufficiently homogeneous that the resistance R_i of the YSZ segments is proportional to the distance between the nodes Δx and inversely proportional to the area A . Thus

$$R_i \approx \frac{\Delta x}{\sigma_{\text{ion,eff}}A} = \chi_1 \Delta x \quad (\text{A.48})$$

where $\sigma_{\text{ion,eff}}$ in S/m denotes the effective conductivity of the ions within YSZ and χ_1 (in Ω/m) is the corresponding ionic resistance of YSZ specific to the thickness of the AFL.

In contrast, the current J flows orthogonal to x and the corresponding impedance Z_i should scale inversely with the length of the TPB contained within the segment of thickness Δx . This length may be expressed by the active TPB length per unit volume l_{ATPB} multiplied by the volume of a segment $\Delta V = A\Delta x$ and hence

$$Z_i \approx \frac{z_{\text{LSR}}}{l_{\text{ATPB}}A\Delta x} = \frac{\zeta}{\Delta x}. \quad (\text{A.49})$$

with some line-specific impedance z_{LSR} in Ωm and a corresponding impedance ζ (also in Ωm) inversely specific to the thickness of the AFL. Dividing equations (A.46)-(A.47) by Δx and going to the limit of an infinite number of segments

($N \rightarrow \infty, \Delta x \rightarrow 0$) this discrete equations turn out to be differential equations for the unknown functions $U(x)$ and $I(x)$

$$U'(x) = -\chi_1 I(x) \quad (\text{A.50})$$

$$I'(x) = -\frac{U(x)}{\zeta} \quad (\text{A.51})$$

that may be expressed solely in terms of the voltage

$$U''(x) = \frac{\chi_1}{\zeta} U(x) \quad (\text{A.52})$$

as a second order ordinary differential equation.

Thus, the $3N - 1$ unknown constants turned into a single unknown function $U(x)$ which clearly simplifies the problem.

The boundary conditions (Eq. (A.38)-(A.40)) now write as

$$Z_{\text{TLM}} = \frac{U(0)}{I(0)} = -\frac{\chi_1 U(0)}{U'(0)} \quad (\text{A.53})$$

$$I(L) = 0 = U'(L). \quad (\text{A.54})$$

Solving Eq. (A.52) subject to these boundary condition, one obtains

$$U(x) = \frac{U(0)}{2} \left(\left(1 - \frac{\sqrt{\zeta \chi_1}}{Z_{\text{TLM}}} \right) e^{\sqrt{\frac{\chi_1}{\zeta}} x} + \left(1 + \frac{\sqrt{\zeta \chi_1}}{Z_{\text{TLM}}} \right) e^{-\sqrt{\frac{\chi_1}{\zeta}} x} \right) \quad (\text{A.55})$$

with the impedance of the TLM

$$Z_{\text{TLM}} = \sqrt{\zeta \chi_1} \coth \left(\sqrt{\frac{\chi_1}{\zeta}} L \right) \quad (\text{A.56})$$

which is the final result.

List of Figures

1.1	Sketch of a two-phase system described by a continuously varying phase field $\phi_\alpha(\mathbf{x}, t)$	3
2.1	Schematic coarse-graining procedure in the bulk with a Gaussian kernel.	8
2.2	Schematic coarse-graining procedure for an interface with a Gaussian kernel.	11
2.3	Schematic of a moving curvilinear coordinate system.	20
2.4	Schematic of a moving surface.	23
2.5	Schematic of an evolving surface.	23
2.6	Schematic of a control volume which moves with a surface.	26
2.7	Equilibrium phase-field profiles for a planar interface in a two-phase model.	40
3.1	Sketch of a symmetric thermal groove and the corresponding quantities: Height h , depth d and width w of the groove.	83
3.2	Small-slope sharp-interface solutions of the groove geometry in non-dimensional form $z_s(u, p)$ from [25].	87
3.3	Two-dimensional simulation setup for the multiphase-field simulation of thermal grooving under a combination of surface and volume diffusion.	88
3.4	Evolution of the thermal groove evaluated by means of the $\phi_\delta = 1/2$ contour under combined surface and volume diffusion in the MPF simulation.	91
3.5	Growth kinetics of characteristic groove dimensions in the MPF model.	93
3.6	Comparison of rescaled groove geometries from the analytical solution [25] and the MPF simulation at three different times.	94

3.7	Chemical potential field $\mu(\mathbf{x}, t)$ (its unit u_E/u_l^3 is omitted) at half the simulation time ($t = 10^5 u_t$) in the vicinity of the grain boundary ($x = 0$).	98
3.8	Chemical potential μ , order parameter ϕ_δ and chemical mobility of the MPF simulation in normal direction at a point close to the triple-junction region.	99
4.1	Different choices of interpolation functions and their corresponding derivatives.	107
4.2	Dimensionless interface velocity \tilde{v} and interfacial energy $\tilde{\sigma}$ as well as dimensionless interface thickness $\tilde{\delta}$ as a function of the dimensionless driving force $\tilde{\epsilon}$	120
4.3	Rescaled order parameter $\varphi(\eta)$ in terms of the dimensionless moving coordinate η for various choices of $\tilde{\epsilon}$	121
4.4	The first six corrections $\varphi_n(\eta)$, $1 \leq n \leq 6$ to the interface profile as a function of the rescaled interface normal coordinate η	136
4.5	Even interface velocity coefficients \tilde{v}_n for three different interpolation functions of integer type.	137
4.6	Even interface thickness coefficients $\tilde{\delta}_n$ for three different interpolation functions of integer type.	139
4.7	Even interface energy coefficients $\tilde{\sigma}_n$ for three different interpolation functions of integer type.	140
4.8	Rescaled order parameter $\varphi(\eta)$ obtained from the numerical simulation and the analytical treatments at a dimensionless driving force of $\tilde{\epsilon} = 3/4$	147
4.9	Comparison between dimensionless interface velocity obtained from the analytic treatment and numerical simulations in the small and large driving-force regime.	148
4.10	Comparison between dimensionless interface width obtained from the analytic treatment and numerical simulations in the small and large driving-force regime.	149
4.11	Comparison between dimensionless interfacial energies obtained from the analytic treatment and numerical simulations in the small and large driving-force regime.	150

5.1	Sketch of the electrochemical processes occurring in a solid-oxide fuel cell (SOFC).	158
5.2	Schematic microstructural view on the transport processes occurring in the porous anode functional layer of an SOFC.	159
5.3	Geometries used for the validation of the tortuosity tool.	164
5.4	Solutions to the Laplace equation obtained by means of the in-house tortuosity solver for a plate with a hole of varying radius.	165
5.5	Solutions to the Laplace equation obtained by means of the in-house tortuosity solver for a cylinder with a neck.	166
5.6	Comparison between tortuosities obtained with the developed PACE3D tool and the FEM software DEALII for two-dimensional and three-dimensional geometries.	167
5.7	Tortuosities at different grid refinement levels for both the PACE3D tool and the FEM software DEALII for two-dimensional and three-dimensional geometries.	168
5.8	Three consecutively refined grids in a top view at $x = H/2$ of the cylinder with neck for $R_1 = R_2/2$	169
5.9	Skeletonization procedure for the detection of the triplephase-boundary for a three-phase system.	171
5.10	Conversion of the thinned voxel skeleton to curved line segments within the three-phase boundary detection algorithm.	173
5.11	Overlay of the initial classified channels with the detected and smoothed TPB (left). Input raw data with one phase removed and the corresponding smoothed TPB network (right).	174
5.12	Schematic highlighting the determination of the continuous particle-size distribution.	176
5.13	Filled volumes detected during the PSD calculation for a 2D and 3D geometry at varying radii.	177
5.14	Plots of the continuous particle-size distribution for well-defined 2D and 3D geometries.	178
5.15	Two-dimensional cross-sections of the Voronoi-constructed anode structures.	182
5.16	Initial particle size distributions of Voronoi-based structures at a variation of YSZ particle diameter and at constant $X_{Ni} = 33\%$	184

5.17	Two-dimensional cross-section of the evolution of the microstructure at $X_{Ni} = 25\%$ and $d_{50}^{YSZ} = 0.92\mu m$	187
5.18	Evolution of the mean nickel diameter with time for MPF simulations of artificially generated SOFC-anode structures at three different nickel content.	188
5.19	Evolution of the nickel tortuosity with time for MPF simulations of artificially generated SOFC-anode structures at three different nickel content.	190
5.20	Streamlines of the electric current (lines parallel to \vec{j}_{ei}) in the tortuosity calculation for generated SOFC-anode structures at varying nickel content.	191
5.21	Evolution of the relative triple-phase boundary length with time for MPF simulations of artificially generated SOFC-anode structures at three different nickel content.	193
5.22	Evolution of the relative triple-phase boundary length with time for MPF simulations of artificially generated SOFC-anode structures at three different nickel content.	195
5.23	Initial anode structures with increased nickel content based on the FIB-SEM reconstructed structure from [119].	199
5.24	Cross-sections of the initial anode microstructures for the multiphase-field simulation studies at varying nickel content.	200
5.25	Cross-sections of the anode microstructure at $X_{Ni} = 29\%$ at initial (left), intermediate (center) and final state (right).	202
5.26	Mean nickel diameter evolution for experimentally-based SOFC anodes for a variation in nickel content.	203
5.27	Tortuosity evolution of the nickel phase for experimentally-based SOFC anodes for a variation in nickel content.	204
5.28	Active triple-phase boundary (corresponding to l_{ATPB}) at initial (top row) and final (bottom row) stages of the MPF simulations.	206
5.29	Triple-phase boundary evolution for experimentally-based SOFC anodes for a variation in nickel content.	207
5.30	Relation of the active triple-phase boundary length l_{ATPB} to polarization resistance R_{pol} for the experimentally-based structures.	209
A.1	Schematic for the derivation of the continuous PSD for a cylinder with neck.	225

A.2 Electric circuits representing the transmission-line model:
Equivalent circuit element (a) and underlying circuit network (b). . . 228

List of Tables

3.1	Normal integral of the dimensionless surface diffusion function I_g for several choices of g	82
3.2	Parameter set utilized for the simulations performed in the current work.	89
4.1	Considered interpolation functions and corresponding derivatives. . .	106
4.2	First order correction to the phase-field profile $\varphi_1(\eta)$ for all common interpolation functions used in PF-models of the obstacle type.	135
4.3	Second order correction to the phase-field profile $\varphi_2(\eta)$ for all common interpolation functions used in PF-models of the obstacle type.	135
4.4	Dimensionless interface velocity coefficients up to order ten for all common interpolation functions.	138
4.5	Dimensionless interface thickness coefficients up to order ten for all common interpolation functions.	139
4.6	Dimensionless interfacial energy coefficients up to order ten for all common interpolation functions.	141
4.7	Parameter set used for the driving force simulations in terms of model units.	145
5.1	Relative errors $e_{\text{rel}} = (\tau_x - \tau_x^{\text{fine}}) / \tau_x^{\text{fine}}$ in percent for various refinement steps of the 2D plate at three selected hole radii.	167
5.2	Relative errors $e_{\text{rel}} = (\tau_x - \tau_x^{\text{fine}}) / \tau_x^{\text{fine}}$ in percent for various refinement steps of the 3D cylinder at three selected neck radii.	168
5.3	Parameter set utilized for the MPF simulations based on the artificially constructed Voronoi AFL-microstructures.	185
5.4	Initial TPB lengths ($l_{\text{TPB}}(0)$) corresponding to the evolution shown in Fig. 5.21.	193

5.5	Spearman correlation coefficients for the MPF simulation studies of nickel coarsening in artificially generated SOFC anode structures.	197
5.6	Parameter set utilized for the MPF simulations based on the experimental FIB-SEM microstructures.	201

Bibliography

- [1] Umberto Lucia. Overview on fuel cells. *Renewable and Sustainable Energy Reviews*, 30:164–169, feb 2014. ISSN 13640321. doi: 10.1016/j.rser.2013.09.025.
- [2] A. Kirubakaran, Shailendra Jain, and R. K. Nema. A review on fuel cell technologies and power electronic interface. *Renewable and Sustainable Energy Reviews*, 13(9):2430–2440, 2009. ISSN 13640321. doi: 10.1016/j.rser.2009.04.004.
- [3] Harumi Yokokawa, Hengyong Tu, Boris Iwanschitz, and Andreas Mai. Fundamental mechanisms limiting solid oxide fuel cell durability. *Journal of Power Sources*, 182(2):400–412, aug 2008. ISSN 03787753. doi: 10.1016/j.jpowsour.2008.02.016.
- [4] San Ping Jiang and Siew Hwa Chan. A review of anode materials development in solid oxide fuel cells. *Journal of Materials Science*, 39(14): 4405–4439, 2004. ISSN 0022-2461. doi: 10.1023/B:JMSC.0000034135.52164.6b.
- [5] Long Qing Chen. Phase-field models for microstructure evolution. *Annual Review of Materials Science*, 32:113–140, 2002. ISSN 00846600. doi: 10.1146/annurev.matsci.32.112001.132041.
- [6] W. J. Boettinger, James A. Warren, C. Beckermann, and A. Karma. Phase-field simulation of solidification. *Annual Review of Materials Science*, 32:163–194, 2002. ISSN 00846600. doi: 10.1146/annurev.matsci.32.101901.155803.

- [7] Ingo Steinbach. Phase-field models in materials science. *Modelling and Simulation in Materials Science and Engineering*, 17(7), 2009. ISSN 09650393. doi: 10.1088/0965-0393/17/7/073001.
- [8] J. S. Rowlinson. Translation of J. D. van der Waals' "The thermodynamik theory of capillarity under the hypothesis of a continuous variation of density". *Journal of Statistical Physics*, 20(2):197–200, feb 1979. ISSN 0022-4715. doi: 10.1007/BF01011513.
- [9] John W. Cahn and John E. Hilliard. Free energy of a nonuniform system. I. Interfacial free energy. *The Journal of Chemical Physics*, 28(2):258–267, 1958. ISSN 00219606. doi: 10.1063/1.1744102.
- [10] Samuel M. Allen and John W. Cahn. A microscopic theory for antiphase boundary motion and its application to antiphase domain coarsening. *Acta Metallurgica*, 27(6):1085–1095, jun 1979. ISSN 00016160. doi: 10.1016/0001-6160(79)90196-2.
- [11] Alain Karma and Wouter-Jan Rappel. Phase-field method for computationally efficient modeling of solidification with arbitrary interface kinetics. *Physical Review E*, 53(4):R3017–R3020, apr 1996. ISSN 1063-651X. doi: 10.1103/PhysRevE.53.R3017.
- [12] Alain Karma and Wouter Jan Rappel. Quantitative phase-field modeling of dendritic growth in two and three dimensions. *Physical Review E - Statistical Physics, Plasmas, Fluids, and Related Interdisciplinary Topics*, 57(4):4323–4349, apr 1998. ISSN 1063651X. doi: 10.1103/PhysRevE.57.4323.
- [13] Alain Karma. Phase-Field Formulation for Quantitative Modeling of Alloy Solidification. *Physical Review Letters*, 87(11):115701, aug 2001. ISSN 0031-9007. doi: 10.1103/PhysRevLett.87.115701.
- [14] I. Steinbach, F. Pezzolla, B. Nestler, M. Seeßelberg, R. Prieler, G. J. Schmitz, and J. L.L. Rezende. A phase field concept for multiphase systems. *Physica D: Nonlinear Phenomena*, 94(3):135–147, 1996. ISSN 01672789. doi: 10.1016/0167-2789(95)00298-7.

-
- [15] J. Tiaden, B. Nestler, H.J. Diepers, and I. Steinbach. The multiphase-field model with an integrated concept for modelling solute diffusion. *Physica D: Nonlinear Phenomena*, 115(1-2):73–86, apr 1998. ISSN 01672789. doi: 10.1016/S0167-2789(97)00226-1.
- [16] I. Steinbach and F. Pezzolla. A generalized field method for multiphase transformations using interface fields. *Physica D: Nonlinear Phenomena*, 134(4):385–393, 1999. ISSN 01672789. doi: 10.1016/S0167-2789(99)00129-3.
- [17] Britta Nestler, Harald Garcke, and Björn Stinner. Multicomponent alloy solidification: Phase-field modeling and simulations. *Physical Review E*, 71(4):041609, apr 2005. ISSN 1539-3755. doi: 10.1103/PhysRevE.71.041609.
- [18] J. Eiken, B. Böttger, and I. Steinbach. Multiphase-field approach for multicomponent alloys with extrapolation scheme for numerical application. *Physical Review E - Statistical, Nonlinear, and Soft Matter Physics*, 73(6): 1–9, 2006. ISSN 15393755. doi: 10.1103/PhysRevE.73.066122.
- [19] Mathis Plapp. Unified derivation of phase-field models for alloy solidification from a grand-potential functional. *Physical Review E - Statistical, Nonlinear, and Soft Matter Physics*, 84(3):1–15, sep 2011. ISSN 15393755. doi: 10.1103/PhysRevE.84.031601.
- [20] Abhik Choudhury and Britta Nestler. Grand-potential formulation for multicomponent phase transformations combined with thin-interface asymptotics of the double-obstacle potential. *Physical Review E - Statistical, Nonlinear, and Soft Matter Physics*, 85(2):021602, feb 2012. ISSN 1539-3755. doi: 10.1103/PhysRevE.85.021602.
- [21] P. G. Kubendran Amos, Ephraim Schoof, Daniel Schneider, and Britta Nestler. Chemo-elastic phase-field simulation of the cooperative growth of mutually-accommodating Widmanstätten plates. *Journal of Alloys and Compounds*, 767:1141–1154, 2018. ISSN 09258388. doi: 10.1016/j.jallcom.2018.07.138.

- [22] Daniel Schneider, Oleg Tschukin, Abhik Choudhury, Michael Selzer, Thomas Böhlke, and Britta Nestler. Phase-field elasticity model based on mechanical jump conditions. *Computational Mechanics*, 55(5):887–901, 2015. ISSN 01787675. doi: 10.1007/s00466-015-1141-6.
- [23] Daniel Schneider, Ephraim Schoof, Oleg Tschukin, Andreas Reiter, Christoph Herrmann, Felix Schwab, Michael Selzer, and Britta Nestler. Small strain multiphase-field model accounting for configurational forces and mechanical jump conditions. *Computational Mechanics*, 61(3):297–297, mar 2018. ISSN 0178-7675. doi: 10.1007/s00466-017-1485-1.
- [24] Paul W. Hoffrogge, Arnab Mukherjee, E. S. Nani, P. G. Kubendran Amos, Fei Wang, Daniel Schneider, and Britta Nestler. Multiphase-field model for surface diffusion and attachment kinetics in the grand-potential framework. *Physical Review E*, 103(3):033307, mar 2021. ISSN 2470-0045. doi: 10.1103/PhysRevE.103.033307.
- [25] S.R Srinivasan and R Trivedi. Theory of grain boundary grooving under the combined action of the surface and volume diffusion mechanisms. *Acta Metallurgica*, 21(5):611–620, may 1973. ISSN 00016160. doi: 10.1016/0001-6160(73)90070-9.
- [26] Robert W. Balluffi, Samuel M. Allen, and W. Craig Carter. *Kinetics of materials*. Wiley-Interscience, Hoboken, NJ, 2005. ISBN 0471246891; 9780471246893.
- [27] Gretchen M Mavrovouniotis and Howard Brenner. A Micromechanical Investigation of Interfacial Transport Processes. I. Interfacial Conservation Equations. *Philosophical Transactions: Physical Sciences and Engineering*, 345(1675):165–207, 1993. ISSN 09628428.
- [28] Eun-Suok Oh John C. Slattery, Leonard Sagis. *Interfacial Transport Phenomena*. Springer US, Boston, MA, 2007. ISBN 978-0-387-38438-2. doi: 10.1007/978-0-387-38442-9.

-
- [29] G. P. Moeckel. Thermodynamics of an interface. *Archive for Rational Mechanics and Analysis*, 57(3):255–280, 1975. ISSN 0003-9527. doi: 10.1007/BF00280158.
- [30] Ingo Müller. *Thermodynamics*. Interaction of mechanics and mathematics series. Pitman Advanced Publ. Program, Boston, 1985. ISBN 0273085778.
- [31] William M Deen. *Analysis of transport phenomena*. Oxford University Press, New York, second edition, 2013. ISBN 9780199740253; 0199740259.
- [32] P. W. Voorhees. The theory of Ostwald ripening. *Journal of Statistical Physics*, 38(1-2):231–252, jan 1985. ISSN 0022-4715. doi: 10.1007/BF01017860.
- [33] Harald Garcke, Britta Nestler, and Bjorn Stinner. A Diffuse Interface Model for Alloys with Multiple Components and Phases. *SIAM Journal on Applied Mathematics*, 64(3):775–799, jan 2004. ISSN 0036-1399. doi: 10.1137/S0036139902413143.
- [34] Herbert B Callen. *Thermodynamics and an introduction to thermostatistics*. Wiley, New York, NY [u.a.], 2. ed. edition, 1985. ISBN 9780471862567; 0471862568; 0471610569.
- [35] Robert T DeHoff. *Thermodynamics in materials science*. Number 1. Taylor and Francis, Boca Raton, Fla. [u.a.], 2. ed. edition, 2003. ISBN 0849340659; 9780849340659. doi: 10.16309/j.cnki.issn.1007-1776.2003.03.004.
- [36] H. J. V. Tyrrell. The origin and present status of Fick’s diffusion law. *Journal of Chemical Education*, 41(7):397, jul 1964. ISSN 0021-9584. doi: 10.1021/ed041p397.
- [37] Richard P. Feynman, Robert B. Leighton, and Matthew Sands. *The Feynman Lectures on Physics, Vol. 2: Mainly Electromagnetism and Matter*. Addison-Wesley, Inc., Reading, MA, 1964.
- [38] Erwin Kreyszig. *Differential Geometry*. Dover Publications, Inc., New York, 1991. ISBN 9780486667218; 0486667219.

- [39] Paolo Cermelli, Eliot Fried, and Morton E. Gurtin. Transport relations for surface integrals arising in the formulation of balance laws for evolving fluid interfaces. *Journal of Fluid Mechanics*, 544:339, nov 2005. ISSN 0022-1120. doi: 10.1017/S0022112005006695.
- [40] Morton E Gurtin, Allan Struthers, and William O Williams. A TRANSPORT THEOREM FOR MOVING INTERFACES. *Quarterly of Applied Mathematics*, 47(4):773–777, 1989. ISSN 0033569X, 15524485.
- [41] Clifford A. Truesdell. Cauchy and the modern mechanics of continua. *Revue d'histoire des sciences*, 45(1):5–24, 1992. ISSN 0151-4105. doi: 10.3406/rhs.1992.4229.
- [42] William W. Mullins. Theory of thermal grooving. *Journal of Applied Physics*, 28(3):333–339, mar 1957. ISSN 00218979. doi: 10.1063/1.1722742.
- [43] David Turnbull. Theory of Grain Boundary Migration Rates. *JOM*, 3(8): 661–665, aug 1951. ISSN 1047-4838. doi: 10.1007/BF03397362.
- [44] F. J Humphreys and M. Hatherly. *Recrystallization and Related Annealing Phenomena*. Elsevier, 2. ed. edition, 2004. ISBN 9780080441641. doi: 10.1016/B978-0-08-044164-1.X5000-2.
- [45] Günter Gottstein and Lasar S. Shvindlerman. *Grain Boundary Migration in Metals*, volume 31. CRC Press, Boca Raton, Fla. [u.a.], 2nd edition, dec 2009. ISBN 9780429147388. doi: 10.1201/9781420054361.
- [46] J.W. Cahn and J.E. Taylor. Surface motion by surface diffusion. *Acta Metallurgica et Materialia*, 42(4):1045–1063, apr 1994. ISSN 09567151. doi: 10.1016/0956-7151(94)90123-6.
- [47] Andreas Rätz, Angel Ribalta, and Axel Voigt. Surface evolution of elastically stressed films under deposition by a diffuse interface model. *Journal of Computational Physics*, 214(1):187–208, may 2006. ISSN 00219991. doi: 10.1016/j.jcp.2005.09.013.

-
- [48] Mathis Plapp. Phase-Field Models. In *Handbook of Crystal Growth*, pages 631–668. Elsevier, 2015. ISBN 9780444563699. doi: 10.1016/B978-0-444-56369-9.00015-0.
- [49] Britta Nestler. A 3D parallel simulator for crystal growth and solidification in complex alloy systems. *Journal of Crystal Growth*, 275(1-2):273–278, 2005. ISSN 00220248. doi: 10.1016/j.jcrysgro.2004.10.121.
- [50] Abhik Narayan Choudhury. *Quantitative phase-field model for phase transformations in multi-component alloys*. PhD thesis, 2013.
- [51] Johannes Hötzer, Oleg Tschukin, Marouen Ben Said, Marco Berghoff, Marcus Jainta, Georges Barthelemy, Nikolay Smorchkov, Daniel Schneider, Michael Selzer, and Britta Nestler. Calibration of a multi-phase field model with quantitative angle measurement. *Journal of Materials Science*, 51(4): 1788–1797, 2016. ISSN 15734803. doi: 10.1007/s10853-015-9542-7.
- [52] A. Choudhury, Geeta M., and B. Nestler. Influence of solid-solid interface anisotropy on three-phase eutectic growth during directional solidification. *EPL (Europhysics Letters)*, 101(2):26001, jan 2013. ISSN 0295-5075. doi: 10.1209/0295-5075/101/26001.
- [53] Sumanth Nani Enugala. *Some refinements in the phase-field and sharp interface treatments of eutectic growth*. PhD thesis, Karlsruher Institut für Technologie (KIT), 2021.
- [54] A. A. Wheeler, W. J. Boettinger, and G. B. McFadden. Phase-field model for isothermal phase transitions in binary alloys. *Physical Review A*, 45(10): 7424–7439, may 1992. ISSN 1050-2947. doi: 10.1103/PhysRevA.45.7424.
- [55] Seong Gyoon Kim, Won Tae Kim, and Toshio Suzuki. Phase-field model for binary alloys. *Physical Review E*, 60(6):7186–7197, dec 1999. ISSN 1063-651X. doi: 10.1103/PhysRevE.60.7186.
- [56] Britta Nestler and Abhik Choudhury. Phase-field modeling of multi-component systems. *Current Opinion in Solid State and Materials*

- Science*, 15(3):93–105, 2011. ISSN 13590286. doi: 10.1016/j.cossms.2011.01.003.
- [57] Blas Echebarria, Roger Folch, Alain Karma, and Mathis Plapp. Quantitative phase-field model of alloy solidification. *Physical Review E*, 70(6):061604, dec 2004. ISSN 1539-3755. doi: 10.1103/PhysRevE.70.061604.
- [58] J. C. Ramirez, C. Beckermann, A. Karma, and H.-J. Diepers. Phase-field modeling of binary alloy solidification with coupled heat and solute diffusion. *Physical Review E*, 69(5):051607, may 2004. ISSN 1539-3755. doi: 10.1103/PhysRevE.69.051607.
- [59] L S Darken. Diffusion, Mobility And Their Interrelation Through Free Energy In Binary Metallic Systems. *Trans AIME*, 175:184–201, 1948.
- [60] Abhik Choudhury, Michael Kellner, and Britta Nestler. A method for coupling the phase-field model based on a grand-potential formalism to thermodynamic databases. *Current Opinion in Solid State and Materials Science*, 19(5):287–300, 2015. ISSN 13590286. doi: 10.1016/j.cossms.2015.03.003.
- [61] Sanjay Puri, Alan J. Bray, and Joel L. Lebowitz. Phase-separation kinetics in a model with order-parameter-dependent mobility. *Physical Review E*, 56(1):758–765, jul 1997. ISSN 1063-651X. doi: 10.1103/PhysRevE.56.758.
- [62] Jingzhi Zhu, Long-Qing Chen, Jie Shen, and Veena Tikare. Coarsening kinetics from a variable-mobility Cahn-Hilliard equation: Application of a semi-implicit Fourier spectral method. *Physical Review E*, 60(4):3564–3572, oct 1999. ISSN 1063-651X. doi: 10.1103/PhysRevE.60.3564.
- [63] D. J. Seol, S. Y. Hu, Z. K. Liu, L. Q. Chen, S. G. Kim, and K. H. Oh. Phase-field modeling of stress-induced surface instabilities in heteroepitaxial thin films. *Journal of Applied Physics*, 98(4):044910, aug 2005. ISSN 0021-8979. doi: 10.1063/1.1996856.
- [64] Junseok Kim. A numerical method for the Cahn–Hilliard equation with a variable mobility. *Communications in Nonlinear Science and Numerical*

-
- Simulation*, 12(8):1560–1571, dec 2007. ISSN 10075704. doi: 10.1016/j.cnsns.2006.02.010.
- [65] Solmaz Torabi, John Lowengrub, Axel Voigt, and Steven Wise. A new phase-field model for strongly anisotropic systems. *Proceedings of the Royal Society A: Mathematical, Physical and Engineering Sciences*, 465(2105): 1337–1359, 2009. ISSN 14712946. doi: 10.1098/rspa.2008.0385.
- [66] Wei Jiang, Weizhu Bao, Carl V. Thompson, and David J. Srolovitz. Phase field approach for simulating solid-state dewetting problems. *Acta Materialia*, 60(15):5578–5592, sep 2012. ISSN 13596454. doi: 10.1016/j.actamat.2012.07.002.
- [67] D Yeon, P Cha, and M Grant. Phase field model of stress-induced surface instabilities: Surface diffusion. *Acta Materialia*, 54(6):1623–1630, apr 2006. ISSN 13596454. doi: 10.1016/j.actamat.2005.12.002.
- [68] Shibin Dai and Qiang Du. Coarsening Mechanism for Systems Governed by the Cahn–Hilliard Equation with Degenerate Diffusion Mobility. *Multiscale Modeling & Simulation*, 12(4):1870–1889, jan 2014. ISSN 1540-3459. doi: 10.1137/140952387.
- [69] Alpha A. Lee, Andreas Münch, and Endre Süli. Degenerate mobilities in phase field models are insufficient to capture surface diffusion. *Applied Physics Letters*, 107(8):081603, aug 2015. ISSN 0003-6951. doi: 10.1063/1.4929696.
- [70] Alpha Albert Lee, Andreas Münch, and Endre Süli. Sharp-Interface Limits of the Cahn–Hilliard Equation with Degenerate Mobility. *SIAM Journal on Applied Mathematics*, 76(2):433–456, jan 2016. ISSN 0036-1399. doi: 10.1137/140960189.
- [71] Alpha Albert Lee, Andreas Münch, and Endre Süli. Response to “Comment on ‘Degenerate mobilities in phase field models are insufficient to capture surface diffusion’” [Appl. Phys. Lett. 108 , 036101 (2016)]. *Applied*

- Physics Letters*, 108(3):036102, jan 2016. ISSN 0003-6951. doi: 10.1063/1.4939931.
- [72] Axel Voigt. Comment on “Degenerate mobilities in phase field models are insufficient to capture surface diffusion” [Appl. Phys. Lett. 107 , 081603 (2015)]. *Applied Physics Letters*, 108(3):036101, jan 2016. ISSN 0003-6951. doi: 10.1063/1.4939930.
- [73] Marco Salvalaglio, Roberto Bergamaschini, Rainer Backofen, Axel Voigt, Francesco Montalenti, and Leo Miglio. Phase-field simulations of faceted Ge/Si-crystal arrays, merging into a suspended film. *Applied Surface Science*, 391:33–38, jan 2017. ISSN 01694332. doi: 10.1016/j.apsusc.2016.05.075.
- [74] W. Beck Andrews, Kate L. M. Elder, Peter W. Voorhees, and Katsuyo Thornton. Effect of transport mechanism on the coarsening of bicontinuous structures: A comparison between bulk and surface diffusion. *Physical Review Materials*, 4(10):103401, oct 2020. ISSN 2475-9953. doi: 10.1103/PhysRevMaterials.4.103401.
- [75] Marco Salvalaglio, Mohammed Bouabdellaoui, Monica Bollani, Abdennacer Benali, Luc Favre, Jean-Benoit Claude, Jerome Wenger, Pietro de Anna, Francesca Intonti, Axel Voigt, and Marco Abbarchi. Hyperuniform Monocrystalline Structures by Spinodal Solid-State Dewetting. *Physical Review Letters*, 125(12):126101, sep 2020. ISSN 0031-9007. doi: 10.1103/PhysRevLett.125.126101.
- [76] Clemens Gugenberger, Robert Spatschek, and Klaus Kassner. Comparison of phase-field models for surface diffusion. *Physical Review E*, 78(1): 016703, jul 2008. ISSN 1539-3755. doi: 10.1103/PhysRevE.78.016703.
- [77] Marco Salvalaglio, Axel Voigt, and Steven M. Wise. Doubly degenerate diffuse interface models of surface diffusion. *Mathematical Methods in the Applied Sciences*, 44(7):5385–5405, may 2021. ISSN 0170-4214. doi: 10.1002/mma.7116.

- [78] Yu U. Wang. Computer modeling and simulation of solid-state sintering: A phase field approach. *Acta Materialia*, 54(4):953–961, feb 2006. ISSN 13596454. doi: 10.1016/j.actamat.2005.10.032.
- [79] Nele Moelans, Bart Blanpain, and Patrick Wollants. A Phase Field Model for grain Growth and Thermal Grooving in Thin Films with Orientation Dependent Surface Energy. *Solid State Phenomena*, 129:89–94, nov 2007. ISSN 1662-9779. doi: 10.4028/www.scientific.net/SSP.129.89.
- [80] A. Novick-Cohen. Triple-junction motion for an Allen–Cahn/Cahn–Hilliard system. *Physica D: Nonlinear Phenomena*, 137(1-2):1–24, mar 2000. ISSN 01672789. doi: 10.1016/S0167-2789(99)00162-1.
- [81] Amy Novick-Cohen and Lydia Peres Hari. Geometric motion for a degenerate Allen-Cahn/Cahn-Hilliard system: The partial wetting case. *Physica D: Nonlinear Phenomena*, 209(1-4):205–235, sep 2005. ISSN 01672789. doi: 10.1016/j.physd.2005.06.028.
- [82] Lynda Amirouche and Mathis Plapp. Phase-field modeling of the discontinuous precipitation reaction. *Acta materialia*, 57(1):237–247, 2009.
- [83] Johannes Hötzer, Marco Seiz, Michael Kellner, Wolfgang Rheinheimer, and Britta Nestler. Phase-field simulation of solid state sintering. *Acta Materialia*, 164:184–195, 2019. ISSN 13596454. doi: 10.1016/j.actamat.2018.10.021.
- [84] Donald Ervin Knuth. *The art of computer programming*, volume 3: Sorting. Addison-Wesley, Reading, Mass., 2. ed. edition, 1998. ISBN 0201896850.
- [85] P. S. Maiya and J. M. Blakely. Surface Self-Diffusion and Surface Energy of Nickel. *Journal of Applied Physics*, 38(2):698–704, feb 1967. ISSN 0021-8979. doi: 10.1063/1.1709399.
- [86] B. Mills, P. Douglas, and G.M. Leak. Surface self-diffusion of nickel. *Trans Met Soc AIME*, 245(6):1291–1296, 1969.

- [87] R. F. Canon and J. P. Stark. Grain Boundary Self-Diffusion in Nickel. *Journal of Applied Physics*, 40(11):4366–4373, oct 1969. ISSN 0021-8979. doi: 10.1063/1.1657200.
- [88] E. E. Latta and H. P. Bonzel. Anisotropy of Surface Self-Diffusion on Ni(110). *Physical Review Letters*, 38(15):839–841, apr 1977. ISSN 0031-9007. doi: 10.1103/PhysRevLett.38.839.
- [89] H.P. Bonzel and E.E. Latta. Surface self-diffusion on Ni(110): Temperature dependence and directional anisotropy. *Surface Science*, 76(2):275–295, sep 1978. ISSN 00396028. doi: 10.1016/0039-6028(78)90098-5.
- [90] Sergiy V. Divinski, Gerrit Reglitz, and Gerhard Wilde. Grain boundary self-diffusion in polycrystalline nickel of different purity levels. *Acta Materialia*, 58(2):386–395, jan 2010. ISSN 13596454. doi: 10.1016/j.actamat.2009.09.015.
- [91] W.W. W Mullins. Grain boundary grooving by volume diffusion. *Transactions of the American Institute of Mining and Metallurgical Engineers*, 218(2):354–361, 1960.
- [92] Simon Daubner, Paul W Hoffrogge, Martin Minar, and Britta Nestler. Triple junction benchmark for multiphase-field and multi-order parameter models. *Computational Materials Science*, 219(December 2022):111995, feb 2023. ISSN 09270256. doi: 10.1016/j.commatsci.2022.111995.
- [93] PC Fife and Oliver Penrose. Interfacial dynamics for thermodynamically consistent phase-field models with nonconserved order parameter. *Electron. J. Differential Equations*, 1995(16):1–49, 1995.
- [94] Robert F Almgren. Second-Order Phase Field Asymptotics for Unequal Conductivities. *SIAM Journal on Applied Mathematics*, 59(6):2086–2107, 1999. ISSN 00361399.
- [95] Munekazu Ohno, Tomohiro Takaki, and Yasushi Shibuta. Variational formulation and numerical accuracy of a quantitative phase-field model for

- binary alloy solidification with two-sided diffusion. *Physical Review E*, 93(1), 2016. ISSN 24700053. doi: 10.1103/PhysRevE.93.012802.
- [96] R. Folch, J. Casademunt, A. Hernández-Machado, and L. Ramírez-Piscina. Phase-field model for Hele-Shaw flows with arbitrary viscosity contrast. I. Theoretical approach. *Physical Review E*, 60(2):1724–1733, aug 1999. ISSN 1063-651X. doi: 10.1103/PhysRevE.60.1724.
- [97] Daniel Schneider. *Phasenfeldmodellierung mechanisch getriebener Grenzflächenbewegungen in mehrphasigen Systemen*. PhD thesis, Karlsruher Institut für Technologie (KIT), 2017.
- [98] W. M. Robertson. Grain-boundary grooving by surface diffusion for finite surface slopes. *Journal of Applied Physics*, 42(1):463–467, jan 1971. ISSN 00218979. doi: 10.1063/1.1659625.
- [99] E. S. Nani and Britta Nestler. Asymptotic analysis of multi-phase-field models: A thorough consideration of binary interfaces. *Physical Review E*, 105(1), 2022. ISSN 24700053. doi: 10.1103/PhysRevE.105.014802.
- [100] E. S. Nani and Britta Nestler. Asymptotic analysis of multi-phase-field models: A thorough consideration of junctions. *Physical Review E*, 107(2): 1–21, 2023. ISSN 24700053. doi: 10.1103/PhysRevE.107.024803.
- [101] G. B. McFadden, A. A. Wheeler, and D. M. Anderson. Thin interface asymptotics for an energy/entropy approach to phase-field models with unequal conductivities. *Physica D: Nonlinear Phenomena*, 144(1-2): 154–168, 2000. ISSN 01672789. doi: 10.1016/S0167-2789(00)00064-6.
- [102] Ephraim Schoof, Daniel Schneider, Nick Streichhan, Tobias Mittnacht, Michael Selzer, and Britta Nestler. Multiphase-field modeling of martensitic phase transformation in a dual-phase microstructure. *International Journal of Solids and Structures*, 134:181–194, mar 2018. ISSN 00207683. doi: 10.1016/j.ijsolstr.2017.10.032.
- [103] P G Kubendran Amos, L T Mushongera, and Britta Nestler. Phase-field analysis of volume-diffusion controlled shape-instabilities in metallic

- systems-I : 2-Dimensional plate-like structures. *Computational Materials Science*, 144:363–373, 2018. ISSN 0927-0256. doi: 10.1016/j.commatsci.2017.12.045.
- [104] Kumar Ankit, Britta Nestler, Michael Selzer, and Mathias Reichardt. Phase-field study of grain boundary tracking behavior in crack-seal microstructures. *Contributions to Mineralogy and Petrology*, 166(6): 1709–1723, 2013. ISSN 00107999. doi: 10.1007/s00410-013-0950-x.
- [105] Kumar Ankit, Hui Xing, Michael Selzer, Britta Nestler, and Martin E. Glicksman. Surface rippling during solidification of binary polycrystalline alloy: Insights from 3-D phase-field simulations. *Journal of Crystal Growth*, 457:52–59, 2017. ISSN 00220248. doi: 10.1016/j.jcrysgro.2016.05.033.
- [106] Carl M. Bender and Steven A. Orszag. *Advanced mathematical methods for scientists and engineers*, volume 1: Asymptotic methods and perturbation theory. Springer, New York, 1999. ISBN 0387989315; 9780387989310; 9781441931870.
- [107] George E. P. Box. Science and Statistics. *Journal of the American Statistical Association*, 71(356):791, dec 1976. ISSN 01621459. doi: 10.2307/2286841.
- [108] Jochen Joos, Thomas Carraro, André Weber, and Ellen Ivers-Tiffée. Reconstruction of porous electrodes by FIB/SEM for detailed microstructure modeling. *Journal of Power Sources*, 196(17):7302–7307, 2011. ISSN 03787753. doi: 10.1016/j.jpowsour.2010.10.006.
- [109] Jochen Joos. *Microstructural Characterisation, Modelling and Simulation of Solid Oxide Fuel Cell Cathodes*. PhD thesis, Karlsruher Institut für Technologie (KIT), 2017.
- [110] David J Griffiths. *Introduction to Electrodynamics*. Pearson Education, Inc., Glenview, 4. ed. edition, 2013. ISBN 978-0-321-85656-2.
- [111] Daniel Arndt, Wolfgang Bangerth, Denis Davydov, Timo Heister, Luca Heltai, Martin Kronbichler, Matthias Maier, Jean-Paul Pelteret, Bruno

- Turcksin, and David Wells. The deal.II finite element library: Design, features, and insights. *Computers & Mathematics with Applications*, 81: 407–422, 2021. ISSN 0898-1221. doi: 10.1016/j.camwa.2020.02.022.
- [112] Naoki Shikazono, Daisuke Kanno, Katsuhisa Matsuzaki, Hisanori Teshima, Shinji Sumino, and Nobuhide Kasagi. Numerical Assessment of SOFC Anode Polarization Based on Three-Dimensional Model Microstructure Reconstructed from FIB-SEM Images. *Journal of The Electrochemical Society*, 157(5):B665, 2010. ISSN 00134651. doi: 10.1149/1.3330568.
- [113] Kàlmàn Palàgyi and Attila Kuba. A 3D 6-subiteration thinning algorithm for extracting medial lines. *Pattern Recognition Letters*, 19(7):613–627, may 1998. ISSN 01678655. doi: 10.1016/S0167-8655(98)00031-2.
- [114] Beat Münch and Lorenz Holzer. Contradicting geometrical concepts in pore size analysis attained with electron microscopy and mercury intrusion. *Journal of the American Ceramic Society*, 91(12):4059–4067, 2008. ISSN 00027820. doi: 10.1111/j.1551-2916.2008.02736.x.
- [115] Moses Ender. *Mikrostrukturelle Charakterisierung, Modellentwicklung und Simulation poröser Elektroden für Lithiumionenzellen*, volume 26. 2014. ISBN 9783731502050.
- [116] Toyofumi Saito and Jun-Ichiro Toriwaki. New algorithms for euclidean distance transformation of an n-dimensional digitized picture with applications. *Pattern Recognition*, 27(11):1551–1565, nov 1994. ISSN 00313203. doi: 10.1016/0031-3203(94)90133-3.
- [117] M. Trini, P. S. Jørgensen, A. Hauch, J. J. Bentzen, P. V. Hendriksen, and M. Chen. 3D Microstructural Characterization of Ni/YSZ Electrodes Exposed to 1 Year of Electrolysis Testing. *Journal of The Electrochemical Society*, 166(2):F158–F167, feb 2019. ISSN 0013-4651. doi: 10.1149/2.1281902jes.

- [118] Florian Wankmüller. *Mehrskalige Charakterisierung der Hochtemperatur-Brennstoffzelle (SOFC)*. PhD thesis, Karlsruher Institut für Technologie (KIT), 2022.
- [119] Paul W. Hoffrogge, Daniel Schneider, Florian Wankmüller, Matthias Meffert, Dagmar Gerthsen, André Weber, Britta Nestler, and Matthias Wieler. Performance estimation by multiphase-field simulations and transmission-line modeling of nickel coarsening in FIB-SEM reconstructed Ni-YSZ SOFC anodes I: Influence of wetting angle. *Journal of Power Sources*, 570(April):233031, jun 2023. ISSN 03787753. doi: 10.1016/j.jpowsour.2023.233031.
- [120] Patricia Haremski, Lars Epple, Matthias Wieler, Piero Lupetin, Leonid Klinger, Eugen Rabkin, and Michael J. Hoffmann. Grain Boundary Grooving by Surface Diffusion in Nickel Bicrystals. *Acta Materialia*, 241: 118334, dec 2022. ISSN 13596454. doi: 10.1016/j.actamat.2022.118334.
- [121] Patricia Haremski. Diffusionseigenschaften von Nickel in einer Festoxid-Brennstoffzelle. (November), 2022.
- [122] Richard Tran, Zihan Xu, Balachandran Radhakrishnan, Donald Winston, Wenhao Sun, Kristin A. Persson, and Shyue Ping Ong. Data Descriptor: Surface energies of elemental crystals. *Scientific Data*, 3:0–13, 2016. ISSN 20524463. doi: 10.1038/sdata.2016.80.
- [123] Matthias Kappeler, Anika Maruszczyk, and Benedikt Ziebarth. Simulation of nickel surfaces using ab-initio and empirical methods. *Materialia*, 12 (March):100675, aug 2020. ISSN 25891529. doi: 10.1016/j.mtla.2020.100675.
- [124] Fengcheng Cai. Phase-field simulation studies of microstructural effects on nickel-coarsening in solid-oxide fuel-cell anodes. Master’s thesis, Karlsruher Institut für Technologie (KIT), 2020.
- [125] Patricia Haremski, Lars Epple, Matthias Wieler, Piero Lupetin, Richard Thelen, and Michael J. Hoffmann. A thermal grooving study of relative

- grain boundary energies of nickel in polycrystalline Ni and in a Ni/YSZ anode measured by atomic force microscopy. *Acta Materialia*, 214:116936, aug 2021. ISSN 13596454. doi: 10.1016/j.actamat.2021.116936.
- [126] John Melngailis. Focused ion beam technology and applications. *Journal of Vacuum Science & Technology B: Microelectronics Processing and Phenomena*, 5(2):469–495, mar 1987. ISSN 0734-211X. doi: 10.1116/1.583937.
- [127] L. Holzer and M. Cantoni. Review of FIB-Tomography. *Nanofabrication Using Focused Ion and Electron Beams: Principles and Applications*, pages 410–435, 2011.
- [128] Marco Cantoni and Lorenz Holzer. Advances in 3D focused ion beam tomography. *MRS Bulletin*, 39(4):354–360, apr 2014. ISSN 0883-7694. doi: 10.1557/mrs.2014.54.
- [129] M. Meffert, F. Wankmüller, H. Störmer, A. Weber, P. Lupetin, E. Ivers-Tiffée, and D. Gerthsen. Optimization of Material Contrast for Efficient FIB-SEM Tomography of Solid Oxide Fuel Cells. *Fuel Cells*, 20(5):580–591, oct 2020. ISSN 1615-6846. doi: 10.1002/fuce.202000080.
- [130] Florian Wankmüller, Matthias Meffert, Niklas Russner, André Weber, Johannes Schmiege, Heike Störmer, Thorsten Dickel, Piero Lupetin, Nicolas Maier, Dagmar Gerthsen, and Ellen Ivers-Tiffée. Multi-scale characterization of ceramic inert-substrate-supported and co-sintered solid oxide fuel cells. *Journal of Materials Science*, 55(25):11120–11136, sep 2020. ISSN 0022-2461. doi: 10.1007/s10853-020-04873-3.
- [131] Daniel Westhoff, Ingo Manke, and Volker Schmidt. Generation of virtual lithium-ion battery electrode microstructures based on spatial stochastic modeling. *Computational Materials Science*, 151(February):53–64, aug 2018. ISSN 09270256. doi: 10.1016/j.commatsci.2018.04.060.
- [132] Sebastian Dierickx, Jochen Joos, André Weber, and Ellen Ivers-Tiffée. Advanced impedance modelling of Ni/8YSZ cermet anodes. *Electrochimica*

Acta, 265:736–750, mar 2018. ISSN 00134686. doi:
10.1016/j.electacta.2017.12.029.

- [133] Patrick Altschuh. *Skalenübergreifende Analyse makroporöser Membranen im Kontext digitaler Zwillinge*. PhD thesis, Karlsruher Institut für Technologie (KIT), 2020.
- [134] Juan Bisquert. Influence of the boundaries in the impedance of porous film electrodes. *Physical Chemistry Chemical Physics*, 2(18):4185–4192, 2000. ISSN 14639076. doi: 10.1039/b001708f.

Schriftenreihe des Instituts für Angewandte Materialien

ISSN 2192-9963

Eine vollständige Übersicht der Bände finden Sie im Verlagsshop

- Band 50 Michael Selzer
**Mechanische und Strömungsmechanische Topologie-
optimierung mit der Phasenfeldmethode.**
ISBN 978-3-7315-0431-3
- Band 51 Michael Mahler
**Entwicklung einer Auswertemethode für
bruchmechanische Versuche an kleinen Proben
auf der Basis eines Kohäsivzonenmodells.**
ISBN 978-3-7315-0441-2
- Band 52 Christoph Bohnert
**Numerische Untersuchung des Verformungs- und
Bruchverhaltens von einkristallinem Wolfram auf
mikroskopischer Ebene.**
ISBN 978-3-7315-0444-3
- Band 53 Stefan Guth
**Schädigung und Lebensdauer von Nickelbasislegierungen
unter thermisch-mechanischer Ermüdungsbeanspruchung
bei verschiedenen Phasenlagen.**
ISBN 978-3-7315-0445-0
- Band 54 Markus Klinsmann
**The Effects of Internal Stress and Lithium Transport on
Fracture in Storage Materials in Lithium-Ion Batteries.**
ISBN 978-3-7315-0455-9
- Band 55 Thomas Straub
**Experimental Investigation of Crack Initiation in
Face-Centered Cubic Materials in the High and
Very High Cycle Fatigue Regime.**
ISBN 978-3-7315-0471-9

- Band 56 Maren Lepple
Kupfer- und Eisenoxide als Konversions-Elektrodenmaterialien für Lithium-Ionen-Batterien: Thermodynamische und Elektrochemische Untersuchungen.
ISBN 978-3-7315-0482-5
- Band 57 Stefan Andreas Slaby
Charakterisierung und Bewertung der Zug- und Ermüdungseigenschaften von Mikrobauteilen aus 17-4PH Edelstahl. Ein Vergleich von mikropulverspritzgegossenem und konventionell hergestelltem Material.
ISBN 978-3-7315-0484-9
- Band 58 Kumar Ankit
Phase-field modeling of microstructural pattern formation in alloys and geological veins.
ISBN 978-3-7315-0491-7
- Band 59 Kuo Zhang
Characterization and Modeling of the Ratcheting Behavior of the Ferritic-Martensitic Steel P91.
ISBN 978-3-7315-0503-7
- Band 60 Nicht erschienen
- Band 61 Fabian Lemke
Untersuchung des Sinterverhaltens von SrTiO₃ unter Berücksichtigung der Defektchemie.
ISBN 978-3-7315-0510-5
- Band 62 Johannes Kümmel
Detaillierte Analyse der Aufbauschneidenbildung bei der Trockenerspannung von Stahl C45E mit Berücksichtigung des Werkzeugverschleißes.
ISBN 978-3-7315-0518-1
- Band 63 László Hagymási
Modellierung der Stoffübertragung beim Niederdruckcarbonitrieren mit Ammoniak und Acetylen.
ISBN 978-3-7315-0568-6
- Band 64 Reza Eslami
A novel micro-mechanical model for prediction of multiaxial high cycle fatigue at small scales.
ISBN 978-3-7315-0583-9

- Band 65 Sebastian Schulz
Phase-field simulations of multi-component solidification and coarsening based on thermodynamic datasets.
ISBN 978-3-7315-0618-8
- Band 66 Markus Stricker
Die Übertragung von mikrostrukturellen Eigenschaften aus der diskreten Versetzungsdynamik in Kontinuumsbeschreibungen.
ISBN 978-3-7315-0658-4
- Band 67 Luis Straßberger
Untersuchung und Modellierung des viskoplastischen Verformungsverhaltens oxidpartikelverstärkter Stähle.
ISBN 978-3-7315-0674-4
- Band 68 Mark Wobrock
Microplasticity of idealized single crystalline Ag cantilevers characterized with methods of high resolution.
ISBN 978-3-7315-0682-9
- Band 69 Amritesh Kumar
Micromechanical study on the deformation behaviour of directionally solidified NiAl-Cr eutectic composites.
ISBN 978-3-7315-0694-2
- Band 70 Johannes Hötzer
Massiv-parallele und großskalige Phasenfeldsimulationen zur Untersuchung der Mikrostrukturentwicklung.
ISBN 978-3-7315-0693-5
- Band 71 Thomas Hupfer
Herstellung von LATP für den Einsatz als Festkörperelektrolyt und dessen Eigenschaften.
ISBN 978-3-7315-0702-4
- Band 72 Florentin Pottmeyer
Schädigungsverhalten von in CFK-Laminaten eingebetteten Inserts unter bauteilnahen Beanspruchungen.
ISBN 978-3-7315-0719-2
- Band 73 Andres Höweling
Untersuchung der Hochvoltstabilität und Tiefentladung von dotierten $\text{LiNi}_{0,5}\text{Mn}_{1,5}\text{O}_4$ -Hochvoltspinellen.
ISBN 978-3-7315-0728-4

- Band 74 Tabea Gisela Schwark
Deformation and Fracture Properties of the Soft Magnetic Composite Somaloy 700 3P on Different Length Scales.
ISBN 978-3-7315-0759-8
- Band 75 Klaudia Lichtenberg
Metallmatrixverbunde mit Verstärkungselementen aus metallischem Glas $\text{Ni}_{60}\text{Nb}_{20}\text{Ta}_{20}$ – Herstellung und Charakterisierung.
ISBN 978-3-7315-0782-6
- Band 76 Claudio Findeisen
Charakterisierung und Modellierung von instabilen Metamaterialien.
ISBN 978-3-7315-0869-4
- Band 77 Nilesha Mishra
Influence of strain on the functionality of ink-jet printed thin films and devices on flexible substrates.
ISBN 978-3-7315-0853-3
- Band 78 Simon Werner Bonk
Plastische Verformungsmechanismen in hochgradig kaltgewalzten, ultrafeinkörnigen Wolframblechen.
ISBN 978-3-7315-0878-6
- Band 79 Tim Gräning
Herstellung, Charakterisierung und Optimierung von austenitischen ODS Stählen.
ISBN 978-3-7315-0732-1
- Band 80 Peter Rupp
Herstellung, Prüfung und Modellierung neuartiger hybrider Aluminiumschaum-CFK-Sandwichverbunde.
ISBN 978-3-7315-0880-9
- Band 81 Benjamin Sebastian Ehreiser
Einfluss mechanischer Lasten auf die Herstellung von Stahl-Glaskeramik-Verbunden.
ISBN 978-3-7315-0954-7
- Band 82 Hans Giel
Weiterentwicklung experimenteller Methoden zur Ermittlung thermodynamischer Werkstoffdaten von Lithium-Ionen-Batterien.
ISBN 978-3-7315-0981-3

- Band 83 Anna Trauth
Characterisation and Modelling of Continuous-Discontinuous Sheet Moulding Compound Composites for Structural Applications.
ISBN 978-3-7315-0950-9
- Band 84 Jonas Johannes Hüther
The Impact of Recycling on the Fibre and the Composite Properties of Carbon Fibre Reinforced Plastics.
ISBN 978-3-7315-0983-7
- Band 85 Nicolas A. Mayer
Thermodynamik von Kobaltoxid Anodenmaterialien für Lithium-Ionen-Batterien und ihr elektrochemisches Verhalten.
ISBN 978-3-7315-0996-7
- Band 86 Ulrich Führer
Untersuchung und Modellierung des Haltezeiteinflusses auf die zyklische Entfestigung ferritisch-martensitischer Stähle.
ISBN 978-3-7315-0837-3
- Band 87 Ebru Cihan
Structure evolution in tribological interfaces studied by multilayer model alloys.
ISBN 978-3-7315-0999-8
- Band 88 Markus Sudmanns
Entwicklung einer Kontinuumsbeschreibung für die Versetzungsmobilität in Versetzungsnetzwerken.
ISBN 978-3-7315-1001-7
- Band 89 Tao Zhang
Phase-field Modeling of Phase Changes and Mechanical Stresses in Electrode Particles of Secondary Batteries.
ISBN 978-3-7315-1002-4
- Band 90 Markus Ganser
On the Electro-Chemo-Mechanical Coupling in Solid State Batteries and its Impact on Morphological Interface Stability.
ISBN 978-3-7315-1047-5

- Band 91 Michael Kellner
Modellierung mehrkomponentiger Materialsysteme für die Phasenfeldmethode und Analyse der simulierten Mikrostrukturen.
ISBN 978-3-7315-1044-4
- Band 92 Felix Schröckert
Herstellung dünner Folien aus Lithium-Lanthan-Titanat zur Anwendung als Festkörperelektrolyt.
ISBN 978-3-7315-1008-6
- Band 93 Ephraim Schoof
Chemomechanische Modellierung der Wärmebehandlung von Stählen mit der Phasenfeldmethode.
ISBN 978-3-7315-1050-5
- Band 94 Alexander Valentin Brabänder
Registrierende Härtemessung an neutronenbestrahlten Materialien bei hohen Temperaturen.
ISBN 978-3-7315-1097-0
- Band 95 Denny Schmidt
Einfluss der Kompaktierung auf die Elektrodenmikrostruktur und elektrochemische Performance bei Lithium-Ionen-Zellen.
ISBN 978-3-7315-1098-7
- Band 96 Svenja Dittrich
Entwicklung von Siebdruckpasten zur Herstellung von Glaslotfugungen für die Festoxidbrennstoffzelle.
ISBN 978-3-7315-1085-7
- Band 97 Michael Dippon
Bestimmung der Betriebsgrenzen für das Schnellladen von Lithium-Ionen Batterien.
ISBN 978-3-7315-1123-6
- Band 98 Patricia Haremski
Diffusionseigenschaften von Nickel in einer Festoxid-Brennstoffzelle.
ISBN 978-3-7315-1124-3
- Band 99 Florian Wankmüller
Mehrskalige Charakterisierung der Hochtemperatur-Brennstoffzelle (SOFC).
ISBN 978-3-7315-1142-7

- Band 100 Niklas Russner
Modellgestützte Analyse des Stackbetriebs von Festoxidzellen.
ISBN 978-3-7315-1144-1
- Band 101 Theo Fett, Karl G. Schell, Ethel C. Bucharsky, Gabriele Rizzi, Pascal Hettich, Susanne Wagner, Michael J. Hoffmann
Consequences of hydroxyl generation by the silica/water reaction – Part I: Diffusion and Swelling.
ISBN 978-3-7315-1148-9
- Band 102 Theo Fett, Karl G. Schell, Ethel C. Bucharsky, Gabriele Rizzi, Susanne Wagner, Michael J. Hoffmann
**Consequences of hydroxyl generation by the silica/water reaction – Part II: Global and local Swelling
Part III: Damage and Young's Modulus.**
ISBN 978-3-7315-1159-5
- Band 103 Johannes Dornheim
Modellfreies Lernen optimaler zeitdiskreter Regelungsstrategien für Fertigungsprozesse mit endlichem Zeithorizont.
ISBN 978-3-7315-1158-8
- Band 104 Markus Muth
Grundlagenuntersuchungen an intrinsisch gefertigten lasttragenden FVK/Metall-Hybridträgern.
ISBN 978-3-7315-1161-8
- Band 105 Oleg Birkholz
Modeling transport properties and electrochemical performance of hierarchically structured lithium-ion battery cathodes using resistor networks and mathematical half-cell models.
ISBN 978-3-7315-1172-4
- Band 106 Verena Irene Becker
Modellierung der Mechanik und der effektiven Transporteigenschaften von partikulären Kathoden sowie deren Einfluss auf die elektrochemische Performance von Lithium-Ionen-Batterien.
ISBN 978-3-7315-1174-8
- Band 107 Nikolai Zimmer
Nanoskalige Analytik der Mikrostruktur von hochdosig bestrahltem Beryllium.
ISBN 978-3-7315-1178-6

- Band 108 Francesco Mazzocchi
Development of NbN based Kinetic Inductance Detectors on sapphire and diamond substrates for fusion plasma polarimetric diagnostics.
ISBN 978-3-7315-1181-6
- Band 109 Adrian Schmidt
Multiskalige Modellierung von Lithium-Ionen-Batterien.
ISBN 978-3-7315-1227-1
- Band 110 Maximilian Röhe
Dynamic Model-based Analysis of Oxygen Reduction Reaction in Gas Diffusion Electrodes.
ISBN 978-3-7315-1234-9
- Band 111 Michael Späth
Phasenfeldmodellierung von Bruchbildungs-, Kristallisations- und Auflösungsvorgängen in hydrothermalen Umgebungen.
ISBN 978-3-7315-1242-4
- Band 112 Friedemann Streich
Numerische Modellierung und Simulation von bleifreien Relaxor-Ferroelektrikum-Kompositen.
ISBN 978-3-7315-1259-2
- Band 113 Paul S. Zielonka
Entwicklung und Charakterisierung von Siliziumnitrid-/Siliziumkarbidkompositen für den Einsatz in tribologisch hochbeanspruchten Gleitsystemen.
ISBN 978-3-7315-1269-1
- Band 114 Carsten Bonnekoh
Der Spröd-duktil-Übergang in ultrafeinkörnigem Wolfram.
ISBN 978-3-7315-1264-6
- Band 115 Marcel Heinzmann
Analyse und Modellbildung von PEM-Brennstoffzellen mittels elektrochemischer Impedanzspektroskopie.
ISBN 978-3-7315-1319-3
- Band 116 Felix Sutter
Materiell nichtlineare Kontinuumsmodellierung ferroelektrischer Funktionskeramiken mit piezoelektrischen und flexoelektrischen Eigenschaften.
ISBN 978-3-7315-1337-7

- Band 117 Lukas Schöller
Multiscale Modeling of Curing and Crack Propagation in Fiber-Reinforced Thermosets.
ISBN 978-3-7315-1340-7
- Band 118 Benjamin Hauck
Impedanzbasierte Spannungsprädiktion von Lithium-Ionen-Batterien.
ISBN 978-3-7315-1347-6
- Band 119 Yannick Lingelbach
Application of Data Mining and Machine Learning Methods to Industrial Heat Treatment Processes for Hardness Prediction.
ISBN 978-3-7315-1352-0
- Band 120 Philipp Lied
Steigerung der thermischen Stabilität von warm- und kaltgewalztem Wolfram durch Kalium-Dotierung für die Fusionsenergie-technik.
ISBN 978-3-7315-1356-8
- Band 121 Paul Wilhelm Hoffrogge
Understanding Degradation Phenomena in Solid-Oxide Fuel-Cell Anodes by Phase-Field Modeling and Analytics.
ISBN 978-3-7315-1363-6

KARLSRUHER INSTITUT FÜR TECHNOLOGIE (KIT)
SCHRIFTENREIHE DES INSTITUTS FÜR ANGEWANDTE MATERIALIEN

Numerical and analytical methods are applied to enable quantitative microstructure modeling in a broad category of material systems. An existing multiphase-field model for multicomponent systems is augmented with an interface diffusion term. The model is consistent with an extended interfacial balance as well as surface diffusion theory for a vanishing interface thickness. Analytical predictions of high order shed light on the influence of interpolation functions in phase-field models of obstacle type. The extended multiphase-field model is applied to Ni-YSZ solid-oxide fuel cell anodes. Extensive large-scale 3D-simulations deliver insights regarding the influence of the composition of the anode material on important properties and their temporal evolution. This facilitates prediction of anode-sided degradation and leads to a better understanding of the underlying phenomena.

ISSN 2192-9963
ISBN 978-3-7315-1363-6

